Politecnico di Torino

ScuDo
Scuola di Dottorato ~ Doctoral School
WHAT YOU ARE, TAKES YOU FAR

Doctoral Dissertation
Doctoral Program in Mechanical Engineering (38^{th}cycle)

Analysis of fuel cell systems for off-road agricultural vehicles

By

Valerio Martini

******

Supervisor(s):
Prof. Aurelio Somà, Supervisor
Prof. Francesco Mocera, Co-Supervisor

Doctoral Examination Committee:
Prof. Carmine Maletta, Referee, Università della Calabria
Prof. Francesco Frendo, Referee, Università degli Studi di Pisa

Politecnico di Torino
2026

Declaration

I hereby declare that, the contents and organization of this dissertation constitute my own original work and does not compromise in any way the rights of third parties, including those relating to the security of personal data.

Valerio Martini
2026

* This dissertation is presented in partial fulfillment of the requirements for **Ph.D. degree** in the Graduate School of Politecnico di Torino (ScuDo).

I would like to dedicate this thesis to everyone who supported me throughout these years. My family, who always believed in me and pushed me to follow my ambitions and my dreams. My closest friends, who helped me live these intense years in a lighter and happier way. My colleagues, who have been helpful from both a professional and a personal point of view. Lastly, I would like to dedicate this work to Iris, the love of my life and my greatest supporter.

Acknowledgements

I would like to express my sincere gratitude to my supervisors, Prof. Aurelio Somà and Prof. Francesco Mocera, for their guidance and support throughout the whole research. I would also like to thank my research colleagues at DIMEAS department and the whole team of Ecothea, whose support was indispensable to this work.

Abstract

To improve the sustainability of agriculture, hybrid fuel cell systems have gained attention due to their properties featuring zero local emissions, high energy density, low refueling time, and high efficiency. The research activity focused on the analysis of fuel cell systems applied to agricultural vehicles.

Starting from a case study of an orchard tractor, a hybrid fuel cell powertrain was designed considering the vehicle constraints. Numerical models of both the traditional and the fuel cell powered vehicles were developed in MATLAB/Simulink environment, and a monitoring campaign was conducted on a traditional vehicle during the most common workday activities. The extrapolated load profiles were used to perform numerical simulations and compare the performance of the two solutions. The results demonstrated that the fuel cell tractor can exhibit almost the same performance as the traditional counterpart, but with a relevant reduction of -50% on average in the use phase equivalent CO_2 emissions, even considering grey hydrogen. The analysis was then expanded to the whole life cycle of the two vehicles, according to a cradle-to-grave approach, and including different impact categories. The results showed that the fuel cell tractor can significantly reduce the total life cycle emissions, with reductions ranging from -60 to -95% depending on the considered category. A further reduction in some categories can be obtained using green hydrogen.

Subsequently, a scaled Hardware-in-the-loop test bench was developed for powertrain emulation, and several tests were conducted considering different hybrid fuel cell system topologies: fuel cell + battery, fuel cell + battery + supercapacitors, and fuel cell + supercapacitors. The three alternatives were designed considering the same overall volume and the same fuel cell system. To test different energy management strategies, both a power follower and a fuzzy logic control algorithms were developed for each configuration. Given the load profiles derived from the

previously mentioned monitoring campaign, the three architectures were compared in terms of fuel economy and durability. The results showed that the architecture fuel cell + battery outperformed the other two in terms of expected fuel cell system durability, while no relevant differences were noted in fuel economy. In addition, it was noted that the control strategy had a non-negligible impact on durability.

In the last part of the research activity, a hybrid fuel cell powertrain for an autonomous driving rover, specifically designed for orchards, was developed. A co-simulation model was established, including the rover multibody model, the autonomous driving algorithm and the powertrain model. To develop the numerical model of the powertrain, experimental tests were carried out on the fuel cell system and the hydrogen tank. Numerical simulations considering common work scenarios were performed, showing potential in terms of endurance improvements. Next, a full-scale Hardware-in-the-loop test bench was developed to test the physical hardware of the powertrain. Once validated the hardware, the fuel cell and the tank were implemented on the rover prototype, and experimental tests on the rover were conducted. The results showed that the unit operated as expected and significantly extended the rover endurance.

Introduction

The awareness of the negative effects of anthropic activities on environment, human health, and economics is pushing both the academic and industrial worlds towards the analysis and implementation of more sustainable solutions. In this context, agriculture is an important source of emissions. According to the most recent studies, it is responsible for around 20-25% of the total CO_2 equivalent emissions. At the same time, it plays a key role in the food supply chain and must ensure the food demand of a growing population.

Consequently, it is critical to reduce its impact without negatively affecting productivity. Traditional agricultural machinery is powered with oversized Diesel engines, which generally operate far from their optimal point and emit several pollutants and greenhouse gases at the exhaust. Taking into account this premise, a feasible solution to achieve both sustainability and productivity is represented by the substitution of traditional machinery with innovative systems, including alternative powertrain and autonomous vehicles. Electrification demonstrated in many applications that the overall performance of a vehicle can be improved, reducing the amount of pollutant emissions. Into detail, fuel cell hybrid powertrain are a promising solution in those cases where compactness and endurance are critical. Indeed, they feature zero local emission levels, higher efficiency compared to thermal engines, and higher energy density and low refueling time compared to pure battery solutions. The present work focused on the analysis of fuel cell systems for agricultural off-road vehicles, in particular for orchard applications, with the aim of investigating their potential in reducing emissions without reducing the vehicle performance. The adopted approach involved both numerical analysis, thus numerical models were developed and simulations were carried out, and experimental analysis, in particular using hardware-in-the-loop technique.

The implementation of alternative systems to replace the traditional powertrain of a vehicle, however, is not the only feasible solution to improve the efficiency and sustainability of agricultural practices. Indeed, low-power tasks can be performed using autonomous driving rovers, which can complete the mission with significant improvements in terms of cost reduction, resource optimization and operational efficiency. As a consequence, these systems have gained attention in the last years, and their diffusion has been increasing. These rovers, apart few prototypes, are generally powered using a pure battery electric powertrain. However, the limited endurance related to the limited energy density of batteries is a critical aspect and, at present, a strong barrier to their widespread adoption. In this context, fuel cell systems can be used to extend the rover autonomy. According to this, given a case study of an autonomous driving rover specifically designed for orchards, thus for replacing the traditional orchard tractor, a fuel cell range extender unit was developed and, after numerical and experimental validation on a test bench of the configuration, it was implemented on the rover prototype. Experimental tests on the rover were performed, outlining that the adoption of fuel cell systems can be a promising solution to extend rovers autonomy.

The thesis work is structured as follows: Chapter 1 describes the current state of the art of fuel cell systems applied to off-road vehicles, Chapter 2 presents the case study, namely an orchard tractor, and a numerical analysis of a fuel cell powered vehicle with a view to compare its performance and environmental impact with those of a traditional vehicle, Chapter 3 describes the development of a Hardware-in-the-loop test bench for hybrid fuel cell powertrain emulation and presents a comparative analysis of different architectures to find the best configuration for the orchard tractor, Chapter 4 introduces the application of agricultural rovers to substitute tractors in low power tasks and field operations, and present the development and experimental analysis of the Smilla H2 prototype, a rover designed for orchards featuring a hybrid fuel cell powertrain, lastly Chapter 5 summarizes the conclusions and describes the possible future works.

Contents

List of Figures

List of Tables

Chapter 1

Overview of the application of fuel cell systems for off-road vehicles.

Today, increasing awareness about the impact of anthropic activities on the environment and human health is pushing both the industrial and academic worlds towards the investigation of innovative and alternative solutions to produce and convert energy. The adoption of fossil fuels is a widely used solution to satisfy the demand for energy. In vehicular applications, especially off-road vehicles, also known as Non-road Mobile Machineries (NRMMs), internal combustion engines (ICEs) are, at present, the most adopted solution to generate power on-board to propel the vehicles and to satisfy the power required by the auxiliaries. However, the mandatory need to mitigate the climate change effects is causing a growing interest in alternative propulsion systems, such as hybrid-electric, full-electric, and hybrid fuel cell powertrain. Fuel cell hybrid solutions are emerging due to their characteristics, featuring zero-local emissions, high energy density, high efficiency and the possibility to be re-filled within a few minutes. These properties are of particular interest for NRMMs, as these vehicles, depending on the specific case, might have to satisfy several constraints in terms of compactness, endurance, and productivity.

1.1 Fuel cell systems principles.

Fuel cell systems are electrochemical systems that produce direct current electricity through the reaction of a fuel (generally hydrogen, but other fuels can be used)

and an oxidant (usually oxygen in ambient air) [1]. There are many types of fuel cell available on the market, with different properties in terms of efficiency, power densities, and operating temperatures, that lead to different application fields. Due to their being electrochemical systems that exploit redox reactions to generate electrical power, fuel cells are usually composed of an anode and a cathode, with their own catalyst layers, and electrolyte material, and are generally classified according to this last element. According to the literature [1, 2], the most relevant types of fuel cells, with their main characteristics, are listed and described below:

- **Low-temperature proton exchange membrane**: the electrolyte material is generally solid Nafion®and the typical anode and cathode catalyst is platinum supported on carbon; the operating temperature is below 100 °C and the fuel used is usually hydrogen; the electrical efficiency is in the range 40-60 %; these systems are characterized by high power density, compactness and rapid start-up time, however they require complex water and thermal management systems and are sensitive to contaminants; these systems are the most promising technology for vehicular applications.
- **High-temperature proton exchange membrane**: the electrolyte material is made of solid composite Nafion®or polybenzimidazole doped in phosphoric acid, the typical anode and cathode catalyst is platinum-ruthenium supported on carbon; the operating temperature is 110-180 °C and the fuel used is usually hydrogen; the electrical efficiency is in the range 50-60 %; these systems are characterized by simple water and thermal management systems and high tolerance to contaminants, however fast degradation and humidification issues are among their main disadvantages.
- **Solid oxide**: the electrolyte material is solid yttria-stabilized zirconia (YSZ), the typical anode catalyst is Nickel-YSZ composite and the cathode catalyst is Strontium-doped lanthanum manganite; the operating temperature is up to 1000 °C and the fuel used is usually methane; the electrical efficiency is in the range 55-65 %; these systems are characterized by high electrical efficiency, possibility of internal reforming, high tolerance to contaminants and fuel flexibility, however there are some disadvantages related to slow start-up, low power density, high thermal stress, durability and sealing issues, thus are mainly used as stationary power generators.

- **Molten carbonate**: the electrolyte material is generally liquid alkali carbonate in Lithium aluminate, the typical anode catalyst is Nickel-Chromium and the cathode catalyst is lithiated Nickel oxide; the operating temperature is in the range 600-700 °C and the fuel used is usually methane; the electrical efficiency is in the range 55-65 %; these systems are characterized by high electrical efficiency, possibility of internal reforming, high tolerance to contaminants and fuel flexibility, while the main disadvantages are related to slow start-up, low power density, corrosion issues, catalyst dissolution and air crossover; these systems are generally used for high power applications.

- **Phosphoric acid**: the electrolyte material is generally concentrated liquid phosphoric acid in silicon carbide, the typical anode and cathode catalyst is platinum supported on carbon; the operating temperature is around 180 °C and the fuel used is usually hydrogen; the electrical efficiency is in the range 36-45 %; these systems are characterized by a mature and reliable technology, with a simple water management, however the main issues are related to slow start-up time, low power density, expensive and bulky auxiliary systems and poor electrical efficiency compared to other fuel cell technologies; these systems are generally adopted as stationary power generators.

- **Alkaline**: the electrolyte material is generally an anion exchange membrane, the typical anode catalyst is Nickel, while the cathode catalyst is silver supported on carbon; the operating temperature ranges from below zero to more than 200 °C and the fuel used is usually hydrogen; the electrical efficiency is in the range 60-70 %; these systems are characterized by high efficiency, wide range of operating temperatures and pressures, and relatively low cost, on the other hand they are extremely sensitive to contaminants, are characterized by low power density and have some issues related to sealing and electrolyte management; they are mainly used as standalone power generators.

- **Direct methanol**: the electrolyte material is usually solid Nafion®, the typical anode catalyst is platinum-ruthenium supported on carbon and the cathode catalyst is platinum supported on carbon; the operating temperature ranges from ambient temperature to approximately 100 °C and the fuel used is liquid methanol-water solution; the electrical efficiency is in the range 35-60 %; these systems are characterized by compactness, simplicity and easy fuel delivery and storage, however their main disadvantages related to low power

density, low voltage, poor efficiency, fuel toxicity and high cost relegate them to low-power portable applications.

It can be stated, due to their properties, that low-temperature proton exchange membrane fuel cells are the most interesting and adopted systems for vehicular applications. In particular, compactness, rapid start-up, high power density and low operating temperatures are the main reasons behind their applicability for vehicle propulsion.

1.1.1 Low-temperature proton exchange membrane fuel cells

Focusing on this technology of fuel cells, the single cell is composed of an anode, which is generally fed using pure hydrogen, a cathode, fed with oxygen coming from ambient air, a proton-exchange membrane and the gas diffusion layers. The membrane is generally made of Nafion®, developed by DuPont in the late 1960s, mainly due to its high conductivity, good chemical, mechanical and thermal properties [3]. Both the anode and cathode feature the presence of a catalyst, which is usually platinum supported on carbon. A schematic representation of the single cell structure is represented in Figure 1.1.

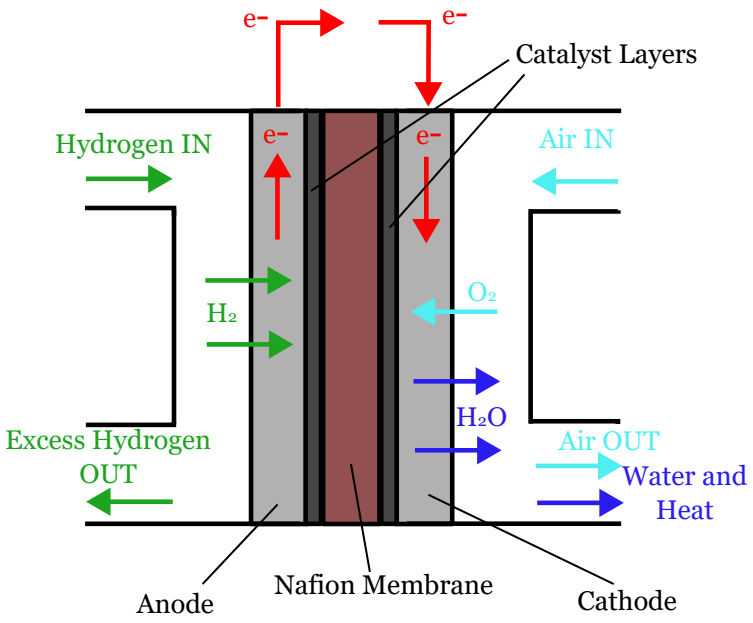

Figure 1.1 Schematic representation of a single proton exchange membrane fuel cell (PEMFC).

The electrochemical reactions that occur on both sides at the electrodes in a PEMFC are the following [4]:

$$Anode: \quad 2H_2 + 4nH_2O \rightarrow 4H^+ \cdot nH_2O + 4e^- \tag{1.1}$$

$$Cathode: \quad O_2 + 4^+ \cdot nH_2O + 4e^- \rightarrow (n+2)H_2O \tag{1.2}$$

$$Overall: \quad O_2 + H_2 \rightarrow H_2O \tag{1.3}$$

The single cell is characterized by a polarization curve, which is a Voltage-Current curve, that represents the voltage level according to the current density. The equation that describes the polarization curve is the following [1]:

$$V_{cell} = E_{Nernst} + V_{act} + V_{conc} + V_{ohm} \tag{1.4}$$

Where V_{cell} is the cell voltage, E_{Nernst} is the Nernst voltage, V_{act} is the voltage drop due to the activation of the process, V_{conc} is the voltage drop resulting from the reduction in the concentration of reactant gasses and V_{ohm} is the voltage drop due to ohmic losses. The open circuit voltage of a fuel cell is less than the theoretical ideal voltage and, for a single cell, is generally around 1 V. A typical polarization curve is shown in Figure 1.2. The figure also shows the voltage loss mechanism that causes the local trend of the curve.

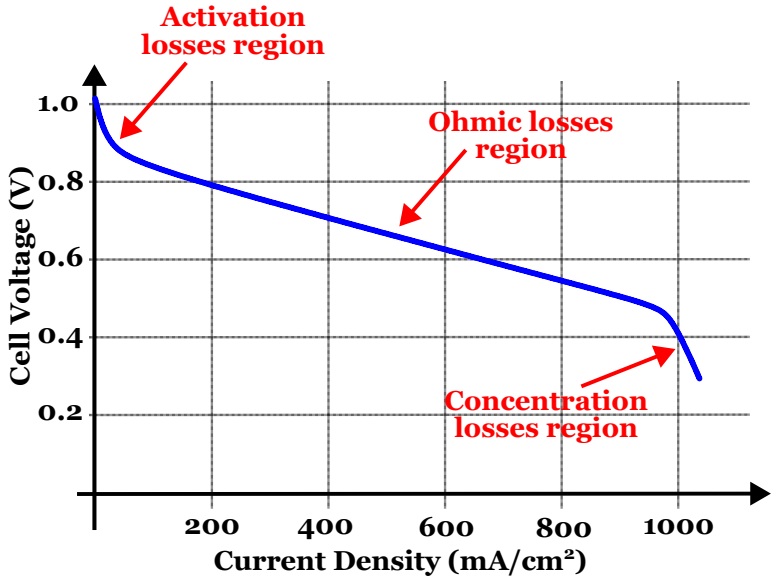

Figure 1.2 Typical polarization curve of a single PEMFC.

As a consequence, to produce enough output voltage, several cells are connected in series and stacked to form a fuel cell stack. From a structural point of view, a PEM fuel cell stack consists of the following elements [5]:

- **Membrane electrode assembly (MEA)**: it consists of the two electrodes separated by the electrolyte; the catalyst layers of the electrodes are in direct contact with the electrolyte, followed by a microporous layer and a gas diffusion layer.
- **Gaskets**: they are required to prevent gas leakage and to keep hydrogen, oxygen, and coolant isolated from each other.
- **Bipolar plates**: they enable the electrical connection of more fuel cell units acting as current collector and providing mechanical support.

According to the actual state-of-the-art of commercial PEM fuel cells [6], the typical thicknesses and material used for the stack are shown in Table1.1.

Table 1.1 Typical thicknesses and materials of commercial PEM fuel cells.

Element	Material	Thickness
Electrolyte	Nafion®	0.01-0.1 mm
Catalyst layers	Carbon-supported Platinum	0.1-50 μm
Gas diffusion layer	Carbon fiber-based porous paper	0.1-0.4 mm
Microporous layer	Carbon black and PTFE binder	0.05 mm
Bipolar plate	Carbon-based composites	0.3-2 mm

However, the fuel cell stack requires a certain number of subsystems to operate in a proper way. These subsystems, combined with the fuel cell stack, constitute the complete fuel cell systems. The set of subsystems is also known as the Balance of Plant (BoP) of the fuel cell system, and is generally made up of the following elements [7]:

- **Hydrogen supply system**: it must supply hydrogen at the anode of the stack with the correct pressure level; its main components generally are a pressure regulator, a solenoid valve, a recirculation system (based on either a pump or an ejector) and a purge valve.

- **Air supply system**: it is usually composed of an air compressor, a air filter, a backpressure valve, an intercooler and, in some solutions, a humidifier; the air compressor is a key element that has a huge impact on system efficiency and should be controlled to guarantee a certain value of Oxygen Excess Rate (OER) [8].
- **Heat management system**: it is generally composed of a coolant tank, a pump, pipes, and a radiator; the proper design of the heat management system is crucial since temperature affects gas transport mechanisms, membrane hydration, and electrochemical balance [9].
- **Water management system**: it consists mainly of humidifiers and a water tank;it is required since the control of the membrane humidity is mandatory in order to enhance the durability of the stack.

The BoP generally absorbs, depending on the work conditions, around 10-20% of the nominal stack power, with the air compressor being the most impactful element in terms of power required [10, 11]. A typical configuration of a whole fuel cell system, comprising its BoP, is shown in Figure1.3. The green color represents the hydrogen supply system, the orange the heat management system, the blue the air supply system, and the light blue the water management system.

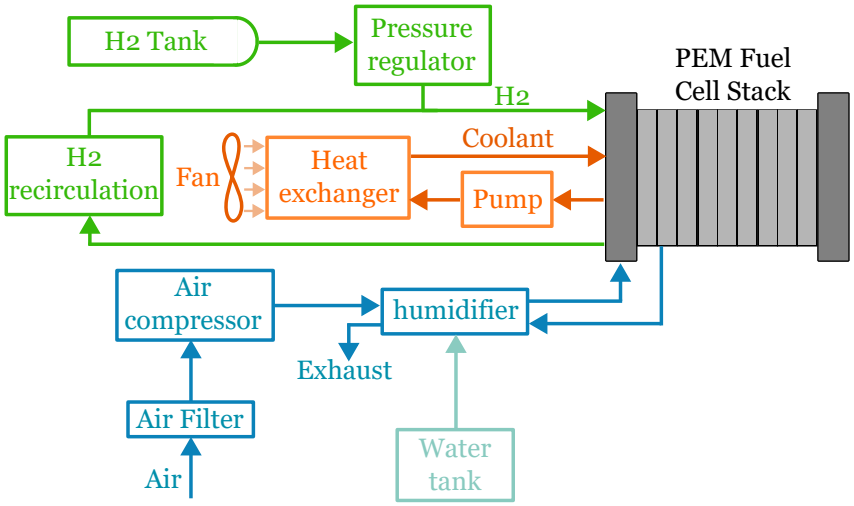

Figure 1.3 Typical configuration of a complete PEMFC system.

It should be noted that this is one of the possible solutions for a fuel cell system, however other designs might be adopted. For example, Toyota developed for the

Toyota Mirai a fuel cell system without an external humidifier [12]. In this case, humidification is guaranteed using an internal circulation system in which the water generated downstream of the cathode is returned upstream of it.

1.2 Hydrogen production

Hydrogen production is a key element for large-scale commercialization of fuel cell systems and, furthermore, has a significant impact in terms of environmental impact of such technology. Indeed, hydrogen can be produced through several different methods, both using non-renewable and renewable sources. From an environmental point of view, hydrogen production methods that exploit renewable sources should be preferred. Nevertheless, according to [13], at present most of the hydrogen is produced from fossil fuels. The most adopted production method is Steam Methane Reforming (SMR), which represents more than 60% of global hydrogen production, followed by coal gasification, as shown in Figure 1.4. Around 15% instead is produced as a by-product in petrochemical industries and refineries. Low-emission methods, namely hydrogen from renewable sources or hydrogen produced by SMR but with carbon capture technology, account for less than 1% of the total production. Into detail, compared to the total 2023 hydrogen production of 97 Mt of H_2, less than 100 kt was green hydrogen, namely hydrogen from water electrolysis.

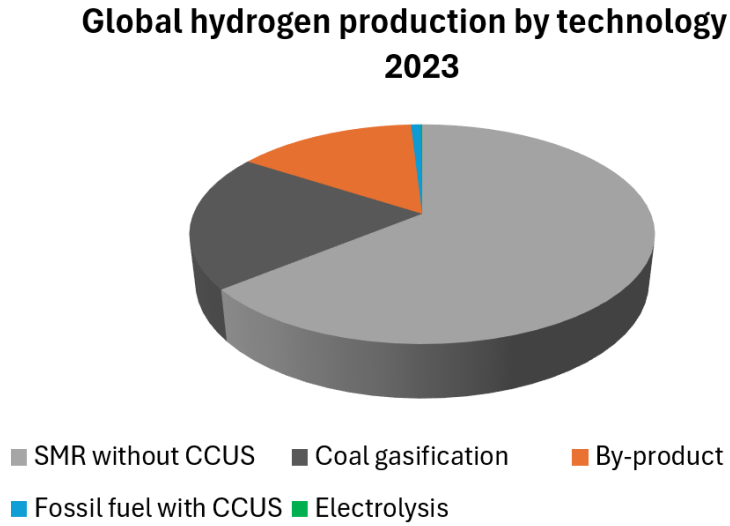

Figure 1.4 Global hydrogen production by technology in 2023 according to the report of the International Energy Agency.

Globally, the most important country in terms of hydrogen production is China, which accounts for about 30% of the total, followed by the United States of America and India, respectively with 14% and 9%. In addition, the Middle East region contributes with approximately 14% to the total production. The global hydrogen production by region is shown in Figure 1.5.

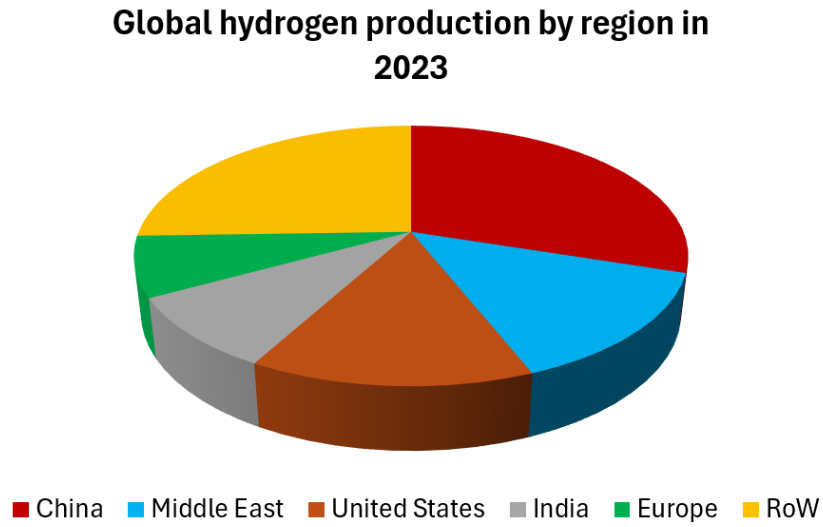

Figure 1.5 Global hydrogen production by region in 2023 according to the report of the International Energy Agency.

1.2.1 Hydrogen from fossil fuels

As previously stated, most of the hydrogen is, at present, produced from fossil fuels. Several methods can be used, however the most adopted one is the steam methane reforming. This process is usually carried out using precious metals or Ni-based materials as catalysts and is performed at temperatures up to 800°C. The process consists of the following steps: firstly methane and water vapor undergo a reforming reaction to produce syngas (mainly composed of H_2 and CO), followed by CO conversion through the water-gas shift reaction, then CO_2 is removed from the gas mixture using an adsorption system to enhance the purity of the hydrogen gas [14]. The whole process has an efficiency ranging from 70 to 85%. The main reactions (excluding the process regarding the removal of CO_2) of the process are the following:

$$CH_4 + H_2O \rightarrow CO + 3H_2 \tag{1.5}$$

$$CO + H_2O \rightarrow CO_2 + H_2 \tag{1.6}$$

SMR is a mature technology, even if improvements, for example reforming at low temperature, are under investigation. In addition, interest in the application of carbon capture technologies to reduce the carbon footprint of the process is increasing significantly.

Another relevant hydrogen production method from fossil fuel resources is Coal Gasification (CG). The most widely adopted solution is surface coal gasification, which mainly consists of drying and grounding the coal, which is then fed into a gasifier where it reacts at high temperatures with oxygen and steam to produce a gas mixture composed mainly of H_2, CO and CO_2 [14]. The main reactions are the following:

$$C + O_2 \rightarrow CO_2 \tag{1.7}$$

$$C + H_2O \rightarrow CO + H_2 \tag{1.8}$$

CG is also a mature technology and accounts for approximately 20% of total hydrogen production. Nevertheless, since its efficiency is lower compared to SMR, it is not used as widely as it. However, it is of particular interest for those countries where coal is abundant and/or the price of natural gas is high. Another important issue related to CG is its high environmental impact. Also in this case, carbon capture technologies can be used to reduce the carbon footprint of the process.

In addition to SMR and CG, there are other hydrogen production methods from fossil fuels, such as partial oxidation of methane, autothermal reforming and partial oxidation of oil products. In the first case, hydrogen is produced by incomplete oxidation of methane, which gives a mixture of H_2 and CO, with oxygen input at less than stoichiometric ratio. As for the autothermal reforming, it can be seen as a combination of both partial oxidation of methane and steam reforming. Indeed, the heat produced by the partial oxidation of natural gas is used to achieve steam reforming. Finally, partial oxidation of oil products is a useful method than can be exploited to produce hydrogen from feed stocks with high carbon-to-hydrogen

ratios. The process requires pure oxygen below the stoichiometric ratio as input and produces a mixture of CO and H_2 at high temperature (more than 1000 °C).

1.2.2 Hydrogen from water electrolysis

Water electrolysis allows for the production of hydrogen from water, with an input of direct current. To achieve this, electrolyzers are used as they perform the reverse reaction of a fuel cell, thus decomposing water to obtain H_2 and oxygen using electric power. Commonly used electrolyzers are based on PEM or alkaline technology. According to [13], in 2023 more than 60% of the total installed electrolyzer capacity was with alkaline technology, while PEM technology followed with 22%. The most important producers of hydrogen using electrolysis are China, Europe, and the United States

The reactions that take place to produce hydrogen in the alkaline electrolyzer are the following:

$$Anode: \quad 2H_2O \rightarrow O_2 + 4H^+ + 4e^- \tag{1.9}$$

$$Cathode: \quad 4H_2O + 4e^- \rightarrow 2H_2 + 4OH^- \tag{1.10}$$

$$Overall: \quad H_2O \rightarrow O_2 + H_2 \tag{1.11}$$

The biggest difference between alkaline and PEM electrolyzers is that in the latter the charge carriers in the electrolyte are hydrogen ions and not hydroxide ions. Indeed, in a PEM electrolyzer the following reactions occur:

$$Anode: \quad 2H_2O \rightarrow O_2 + 4H^+ + 4e^- \tag{1.12}$$

$$Cathode: \quad 4H^+ + 4e^- \rightarrow 2H_2 \tag{1.13}$$

The efficiency of these types of electrolyzers is generally in the range of 65-85% depending on the operating conditions [15]. However, to improve efficiency, solid oxide electrolyzers are under investigation. In this case, the charge carriers are O^{2-}, and thus the reactions that occur are the following:

$$Anode: \quad 2O^{2-} \rightarrow O_2 + 4e^- \tag{1.14}$$

$$Cathode: \quad 2H_2O + 4e^- \rightarrow 2H_2 + 2O^{2-} \tag{1.15}$$

Solid oxide electrolyzers are characterized by efficiencies up to 90%. Despite the higher efficiency, there are some technical challenges related to high temperatures, sealing, and electrode instability that must be addressed. A schematic representation of the three different electrolyzer technologies cells is shown in Figure 1.6 [15].

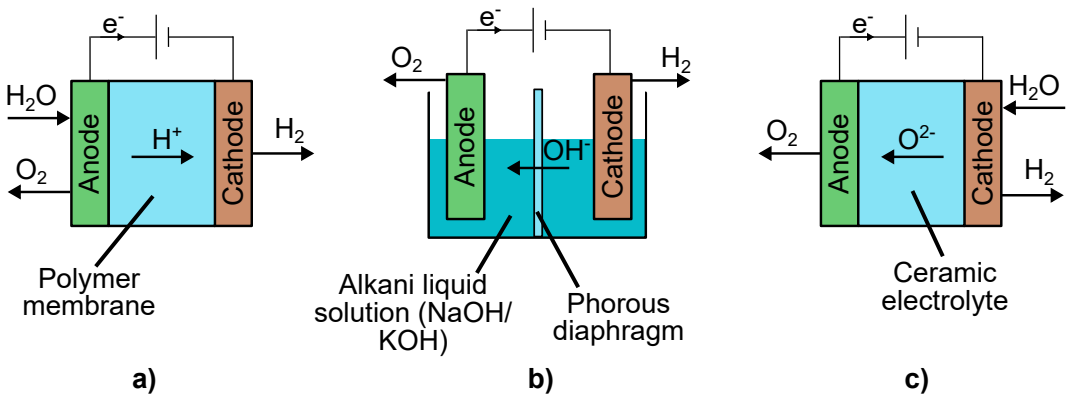

Figure 1.6 Types of electrolyzers: a) PEM, b) alkaline, c) solid oxide.

From an environmental point of view, hydrogen from water electrolysis is the most promising technology. Indeed, if the electrolyzer is powered using electricity coming from renewable sources, such as solar, wind, or biomass, producing the so-called green hydrogen, the environmental impact can be significantly reduced.

1.2.3 Other hydrogen production processes

Hydrogen can also be produced through other processes. Indeed, hydrogen can be produced from biomass in different ways. One of the most investigated method is the production from biomass gasification using steam, oxygen, or air. The process is generally carried out at high temperatures (700-1200°C) and has an efficiency of around 50% [16]. From an environmental point of view, hydrogen from biomass has a lower impact than hydrogen from fossil fuels; however, the main technical challenges are related to impurities in the product due to the biomass composition.

Another hydrogen production method using biomass exploits biological conversion. Indeed, some microorganisms are characterized by the presence of enzymes that allow them to produce hydrogen by biochemical action. Different processes

can be adopted, including biophotolysis, photo fermentation and dark fermentation [17, 18]. In case of biophotolysis, hydrogen is produced by decomposition of water with photoautotrophic microorganisms that use the energy of sunlight to produce H_2 [19]. In case of photo fermentation, microorganisms instead produce hydrogen using light energy to convert organic substrates. On the other hand, other microorganisms can produce hydrogen degrading complex organic matter in anaerobic conditions and without the need for light, thus the process is called dark fermentation. The main advantage of using biological conversion with respect to biomass gasification is that the process can be carried out at room temperature.

Another way to produce hydrogen is to adopt thermochemical cycles. According to these cycles, thermal energy can be used to produce H_2 through decomposition of water. Several different thermochemical cycles have been studied, but the one that is expected to be the most adoptable is the sulfur-iodine cycle. This cycle involves the Bunsen reaction to produce hydrogen iodide (HI) and sulfuric acid (H_2SO_4), the hydrogen is produced by decomposition of HI, while sulfuric acid is decomposed to produce oxygen, water and SO_2 [20]. The thermal efficiency of this process is around 30%. Apart from the sulfur-iodine cycle, other promising methods are copper-chlorine cycle and metal oxide cycle [14].

1.2.4 Hydrogen production methods comparison

When comparing hydrogen production methods, the main parameters that can be used are efficiency, environmental impact, and cost. The efficiency of the production process is generally evaluated as the ratio between the energy content of the produced hydrogen quantity and the sum of the chemical energy content introduced upstream the process with other inputs such as electricity and heat. For water electrolysis, electricity is the main input, while in the case of SMR the main input is the chemical energy of the methane. As for the environmental impact comparison, the global warming potential impact category was chosen. The comparison of the most relevant hydrogen production processes is proposed in Table 1.2. Data were obtained from references [14, 15].

From these data, it can be noted that electrolysis can significantly reduce the environmental impact of hydrogen production, but at present it may not be cost-competitive with hydrogen from fossil fuel. Furthermore, the electrolyzer should be

powered using electricity from renewables, otherwise the benefits can be reduced to the point that performance worsens compared to the case of SMR or CG. Considering hydrogen from fossil fuels, it can be stated that production through SMR has almost half the impact of hydrogen through CG. However, CG is the production method with the lowest cost. Regarding carbon capture technologies, they can significantly reduce the environmental impact to 1/3 or 1/4, but an increase in the cost production is expected. Considering alternative methods, thermochemical cycles performance depends on the adopted cycle, but it can be stated that they can be environmentally friendly if powered with nuclear energy, and also cost competitive under certain circumstances. Lastly, hydrogen from biomass gasification is characterized by good environmental performances and can be cost-competitive with hydrogen from SMR. In terms of efficiency, the most performing method are SMR and water electrolysis with solid oxide electrolyzers.

Table 1.2 Comparison of the most relevant hydrogen production processes.

Method	**Efficiency** (%)	**Environmental impact** (kg_{CO_2eq}/kg_{H_2})	**Cost** ($\$/kg_{H_2}$)
SMR	70 - 85	10.5 - 13.8 3.5 - 3.9 with CCUS	2.1 2.3 with CCUS
CG	60 - 75	19.4 - 25.3 4.1 - 7.1 with CCUS	1.3 1.6 with CCUS
Electrolysis	62 - 90	0.03 - 3 renewables 29 grid	3 - 23
Thermochemical cycles	20 - 60	0.4 - 1.4 nuclear 12.3 - 15.9 grid	1.7 - 15
Biomass gasification	50	2.7 - 4.4	1.8 - 2.8

1.3 Hydrogen Storage in vehicular applications

Hydrogen storage is an important issue for the widespread use of fuel cell vehicles. Desirable characteristics are high volumetric and gravimetric densities. Furthermore,

the speed of hydrogen release kinetics is also an important parameter, since it should fit the typical energy demand of vehicular applications. Other important parameters are the storage temperature, which may imply a heat management system for proper operation of the storage unit, and the operating pressure. In addition to those parameters, another relevant element is safety. Indeed, the storage system should be designed and implemented in the vehicle avoiding danger of explosion or other risk-related phenomenons [21, 22].

1.3.1 High-pressurized gaseous tanks

Currently, the implementation of high-pressurized gaseous tanks is the most adopted solution for hydrogen storage in vehicular applications. Depending on the materials and operating pressure, different types of tanks are defined: type I, II, III, and IV.

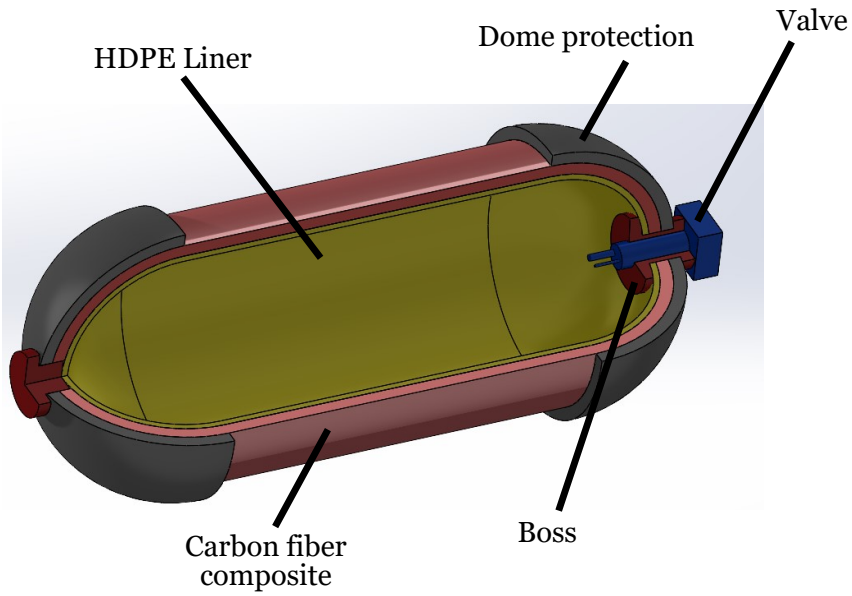

Figure 1.7 Type IV hydrogen tank configuration.

Type I and type II vessels are used for stationary applications or in particular applications with very high space and load capacity. Instead, type III and type IV tanks are feasible solutions for vehicles due to their higher gravimetric capacity. Both type III and type IV can indeed be used to store hydrogen at 700 bar, while type I and II generally operate at 200-300 bar. Both type III and type IV vessels are made with wrapped carbon fiber (Tory T700S or T800S), with the only difference that the

first adopts a metallic liner (made with AA6061 or AA7000) while the latter adopts a polymeric liner [23]. A schematic representation of a Type IV composite tank is shown in Figure1.7 [21]. Considering a whole hydrogen storage system with a type IV tank, the gravimetric capacity is around 4.2 wt%, while the volumetric capacity is 24.4 gH_2/L [24].

1.3.2 Liquid hydrogen

Hydrogen can be stored in liquid form by reducing its temperature below the boiling point of H_2, which corresponds to -253°C at ambient pressure [21]. To reduce the vaporization of hydrogen and reduce heat transfer, very highly insulated cryogenic tanks should be adopted. However, since a minimum heat transfer is unavoidable, a relief valve is implemented to allow hydrogen that boils to escape. As a consequence, a certain amount of hydrogen will always deplete and, furthermore, a cryogenic tank progressively discharges if hydrogen is stored for a long time [25]. As a consequence, even if this is a mature technology, several solutions to minimize H_2 boil-off losses during storage are currently under investigation. Despite the boil-off losses, that constitutes a major disadvantage, this storage technique allows for a higher gravimetric energy density compared to compressed hydrogen, equal to more than 7-8 wt%. The volumetric capacity is also higher and can reach up to 45-50 gH_2/L. Nevertheless, liquid hydrogen storage have a relevant issue related to the energy required for H_2 liquefaction. Considering the current state-of-the-art, liquid hydrogen is not widely used for mobility.

1.3.3 Metal hydride tanks

This technology have gained attention since it offers high volumetric energy density and allows for storing hydrogen at significant lower pressures without requiring liquefaction. According to this technology, hydrogen is absorbed and chemically bound with a metal alloy. The general reaction that describes the reversible process of absorption/desorption is the following [26]:

$$M + \frac{x}{2} H_2 \leftrightarrow MH_2 + \text{Heat} \tag{1.16}$$

Depending on the metal alloy used, the properties of the storage tank, including gravimetric capacity, internal pressure and so on, may vary significantly. The internal pressure of the tank depends on the temperature and hydrogen concentration according to the pressure-concentration-isotherms (PCI, also called pressure-concentration-temperature PCT) diagram. Another plot that is useful to determine the operating conditions, in particular for evaluating the influence of temperature on the equilibrium pressure, is the van't Hoff plot [27, 28]. The van't Hoff equation describes how the equilibrium pressure in the plateau region of the PCI diagram varies with temperature and can be written as follows:

$$\frac{\Delta H}{R_g T} - \frac{\Delta S}{R_g} = \ln \frac{p_{eq}}{p_0} \tag{1.17}$$

Where ΔH and ΔS are respectively the enthalpy and entropy of the reaction, R_g is the universal gas constant, equal to 8.314 $\frac{J}{molK}$, T is the temperature, p_{eq} is the equilibrium pressure, and p_0 is the atmospheric pressure. A typical PCI curve of a metal hydride tank is shown in Figure1.8.

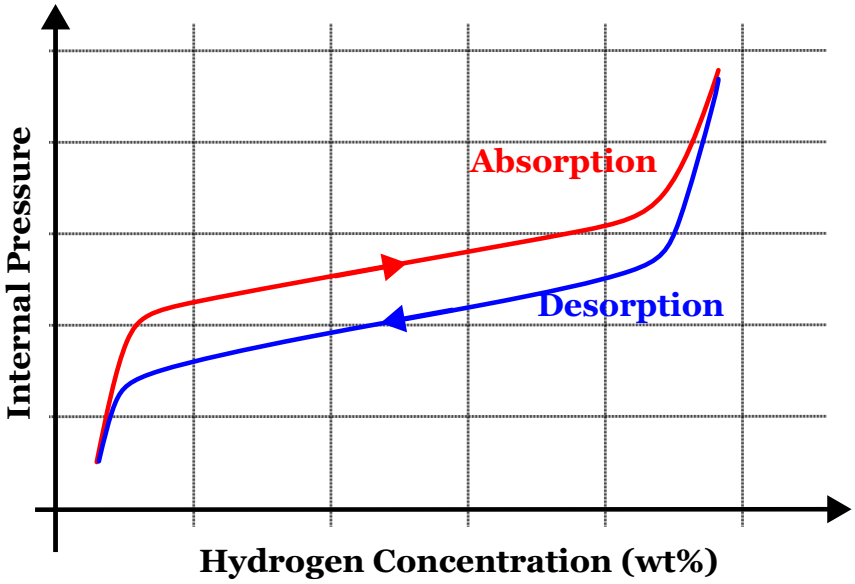

Figure 1.8 Typical PCI curve of a metal hydride tank. It should be noted that the curve is given at a fixed temperature.

It can be noted that the absorption and desorption processes are characterized by a different equilibrium pressure, indeed the whole charge/discharge process exhibits a typical phenomenon of hysteresis. As a consequence, also the thermodynamic

parameters, namely enthalpy and entropy, are different for the hydrogen desorption and absorption processes. The equilibrium pressure can be evaluated using the following equation [29]:

$$p_{\text{eq}} = f\left(\frac{H}{M}\right) \cdot \exp\left(\frac{\Delta H}{R_g} \cdot \left(\frac{1}{T} - \frac{1}{T_{\text{ref}}}\right)\right) \tag{1.18}$$

Where H/M mean the hydrogen-metal concentration ratio and T_{ref} is the reference temperature. Hysteresis can be expressed by the following equation [28]:

$$\text{Hysteresis} = \ln \frac{p_{\text{abs}}}{p_{\text{des}}} \tag{1.19}$$

Where p_{abs} and p_{des} are the average pressures for the absorption and desorption processes, respectively.

As previously mentioned, the properties of a metal hydride system strongly depend on the metal alloy. Alloys commonly used in these systems include magnesium, titanium, lanthanum, and lithium. The properties of these systems are reported in Table 1.3 according to [27]:

Table 1.3 Storage capacities and volumetric energy densities for some of the most studied metal hydrides systems. The gravimetric and volumetric densities are reported considering the amount of hydrogen that can be reversibly absorbed/released.

Metal Hydride	**Gravimetric capacity (wt%)**	**Volumetric energy density (kWh/dm^3)**
M_gH_2	5.5	2.65
T_iF_e	1.5	3.25
$T_iM_{n_2}$	1.15	2.53
$L_aN_{i_5}$	1.28	3.53
L_iBH_4	13.4	3.02
$N_aA_lH_4$	3.7	1.58

It can be stated that metal hydride systems offer the highest volumetric energy density when compared to other hydrogen storage methods, which is on average almost two times that of liquid hydrogen and up to more than three times that of 700 bar tanks. On the other hand, the gravimetric energy density of the commonly

used hydrides for mobile applications is generally lower than liquid hydrogen and high-pressurized tanks. Thus, metal hydrides are of interest in those applications where compactness is crucial and the overall weight is not critical. Indeed, they are a feasible solution for heavy-duty applications, trains, and maritime sector, rather than for passenger cars. Apart from weight issues, the adoption of metal hydrides has two other major disadvantages. One is related to the thermodynamic behavior of the system, indeed the absorption process is exothermic and the desorption process is endothermic. As a consequence, the tank requires heat when hydrogen is released and should be cooled when it is absorbed. To properly address this aspect, the design of the hydride tank should optimize the heat transfer (for example including fins) and a heat management system should be integrated in the vehicle [26, 30]. The heat absorbed or released by the tank during its operation can be evaluated using the following equation [28]:

$$Q_{tank} = n_{H_2} \cdot \Delta H \tag{1.20}$$

Where Q_{tank} is the thermal power, and n_{H_2} is the hydrogen molar flow rate.

To improve overall efficiency, a possible solution is the thermal coupling of the metal hydride tank with the fuel cell system [31]. The other limiting factor is the reaction kinetics. Indeed, hydrogenation and dehydrogenation reaction rates depend on several factors, including temperature, pressure and morphology [32].

1.4 Applicability of fuel cell systems for vehicular applications

Fuel cell systems can represent a feasible solution to reduce the pollutant emissions produced by vehicles. However, to evaluate the effectiveness of introducing these systems in vehicular applications, several elements must be considered and a comparison with the other alternatives should be performed. Starting from this premise, considering the current state-of-the-art, there are several barriers that are currently limiting the adoption of fuel cell powertrain. According to the literature [33–35], the most important barriers are:

- **High costs**: including vehicle production and maintenance costs, high capital cost associated with building the hydrogen infrastructure, along with low stations profitability due to low fuel demand, high fuel cost (in particular for green hydrogen).
- **Lack of hydrogen refueling network**: including the limited number of fuel stations, and lack of supply infrastructure.
- **Consumer perception**: including misperception of safety issues due to H_2 properties, negative perception about environmental performance, and low visibility.
- **Regulatory issues**: including the lack of incentives and supporting policies.

According to [33], the most relevant barriers are the high ownership cost of fuel cell vehicles, the lack of supply infrastructure, and the lack of awareness about hydrogen as fuel and, consequently, about its performance from an energetic and environmental point of view.

The high cost of fuel cell systems is related to the presence of precious metals within the stack (Pt used as catalyst) and to the hydrogen storage system, thus several efforts are made by industrial companies towards the adoption of low-cost materials and components. Furthermore, the high fuel cost reduce the attractiveness of fuel cell vehicles, thus governmental support through incentives or policies that help reduce overall ownership cost is required.

As for the hydrogen supply infrastructure, since it is still at a very early stage of development, it needs to expand significantly to make fuel cell vehicles an attractive alternative to ICE and pure battery counterparts. A challenge of primary importance is the investment cost related to building a hydrogen refueling station, which is currently significantly higher compared to traditional stations or battery charging stations. Furthermore, the low diffusion of fuel cell vehicles and the uncertainty about their future adoption limit the profitability of these stations, discouraging further investments.

Finally, overcoming consumer perception issues is mandatory to promote the diffusion of fuel cell vehicles. Increasing the rate of low-emission hydrogen can be a feasible solution to entice the consumer to purchase these vehicles. Furthermore,

increasing the awareness about the high level of safety of this technology might be a relevant allied.

Despite the aforementioned barriers, fuel cell powertrain have some key features that can make them a very attracting solution to reduce pollutants emissions from vehicles. Since the fuel cell system only produce water at the exhaust, these vehicles produce locally almost zero-emission, thus their impact is mainly related to the hydrogen production process. Indeed, if hydrogen is produced with low-emission processes, the environmental impact can be significantly reduced. Furthermore, even if hydrogen is produced by steam methane reforming, reductions of almost all the pollutants and CO_2 can be achieved compared to the traditional counterparts powered with gasoline or diesel fuel [36].

Another important advantage when comparing FCEVs with ICEVs is their higher efficiency. Indeed, a fuel cell system can offer a maximum efficiency of up to 50%, but the real key point is that the efficiency is generally over 40% for almost all the load spectrum. On the contrary, internal combustion engines generally operate around 25-30% of efficiency.

When comparing FCEVs with pure battery electric vehicles, the main advantage is related to the endurance. Indeed, due to hydrogen high energy content, a fuel cell vehicle can store a high amount of energy on-board without requiring a bulky storage system. Furthermore, the refueling time of a gaseous tank is comparable to that of a traditional vehicle [37].

Summarizing the previously mentioned factors, it can be pointed out that fuel cell powertrain are of particular interest in those applications where productivity and/or compactness are crucial. These requirements are common for off-road heavy-duty vehicles and NRMMs. Indeed, in literature there is a growing interest towards the application of fuel cells to NRMMs, including tractors, excavators, ships, yard tractors and so on [38–41]. For most of these vehicles, the pure electric solution is not feasible due to the low volumetric energy density of batteries, which can significantly affect the productivity and overall weight.

1.5 Review of hybrid fuel cell powertrain topologies

Fuel cell powertrain generally feature the presence of a fuel cell system and of an additional power source, which can be composed of a battery pack, a supercapacitor module or both. The implementation of this additional unit is necessary to avoid fast degradation of the fuel cell stack, which indeed is affected by load changes [42]. To enhance the durability of the system, the fuel cell power output should follow a low dynamic behaviour, avoiding fast and abrupt variations. As a consequence, the auxiliary unit is introduced with a view to manage the high dynamic part of the load, while the fuel cell operates following the average power profile. Depending on the whether the auxiliary unit is made of batteries or supercapacitors, and on the adoption of DC-DC converters, several different configurations of powertrain can be defined.

1.5.1 Fuel cell and battery architectures

The fuel cell and battery topology is the most adopted one [43]. Generally, the fuel cell is used as primary energy source, while the battery pack is used to handle sudden changes and peaks in the external load. Depending on the connection between the fuel cell, the battery pack and the DC bus, four different topologies can be defined, as shown in Figure 1.9.

In topology 1, the fuel cell system and the battery pack are directly connected to the DC bus, without any DC-DC converter. This is the simplest architecture, however it is not generally adopted since it could lead to large voltage fluctuations. Furthermore, there is no degree of freedom in controlling the power split among the two sources.

In topology 2 instead the fuel cell is connected to the DC bus with a unidirectional DC-DC, while the battery is directly connected. In this case, the voltage level of the DC bus is determined by the battery voltage, thus it requires a properly sized and performing battery pack. The presence of the power converter allows for proper control of the fuel cell output, enhancing its lifetime and optimizing its efficiency.

In topology 3, the fuel cell is directly connected to the DC bus, while the battery pack is connected with a DC-DC. In this case, the DC bus voltage level is determined

by the fuel cell system, which strongly depends on its power output. Consequently, higher voltage fluctuations are expected with respect to topology 2.

Finally, in topology 4 both the fuel cell and battery pack are connected with DC-DC converters. From voltage stability point of view, this configuration is optimal since it allows for a more stable DC bus voltage level. Nevertheless, the presence of two power converters leads to a more complex and bulkier powertrain layout, along with higher power losses. Furthermore, filter capacitors should be introduced to reduce ripple currents [43].

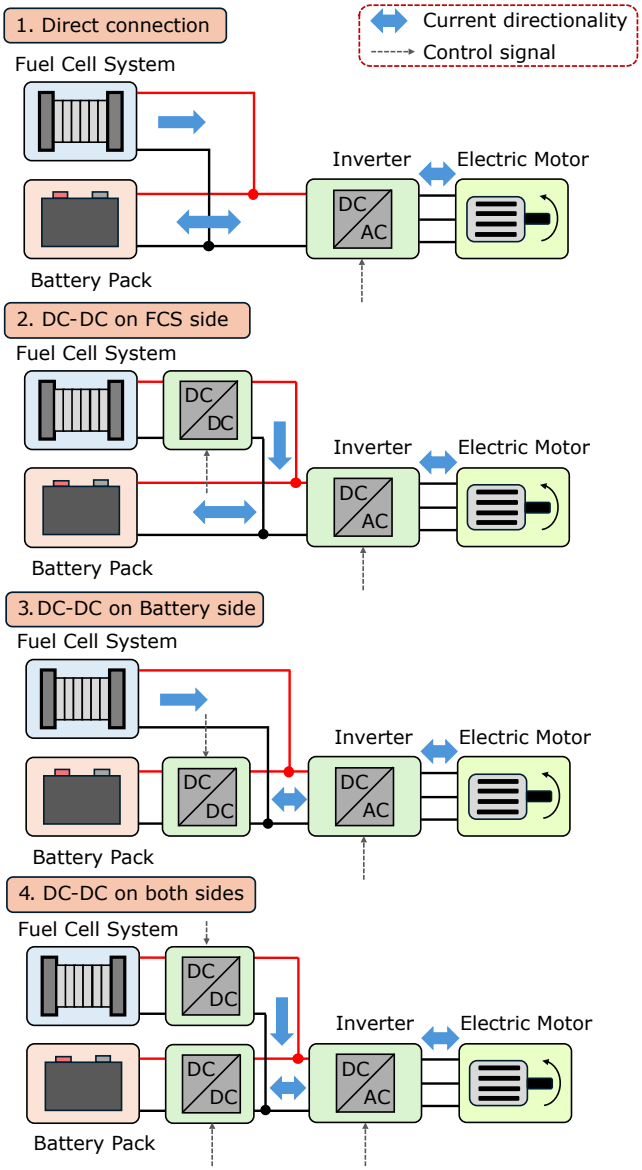

Figure 1.9 FCS + battery pack topologies.

1.5.2 Fuel cell and supercapacitors architectures

Compared to batteries, supercapacitors are characterized by higher power capability and lower power losses due to lower internal resistance. Furthermore, the expected life is significantly higher than that of batteries. On the other side, since they have a lower energy density, the whole powertrain should be properly designed to avoid excessive depth of discharge during transient phases. Indeed, the voltage level of a supercapacitor is proportional to its state of charge, so when it provides power, its voltage starts to decrease rapidly. A comparison between the main properties of supercapacitors and lithium-ion batteries is shown in Table 1.4 according to [44].

Table 1.4 Comparison between Li-ion batteries and supercapacitors for energy storage applications.

Parameter	**Li-ion Batteries**	**Supercapacitors**
Energy density (kWh/kg)	150-200	1-10
Power density (kW/kg)	2000	10000
Life expectancy (cycles)	5000	>50000
Charge and discharge efficiency	99%	85-98%
Operation temperature (°C)	-30 to 60	-40 to 75

Given these premises, the fuel cell and supercapacitors architectures are the same of the previous case of fuel cell and batteries. Furthermore, the main advantages and disadvantages of the topologies are almost the same. The main differences are related to the energy management strategy due to the lower energy density of supercapacitors. Indeed, the energy management strategy should be properly designed to avoid excessive low voltage of the supercapacitor module (25% of the rated voltage is generally used as inferior limit) and, at the same time, to limit fluctuations in the power output of the fuel cell to enhance its durability. Matching these two objectives may be challenging and can be a bottleneck for the diffusion of this kind of powertrain. As a consequence, these configurations can be a feasible solution in applications where high-load conditions are very demanding in terms of power but short in time.

1.5.3 Fuel cell, supercapacitors and batteries architectures

Considering that supercapacitors and batteries have complementary features, to meet both power and energy requirements of the auxiliary unit, a feasible solution is represented by architectures with a hybrid unit comprising both of them. In this case, the supercapacitors are used to satisfy very high peaks in the power demand, avoiding excessive C-rates on the batteries. On the contrary, batteries are used to compensate for the short discharge time of supercapacitors [43].

Also in this case, several topologies can be defined depending on the number and positioning of the DC-DC converters used to interface the three power sources. However, for vehicular applications, the two most widely adopted topologies are shown in Figure1.10.

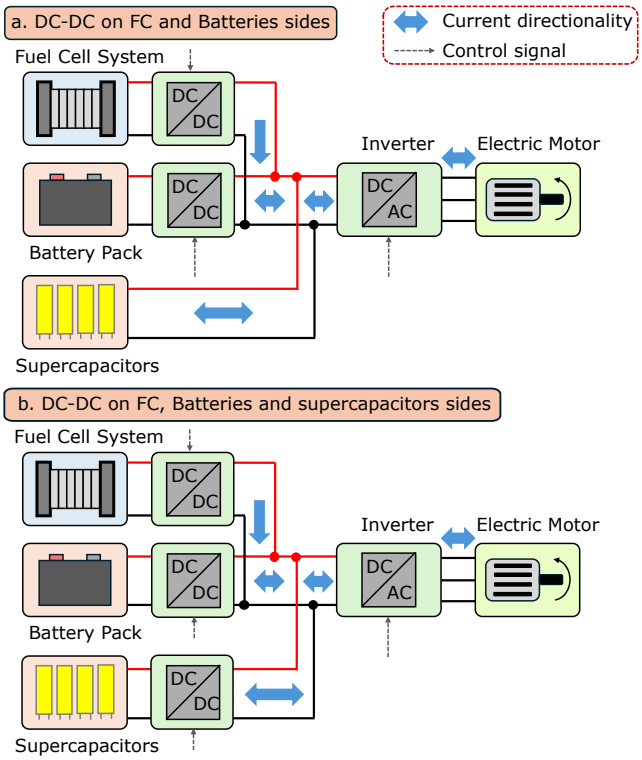

Figure 1.10 FCS + battery pack + supercapacitors topologies.

In case of topology A, the main advantage is that the direct connection of the supercapacitors to the DC bus allows them to respond immediately to sudden peaks in the power demand. On the contrary, the main disadvantage is that the voltage level of the DC bus is defined by the supercapacitors state of charge, thus they

cannot be discharged deeply. In case of topology B instead, a more stable voltage level of the DC bus is expected, however the presence of three DC-DC converters increases conversion losses and complexity in terms of both space layout and energy management.

Table 1.5 provides a comparison of the main advantages and disadvantages of the different fuel cell powertrain topologies.

Table 1.5 Advantages and disadvantages of the different fuel cell powertrain architectures.

Topology	**Advantages**	**Disadvantages**
Fuel cell + battery	• Requires simpler energy management. • Can handle long-lasting high-load conditions.	• Limited peak power capability of the battery pack. • Limited battery durability.
Fuel cell + supercapacitors	• Can handle very high power peaks. • Long supercapacitors durability.	• Supercapacitors cannot handle long-lasting high power conditions. • Requires a proper control of supercapacitors voltage level.
Fuel cell + supercapacitors + battery	• Allows for exploiting the complementary features of supercapacitors and batteries.	• Complex layout. • Requires a more complicated energy management strategy. • High costs.

1.6 Energy management strategies in hybrid vehicles

Since fuel cell powertrain feature the presence of more than one energy source, they are considered as hybrid systems. Consequently, the development of an energy management strategy (EMS) is mandatory to optimize performance. The EMS must be designed to properly determine the power split among the on-board energy sources, in order to enhance fuel economy, durability or both [43].

Generally, EMS can be divided into three big categories: rule-based strategies (RBS), optimization-based strategies (OBS), and learning-based strategies (LBS). RBS are characterized by lower computational effort, since they are generally based on a predefined set of rules based on engineering experience or numerical models, and good reliability in terms of robustness. Instead, OBS are designed to optimize an objective function through optimization algorithms. Depending on the optimization method, OBS may be or may not be implementable in real-time applications. Finally, LBS use machine learning techniques or neural networks to determine the optimal allocation of power according to collected data. These strategies can adapt to different situations, allowing for optimal solution even in the case of completely random power profiles. A scheme representing the classification of the EMS used in FCHEVs is shown in Figure 1.11.

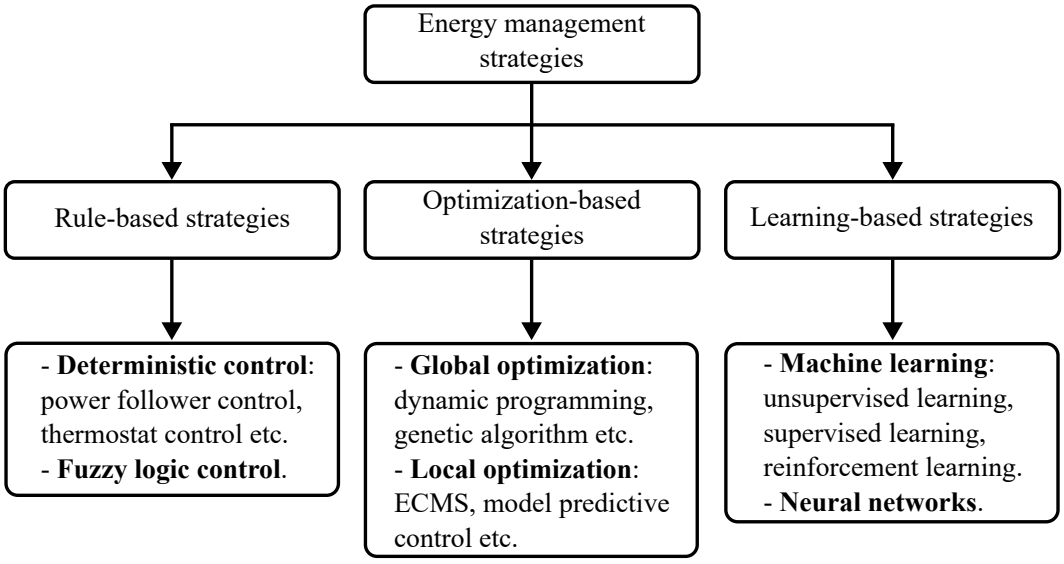

Figure 1.11 Classification of EMSs used in fuel cell hybrid electric vehicles.

1.6.1 Rule-based strategies

Rule-based strategies generally requires a set of rules and the definition of the system state parameters. These strategies can be classified into deterministic and fuzzy logic strategies [45]:

- **deterministic RBS**: these strategies determine the output of the control variables using a look-up table or a simple mathematical model depending on the input variables; the most adopted deterministic RBS are the thermostat control and the power follower control.
- **fuzzy logic RBS**: these strategies are based on if-then rules and membership functions to determine the output variables depending on the input ones.

In thermostat control strategies, the fuel cell generally operates at its optimal efficiency point and is turned off when a predefined input variable, for example batteries SOC, reaches a threshold value [46]. Instead, in power follower strategies, the output of the fuel cell is adjusted considering the power requirement of the vehicle. Generally, the rules of a power follower are based on heuristics or engineering experience. Apart from thermostat and power follower controls, other deterministic strategies have been proposed, including frequency decoupling strategies, based on the decoupling of the low- and high- frequency parts of the load, and state machine strategies, based on the definition of different operating modes according to the values of input variables [45].

In fuzzy logic strategies, the design process involves three main steps: fuzzification, fuzzy reasoning, and defuzzification. In the first step, the input variables are associated with membership functions and truth values. Fuzzy reasoning then involves the definition of the if-then rules (for example: IF the batteries SOC is LOW, THEN the fuel cell output is HIGH). Finally, the defuzzification step defines the values of the output variables according to the combined results of the first two steps.

Since RBS are quite simple and reliable, they are widely adopted in real-time applications. Nevertheless, they can deviate from the optimal solution, resulting in a poorer fuel economy and/or components lifetime compared to other strategies. To enhance the performance of these controllers, an offline optimization algorithm

can be used. In addition, in some cases, adaptive or predictive algorithms can be integrated into rule-based strategies to improve their performance.

1.6.2 Optimization-based strategies

OBS involve the definition of an objective function using operating parameters and tries to minimize it according to optimization algorithms. Constraints are imposed to avoid operating in non-optimal conditions. Consequently, the algorithm tries to find the optimal control that minimizes the objective function while meeting operational constraints. OBS can be classified into two main groups, namely global optimization and local optimization [43, 45]:

- **Global optimization**: global optimization algorithms generally require the complete "a priori" knowledge of the load profile, thus they can be used offline and are not suitable for real-time applications; despite this, they can be used as benchmarks for other control strategies; the most adopted global optimization algorithms are dynamic programming, genetic algorithm, and Pontryagin's minimum principle (PMP).
- **Local optimization**: in contrast with global optimization, local optimization does not require the "a priori" knowledge of the driving cycle; indeed, the local optimization algorithm consists of solving an instantaneous optimization problem, thus it requires limited computational effort and is implementable in real-time controllers; the most adopted local optimization algorithms are the equivalent consumption minimization strategy (ECMS) and model predictive control.

Dynamic programming is based on the Bellman principle. The global problem is divided into a series of sub-problems, and the solution is recursively obtained from the end state to the initial state. Even if dynamic programming can obtain the best solution, it has some issues related to heavy computational effort and curse of dimensionality. However, dynamic programming is generally used as benchmark or to optimize the parameters of a real-time control strategy.

As for the PMP, the global optimization problem is reduced into a local Hamiltonian minimization problem. The Hamiltonian function is characterized by a co-state,

which indicates the effect of a state variation. The optimization process takes place imposing that the control minimizes the Hamiltonian through an iterative process. The computational effort of the PMP is generally lower than that of the dynamic programming and avoids the curse of dimensionality, however it strongly depends on the initial co-state and may obtain a less optimal solution compared to it. Furthermore, it is not suitable for highly nonlinear systems.

Genetic algorithms instead take inspiration from the dynamics of natural selection, involving the concepts of reproduction and mutation. The algorithm generally consists of generating an initial population of solutions, then the best ones are selected according to an objective function and are used to generate the next generation. The iterative process is repeated to find the optimal solution. These algorithms have the advantage of being particularly feasible for nonlinear and non-convex optimization problems. Despite the advantages, these algorithms may obtain suboptimal solutions compared to dynamic programming.

As for local optimization methods, the ECMS is one of the most adopted. The idea is to minimize at each time step the objective function, which is generally defined by the sum of the actual fuel consumption in the fuel cell and the equivalent fuel consumption related to the charge/discharge of the auxiliary unit. In this control, the definition of the equivalence factor that relates the batteries SOC variation to an equivalent fuel consumption is critical and may significantly affect the performance of the strategy. Consequently, this factor is generally obtained and optimized offline. In some cases, adaptive ECMS have been developed [47], so that the system can recognize specific working conditions or predict the power profile, or adapt considering the batteries SOC. The ECMS represents a good compromise between achieving suboptimal results and real-time applicability.

Another widely adopted local optimization control is the model predictive control. In this case, the system tries to predict, within a predefined prediction horizon, the future behavior of the driver or external load. Based on future prediction, the system finds the best solution to minimize the objective function. Depending on the prediction algorithm, different subclasses of model predictive controls can be defined.

1.6.3 Learning-based strategies

LBS exploits learning algorithms to find the optimal solution exploiting historical data. These strategies are generally classified into:

- **Machine learning**: the algorithm can learn the optimal EMS from historical data and interactions with the environment using, for example, a reward system that penalizes the non-optimal solutions.
- **Neural networks**: neural networks are inspired by neurons in the human brain; the network consists of nodes, which are connected by edges, and each neuron receives signals from the other neurons to which it is connected; the signal is processed and the computed output of the neuron is sent to other neurons.

Machine learning techniques are classified into unsupervised learning, supervised learning and reinforcement learning [45].

A reinforcement learning algorithm involves a learning agent that chooses an action and receives a reward, according to the feedback received, that is used to define a control policy. Consequently, it can be defined as a machine learning paradigm where an agent learns to make optimal decisions by interacting with an environment through a trial-and-error process and whose goal is to maximize a cumulative reward over time. By learning from experience, the agent improves its decision-making to maximize long-term rewards. The main issues of this kind of algorithm are related to the high amount of data required for training, and the to find the right equilibrium between trying new actions and using known actions.

As for supervised learning, it is based on an error-correction approach. Into detail, a model is trained through a process that requires making predictions and adjusting based on the prediction errors. It can be defined as a machine learning paradigm in which an algorithm learns from labeled data, trying to find patterns in them, and making predictions on unseen inputs. Thus it involves preparing a dataset with known input-output, train the model using those data, then test it on unseen data and, finally, use it to predict outputs for new inputs. The main challenges related to this kind of algorithms are that it requires a large labeled dataset and it may not generalize well on unseen data.

Lastly, in unsupervised learning an algorithm learns patterns and structures without labeled data, thus the model discovers hidden relationships or patterns in the

data and learns without explicit guidance. Since there are no labels, the model learns from the data itself, identifying natural patterns instead of being explicitly told what to learn. This kind of algorithms, since it does not require labeled data, saves time and effort in data preparation. Furthermore, it can find interesting hidden patterns previously unnoticed and can adapt to new unseen data. On the contrary, it can be very sensitive to parameters and the results can be hard to interpret.

1.7 Fuel cell-powered NRMM prototypes

In the last years, the growing interest towards fuel cell-powered NRMMs has pushed several manufacturers to develop prototypes of different kind of vehicles. One of the very first prototypes was the New Holland NH2, which was presented at the SIMA farm equipment show in Paris, France, in 2009 and won the gold medal at the innovation awards [48]. This tractor was develepoed on the basis of the New Holland T6000 and features the presence of two electric motors, one for the traction and the other for PTO operations and auxiliaries. The total rated power of the motors is equal to 79 kW. The hydrogen is stored in high-pressurized tanks at a pressure of 350 bar. Despite promising expectations, the NH2 remains a prototype and is currently not in production at an industrial level. Nevertheless, other agricultural vehicles with fuel cell powertrain have been developed.

In 2022, EOX Tractors developed an hydrogen-powered version of its EOX175 model [49]. In this case, the fuel cell system is used as a range extender to enhance the endurance and productivity of the vehicle. The powertrain also features a 50 kWh battery pack. Also for this vehicle, the hydrogen is stored at 350 bar in pressurized tanks. The total power at the wheels is equal to 129 kW.

In 2023, Fendt showed a prototype of an hydrogen tractor that was developed during the H2Agrar project [50]. The prototype, named Helios, is characterized by the presence a 100 kW fuel cell and of a 25 kWh battery pack. The hydrogen is stored in five tanks at 700 bars, each one with a capacity of 4.2 kg of hydrogen [51]. In April 2023, two Fendt Helios prototypes were delivered to farms in the Harem region to perform on-field tests.

Furthermore, in 2023 at World FIRA, EXXACT Robotics unveiled its TRAXX Concept H2, an autonomous vineyard tractor with a fuel cell system [52]. The vehicle

is equipped with two hydrogen tanks that can store up to 9 kg of hydrogen. The manufacturer claimed that it can operate for 12 hours in one go.

Lastly, in 2024 the Steyr FCtract was presented, which was developed by a joint collaboration between CNH, TU Wien and Steyr. The vehicle develops a power of 95 kW and feature the presence of a 14 kWh 400 V battery pack [53].

Another kind of vehicle towards which manufacturers showed interest in developing a fuel cell version is excavator. In 2020, JCB manufactured a 20-ton hydrogen-powered excavator [54].

In 2022 at Bauma, Hyundai presented the concept HW155H, a 15-ton fuel cell-powered excavator with a 100 kW stack. At Bauma 2025, the prototype was operated on a demonstration platform. Hyundai also developed a hydrogen-powered forklift, featuring a 50 kW fuel cell stack and a high-voltage battery [55].

In 2023, Komatsu, in collaboration with Toyota, developed a medium-sized hydraulic excavator with a hydrogen fuel cell system [56]. The company claimed that this vehicle aims to reduce CO_2 emissions of 50% but ensuring the same performance as the traditional diesel-powered counterpart. In this case, the powertrain features the presence of a capacitor to provide additional power to the motor [57].

In the same year, the Japanese company Kobelco Construction Machinery Co. developed a prototype of mid-size hydraulic excavator equipped with a Toyota fuel cell system and hydrogen tank. Several tests were carried out to assess the performance of this prototype, showing promising results [58].

In addition to agricultural tractors and excavators, the development of hydrogen-powered of-road vehicles also involved other kinds of machinery. In 2022 Volvo Construction Equipment presented the HX04 prototype, a fuel cell articulated hauler [59]. According to the manufacturer, the vehicle can be charged with 12 kg of hydrogen in about 7.5 minutes, ensuring satisfactory performance in terms of productivity.

Manitou presented a prototype of a fuel cell telehandler as a part of their program to reduce greenhouse gas emissions by 34% per hour of use of its machines [60]. The development of a second rotating telehandler prototype has been announced.

A comprehensive classification of the previously mentioned prototypes is showed in Table 1.6. Despite some information about these prototypes being available, in most cases very low details are currently accessible. Indeed, the powertrain architecture is generally not completely described. However, given the available

details, it can be noted that the most adopted solution involves batteries as additional on-board energy storage system, rather than supercapacitors.

Table 1.6 Classification of fuel cell-powered NRMM prototypes in the agri-construction sector. "-" means that the information is not available.

Company	**Prototype**	**Year**	**Vehicle type**	**Configuration**
New Holland	NH_2	2009	Agricultural tractor	FC + batteries
EOX Tractors	EOX175H	2022	Agricultural tractor	FC + batteries
Fendt	Helios	2023	Agricultural tractor	FC + batteries
Steyr	FCtrac	2024	Agricultural tractor	FC + batteries
EXXACT Robotics	TRAXX Concept H2	2023	Autonomous vineyard rover	FC + batteries
JCB	220X	2020	Excavator	FC + batteries
Hyundai	HW155H	2022	Excavator	FC + batteries
Komatsu	-	2023	Excavator	FC + capacitor
Kobelco	-	2023	Excavator	-
Volvo CE	HX04	2022	Articulated Hauler	-
Hyundai	-	2023	Forklift	FC + batteries
Manitou	-	2023	Telehandler	-

1.8 Conclusions

In the last decades, the increasing awareness about the impact of human activities on air quality and environment has been a driving factor towards the development of innovative solutions to improve sustainability. In this scenario, agriculture is an important source of emissions but, at the same time, a key element in the food supply chain. Accordingly, sustainability must be improved without negatively affecting productivity.

Traditional agricultural machinery is generally powered with oversized Diesel engines, resulting in reduced efficiency and poor fuel economy. In this scenario, fuel cell systems powered with hydrogen have gained attention due to their properties, including compactness, zero local emissions, and higher efficiency. The most

promising technology for vehicular application is low temperature proton exchange membrane fuel cell.

Hydrogen, at present, is mainly produced from steam methane reforming, a process far from being without emissions. Low-impact production processes are limited to less than 1% of the total production, even if a positive trend is noted in the last years. These processes include hydrogen from fossil fuels but with carbon capture technology, and hydrogen from water electrolysis. This last process, if the electrolyzer is powered with electricity coming from renewables, is a promising solution to reduce the environmental impact of hydrogen production.

In vehicular applications, hydrogen is usually stored on-board using high pressurized tanks. This is a mature technology that combines good energy density with fast refueling times. Other possibilities of hydrogen storage are cryogenic tanks, which store hydrogen in liquid form, and metal hydride tanks, which instead absorb hydrogen chemically to form an alloy. Metal hydride tanks are an interesting solution as they can reach very high volumetric energy densities but with a lower operating pressure (generally < 30 bar) compared to gaseous tanks. In addition, they can be easily integrated in off-road heavy vehicles. However, the thermal behavior and the kinetic of the absorption/desorption reactions are limiting factors that must be considered.

When developing a fuel cell powertrain, different configuration can be defined depending on the auxiliary power source, which can be composed of a battery pack, a supercapacitor module, or both. Depending on the constraints and operative requirements, power or energy density might be preferred. DC-DC power converters are used to interface the different electric components and as power conditioning units. In addition, an energy management strategy must be defined to properly split the power between the different sources. The energy management strategy can directly affect the powertrain performance.

At present, different concepts and prototypes of fuel cell-powered off-road vehicles for the agri-construction sector have been proposed. In details, agricultural tractors, excavators and telehandlers have been presented at fairs around the world. However, no products is, at present, commercially available, indicating that the development of these systems is still at an early stage from an industrial perspective.

Chapter 2

Numerical analysis of a fuel cell-powered orchard tractor

The agricultural sector plays an important role in providing food for the growing worldwide population. Indeed, the need for highly efficient and productive agricultural machinery is pushing the industrial world toward the study of innovative mechanization and automation solutions that can increase the productivity of farms [61, 62]. At the same time, the growing awareness about environmental pollution and its consequences, in particular on air quality and climate change, is also forcing the agricultural machinery manufacturer to investigate solutions that allow for a significant decrease in terms of pollutants and greenhouse gasses emissions. To satisfy both these aspects, thus ensuring high productivity using greener and more sustainable solutions, a possible solution is to substitute traditional propulsion systems with electrified powertrain [63]. This can be achieved implementing hybrid or full-electric solutions. Depending on the specific vehicle, different solutions can be adopted. Indeed, agricultural machinery can include a wide variety of different vehicles with different requirements and constraints. Consequently, each specific case deserves a dedicated analysis and the results obtained for one kind of vehicle might not be valid for others. In this chapter, the analysis focuses on the electrification, through the adoption of a hybrid fuel cell powertrain, of a compact orchard tractor. Into details, a numerical investigation was carried out to evaluate the feasibility and the environmental benefits deriving from the substitution of the traditional diesel powered vehicle with the hydrogen powered counterpart. The numerical models were

developed in MATLAB Simulink, a graphical programming environment developed by MathWorks (The MathWorks Inc., Natick, MA, USA).

2.1 Orchard tractors

2.1.1 Main properties

When developing an innovative powertrain, the typical work scenarios and performance requirements of the vehicle must be well-known. Focusing on agricultural tractors, to address this issue a good starting point is analyzing the definition proposed by the ISO 12934 standard [64]:

"The agricultural tractor is a self-propelled agricultural vehicle having at least two axles and wheels, endless tracks, or a combination of wheels and endless tracks, particularly designed to pull, push, carry or provide power to operate implements or pull agricultural trailers and implements, or any combination of these functions used for agricultural work (including forestry work), which may be provided with a load platform."

As can be stated, these vehicles are multipurpose machines that can perform different tasks, ranging from transportation to field activities. Agricultural tractors can be divided into two main groups:

- **Open field**: these vehicles are generally used for heavy-duty tasks, such as plowing, arrowing, sowing, or transportation, to be performed on very large farm areas or between farm fields.
- **Specialized**: these tractors are generally adopted for specific operations in orchards, vineyards, etc., and are characterized by higher compactness and maneuverability.

Apart from technical aspects, there is also a great difference in terms of typical work scenarios between open field and specialized tractors [65]. While the first are generally used to perform tasks that require a high amount of power, the latter are

mainly used to power attached implements used for orchard and vineyard activities (use of an atomizer, weeding, or light transportation using small trailers).

Focusing on orchard tractors, these vehicles must have the following characteristics:

- **Compactness**: they must be designed to move among the narrow rows of fruit trees or vines.
- **Maneuverability**: they have to move agilely among rows and need a tight turning radius.
- **Reduced Ground Pressure**: they must reduce soil compaction and minimize damage to roots, thus they typically adopt wide or low-pressure tires.
- **Visibility**: they must ensure high visibility to operate safely in rows.
- **Versatility**: they must be able to perform a wide variety of tasks since they have to adapt to different types of orchards.

When performing field activities, tractors usually use implements, such as sprayers, mechanical weeders etc., which are usually powered by the vehicle itself by means of a mechanical connection called Power Take Off (PTO). This power connection has specific requirements in terms of rotational speed and geometries. The reference speed can be set at 540 rpm or 1000 rpm depending on the implement and the operating conditions. Since the PTO is mechanically coupled to the engine, it is clear that, to operate at different vehicle speeds in the orchard but with the PTO at its nominal speed, a high number of gear ratios is required. Indeed, orchards tractors have very complex mechanical gearboxes as shown in Figure 2.1.

Another way in which the tractor can transfer power to the attached implements is by means of a hydraulic power connection. In this case, the power is transferred by an hydraulic circuit with an hydraulic pump directly connected to the engine.

2.1.2 Orchard tractors electrification

Due to their peculiar properties, electrification of orchard tractors has been characterized by challenging issues. Full-electric configurations are the simplest solutions

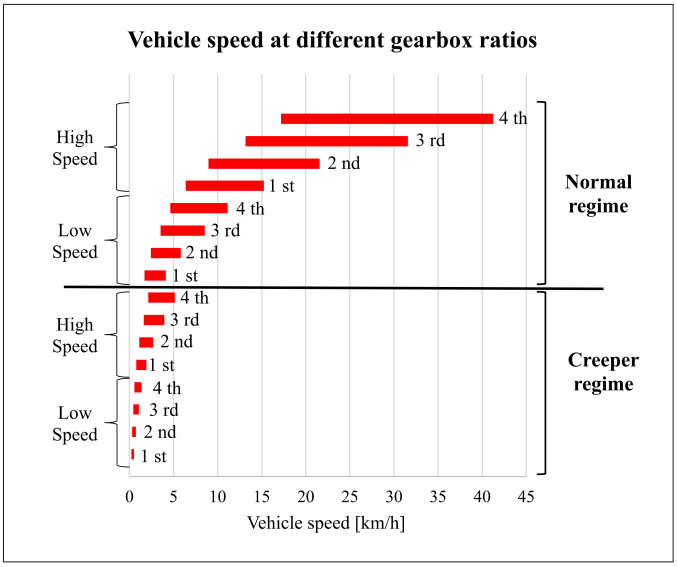

Figure 2.1 Typical orchard tractor gearbox configuration.

since they only feature a Li-ion battery storage system, one or more electric motors and power converters to manage the electric power, in particular converting DC current, coming from the batteries, into AC current, which is used to feed the motors. Despite its simplicity, this configuration has a huge issue related to the limited on-board space availability and to the energy density of batteries. Indeed, orchard tractors may have to operate for several hours in a row, but this may not be possible when introducing pure battery vehicles. Furthermore, the limited availability of a charging infrastructure in rural area is also a limiting factor.

Despite these limiting factors, several full-electric prototypes have been proposed throughout the years. One of the most relevant was presented in 2017: the Fendt e100 Vario [66]. In this case, the powertrain featured the presence of an electrical motor generator with a rated power of 50 kW, and a 100 kWh battery pack. This unit provided power both to the PTO and to the wheels, in this last case by means of a continuously variable transmission (CVT). The machine was also characterized by the presence of an electrical connection for electric implements. Other relevant full-electric prototypes of orchard tractors were presented by Kubota and Monarch [67, 68].

To overcome the limits related to full-electric configurations, several efforts have also been made in the development of hybrid thermal-electric vehicles. Depending on the configuration, these powertrain can be divided into series hybrid, parallel

hybrid, and complex hybrid. Studies available in the literature have shown that these vehicles can achieve significant fuel savings, up to more than 20%, without reducing productivity [69, 70]. Also in this case, several prototypes have been presented in the last years, showing a growing interest towards hybrid systems [71, 72]. Indeed, the presence of the thermal unit allows the guarantee of a satisfactory productivity which instead may not be achieved with the full-electric counterpart.

In this context, fuel cell powertrain can be an interesting solution since they can meet zero-local emissions as full-electric vehicles, but without reducing the productivity. Indeed, the high energy density of hydrogen and the refueling time comparable with the conventional counterpart are key feature that particularly fit the operative requirements of orchard tractors. As previously mentioned in 1.7, a prototype of a fuel-cell powered orchard tractor was presented by Steyr in 2024, showing that the industrial world is starting to consider this powertrain as a feasible solution for the future of orchard cultivations.

2.2 Numerical modeling of a fuel cell system

Several approaches can be adopted to model a fuel cell system. In the proposed study, the adopted methodology consisted of a Physical Network (PN) modeling technique. According to this approach, each element is considered as a physical entity capable of exchanging energy with all the other subsystems to which it is connected. The solution of the systems must satisfy the power balance equations for each component at each time step. The PN approach was chosen due to its properties, which include:

- Physical consistency.
- Possibility to substitute models of different levels of complexity without introducing changes to the schematic (incremental modeling).
- The connection ports of the model mimic the physical connections between elements.
- It automatically resolves all the traditional issues with variables, directionality, and so on with its Through and Across variables and nondirectional physical connections.

Compared to object-oriented modeling, the governing equations are derived automatically from the interconnection of physical components, thus the model closely reflects the real system multiphysics behavior. Consequently, PN ensures a physical consistent energy-based system, which was deemed more suitable for the proposed analysis.

Given these premises, the modeling of a fuel cell system should include the stack and its BoP to properly evaluate the efficiency and dynamic behavior.

2.2.1 Fuel Cell stack modeling

As introduced in section 1.1, a PEM fuel cell stack is composed by a series of cells connected in series. Indeed, the series connection allows for producing enough voltage. The stack can be modeled using the following equations [73]:

$$V_{\text{stack}} = N_{\text{cell}} \cdot (V_{\text{Nernst}} - V_{\text{act}} - V_{\text{ohm}} - V_{\text{conc}}) \tag{2.1}$$

Where:

- V_{stack} is the overall stack voltage.
- N_{cell} is the number of cells in the stack.
- V_{Nernst} is the Nernst voltage.
- V_{act} is the voltage loss due to activation.
- V_{ohm} is the voltage loss due to ohmic resistance.
- V_{conc} is the voltage loss due to concentration.

The Nernst voltage can be evaluated according to:

$$V_{\text{Nernst}} = V_{\text{cell}}^{0} - \frac{R_g T}{2F} \cdot \ln\left(\frac{p_{H_2O}}{p_{O_2}^{0.5} p_{H_2}}\right) \tag{2.2}$$

The term V_{cell}^{0} represents the standard cell potential, equal to 1.229 V. The standard cell potential is the ratio between the Gibbs free energy of water, equal to

-237.14 kJ/mol, and -2F, where F is the Faraday constant, equal to 96,485.33 C/mol. R_g is the ideal gas constant, p_{H_2O}, p_{O_2} and p_{H_2} are, respectively, the water, oxygen and hydrogen partial pressures, and T is the stack temperature.

The activation, ohmic and concentration losses can be expressed using:

$$V_{\text{act}} = \frac{R_g T}{2F\alpha} \cdot log(\frac{i_{\text{dens}}}{i_0}) \tag{2.3}$$

$$V_{\text{ohm}} = R_{\text{ohm}} \cdot i_{\text{dens}} \tag{2.4}$$

$$V_{\text{conc}} = \frac{R_g T}{2F} \cdot log(1 - \frac{i_{\text{dens}}}{i_{\text{lim}}}) \tag{2.5}$$

where α is the charge transfer coefficient, i_{dens} is the current density, i_0 is the reaction exchange current density and i_{lim} is the maximum current density. The term R_{ohm}, which represents the ohmic resistance, is generally dependent from the membrane water content, the temperature and the thickness. Into details, the following relationships can be used to model R_{ohm} [74]:

$$\sigma_{\text{mem}} = (0.5139 \cdot \lambda_{\text{mem}} - 0.326) \cdot exp[1268 \cdot (\frac{1}{303.15} - \frac{1}{T})] \tag{2.6}$$

$$R_{\text{ohm}} = \frac{t_{\text{membrane}}}{\sigma_{\text{mem}}} \tag{2.7}$$

where λ_{mem} is the number of water molecules held per sulfonic acid group, t_{membrane} is the thickness of the membrane and σ_{mem} is the membrane conductivity per unit of length of membrane thickness.

2.2.2 Hydrogen adduction system modeling

The hydrogen adduction system can be modeled considering its main components: a hydrogen source, a pressure-reducing valve, and a recirculating system, consisting of a hydrogen recirculation pump or an ejector. In the proposed modeling, a recirculation pump was considered, which was modeled as a controlled mass flow rate source. From a numerical point of view, the scheme reported in Figure 2.2 was considered.

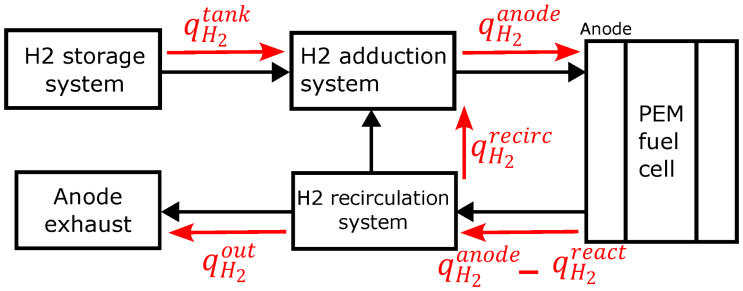

Figure 2.2 Schematic representation of the hydrogen adduction system from the numerical point of view.

The hydrogen storage system was supposed to be a 700 bar tank with a temperature set at 298.15 K. According to the figure, the following mass flows were defined: $q_{H_2}^{\text{anode}}$, which represented the hydrogen flowing into the stack anode, $q_{H_2}^{\text{react}}$, which corresponded to the hydrogen reacting in the stack, $q_{H_2}^{\text{recirc}}$, which indicated the hydrogen flow through the recirculation system, $q_{H_2}^{\text{tank}}$, which was the hydrogen flow coming from the tank, and finally $q_{H_2}^{\text{out}}$, which instead referred to unused hydrogen that was not actually recirculated. The hydrogen reacting in the stack was evaluated according to the following equation:

$$q_{H_2}^{\text{react}} = \frac{N_{\text{cell}} i_{\text{FC}} MM_{H_2}}{2F} \tag{2.8}$$

where MM_{H_2} is the molar mass of H_2 and i_{FC} is the current delivered by the stack. According to the scheme represented in Figure 2.2, the following flow mass balance equation was defined:

$$q_{H_2}^{\text{anode}} = q_{H_2}^{\text{tank}} + q_{H_2}^{\text{recirc}} \tag{2.9}$$

As for $q_{H_2}^{\text{out}}$, it was evaluated proportional to the hydrogen pressure with an empirical coefficient [75], while $q_{H_2}^{\text{recirc}}$ was controlled based on the actual stack current. The pressure reducing valve was modeled as a localized reduction in the flow area, whose value was regulated as a function of the anode pressure. Indeed, knowing the anode volume, the hydrogen pressure variation can be evaluated combining the ideal gas law with the mass conservation law. Into detail, the value of the restriction area was evaluated using the following approach function:

$$A_{\text{restr}} = \begin{cases} A_{\text{restr,max}} & \text{if } p_{\text{H}_2} < (p_{\text{H}_2,\text{nom}} - p_{\text{range}}) \\ A_{\text{restr}}(p_{\text{H}_2}) & \text{if } (p_{\text{H}_2,\text{nom}} - p_{\text{range}}) < p_{\text{H}_2} < (p_{\text{H}_2,\text{nom}}) \\ A_{\text{restr,min}} & \text{if } p_{\text{H}_2} > (p_{\text{H}_2,\text{nom}}) \end{cases} \tag{2.10}$$

As can be stated, the restriction area increased as the pressure in the anode decreased, thus compensating for the hydrogen reacting in the stack by increasing the mass flow from the tank.

2.2.3 Air adduction system modeling

The oxygen mass flow reacting at the cathode of the stack can be evaluated according to:

$$q_{O_2}^{\text{react}} = \frac{N_{\text{cell}} i_{\text{FC}} MM_{O_2}}{4F} \tag{2.11}$$

The air compressor is the main element of the air adduction system. Furthermore, it is the most power-absorbing element in the BoP. Consequently, its power absorption must be considered during the numerical analysis. To address this issue, the compressor was modeled as a controlled mass flow rate source that was controlled considering the OER (oxygen excess ratio). This parameter is defined as the ratio between the oxygen flow rate into the cathode and the oxygen flow rate that actually reacts in it. To achieve optimal efficiency, the OER that the compressor should provide is function of the stack properties, the compressor itself and the fuel cell power output [74, 75]. Fixed the OER value, the compressor can be controlled using a PI controller that follows the target mass flow.

To estimate the power absorption of the compressor, its max isentropic efficiency was imposed equal to 60%. The oxygen partial pressure was evaluated using the same approach of the hydrogen adduction system. The cathode exhaust instead was numerically simulated as a pressure relief valve (local restriction function of the actual cathode pressure).

2.2.4 Heat management system modeling

The heat management system was modeled considering the presence of the following elements: a radiator, a pump and the fuel cell coolant channels. The heat produced by the fuel cell, which can be evaluated considering the actual stack efficiency, is transferred to the coolant fluid by means of the coolant channels.

The heat exchanged at the coolant channels between the wall and the thermal fluid is evaluated considering two heat exchanging processes, namely convection and conduction, as expressed in the following equation:

$$Q_{\text{heat}} = Q_{\text{conv}} + \frac{kS_H}{D} \cdot (T_H - T) \tag{2.12}$$

where:

- Q_{heat} is the heat flow rate.
- Q_{conv} is the portion of heat attributed to convection.
- k is the thermal conductivity of the thermal liquid.
- S_H is the surface area of the pipe wall.
- T_H is the temperature of the pipe wall.
- D is the hydraulic diameter of the pipe.

The convective portion was evaluated as function of the mass flow rate of thermal fluid, its specific heat, its temperature and the exchanging area according to the following equation:

$$Q_{\text{conv}} = |\dot{m}_{\text{coolant}}|\, c_{p,\text{coolant}} (T_H - T_{\text{in}}) \left(1 - \exp\left(-\frac{h_{\text{coeff}} A_H}{|\dot{m}_{\text{coolant}}|\, c_{p,\text{coolant}}}\right)\right) \tag{2.13}$$

The same approach was adopted to model the heat exchange between the thermal fluid and the radiator. In addition, the radiator exchanged temperature with the environment with forced convective heat transfer due to the presence of the fan. The mass flow of the thermal fluid was controlled with a PI controller to have a stack temperature of 80 °C.

2.3 Numerical modeling of traditional and fuel cell-powered orchard tractors

2.3.1 Traditional vehicle

The numerical modeling of a tractor should include all the main powertrain elements, namely the power generation system, the driveline, the longitudinal dynamics, the PTO and the vehicle control unit. The schematic representation of the traditional diesel-powered vehicle under consideration is shown in Figure 2.3.

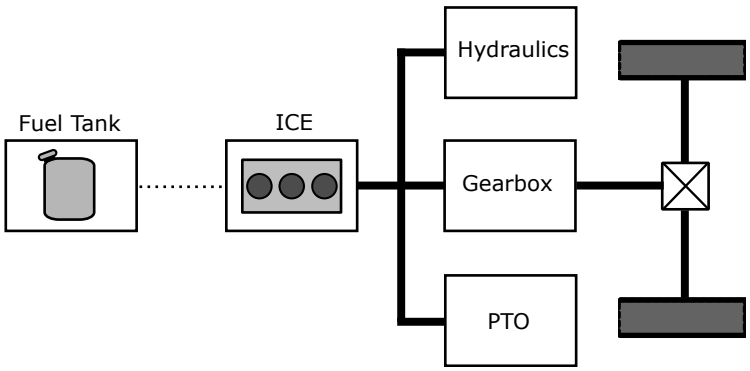

Figure 2.3 Schematic representation of the hydrogen adduction system from the numerical point of view.

The vehicle dynamics was described using a 1D longitudinal model, characterized by the following equations:

$$m\dot{V}_x = 2\left(F_{xf} + F_{xr}\right) - F_d - mg \cdot \sin\beta \tag{2.14}$$

$$F_{xf} = \frac{-h\left(F_d + mg \cdot \sin\beta\right) + b \cdot mg \cdot \cos\beta}{2(a+b)} \tag{2.15}$$

$$F_{zr} = \frac{+h\left(F_d + mg \cdot \sin\beta\right) + a \cdot mg \cdot \cos\beta}{2(a+b)} \tag{2.16}$$

Where:

- a,b and h are the relative positions of the center of gravity of the vehicle with respect to the front and rear axles.
- m is the tractor mass.
- β is the road slope angle.
- V_x is the longitudinal speed of the tractor.
- F_d is the aerodynamic drag force, as $F_d = 0.5\rho C_d A V_x^2 sign(V_x)$ with ρ the air density, C_d the drag coefficient and A the frontal cross-sectional area.
- F_{xf} and F_{xr} are the contact forces between the wheels and the ground on the longitudinal direction (r: rear axle, f: front axle).
- F_{zf} and F_{zr} are the normal contact forces between the wheels and the ground (r: rear axle, f: front axle).

According to this model, the vehicle motion was the result of all the forces and torques applied to the body of the tractor. When considering the presence of a trailer or an implement with a relevant mass, the connection between the two bodies was considered rigid and thus the they shared the same longitudinal speed.

The contact between the tires and the soil was modeled considering static and kinetic coefficients, the first determining the applied torque at which the tire loses traction and begins to slip, and the second determining the amount of torque the tire is capable of transmitting to the terrain once it starts to slip. According to this approach, the following equation was derived:

$$F_{xi} = \begin{cases} \frac{T_{wheel}}{R_{wheel}} & \text{if } \frac{T_{wheel}}{R_{wheel}} \leq \mu_{static} \cdot F_{zi} \\ \mu_{kinetic} \cdot F_{zi} & \text{if } \frac{T_{wheel}}{R_{wheel}} > \mu_{static} \cdot F_{zi} \end{cases} \tag{2.17}$$

where F_{xi} is the traction force on the i-axle, F_{zi} is the normal force on the i-axle, T_{wheel} is the torque at the wheel downstream from the driveline, R_{wheel} is the wheel radius, and μ_{static} and μ_{kinetic} are, respectively, the static and kinetic friction coefficients.

As for the transmission, the gearbox was modeled considering groups of simple gears connected in series or parallel with the help of disengaging friction clutches

to achieve the desired gear ratio. Each pair of gears was modeled considering a transmission efficiency. Lastly, each transmission element was modeled considering reasonable values in terms of inertia and damping.

The diesel engine was modeled through a tabulated torque data approach using its torque-speed curves. To determine the fuel consumption, the efficiency map was modeled using the approach proposed in [76]. According to this model, the actual brake specific fuel consumption (BSFC) can be evaluated considering the actual operating point, the rated torque and speed of the engine and the minimum BSFC:

$$Z = b_1 + b_2 \cdot X + b_3 \cdot Y + b_4 \cdot X^2 + b_5 \cdot X \cdot Y + b_6 \cdot Y^2 \tag{2.18}$$

where:

- **X** is the normalized engine speed: $X = \frac{n}{n_{nom}} \cdot 100$.
- **Y** is the normalized brake torque: $Y = \frac{T}{T_{nom}} \cdot 100$.
- **Z** is the normalized BSFC: $Z = \frac{BSFC}{BSFC_{min}} \cdot 100$.
- $b_{i=1,\ldots,6}$ are the polynomial coefficients.

According to this model, the region of the minimum BSFC is usually located at about 73–77% of the nominal engine rotational speed and at a high load, namely 85–95% of the nominal torque.

Lastly, the PTO and AUX loads were modeled using a resistive torque applied to the tractor. The PTO load represented the power required by the implements connected to the tractor, while the AUX load represented the power required by auxiliaries and accessories.

Given the details of the numerical approach, the main properties of the orchard tractor that was considered for the numerical analysis are reported in Table 2.1.

Table 2.1 Main properties of the traditional orchard tractor considered in the study.

Vehicle properties	
Mass	2571 kg
Wheelbase	1.9 m
Track width	1.85 m
Wheel radius	0.68 m
Engine rated power	73 kW @ 2600 rpm
Top speed	42 km/h
Transmission	Manual with 32 gears

As for the vehicle control, agricultural tractors mainly operate with a reference speed control, in contrast with the automotive sector, where passenger cars operate with the driver that directly imposes the torque using the pedal. In orchard tractors instead, the driver sets the engine speed and the system automatically determines the torque to achieve the desired regime. Following these premises, the powertrain control was obtained using a PI controller that determined the torque from the difference between the actual speed and the target speed.

2.3.2 Fuel cell-powered vehicle

The layout of the proposed fuel cell powertrain is shown in Figure 2.4. The proposed architecture was the FC + battery configuration. This configuration was chosen since, due to the limited on-board space availability of the vehicle due to the need of high compactness and maneuverability, a higher energy storage density was preferred. Apart from the fuel cell system, whose numerical modeling has already been described in Section 2.2, the powertrain elements that differed from the traditional vehicle and that had to be modeled where the electric motor, the inverter, the unidirectional DC-DC and the battery pack.

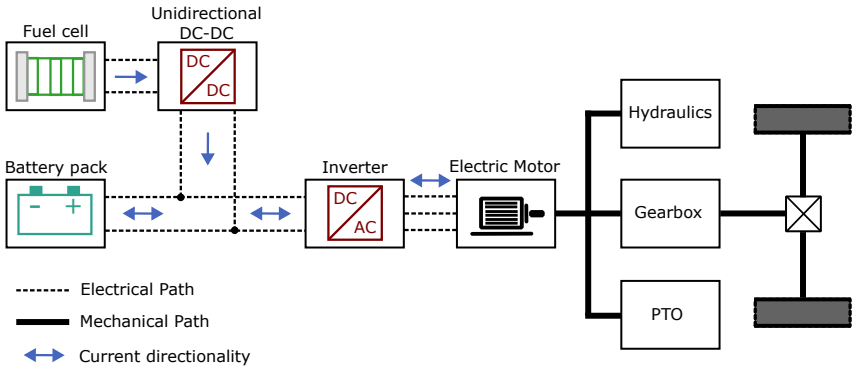

Figure 2.4 Layout of the proposed Fuel Cell powertrain

The mechanical transmission was maintained the same of the traditional counterpart. Even though this approach might appear not optimal, it cannot be avoided in order to achieve at least comparable performance of the diesel-powered vehicle. Indeed, due to the mechanical link between the PTO and the electric motor, a high number of ratios is mandatory to allow for operating in the field at a satisfactory number of different speeds. Furthermore, also the overcoming of slopes capabilities must be maintained.

The electric motor was modeled considering the properties reported in Table 2.2, in order to be very close to the reference diesel engine. Efficiency was modeled using a tabulated map function of torque and speed.

Table 2.2 Main properties of the electric motor.

Electric motor properties	
Rated power	75 kW @ 2600 rpm
Rated torque	258 Nm
Max efficiency	94 %

The inverter was modeled considering only its efficiency, which was assumed constant. On the contrary, the DC-DC converter was modeled considering its control and mapping its efficiency as function of the output current. According to this approach, at low output currents the efficiency is very low (around 60%), then it increases reaching its max, and then starts to decrease due to ohmic losses that become predominant at high output currents.

As for the battery pack, it was modeled considering the equivalent circuit shown in Figure 2.5 [77]. According to this model, the V_{OC} represented the open circuit voltage, R_o the ohmic resistance, R_aC_a the activation dynamic, and R_cC_c the concentration dynamic.

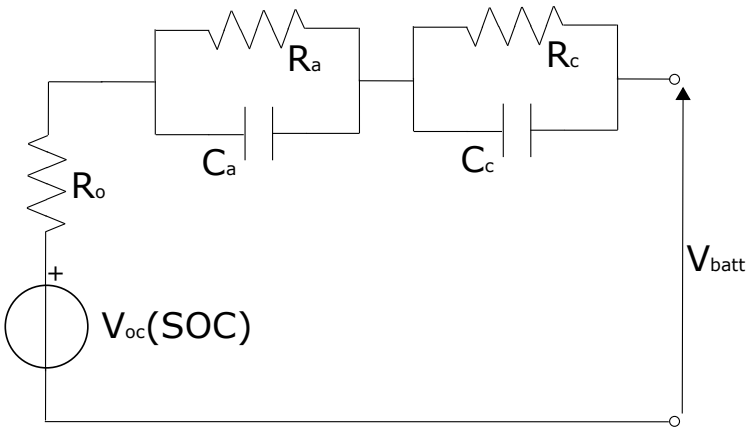

Figure 2.5 Battery pack equivalent circuit model

The relationship between the open circuit voltage and the battery SoC was described using the following equation:

$$V_{\mathrm{OC}} = V_{\mathrm{nom}} \cdot \frac{SOC}{1 - k(1 - SOC)} \tag{2.19}$$

where k is a coefficient that depends on the battery pack. To evaluate the actual SoC of the battery pack, a simple Coulomb-counting strategy was used, neglecting more detailed models available in the literature. According to this, the following equations were adopted:

$$C_{\mathrm{used}} = \int_{t_1}^{t_2} i_{\mathrm{batt}} dt \tag{2.20}$$

$$\mathrm{SOC} = \frac{C_{\mathrm{nom}} - C_{\mathrm{used}}}{C_{\mathrm{nom}}} \tag{2.21}$$

where C_{nom} and C_{used} are the nominal and used capacities respectively, and i_{batt} is the battery current.

Once the numerical modeling was performed, the definition of the main vehicle parameters was carried out. To properly size the main characteristics of the fuel cell powertrain, the on-board space availability must be taken into account. Given this premise, the parameters presented in Table 2.3 were considered feasible for the fuel cell system and the battery pack.

Table 2.3 Main properties of the fuel cell and battery pack.

Fuel cell system	
Rated power	66 kW
Number of cells	360
Battery Pack	
Nominal open circuit voltage	240 V
Nominal capacity	6 kWh

As for vehicle control, the electric motor was controlled in the same way as the diesel counterpart. However, since the powertrain features two power sources, an energy management strategy had to be defined to determine how to split the electric power among the fuel cell and the battery pack. Giving priority to robustness and reliability, a control strategy based on the power follower concept was defined. Thus, the current set-point of the fuel cell system was defined as a function of the power demand so that the fuel cell followed the load. In addition, penalty factors were introduced to account for SoC consumption and for limiting the battery current to preserve its state of health. Into details, the following limits were considered when defining the EMS [38, 78]:

- Max current during continuous discharge equal to 3C.
- Max current during instantaneous discharge equal to 5C.
- Max current during continuous discharge equal to 1C.
- Max current during continuous discharge equal to 1.5C.

A PI controller was implemented to follow the current set-point, with the coefficients that were tuned to have a smooth behavior to prolong the system durability. A schematic representation of the control strategy is shown in Figure 2.6.

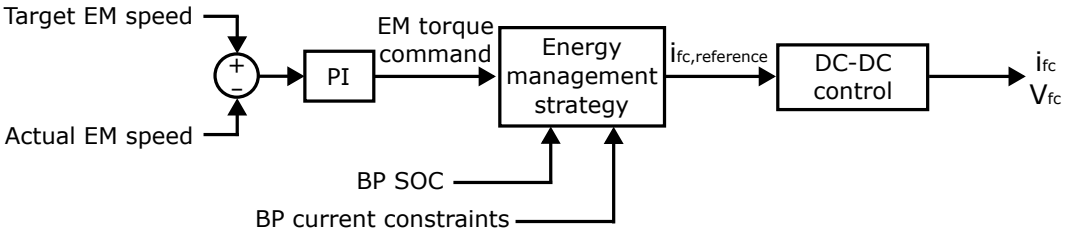

Figure 2.6 Schematic representation of the fuel cell powertrain control strategy.

2.4 Experimental analysis of orchard tractors mission profiles

To perform a reliable analysis, the definition of realistic load profiles is mandatory. Indeed, depending on the actual task the vehicle is performing, several different work conditions can occur, thus a comprehensive characterization of the most common scenarios, ranging from the handling of trailers to the use of implements, such as atomizers and so on, had to be tackled. Furthermore, the actual behavior of a real vehicle can be used to tune the numerical model.

2.4.1 Methods

To characterize the mission profiles of an orchard tractor without implementing additional transducers, the attention focused on the vehicle CAN BUS.

The Controlled Area Network (CAN) protocol is a robust and widely used communication system designed for real-time data exchange between electronic control units in vehicles. Originally developed by Bosch in the 1980s, it has become a standard in automotive and industrial applications due to its high reliability, flexibility, and fault tolerance [79]. The main features of this protocol can be summarized as follows:

- It requires only two wires, namely CAN HIGH and CAN LOW, and two 120 Ohm resistors.
- It has a maximum data rate of 1 megabit per second.

- Each message (frame) is characterized by an identifier and 8 bytes, which contains the data information.
- It has a prioritizing procedure, thus if two nodes attempt to transmit at the same time, the one with the lower priority identifier value (higher priority) wins, while the other waits without causing collisions.
- It includes Cyclic Redundancy Check, bit monitoring, and acknowledgment mechanisms to ensure data integrity.

Depending on the CAN bus variant, different properties of the protocol are observed. For example, using the CAN 2.0A protocol (standard), the frame uses 11-bit identifiers, while in case of the CAN 2.0B protocol (extended), the frame uses 29-bit identifiers.

Starting from the CAN bus protocol, the SAE J1939 standard was designed for heavy-duty vehicles, including agricultural machinery [80]. The main features of the J1939 standard are described in the following list:

- It has a prescribed baud rate of 250 kilobit per second.
- It uses the CAN 2.0B protocol, thus 29-bit identifiers.
- It allows a maximum of 30 nodes and 253 controller applications.
- It defines a set of Parameter Group Numbers (PGNs) to address predefined vehicle parameters.
- It adopts a 8-bit address system to identify the nodes and supports two types of communications: Broadcast (messages sent to all the nodes on the network) and Peer-to-Peer (messages sent to a specific node).

Into detail, the identifier in the protocol J1939 contains the following information: priority (3 bit), data page (1 bit), PDU format (8 bit), PDU specifics (8 bit) and source address (8 bit). An additional bit is reserved for future expansions.

Following these premises, data can be collected from a vehicle during its operation by implementing a listening device that is able to acquire the data sent by the single vehicle units in the CAN bus. Consequently, an experimental set-up was defined to develop a data-logging system to be placed on an orchard tractor.

The experimental set-up featured a PCAN-GPS device developed by PEAK System (PEAK-System Technik GmbH, Darmstadt, Germany) and a micro SD for storing the collected data. Given the vehicle CAN protocol, the attention focused on the following parameters:

- Driver pedal signal as reference of the desired working speed.
- Actual engine rotational speed.
- Actual engine load estimated by the vehicle control unit.
- Vehicle speed.
- PTO activation.

The data acquisition system was also provided with a GPS. Data were collected during normal daily work activities performed in northern Italy and the tests were not predefined for this investigation to avoid unwanted bias from users. Two work activities were recorded, one on the use of a sprayer and the other on the use of a weeder. Data were collected on a tractor with properties very close to those reported in 2.1.

2.4.2 Field tests and data analysis

Data were collected during two different typical workday activities. In the first case, the tractor performed a weeding activity, while in the second case it used an atomizer. The results of the monitoring campaign are shown in Figures 2.7-2.8.

Weed control in orchards is an essential agricultural practice that is used to limit unwanted vegetation that might compete with fruit trees for water, nutrients, and sunlight. Effective weed control improves tree growth, improves fruit yield, and reduces the risk of pests and diseases that can thrive in unmanaged vegetation. Weeding can be carried out in different ways: mechanical, chemical, cultural, and biological. In the specific case that was monitored, a chemical weeder was in use.

An atomizer is a special agricultural implement used in orchards for applying liquid treatments to fruit trees. It has to distribute pesticides, fungicides, herbicides, and foliar fertilizers (nutrient) efficiently by generating fine droplets and using a

powerful air stream to ensure thorough penetration of the canopy. An atomizer is generally composed of a tank, usually made of polyethylene or stainless steel, which stores the liquid solution; a pump, which is used to pressurize the solution before it reaches the nozzles; nozzles, which are used to control the droplet size and spray pattern and are adjustable to change spray angle and mass flow; an air fan, used to spread the liquid solution droplets. Furthermore, pressure regulators, control valves and an electronic control system are usually present.

Analyzing the results, three main operating conditions could be defined:

- **Idle:** the vehicle was turned on but was not performing any task.
- **On-road travel:** the vehicle was traveling from the farm to one field, or from one field to another.
- **Field work activity:** the vehicle was performing field activities with the attached implements.

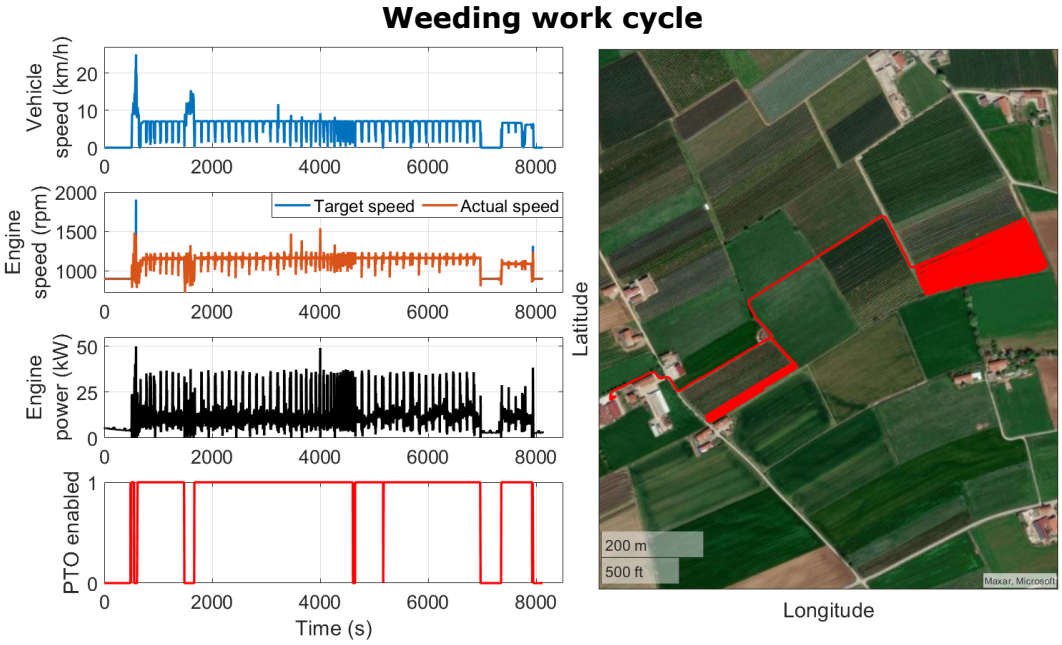

Figure 2.7 Experimental data for the weeding work cycle.

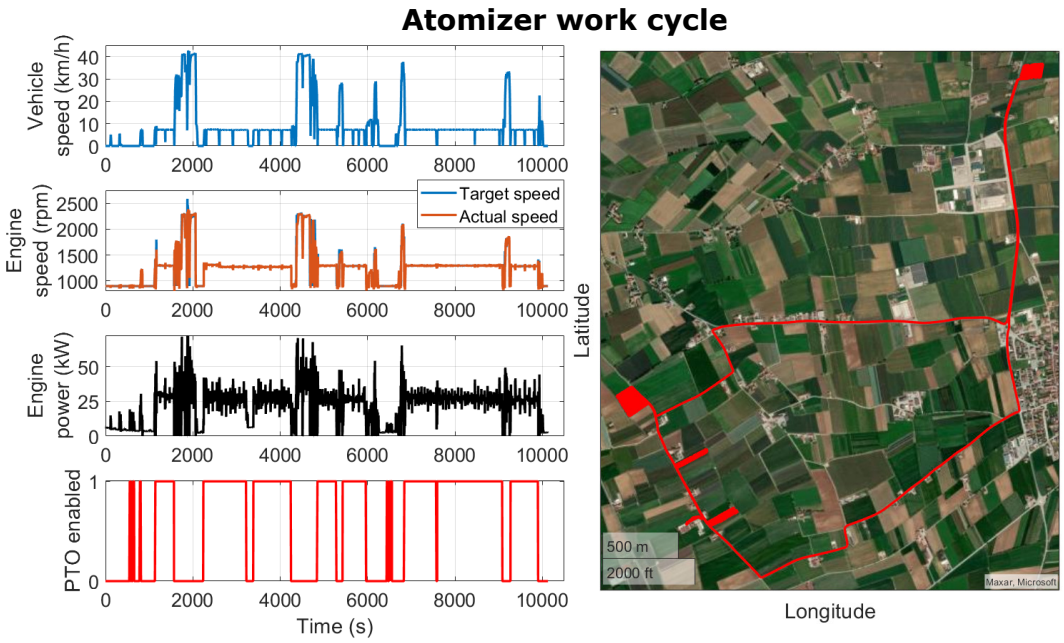

Figure 2.8 Experimental data for the atomizer work cycle.

It can be pointed out that the most demanding situations were strong acceleration during on-road travel, in which the engine load almost reached 100%. Regarding the field activities, during weeding the average engine load was equal to 25%, while during atomizer use it was slightly above 60 %. Consequently, it was possible to state that, apart from short peak power conditions, during most of the time the tractor operated significantly below its rated power.

2.5 Numerical simulations

Data collected during the monitoring campaign was used to tune the numerical model and determine the load scenarios during the simulations. Into details, the numerical analysis regarded the evaluation of the powertrain behaviors during the complete work cycles, focusing on diesel and hydrogen consumptions, and during a peak power condition, namely a 0-40 km/h acceleration when carrying a trailer of approximately 2 tons. The acceleration test was deemed of interest since the fuel cell powertrain should guarantee performance similar to that of the traditional system. The experimental data for the acceleration test were collected during the same monitoring campaign described in the previous section. On the contrary, the

simulation of a complete work cycle is of interest when performing fuel economy and environmental impact analysis.

2.5.1 Acceleration test

Acceleration tests represent a peak power condition and are useful for evaluating vehicle performance. In the proposed analysis, the attention focused on a 0-40 km/h acceleration on road handling a trailer of 2 tons. The experimental data were first compared with the simulation of the diesel vehicle, in order to tune and validate the numerical model. Then, after the validation, the data were compared with the simulation of the fuel cell/battery powertrain. The results are shown in Figure 2.9.

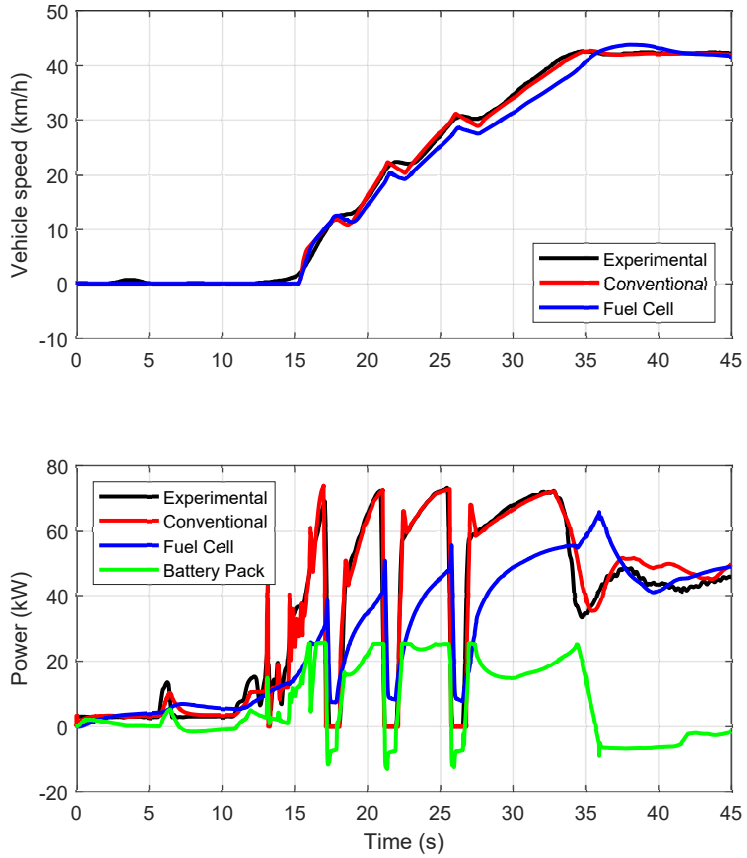

Figure 2.9 Acceleration Test: experimental vs simulations.

Analyzing the results, the first consideration that can be made is that the numerical approach showed a good match with the experimental results. Indeed, comparing the simulation results of the traditional vehicle with the experimental data, the power and speed profiles are very similar. Given that, the simulations also showed a slight increase in the acceleration time for the fuel cell vehicle. This can be related to the torque curve of the diesel engine being higher at medium-low speeds compared to the electric motor. Moreover, constraints on the maximum discharge current of the battery pack had to be respected, thus in some points the electric motor torque was limited. However, the difference was little and thus it can be stated that the fuel cell vehicle had a performance close to that of the diesel counterpart [73].

2.5.2 Work cycle test

The simulation results in terms of vehicle speed, power and battery pack SoC are presented in Figures 2.10 and 2.11. Analyzing the speed profiles, it can be noted that at some points the simulations were not able to fully replicate the experimental vehicle speed. This occurred when the vehicle performed turns, indeed to properly simulate the vehicle behavior during those phases a 2D vehicle dynamics approach must be adopted.

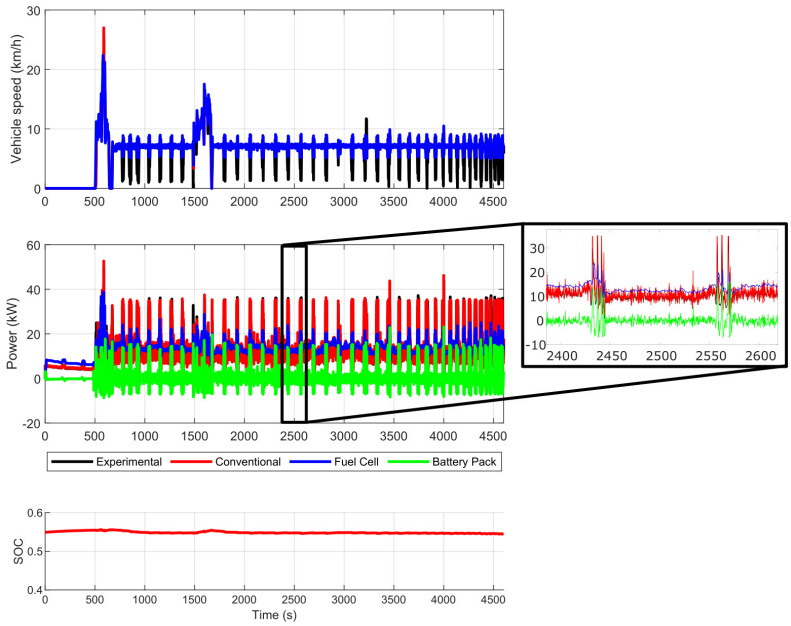

Figure 2.10 Simulation results for the weeding work cycle.

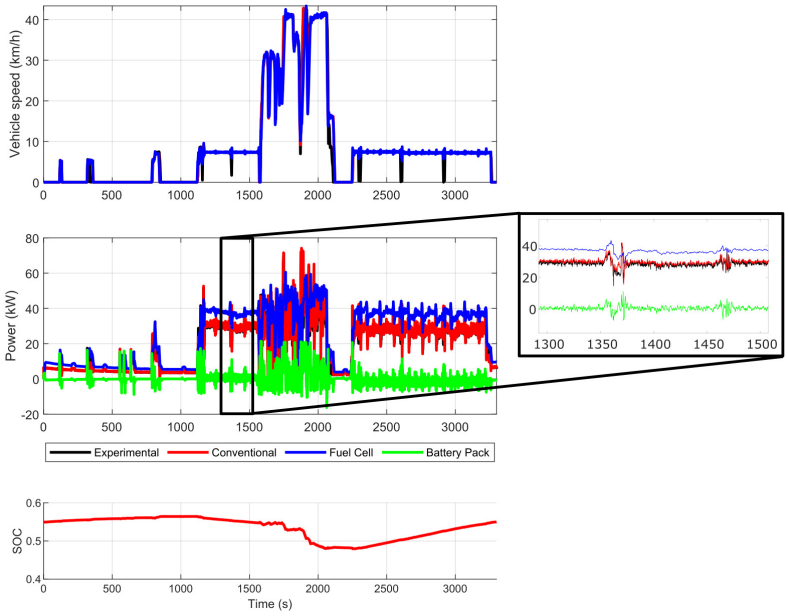

Figure 2.11 Simulation results for the weeding work cycle.

Even if during field operations the vehicle turned many times, in particular when reaching the end of a field row, this aspect did not influence the results since the main goal was to evaluate the fuel economy during the whole cycle.

Analyzing the fuel cell powertrain behavior, it is possible to highlight that it mainly operated in charge sustaining mode, with the fuel cell system that satisfied the average load demand and the battery pack that supplied power during transient phases.

However, to make a comparison between conventional and fuel cell hybrid vehicles, an equivalent indicator was chosen. Into detail, the Well-to-Wheel (WtW) CO_2 emissions related to fuel production and consumption were adopted. Indeed, even if the fuel cell/battery tractor locally emits zero emissions, the hydrogen production process is far from being without environmental impact. According to [81], the WtW emission factors represent the equivalent emissions related to both fuel production and fuel usage. For this purpose, the WtW factors for diesel fuel and hydrogen proposed in [82] and shown in Table 2.4 were adopted. It should be noted that the adopted coefficient for hydrogen refers to gray hydrogen produced through steam methane reforming. The authors considered this production process as it is the most

widely adopted at present and represents more than 60% of the global hydrogen production.

Table 2.4 WtW equivalent CO_2 emission factors for Diesel and H_2 adopted in the analysis.

Emission Source	**WtW Emission Factor**	**unit**
Diesel	3.18	kg CO_2-eq./L
H_2	9.13	kg CO_2-eq./kg

Table 2.5 shows the simulation results in terms of fuel consumption and related WtW CO_2 equivalent emissions [73]. The fuel cell tractor reduced the equivalent emissions of 44% for the sprayer work cycle, and this value reached about 55% for the weeding work cycle. The reduction of the equivalent CO2 emissions was greater in this second case, since the mean power demand was lower, and therefore the conventional diesel tractor operated at a low overall efficiency. In contrast, the fuel cell operated at a greater efficiency, since the maximum efficiency for a PEMFC system is generally at low load.

Table 2.5 Comparison of fuel consumption and CO_2 emissions

	Sprayer Work Cycle		**Weeder Work Cycle**	
	Diesel	**Hydrogen**	**Diesel**	**Hydrogen**
Fuel consumption	5.35 L	1.049 kg	4.58 L	0.714 kg
kg CO_2 equivalent	17.02	9.58	14.56	6.52
Difference CO_2 eq.		**-44%**		**-55%**

2.5.3 Discussion

The simulation results showed that the fuel cell/battery hybrid powertrain was able to achieve peak power performance close to the traditional counterpart, but showed a significant reduction in terms of greenhouse gas emissions. Into detail, during tractor operation, an average reduction of 50% in the CO_2 equivalent emissions was estimated. This result was obtained considering gray hydrogen, thus it can be

enhanced if H_2 produced from greener and more sustainable processes is adopted. In summary, the following considerations can be outlined:

- The fuel cell/battery powertrain showed performance very close to that of the traditional vehicle, guaranteeing the ability to perform the same tasks.
- The fuel cell/battery vehicle was able to reduce WtW greenhouse gas emissions of approximately 50% considering the actual state of the art of hydrogen production; furthermore, local emissions of the fuel cell-powered vehicle are almost zero.
- During the work cycles, the fuel cell power output followed the slow-dynamic part of the load, thus the oscillations in its power output were limited, allowing for achieving a satisfactory durability of the system.

In conclusion, the preliminary analysis showed that the fuel cell/battery powertrain is a feasible solution to substitute traditional systems in compact agricultural vehicles. However, to better evaluate the environmental benefits of adopting these vehicles, a life cycle assessment (LCA) analysis is required.

2.6 Life cycle assessment analysis

Life cycle assessment analysis is a standardized methodology, defined by ISO 14040 [83] and ISO 14044 [84]. According to the ISO standard, the LCA considers the whole life cycle of a product, from its production (raw material extraction, manufacturing, etc.), to use and end of life treatment. The main focus of this kind of analysis is to address the environmental aspects and impacts of a product system.

2.6.1 LCA methodology

LCA is a relative approach and is structured around a functional unit (FU), which defines what is under investigation. All inputs and outputs are related to this FU.

The LCA involves four main phases:

- The definition of the goal and scope.

- Inventory analysis.
- Impact assessment.
- Interpretation.

The goal of LCA describes the objective and application of the study, the target audience, and whether the results are meant for comparative assertions that will be publicly disclosed. The scope definition instead establishes the system boundaries and which life cycle stages are considered, defines the FU, identifies the allocation methods and the selected impact categories, and describes the data sources, limitations, and assumptions adopted.

In the subsequent phase, namely the inventory analysis, the quantification of the relevant inputs and outputs is performed, involving data collection and calculation procedures. Data collection can be carried out using databases, reports, and direct measurements of the elementary flows considered. The quality of the data should be described considering time-related issues, geographical correlations, precision, completeness, representativeness, uncertainty, etc. Inventory analysis provides the necessary set of data for the impact assessment phase.

During the impact assessment phase, the evaluation of the environmental impacts associated to the inventory data is performed. In other words, the collected inventory data is translated into meaningful environmental impact categories. It should be noted that this analysis addresses only the environmental issues indicated in the goal and scope. The outcome of the impact assessment phase is the quantification of the environmental impact indicators and constitutes the basis for the interpretation phase.

The final step of the LCA is represented by the interpretation phase, which involves the analysis of the results obtained from the previous steps to draw conclusions, identify key environmental issues, and suggest recommendations. This phase may also include comparative assertions where applicable. The interpretation should be carried out according to the goal and scope. Furthermore, this phase should consider an evaluation procedure involving completeness, sensitivity, and consistency checks.

2.6.2 Goal and scope

In the following subsections, an LCA analysis to compare the environmental impacts of the traditional vehicle and the fuel cell-powered counterpart is presented [85]. The analysis is aimed at an audience that can include tractor manufacturers, institutional agencies, researchers, and agricultural mechanization specialists. The two vehicles under investigation are the same that were introduced in Section 2.3. Since only vehicles were considered, all implements used during their operative life were not included.

The life cycle of each tractor was divided into three stages:

- **Production:** this stage includes all the processes, from raw material extraction to the final assembly, for vehicle manufacturing.
- **Use Phase:** this stage considers the operational life of the vehicle, including fuel consumption and service maintenance.
- **End-of-life:** this stage includes vehicle disassembly, disposal, recycling, and other recovery processes that allow for circular economy and waste management strategies.

The FU adopted in the analysis was defined as 1 $kg_{vehicle}^{-1} \cdot year^{-1}$. The supposed operational life of the vehicles was considered equal to 10 years. A schematic representation of the stages of the life cycle considered during the analysis is shown in Figure 2.12.

2.6.3 Production phase inventory analysis

The production phase should include the extraction of raw materials, their processing, the manufacture of the various components, and the assembly of the vehicle. To perform the inventory analysis, the main elements of the vehicle were divided into the following subsystems:

- **Power generation:** this subsystem consists of all the elements for power generation on board. For the traditional vehicle, it includes the internal combustion engine and the exhaust gas aftertreatment systems, while for the fuel

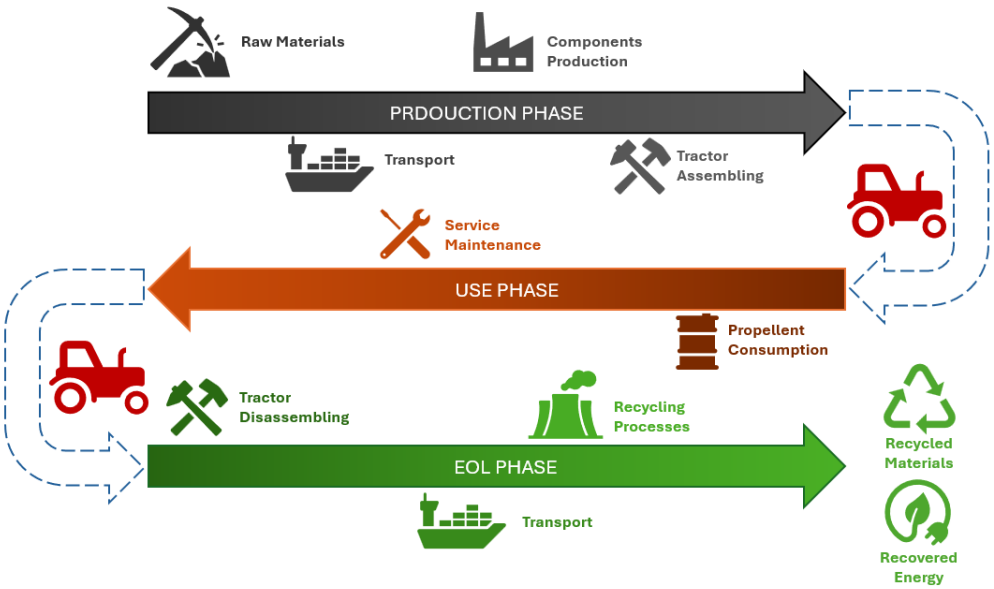

Figure 2.12 Main stages considered during the LCA analysis.

cell-powered vehicle it included the whole FC systems (thus both the stack and the BoP), the hydrogen tank, the Li-ion battery pack, power converters (DC-DC, inverter) and the electric motor.

- **Chassis and transmission:** this subsystem included all elements related to the vehicle chassis, mechanical transmission, and tires. Thus, it comprises the main frame of the vehicle, axles, gearbox and clutches, the transmission casing, and so on. As previously mentioned, this subsystem was considered the same for both traditional and fuel cell-powered tractors.

- **Electrical auxiliaries and services system:** it considers all components related to electrical accessories and services, including the 12 V system (with the lead acid battery), the vehicle control unit, cables, etc.

- **Cooling and Hydraulics:** it comprises the cooling and hydraulic systems. These systems are constituted by pumps, valves, thermostats, pipes, etc. It must be pointed out that the cooling system of the FC system is not included in this subsystem as it is part of the FC BoP, which is instead considered in the power generation subsystem.

- **Other:** it includes all the remaining components that were not included in the other subsystems.

During data collection for the aforementioned subsystems, it was observed that the two vehicles had almost the same mass, equal to approximately 2500 kg. This result was a consequence of the actual state of the art of FC systems, electric machines, and Li-ion battery packs.

Starting from the traditional vehicle, data collection was carried out using data available in datasheet, technical reports, and literature. To evaluate the impact of the processes involved in the manufacturing stage, the Ecoinvent v3.0 database was used. Please see Appendix A for further details. Regarding the diesel engine, a 75 kW EU stage IIIB unit was considered, which is mainly made up of cast iron, steel, and aluminum [86]. As for the aftertreatment system, it was considered composed of a Diesel Particulate Filter (DPF) and a Diesel Oxidation Catalyst (DOC). To evaluate the impact of these systems, data available in the literature were used [87]. The environmental impact for the production of the aftertreatment system is relevant due to the presence of precious metals as catalyst, such as Platinum in the DOC. The chassis was considered to be made up mainly of cast iron and steel sheet, while the transmission was assumed composed of steel shafts and gears. For tires, modeling was performed using the data provided in [88]. The Electrical auxiliaries and services system was modeled considering the commonly used 12 V system for tractors. Thus, cables, lead acid battery, connectors, and the vehicle control unit were considered. Regarding the cooling and hydraulics, the first was assumed made up of mainly aluminum, stainless steel, and brass, with minor presence of other materials. The hydraulic system instead was assumed to be composed primary of brass, steel pipes and rubber. Finally, in the other category all the remaining parts and elements were included, such as the paint, the driver's seat, tractor cab interior, and so on. The output of the traditional tractor production phase life cycle inventory is described in Table 2.6.

Regarding the fuel cell-powered tractor, some of the sub-assemblies were considered the same of the traditional counterpart, thus for these the same inventory was adopted. Instead, the main differences are related to the power generation and electrical auxiliaries and services system.

As for the power generation sub-assembly, the vehicle featured the presence of a PEMFC stack with a rated power of approximately 66 kW, a 6 kWh LiFePO4 battery pack, an electric motor with a rated power of 75 kW, and two power converters,

Table 2.6 Traditional tractor production phase life cycle inventory.

Sub-Assembly	Macro-Component	Value (kg per FU)
Power Generation	Engine	1.30e-2
	Aftertreatment system	8.00e-4
Chassis and Transmission	Chassis	4.54e-2
	Transmission	1.94e-2
	Tires	8.00e-3
Electrical Auxiliary Services System	12 V lead-acid battery	8.00e-4
	PCB	4.00e-5
	Cabling	6.00e-4
	Vehicle control units	1.20e-4
Cooling and Hydraulic Systems	Radiators (aluminum)	1.60e-3
	Steel pipe	2.20e-3
	Rubber	1.12e-3
	Brass	2.60e-3
Other Category	Seat	6.00e-4
	Rollbar	1.20e-3
	Dashboard	4.00e-4
	External bodywork	1.00e-3
	Paint	2.00e-4
	Screw	1.40e-3

namely a unidirectional DC-DC converter for the connection of the fuel cell stack to the DC bus, and an inverter, for the electric motor control.

Starting from the fuel cell system, it was modeled considering three main subsystems:

- **FC stack:** the stack is made up of a membrane, catalyst layer, gas diffusion layers (GDLs), bipolar plates (BPs), the housing, and other minor elements.
- **FC BoP:** BoP comprises the air, heat, hydrogen adduction, and water management systems.
- **Hydrogen storage system:** composed of a high pressurized (700 bar) tank.

To determine the FC stack inventory for the production phase impact assessment, the approach was inspired by the work proposed by Usai et al. [89]. Thus, the stack properties and inventory were evaluated starting from some key parameters that were determined based on data available in the literature and considering the actual state of the art. The first key parameter corresponded to the stack power density, expressed in W/cm^2. This value was assumed to be equal to 1.095 W/cm^2, which is the same as the one adopted in [89] and is consistent with the US DOE targets [90]. The stack power density parameters allowed for determining the stack active area. Then, the total area of the stack was evaluated using another key parameter, namely the total-to-active area ratio, which was assumed to be equal to 0.625 [89]. Regarding the catalyst layer, it was assumed to be composed of a platinum alloy deposited on a porous carbon layer. According to the literature and state of art, the Pt loading is usually in the range 0.15-0.5 mg/cm$^2_{\text{active}}$ [6, 91, 92]. In the proposed analysis, a Pt load of 0.32 mg/cm$^2_{\text{active}}$ was considered. As for the membrane, in PEMFC stack it is usually made of Nafion®, a material developed in the late '60s by the DuPont company (E.I. du Pont de Nemours and Company, Wilmington, USA). This material is a copolymer consisting of perfluorinated vinylether and tetrafluoroethylene [93]. Commonly adopted values for the membrane thickness are in the range of 10-100 μm [6]. The density of the membrane is around 2 g/cm^3. As for the GDLs, in PEMFC stacks they are generally made up with carbon cloth or paper with plytetrafluoroethylene (PTFE) and are characterized a thickness of 100-400 μm [6, 91, 92]. Between the GDL and the catalyst layer, a microporous layer is integrated, usually realized in carbon black and PTFE, with a thickness of 50 μm [6]. Regarding the BPs, different material can be used, including stainless steel, aluminum, carbon-based composites, and titanium [6, 91, 92, 94]. Furthermore, a protective coating is generally applied in case of metallic BPs to improve their resistance to corrosion. In the proposed analysis, BPs realized in stainless steel with a protective coating were considered. Lastly, the stack inventory included other elements not previously considered, such as end plates, current collectors, tie rods, gaskets, etc. To evaluate the electricity required for stack manufacturing, data available in [95] were used. A comprehensive summary of the assumptions adopted during this part of the study is provided in Table 2.7.

As for the fuel cell system BoP, it comprises the hydrogen supply, air supply, heat management, and water management systems. Starting from the air supply system, its main component is the air compressor [89], whose bill of material was evaluated according to [96], while for other components, such as the air filter, the data available

Table 2.7 Assumptions made during the evaluation of the stack production LCI.

Stack power density	1.095 W/cm^2
Total-to-active-area ratio	0.625
Membrane active area	6.03 m^2
Membrane material	Nafion, 25.4 μm thick
Pt load	0.32 mg/cm$^2{}_{\text{active}}$
GDL	Carbon paper with PTFE, 210 μm thick
Microporous layer	Carbon black and PTFE, 50 μm thick
Bipolar plate material	Stainless steel with coating

in [97]. The water management system was modeled considering the air pre-cooler, the humidifier and the tubing. The heat management system modeling included the radiator, the fan and the coolant pump. Lastly, the hydrogen supply system model comprised the hydrogen recirculation system, the valves and the pipes. For most of these elements, the data available in [96, 97] were used.

Regarding the hydrogen storage system, one Type IV tank was considered. The inventory for the production of this tank was modeled considering the data available in [98]. According to these data, one Type IV tank weighs approximately 102 kg and can store up to 5.6 kg of hydrogen. The tank is composed of 76 kg of carbon fiber and 26 kg of epoxy resin. Furthermore, an additional plastic liner made of high-density polyethylene (HDPE), with a weight of 7.5 kg, was included in the inventory.

The Li-ion battery considered in the proposed vehicle had a capacity of 6 kWh, a nominal voltage of 240 V, and adopted the lithium iron phosphate (LFP) technology. To define its inventory, the data available in [99–102] were combined. According to these data, an LFP cell is made up of a negative electrode, made with graphite as active material, and a positive electrode, whose active material is LiFePO4. Generally, the %wt. of the electrodes are around 12-24% for the anode and around 25-33% for the cathode. 2 %wt. of the weight is represented by the binder material, which was assumed to be Polyvinylidene difluoride (PVDC). The electrolyte was assumed to be composed of $LiFP_6$ dissolved in a solution 1:1 ethylene carbonate (EC) and dimethyl carbonate (DMC), and represents around 9-16% of the total weight. As for the separator, it was supposed to be 80% wt. of polypropylene (PP) and 20%

wt. of polyethylene (PE), and accounts for 5% of the total weight. Lastly, the battery management system (BMS), the cell container and the module casing were modeled.

As for the Electric Motor, a permanent-magnet synchronous motor (PMSM) was considered. The stator and rotor cores were assumed to composed of electrical steel, with 2% and 4% wt. of silicon and aluminum respectively. In addition, a thin coating of phenolic resin was considered. The stator and rotor cores masses represents roughly the 40-50% of the whole motor mass. The conducting wire was modeled as composed of copper insulated by one or multiple layers of insulation materials, generally polyester, polyamide or alkyd resins. The stator is commonly subjected to impregnation with a specialized material in order to achieve partial or complete encapsulation. Regarding the rotor endplates and the motor shaft, they were modeled as mainly made of stainless steel, and their size depends on the maximum motor torque. The magnets were assumed to be neodymium magnets Nd(Dy)FeB, accounting for a 3% of the motor mass. In the end, other elements that were considered were the bearings (low-alloyed steel), terminals, screws and nuts. The inventory was elaborated combining the data available in [103–106].

With regard to power converters, the powertrain features the presence of a traction inverter and a high-power DC-DC for the connection between the fuel cell stack and the DC bus. To define the inventories, the data available in [107] were used, scaling the mass according to the rated powers. Due to the lack of more detailed data, in the analysis the same inventory was considered for both the inverter and the DC-DC. Following the approach proposed in the aforementioned study, the power converter consists of several key subcomponents: an aluminum casing coated with protective varnish; the power module, which includes power devices, diodes, chips, and a copper baseplate with galvanized steel terminals; a DC link capacitor; a busbar composed of copper layers insulated with polyethylene terephthalate (PET); a printed circuit board (PCB); and various minor elements such as screws, washers, and spacers. More than 60% of the entire device mass is related to the aluminum casing, while the other subparts account for 7-11% of the overall mass each, apart from the PCB mass which generally is around 2-4%.

The material and mass distributions considered for the battery pack, electric motor, and power converters are summarized in Table 2.8. Combining the data of all elements of the power generation subassembly of the fuel cell hybrid electric tractor, Table 2.9 was obtained.

To complete the life cycle inventory related to the manufacturing of both tractors, two additional intermediate flows must be considered: the energy required for the final vehicle assembly and the impact related to transportation of materials and components. Indeed, once all components have been manufactured, the vehicle elements must be assembled on the final production line to obtain the finished product. To account for the energy required for the vehicle assembly, it was assumed that it was only in the form of electricity and the data available in [108] were used. According to this reference, the vehicle assembly energy consumption generally represents around 13% of the total energy consumed during the whole production phase, thus is not negligible. To evaluate the total energy required for the production of one tractor, 50 MJ per kg of vehicle were considered, as indicated by [109]. To assess the impact of electricity consumption, the generic European grid mix was considered. Lastly, the contribution of the transport of the materials and components had to be considered. Depending on the availability of materials and components around the world, two main groups were defined when considering the impact of transportation:

- **Group 1**: it considered all materials and components whose production could be placed in Europe; in this case, an average distance of 250 km from the assembly plant was assumed, and the transport vehicle was considered a truck equipped with a EURO 6 diesel engine.
- **Group 2**: it considered all materials and components whose production is mainly outside Europe, such as all electronic devices and precious metals; in this case, an average distance of 2500 km was assumed and sea transport by container ship was considered.

Table 2.8 Assumptions made during the evaluation of the battery pack, electric motor and power converters production LCI.

Powertrain Element	Sub-Component	Material	% wt.
Battery Pack	Cathode	$LiFePO_4$ (active material)	25%
	Anode	Graphite (active material)	20%
	Binder	PVDC	2%
	Electrolyte	$LiPF_6$ + solution 1:1 EC and DMC	9%
	Separator	PE + PP	5%
	BMS	-	5%
	Cell container	Aluminum	4%
	Module casing	Aluminum	20%
	Pack case	Aluminum and steel	10%
Electric Motor	Stator and rotor cores	Electrical steel with coating	46%
	Conducting wire	Copper with insulation materials	11%
	Rotor endplates	Stainless steel	1.5%
	Motor shaft	Stainless steel	4%
	Housing	Aluminum	25%
	Magnets	Nd(Dy)FeB	3%
	Other	-	9.5%
Power Converter	Casing	Aluminum with varnish	62%
	Busbar	Copper layers insulated by PET	9%
	Power module	Copper, plastics, silicone gel, galvanized steel	7%
	DC link capacitor	Plastic-film-type capacitance	7%
	PCB	-	4%
	Other	-	11%

Table 2.9 Power generation sub-assembly LCI according to the adopted FU.

Macro-Component	Value FU [kg*kg$_v^{-1}$*y^{-1}]
FC Stack	1.60×10^{-3}
Air Compressor	2.00×10^{-4}
Water Management	3.00×10^{-4}
Heat Management	6.00×10^{-4}
Hydrogen Supply System	1.60×10^{-4}
Hydrogen Tank	4.40×10^{-3}
DC/DC Converter	2.40×10^{-4}
Battery Pack	2.40×10^{-3}
Inverter	2.40×10^{-4}
Electric Motor	1.80×10^{-3}
Signal and Power Cabling	6.00×10^{-4}

2.6.4 Use phase inventory analysis

After production, the vehicle begins its service life, which is characterized by energy and fuel consumption. In this subsection, the quantification of these consumptions is addressed. To consider a reasonable service-life scenario, 1000 hours of annual working time for 10 years were assumed [110]. For both the traditional and the fuel cell powered tractors, the use phase emissions are mainly related to

- Production, supply, and consumption of propellant.
- Service maintenance of lubricants and tires.
- Transportation of maintenance elements.

If for traditional vehicles, fuel production and consumption are generally the most relevant sources of impact considering the whole life cycle [111], for alternative propulsion systems, specially fuel cell powertrain, the impact is strongly related to propellant production [112]. Indeed, if green hydrogen is adopted, the use phase impact may be very low. However, since at present most of the hydrogen comes from fossil fuels, in this analysis it was assumed that all of the hydrogen used during the tractor service life was gray hydrogen. More in detail, it was considered a hydrogen

production mix with more than 60% of hydrogen obtained from steam methane reforming. To evaluate the total hydrogen consumption during the whole use phase, the annual duty cycle of the tractor was defined according to [65]. This duty cycle was defined considering the most common tasks performed by orchard tractors in vineyards. Table 2.10 shows the adopted duty cycle. To evaluate diesel and hydrogen consumptions, the numerical models presented in Section 2.3 were used.

Table 2.10 Annual duty cycle considered in the analysis for an orchard tractor.

Task	Annual Work Time (%)	Avg. Power (kW)
Weeding	14.3%	35.6
Use of atomizer	14.3%	42.1
Grape harvesting	14.3%	20.7
Plant lifting plowing	28.6%	11.0
Use of tying machine	28.6%	5.3

As for the tractors maintenance, the following operations were considered [113]:

- Engine lubricant oil substitution every 300 h (only for the traditional vehicle).
- Hydraulic oil substitution every 1500 h.
- Tire substitution every 2500 h.

Finally, the contribution of transportation of the substituting elements and the supply of the propellant were taken into account. An average distance of 250 km and transport by truck were considered. According to these assumptions, Table 2.11 was obtained.

2.6.5 End-of-life phase inventory analysis

The end-of-life is the last stage of a product and takes into account disassembly of the components and disposal of the materials. In the performed analysis, the scenario consisted of tractor disassembling, transport of dismounted components and materials, and disposal treatments, which can be either recycling, energy recovery, or land-filling depending on the specific case.

Table 2.11 Use phase inventories for the two tractors.

Vehicle	Macro-Component	Value FU [kg_v^{-1}*y^{-1}]
Traditional tractor	Propellant (Diesel)	2.24 kg
	Engine Lubricant Oil	1.08×10^{-2} kg
	Hydraulic Oil	3.6×10^{-3} kg
	Tires	2.40×10^{-2} kg
	Transport (Road)	5.69×10^{2} kgkm
Fuel cell powered tractor	Propellant (Gray Hydrogen)	5.08×10^{-1}
	Hydraulic Oil	3.6×10^{-3} kg
	Tires	2.40×10^{-2} kg
	Transport (Road)	1.34×10^{2} kgkm

Starting from the vehicle disassembling, it was assumed that energy required is the same for the assembling procedure. The transport of the different components obtained downstream the disassembling was considered to be performed by truck with an average distance of 250 km.

In the disposal plants, the final treatment depended on the materials of the single components. Three main categories can be defined:

- **Metal components**: for metal components, a high recycling process was considered. Into details, the following procedure was considered: the different materials are firstly collected, sorted and pressed, then they are recycled according to their specific recycling process. Thus, the results is the production of secondary raw materials from scraps. The recovery rates considered were 88% for steel and cast iron, 96% for aluminum and 100% for brass and copper [114].
- **Plastic components**: plastic components were grouped into three sub-categories: thermoplastic components, thermoset components and rubber-derived products. While thermoplastic materials are usually recyclable (an average recovery rate of 84% was assumed), the other two groups usually are not. Thus, waste-to-energy processes were assumed for them. Into details, for the thermoset components, incineration processes were considered to obtain thermal energy, with a net energy production of 7.66 MJ/kg. Lastly, rubber-derived components, such as tires, were assigned to incineration to avoid steam production from primary sources.

- **Special components and electronic devices**: for special components and electronic devices, the purpose of the end of life process was mainly to recover secondary materials and precious metals; depending on the specific component, different scenarios were considered, including recovery of secondary copper (from PCBs and cables), lead scrap (from 12 V lead-acid battery), steel recovery (from the electric motor). Some special elements, such as the capacitors in the power converters, followed an hazardous waste incineration process, while the traditional vehicle aftertreatment system end-of-life scenario was defined according to typical catalytic converter waste treatments. As for the Li-ion battery pack, its end of life scenario consisted of mechanical dismantling in order to separate the case, wires, plastics, PCBs and the cells. The cells were recycled according to [115], thus the process included pre-treatments, metal extraction of cathode material by hydrometallurgical processing and cathode active material leaching to recover metals. The fuel cell stack end-of-life treatment instead consisted of manual dismantling followed by subdivision by material, which are then recycled according to the aforementioned processes. Particular attention was paid to the recovery of platinum in the stack, which is of primary importance to reduce the whole life cycle impact as it is a critical raw material [116]. Its recycling process was modeled using the process carefully described in [117], consisting of a H_2O_2/HCl solvent leaching with liquid/liquid extraction, that allows for a recovery rate of 76%. Lastly, the hydrogen tank end-of-life scenario included the mechanical separation of HDPE and CFRP, with the first one that was recycled while the second was landfilled.

2.6.6 Results and Discussion

The proposed LCA analysis considered different impact categories defined by ReCiPe 2016 v 1.03 at midpoint level [118]. Into details, the following impact categories were considered:

- **Global warming potential (GWP):** it is related to the emission of greenhouse gas and is expressed in $kg_{CO_2,eq}$.
- **Human toxicity carcinogenic ($\mathbf{HTP_C}$) and non-carcinogenic ($\mathbf{HTP_C}$):** they quantify the contribution of emissions of carcinogenic and non-carcinogenic

substances that can cause adverse health effects on humans; both are expressed in $kg_{1.4DCB,eq}$ (kilograms 1.4 dichlorobenzene equivalents).

- **Particulate matter formation potential (PMFP):** it is related to the emission of particulate matter and is expressed in $kg_{PM_{2.5},eq}$.
- **Terrestrial (TETP) and freshwater (FETP) ecotoxicity:** they quantify the contribution of emissions of substances that can adversely affect terrestrial and aquatic ecosystems; both are expressed in $kg_{1.4DCB,eq}$.
- **Photochemical oxidant formation for terrestrial ecosystems (EOFP) and humans (HOFP):** they quantify the contribution of emissions of substances that can cause the formation of ground-level ozone and other reactive oxidants as a result of emissions of precursors such as nitrogen oxides and volatile organic compounds, which can adversely affect terrestrial ecosystems and human health; both are expressed in $kg_{NO_x,eq}$.
- **Mineral resource scarcity (Surplus Ore Potential, SOP):** it quantifies the long-term implications of resource depletion, particularly for metal ores, and is expressed in $kg_{Cu,eq}$.
- **Fossil resource scarcity (Fossil Fuel Potential, FFP):** it quantifies the depletion of fossil energy resources due to current consumption and is expressed in $kg_{oil,eq}$.

Starting from the production phase, the results are exposed in Figure 2.13. The result are presented in percentage with respect to the ICET case for each impact category. Consequently, in the figure the value for the ICET is always 100%. As for the numerical results, they are shown in Table 2.12. Analyzing the results, several considerations can be outlined:

- Apart from the HTPc impact category, the impact of the production of the fuel cell tractor was higher; into details, for the HTPnc category it was almost 3 times the impact for the production of the traditional vehicle, and it was more than 2 times for the PMFP, FETP and HOFP categories.
- For most of the considered categories, the production of the power generation sub-assembly was the one with the highest impact for the FCHET; into details,

for the GWP100, HTPnc, PMFP, FETP, HOFP and EOFP, the impact for its production had an impact that is higher than the sum of the production impacts of all the other sub-assemblies. Going deeper into the results, it emerged that the production of the fuel cell system and the hydrogen tank were the most relevant, with peaks accounting for 40-50% of the entire vehicle production. The explanation for these results can be found in the large amount of carbon-fiber-reinforced polymer (CFRP) used to produce the tank and in the extraction and production of pure platinum used in the stack.

- For the traditional vehicle, the production of the chassis and transmission is the most relevant in almost all the categories.
- The production of the Li-ion battery pack had a relevant impact in the TETP and FETP categories, representing 7 and 5% respectively of the of the total vehicle production.
- The production of the electric motor had a relevant impact in the SOP category (36% of the total).

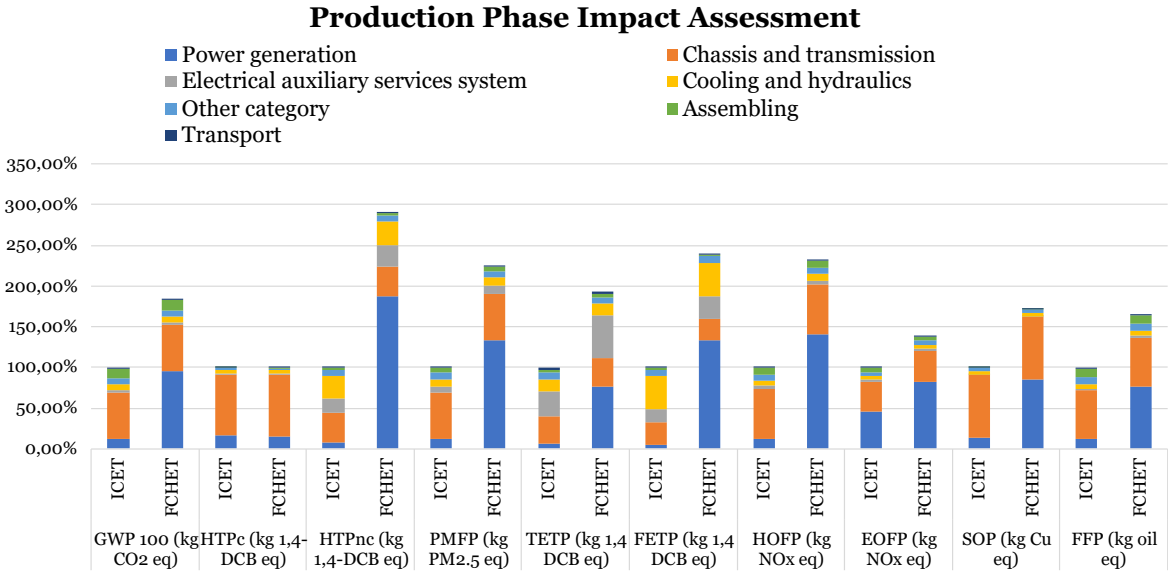

Figure 2.13 Production phase results. Please note that ICET refers to the traditional vehicle, while FCHET refers to the fuel cell-powered counterpart.

Thus, it can be stated that the greater environmental impact observed in the production phase of the FCHET, compared to its conventional counterpart, is pri-

marily attributable to the components of the Power Generation sub-assembly. These components often require significant amounts of precious metals, electronic devices, non-ferrous metals (e.g., lithium, copper), or highly specialized materials with demanding performance characteristics, for example in the case of the hydrogen tank.

Table 2.12 Production phase numerical results. Please note that a positive delta percentage means a higher impact for the FCHET with respect to the ICET.

Impact Category	**ICET**	**FCHET**	**Δ %**
GWP100 [$kgCO_2eq \cdot kg_V^{-1} \cdot y^{-1}$]	6.01×10^{-1}	1.11	83.72%
HTPc [$kg1,4DCB_{eq} \cdot kg_V^{-1} \cdot y^{-1}$]	4.04×10^{-1}	4.03×10^{-1}	-0.34%
HTPnc [$kg1,4DCB_{eq} \cdot kg_V^{-1} \cdot y^{-1}$]	1.22	3.53	189.42%
PMFP [$kgPM_{2.5}eq \cdot kg_V^{-1} \cdot y^{-1}$]	9.88×10^{-4}	2.22×10^{-3}	124.60%
TETP [$kg1,4DCB_{eq} \cdot kg_V^{-1} \cdot y^{-1}$]	3.20	6.17	93.05%
FETP [$kg1,4DCB_{eq} \cdot kg_V^{-1} \cdot y^{-1}$]	7.01×10^{-2}	1.67×10^{-1}	138.85%
HOFP [$kgNO_xeq \cdot kg_V^{-1} \cdot y^{-1}$]	1.52×10^{-3}	3.51×10^{-3}	127.56%
EOFP [$kgNO_xeq \cdot kg_V^{-1} \cdot y^{-1}$]	2.66×10^{-3}	3.67×10^{-3}	38.22%
SOP [$kgCu_{eq} \cdot kg_V^{-1} \cdot y^{-1}$]	1.48×10^{-1}	2.54×10^{-1}	72.01%
FFP [$kgOil_{eq} \cdot kg_V^{-1} \cdot y^{-1}$]	2.11×10^{-1}	3.48×10^{-1}	65.26%

Regarding the use phase results, in terms of fuel usage the results were evaluated considering, in the case of the traditional powertrain, the emissions related to both fuel combustion and fuel production. In case of the FCHET instead, it was assumed that no local emissions are produced as direct consequence of hydrogen consumption, and thus the impact is related to the hydrogen production mix. As previously stated, the authors considered gray hydrogen mainly produced through steam methane reforming. The results are exposed in Figure 2.14, while the numerical results are shown in Table 2.13. Analyzing the results, the following considerations can be highlighted:

- For both tractors, the impact of the use phase was mainly related to fuel usage, with lubricants and tires substitutions that had very low contributions.
- In all impact categories considered, the fuel cell-powered vehicle showed equivalent emission reductions of relevance; into details, for the HTPnc, PMFP, FETP, HOFP, and EOFP an impact reduction higher than 90% was

obtained. The only category in which the reduction was not particularly high (around 10%) was the FFP category, this can be attributed to the fact that gray hydrogen is produced from fossil fuels.

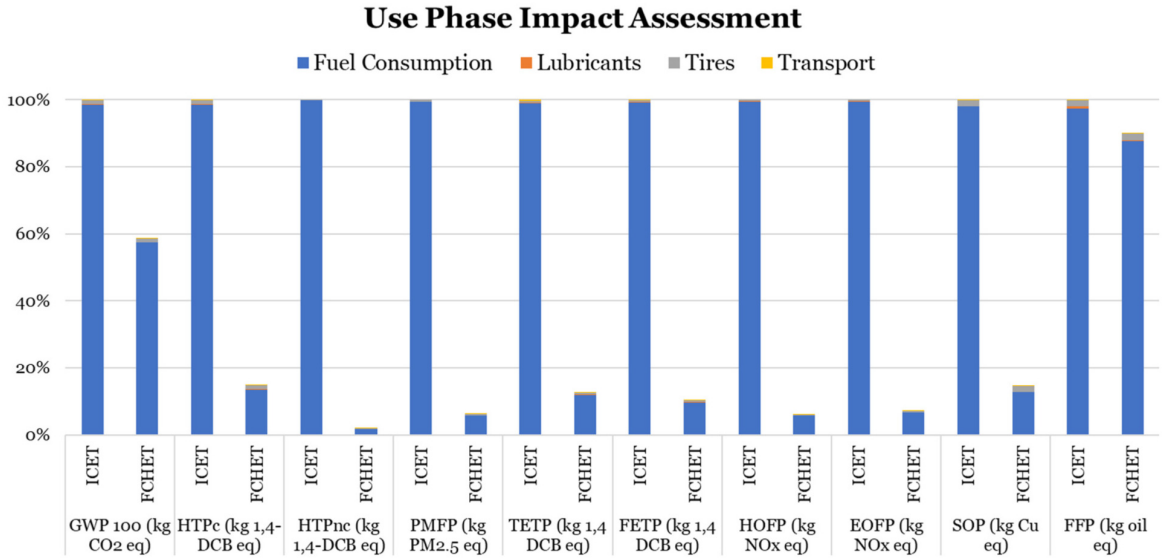

Figure 2.14 Use phase results.

Table 2.13 Use phase numerical results.

Impact Category	**ICET**	**FCHET**	**Δ %**
GWP100 [$kgCO_2eq \cdot kg_V^{-1} \cdot y^{-1}$]	8.60	5.05	-41.28%
HTPc [$kg1,4DCB_{eq} \cdot kg_V^{-1} \cdot y^{-1}$]	6.82×10^{-1}	1.02×10^{-1}	-85.08%
HTPnc [$kg1,4DCB_{eq} \cdot kg_V^{-1} \cdot y^{-1}$]	3.09×10	6.15×10^{-1}	-98.01%
PMFP [$kgPM_{2.5}eq \cdot kg_V^{-1} \cdot y^{-1}$]	2.03×10^{-2}	1.30×10^{-3}	-93.60%
TETP [$kg1,4DCB_{eq} \cdot kg_V^{-1} \cdot y^{-1}$]	3.08×10	3.97	-87.08%
FETP [$kg1,4DCB_{eq} \cdot kg_V^{-1} \cdot y^{-1}$]	3.43×10^{-1}	3.57×10^{-2}	-89.61%
HOFP [$kgNO_xeq \cdot kg_V^{-1} \cdot y^{-1}$]	6.66×10^{-2}	4.08×10^{-3}	-93.88%
EOFP [$kgNO_xeq \cdot kg_V^{-1} \cdot y^{-1}$]	6.84×10^{-2}	4.88×10^{-3}	-92.87%
SOP [$kgCu_{eq} \cdot kg_V^{-1} \cdot y^{-1}$]	2.75×10^{-1}	4.04×10^{-2}	-85.30%
FFP [$kgOil_{eq} \cdot kg_V^{-1} \cdot y^{-1}$]	2.42	2.17	-10.07%

Lastly, the results of the End-of-life phase are shown in Figure 2.15 and in Table 2.14.

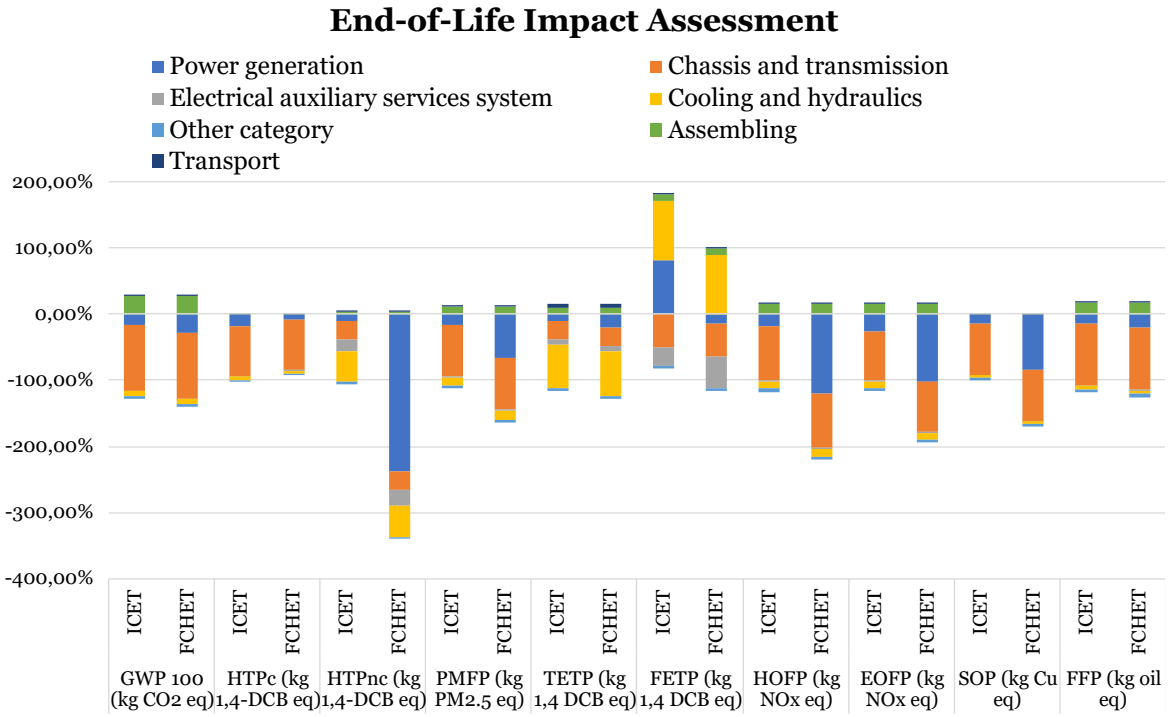

Figure 2.15 EOL results.

Table 2.14 End-of-life numerical results.

Impact Category	**ICET**	**FCHET**	**Δ %**
GWP100 [$kgCO_2eq \cdot kg_V^{-1} \cdot y^{-1}$]	-2.74×10^{-1}	-3.04×10^{-1}	-10.85%
HTPc [$kg1,4DCB_{eq} \cdot kg_V^{-1} \cdot y^{-1}$]	-2.97×10^{-1}	-2.68×10^{-1}	+9.72%
HTPnc [$kg1,4DCB_{eq} \cdot kg_V^{-1} \cdot y^{-1}$]	-5.73×10^{-1}	-1.92	-234.30%
PMFP [$kgPM_{2.5}eq \cdot kg_V^{-1} \cdot y^{-1}$]	-5.15×10^{-4}	-7.80×10^{-4}	-51.42%
TETP [$kg1,4DCB_{eq} \cdot kg_V^{-1} \cdot y^{-1}$]	-1.05×10	-1.16×10^{-1}	-10.70%
FETP [$kg1,4DCB_{eq} \cdot kg_V^{-1} \cdot y^{-1}$]	1.57×10^{-2}	-2.39×10^{-3}	-115.21%
HOFP [$kgNO_xeq \cdot kg_V^{-1} \cdot y^{-1}$]	-7.19×10^{-4}	-1.46×10^{-3}	-102.56%
EOFP [$kgNO_xeq \cdot kg_V^{-1} \cdot y^{-1}$]	-8.59×10^{-4}	-1.53×10^{-3}	-78.24%
SOP [$kgCu_{eq} \cdot kg_V^{-1} \cdot y^{-1}$]	-1.20×10^{-1}	-2.03×10^{-1}	-69.71%
FFP [$kgOil_{eq} \cdot kg_V^{-1} \cdot y^{-1}$]	-1.28×10^{-1}	-1.36×10^{-1}	-6.34%

Combining the results of production, use phase and end-of-life stages, the cradle-to-grave life cycle impacts were determined. The results are shown in Figure 2.16 and in Table 2.15. In Figure 2.16 the results are exposed following the same principle

used for the previous figures, thus the sum of manufacturing, use phase and EoL is equal to 100% for all the considered impact categories.

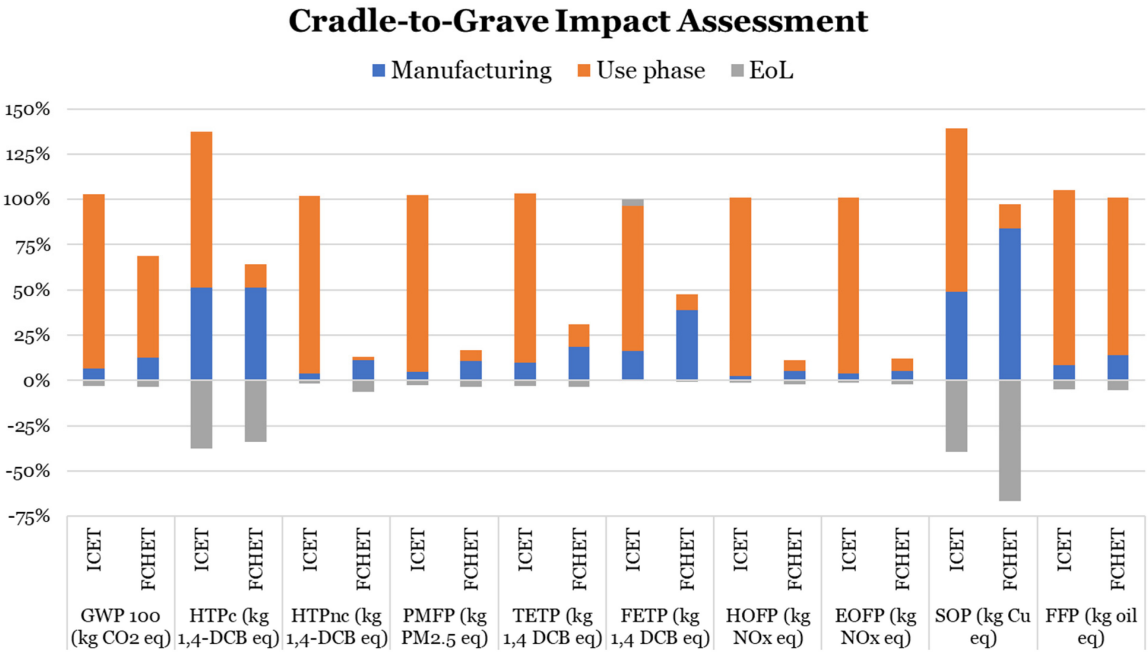

Figure 2.16 LCA cradle-to-grave results.

Table 2.15 Cradle-to-grave numerical results.

Impact Category	**ICET**	**FCHET**	**Δ %**
GWP100 [$kgCO_2eq \cdot kg_V^{-1} \cdot y^{-1}$]	8.93	5.85	-34.46%
HTPc [$kg1,4DCB_{eq} \cdot kg_V^{-1} \cdot y^{-1}$]	7.89×10^{-1}	2.36×10^{-1}	-70.04%
HTPnc [$kg1,4DCB_{eq} \cdot kg_V^{-1} \cdot y^{-1}$]	3.15×10	2.23	-92.92%
PMFP [$kgPM_{2.5}eq \cdot kg_V^{-1} \cdot y^{-1}$]	2.08×10^{-2}	2.74×10^{-3}	-86.82%
TETP [$kg1,4DCB_{eq} \cdot kg_V^{-1} \cdot y^{-1}$]	3.29×10	8.99	-72.71%
FETP [$kg1,4DCB_{eq} \cdot kg_V^{-1} \cdot y^{-1}$]	4.29×10^{-1}	2.01×10^{-1}	-53.20%
HOFP [$kgNO_xeq \cdot kg_V^{-1} \cdot y^{-1}$]	6.75×10^{-2}	6.13×10^{-3}	-90.91%
EOFP [$kgNO_xeq \cdot kg_V^{-1} \cdot y^{-1}$]	7.02×10^{-2}	7.02×10^{-3}	-90.00%
SOP [$kgCu_{eq} \cdot kg_V^{-1} \cdot y^{-1}$]	3.03×10^{-1}	9.19×10^{-2}	-69.71%
FFP [$kgOil_{eq} \cdot kg_V^{-1} \cdot y^{-1}$]	2.50	2.38	-4.55%

Analyzing the results, several considerations can be done. Firstly, the analysis showed that the expected impacts of the FCHET are lower for all the considered

impact categories. Into details, a reduction of more than 90% of the equivalent emissions was noted for the HTPnc, HOFP and EOFP categories. However, for eight of the ten impact categories, the impact reduction is expected to be more than 50%. This result showed a great potential to improve the sustainability of the agricultural sector by introducing fuel cell powertrain in substitution of traditional systems. Regarding the global warming potential, an impact reduction of around 34% was evaluated. The only category in which a not relevant reduction of the impact was noted was the FFP category. in which the difference in the life cycle emissions was estimated at 4.55%. This can be related to the considered hydrogen production process, which involves the adoption of fossil fuel resources.

Another element that can be outlined analyzing the results regards the most impactful stage during the whole life cycle. For the traditional powertrain, the stage with the highest equivalent emissions was always the use phase stage. On the contrary, for the FCHET the manufacturing stage was the most relevant in six of the ten impact categories. As a consequence, improvements in terms of system durability can have a beneficial effect, as prolonging the use phase can enhance the reduction in the life cycle emissions.

Another relevant aspect that can be discussed was the importance of recycling in the EoL phase. Indeed, in some categories, such as HTPc and SOP, the beneficial effects of recycling can significantly reduce the cradle-to-grave emissions. During the analysis, a performance index named "EoL relative effectiveness" (EOL_{RE}) was defined, which was the ratio between the EoL impact (with a minus sign) and the manufacturing impact. This ratio substantially expresses the effectiveness of the EoL stage in reducing the impact with respect to the manufacturing stage, improving the circular economy of the system. The equation of this index can be written as follows:

$$EOL_{RE} = -\frac{EOL_{impact}}{Production_{impact}} \tag{2.22}$$

Applying this index to the proposed analysis, it emerged that, with the only exception of the FETP category, the EOL_{RE} ranged between 25% and 80%, as shown in Figure 2.17. Considering that for the FCHET the manufacturing stage was the most critical in six categories, the importance of the EOL stage was crucial in reducing the cradle-to-grave emissions.

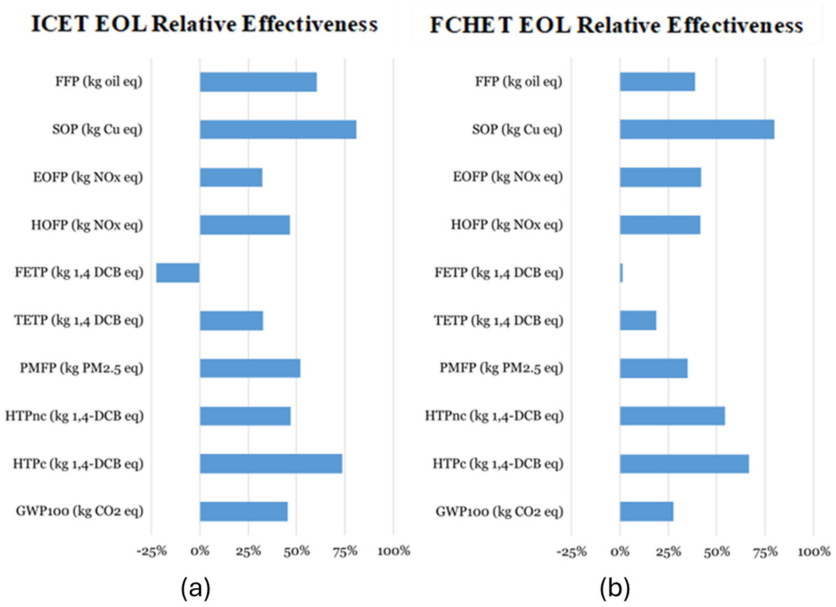

Figure 2.17 EoL relative effectiveness

Although the analysis clearly showed that there are several benefits related to the introduction of fuel cell powertrain in agricultural machinery, there are still margins for further improvements. For instance, increasing the ratio of green and/or blue hydrogen in the global production mix can reduce the use phase impact emission in all those categories, such as GWP and FFP, where the adoption of fossil fuels has a high associated impact [14, 119]. In addition, the analysis highlighted that the manufacturing of the fuel cell stack and the hydrogen tank had a significant impact on the cradle-to-grave results, thus efforts should be done to improve the sustainability of their production, such as considering the reduction of the Pt loading or adopting alternative solutions for hydrogen storage and tanks design. Furthermore, the adoption of techniques to improve fuel cell system efficiency might be a feasible path to reduce hydrogen consumption [120].

To expand the results of the proposed analysis, the evaluation of the adoption of green hydrogen, in substitution of the gray one, was included. Considering a feasible scenario for an agricultural farm, it was assumed that green hydrogen production would occur through the electrolysis of water powered by photovoltaic panels (PVs). Into details, a 3 kWp (peak kW) PV system and a small PEM electrolyzer were considered. The electrolyzer efficiency was assumed to be equal to 80% [121]. Thus, the LCI for the production of 1 kg of green hydrogen consisted of 9 kg

of deionized water and 160 kWh of electrical power. Powering the FCHET with hydrogen produced in this way, the cradle-to-grave results can vary significantly as shown in Table 2.16. As expected, the adoption of green hydrogen can have a relevant beneficial effect in the GWP and FFP categories, reducing the overall impact of 60% and 71% respectively with respect to using gray hydrogen. Thus, if the main target is the reduction of GHG emissions, this solution can be an effective strategy. On the contrary, in all the other categories, an increase in the impact is expected, specially in the TETP and FETP ones, where the impact is expected to be higher even compared to the traditional vehicle. These results may be explained by the use of PVs that may require material with high impacts in those categories [122]. Powering the electrolyzer with electricity coming from other renewables, such as wind farms, may have a lower impact [123]. Despite this, the analysis focused on the case in which the electrolysis was powered using PVs since it is a more feasible way in which a farm can independently produce electricity on its own.

Table 2.16 Cradle-to-grave result comparison between the three cases.

Impact Category	**FCHET with Green H_2**	**Difference vs. ICET**	**Difference vs. FCHET (Gray H_2)**
GWP100 [$kgCO_2eq \cdot kg_V^{-1} \cdot y^{-1}$]	2.31	-74%	-60%
HTPc [$kg1,4DCB_{eq} \cdot kg_V^{-1} \cdot y^{-1}$]	3.67×10^{-1}	-53%	$+55\%$
HTPnc [$kg1,4DCB_{eq} \cdot kg_V^{-1} \cdot y^{-1}$]	9.21	-71%	$+313\%$
PMFP [$kgPM_{2.5}eq \cdot kg_V^{-1} \cdot y^{-1}$]	5.80×10^{-3}	-72%	$+112\%$
TETP [$kg1,4DCB_{eq} \cdot kg_V^{-1} \cdot y^{-1}$]	6.90×10	$+110\%$	$+668\%$
FETP [$kg1,4DCB_{eq} \cdot kg_V^{-1} \cdot y^{-1}$]	1.01	$+135\%$	$+401\%$
HOFP [$kgNO_xeq \cdot kg_V^{-1} \cdot y^{-1}$]	7.19×10^{-3}	-89%	$+17\%$
EOFP [$kgNO_xeq \cdot kg_V^{-1} \cdot y^{-1}$]	7.50×10^{-3}	-89%	$+7\%$
SOP [$kgCu_{eq} \cdot kg_V^{-1} \cdot y^{-1}$]	1.22×10^{-1}	-60%	$+32\%$
FFP [$kgOil_{eq} \cdot kg_V^{-1} \cdot y^{-1}$]	6.80×10^{-1}	-73%	-71%

2.7 Conclusions

In this chapter, a numerical analysis of a fuel cell-powered orchard tractor was presented. The hybrid powertrain was designed considering the constraints in terms

of on-board space availability and performance requirements. Indeed, orchard tractors are characterized by compactness due to their necessity of performing maneuvers in narrow spaces. In addition, they must be able to operate for several hours straight to satisfy productivity requirements. Consequently, a fuel cell + battery configuration was selected, with the FC that acted as the primary energy source while the battery pack handled the high-dynamic part of the load. This configuration was chosen to guarantee high endurance also in heavy tasks without excessively stress the fuel cell system. The mechanical transmission was maintained the same of the traditional vehicle to achieve almost the same traction performance.

Numerical models of both the traditional reference vehicle and the proposed alternative one were developed. In details, all the powertrain elements and the longitudinal dynamic of the vehicle were modeled in Matlab/Simulink environment. The models included the engine, with a fuel consumption estimation model, the transmission, the FC system, the battery pack and the power converters. The BoP of the fuel cell was included as it affected the overall efficiency of the powertrain. To evaluate the typical work scenarios of an orchard tractor, a monitoring campaign during common workday activities was performed using a CAN bus data analyzer. The obtained data were used firstly to tune the numerical models, then in the numerical simulations to perform a comparative analysis between the two solutions.

The simulation results highlighted that the hybrid fuel cell powertrain was capable of performing the same tasks with performance close to that of the traditional vehicle, but with a significant reduction in the equivalent greenhouse gas emissions. In details, an average -50% of equivalent CO2 emissions was noted.

To further evaluate the environmental benefits of introducing fuel cell powertrain in agriculture, a life cycle assessment analysis was performed. The analysis included production, use-phase and end of life, according to a cradle-to-grave approach. Different impact categories were selected to consider effects on environment, human health, and resource depletion. The analysis was performed considering at first the use of gray hydrogen. Analyzing the results, it was noted that the fuel cell powertrain was capable of reducing the impact in almost all proposed categories, with peaks of more than -90% in some cases. With the adoption of green hydrogen produced through electrolysis powered with PV panels, a further reduction was noted in global warming potential and fossil fuel potential categories, but for the other categories an increase in the impact was observed. Considering the single phases,

the manufacturing stage was the most critical for the fuel cell vehicle, showing a significantly higher impact in almost all the impact categories compared to the traditional vehicle. On the contrary, for this last one the most critical stage was the use phase. Lastly, the end of life stage showed that recycling can be a useful strategy to significantly reduce the life cycle impact, in particular for the mineral resource scarcity category.

Chapter 3

Hardware-in-the-loop bench testing of hybrid fuel cell propulsion systems.

Hardware-in-the-loop (HIL) testing methodology is a commonly used technique to test, verify, and validate the performance of embedded control systems in real-time environments. Depending on the kind of HIL simulation, different aspects of the system can be analyzed. An interesting definition of HIL simulator is the following [124]:

"A setup that emulates a system by immersing faithful physical replicas of some of its subsystems within a closed-loop virtual simulation of the remaining subsystems"

In the automotive sector, HIL simulations have been used to validate powertrain controllers under realistic conditions without the need for a complete system, as a real-time simulation environment is used to emulate the behavior of certain subsystems. This approach allows for evaluating the functionality, robustness, reliability and safety of powertrain systems. The flexibility of an HIL platform allows for fast development times as different tests can be carried out. As described in [125], HIL simulations for hybrid electric systems can be developed at different levels:

- **Signal level:** the device under test is the controller, all the other elements, including power electronics, electric machines, batteries, etc. are simulated on a real-time environment.

- **Power level:** in this case both the controller and the power electronics are under testing. Electrical machines and mechanical loads are simulated, while other components, such as batteries and power converters, are physically tested.
- **Mechanical level:** the whole drive system, including control, power electronics, and electric machines, is tested.

The HIL simulation at the mechanical level is the most complete since it covers the control, the electrical and electronic units, and the mechanical powertrain. However, for certain analysis, it is not necessary to have the full prototype of the entire system, thus a HIL simulation at power or signal levels may allow for obtaining very useful results without requiring high investment costs.

3.1 Design and development of a HIL test bench with fuel cell emulation

The set goal of the HIL developed during the activity was to reproduce, with a proper scale factor, the behavior of hybrid fuel cell powertrain in different configurations. All the configurations were defined considering the same orchard tractor as case study. Since the analysis mainly focused on the power balance and control management strategies, the HIL bench was developed at the power level, thus without mechanical elements. A modular approach was adopted, so that, without requiring a complete redesign or reconfiguration of the system, different hybrid architectures could be tested. Furthermore, in the first tests the fuel cell was emulated as a power source with its characteristic polarization curve [126]. Into details, the HIL was developed considering the possibility of testing three different powertrain configurations. These configurations are shown in Figure 3.1. Before describing in detail the reasons behind the choice of these powertrain, an overview of the HIL test bench layout will be provided.

The adoption of a HIL platform to perform the comparative analysis was motivated by the necessity of implementing a real embedded controller to evaluate the behavior of the physical system. In addition, adding real power electronic components and transducers allowed for a more detailed analysis and included the effects of real components on the system behavior, including noises, delays, real-time execution

effects, and so on. Furthermore, as it will be discussed in the following subsections, the durability of the fuel cell system is strictly related to its power output control, thus the effects of a real controller should be included.

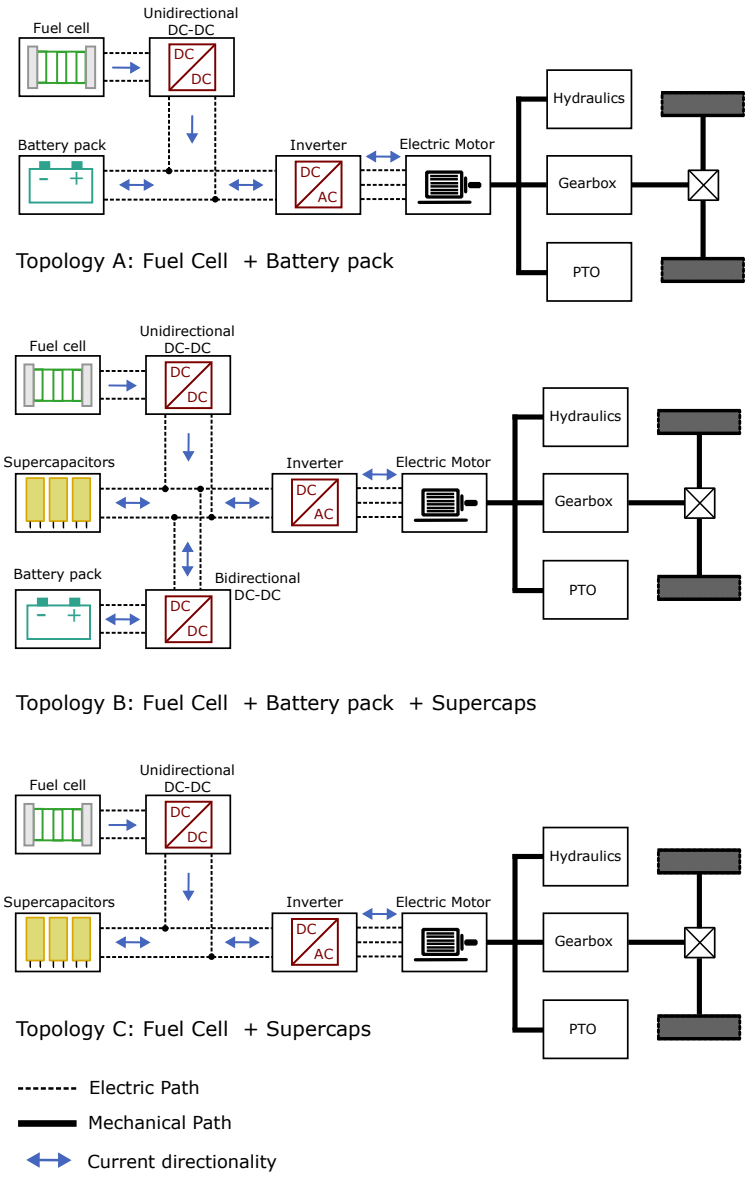

Figure 3.1 Schematic representations of the three configurations tested on the HIL test bench.

3.1.1 Experimental set-up

The experimental setup comprised the following elements:

- **Load Unit**: the load unit had the role of reproducing the power flow from/to the electric motor, and the power absorbed by auxiliaries and services, including the fuel cell BoP.
- **Power supply**: a programmable power supply was adopted to reproduce the behavior of the fuel cell stack.
- **DC-DC converters**: unidirectional and bidirectional DC-DC converters were used for the connection of the power sources to the DC bus.
- **Batteries and supercapacitors modules**: correspond to the secondary power sources of the powertrain.
- **Transducers**: current and voltage transducers were implemented to monitor the actual power flows and to perform the EMS.
- **Control unit**: a control unit that must determine the power split among the different sources (according to the EMS), control the load unit, control the power supply for fuel cell emulation and communicate with a personal computer for data logging.

A schematic representation of the HIL bench (topology B) is shown in Figure 3.2.

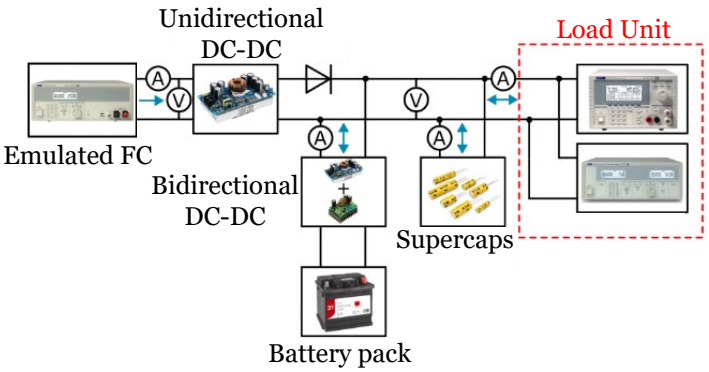

Figure 3.2 Schematic representations of the HIL test bench (topology B).

The load unit was composed of a programmable power supply, whose role was to reproduce regenerative braking events, and a programmable electronic load, whose instead had to emulate the overall power absorption at the DC bus level. According

to this approach, the power absorbed by the load unit was determined according to the following equation:

$$P_{load} = P_{EM} + P_{aux} \tag{3.1}$$

Where P_{load} is the total load power, P_{EM} is the power absorbed by the electric motor (upstream the inverter, thus considering its efficiency) and P_{aux} is the total power absorbed by auxiliaries and services, including vehicle accessories and the fuel cell system BoP. Indeed, the BoP of a fuel cell system has a relevant impact on the system efficiency, thus it must be considered in the analysis. As described in Section1.2, the BoP comprises several elements, however the most demanding in terms of power absorption is, by far, the air compressor. Consequently, since the air compressor is controlled to maintain the proper OER ratio at the cathode, the term P_{aux} must be evaluated at each time step according to the power output of the fuel cell stack. According to studies available in the literature [11, 10, 127], the BoP usually absorbs about 10–20% of the gross power generated by the stack. As demonstrated in [10], the power absorbed by the auxiliaries was approximately equal to around 13% at low loads and increased to around 19% at high loads. According to this, the power required for the BoP was estimated as function of the power output of the stack so that it was approximately equal to 13% at low loads, namely 10–20% of the stack nominal power, and increased linearly to 19% at high loads, or 90–100% of the stack nominal power.

Regarding fuel cell emulation, the adopted approach was to control the power supply so that it reproduced the real polarization curve of the stack. Into detail, at each time step the control unit measures the actual current delivered by the power supply and determines the corresponding voltage, which is sent to the power supply through an analog signal.

As for the DC-DC converters, they act as a power conditioning unit and must be controlled according to the predefined EMS. The converters adopted in the set up were three units, a unidirectional DC-DC converter for the connection of the emulated stack to the DC bus, and two unidirectional DC-DC converters arranged in antiparallel (to reproduce the behavior of bidirectional unit) for the interface between the batteries and the DC bus in topology B configuration.

Regarding the batteries and supercapacitors modules, a modular approach was adopted. According to this, it was possible to have different configurations in terms of voltage and capacity. This was necessary as the properties of the secondary power sources in the three topologies shown in Figure 3.1 were different.

To collect data and monitor the power flows of the different components during the operation of the HIL bench, current and voltage transducers were implemented. Namely, the CAS 15-NP current transducer and the LV 25-P voltage transducer, both manufactured by LEM (LEM International SA, Meyrin, Switzerland), were adopted.

Lastly, a control unit (CU) was developed. The CU had to perform several tasks. Firstly, it had to communicate with a personal computer through serial communication. Indeed, a MATLAB script was designed for data transfer between the PC and the HIL bench. The data transfer mainly regarded the power profiles to be reproduced by the load unit (thus these data were from the PC to the HIL bench) and the data collected by the transducers (in this case, from the HIL bench to the PC). Consequently, other tasks that the CU had to perform were the control of the load unit and the data collection from the transducers. Lastly, the CU had to determine the control signals to the DC-DC converters according to the EMS. A schematic representation of the CU is shown in Figure 3.3, while the experimental setup of the HIL bench (topology B configuration) is shown in Figure 3.4. The circuit schematics of the control unit is available in AppendixB.

3.1.2 Design and scaling of different fuel cell architectures for a compact orchard tractor

The analysis focused on three different fuel cell architectures designed to substitute the traditional powertrain of the orchard tractor described in section 2.3.1. All three alternatives featured the same fuel cell system, namely a 65 kW PEMFC system, but differed in terms of secondary power sources. Substantially, the HIL bench test activity aimed to expand the numerical analysis proposed in Section 2.5 with the aim of finding the optimal powertrain configuration. Other elements that were maintained the same among the three architectures were the electric motor, which was the same of the fuel cell powertrain presented in the numerical analysis in Section 2.5 (75 kW @ 2600 rpm), and the other parts of the vehicle, such as the transmission, which were, furthermore, the same of the traditional vehicle. In this

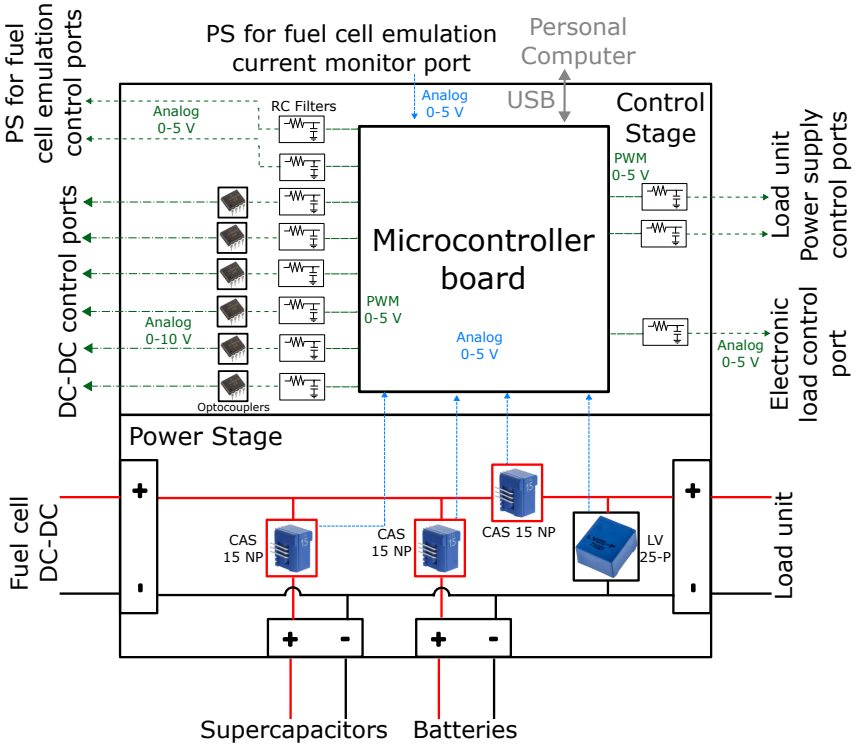

Figure 3.3 Schematic representations of the HIL bench control unit.

way, the only components that differed were the secondary power sources and the power converters.

The three architectures were defined considering the same on-board space availability in order to perform a proper comparison. Starting from Topology A, the secondary power unit was a 6 kWh LFP battery pack. This architecture was designed for the numerical analysis described in Sections 2.5 and 2.6 and was originally developed considering the on-board constraints of the traditional tractor, thus was taken as a reference in terms of the overall dimension of the secondary unit. Considering an energy density of the battery pack equal to 120 Wh/l, which is in accordance with the literature [128], the maximum size of the secondary unit was fixed at 50 liters.

Considering Topology B, the auxiliary power unit was a hybrid unit composed of a battery pack, connected to the bus DC with a bidirectional DC-DC converter, and a supercapacitor module, directly connected to the DC bus. This configuration was chosen to increase the power density of the powertrain. The choice of directly connecting the supercapacitors to the DC bus is motivated by the very limited space availability, indeed it was not feasible to introduce a high-power DC-DC converter.

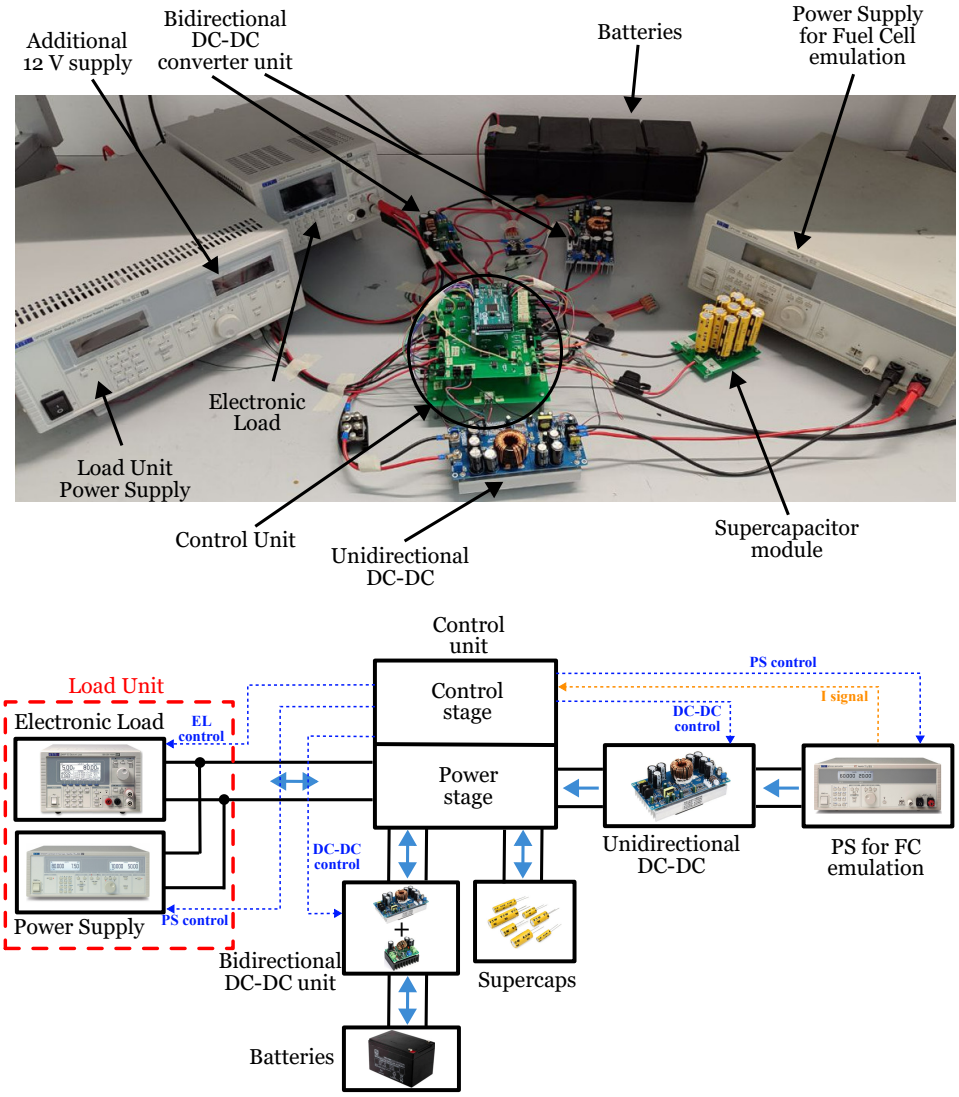

Figure 3.4 HIL bench experimental setup with connection scheme (Topology B).

The consequence of this was that the EMS had to be designed so that there was not an excessive drop in the voltage level, as the voltage of the supercapacitors was directly related to their state of charge. Given these premises, considering the nominal dimensions of bidirectional DC-DC converters and supercapacitors modules according to commercial products [129, 130], the sizes of the battery pack, the power converter, and the supercapacitor module were defined. Into details, the supercapacitor module has an energy capacity of 106 Wh, while the battery pack has a capacity of 1400 kWh. The energy density of the supercapacitor module was found to be equal to 3.60 Wh/l, while the bidirectional DC-DC dimensions were found to be 9.9 litres for a 20-kW converter. The sizing was performed considering that the supercapacitor module should be able to handle alone the maximum motor power for 1 sec with a reduction of its voltage equal to 12.5%, value that was chosen arbitrary.

Lastly, for Topology C the secondary power source was composed of only a supercapacitor module, directly connected to the DC bus, with a energy capacity of 184 Wh. Again, the choice not to implement a high-power DC-DC converter was motivated by the limited space. The properties of the three architectures are summarized in Table 3.1. The maximum power capabilities of the power sources were defined considering references [130, 131]. Indeed, in [131] LFP batteries were discharged at 15C, while in [130] a supercapacitor module with a capacity of 54 Wh has a peak power of 118 kW.

For the HIL bench, a scale factor of approximately 220 was considered. The approach adopted was the following: for the fuel cell emulation, the FCS-C300 system, manufactured by Horizon (Horizon Fuel Cell Technologies, Singapore) was considered as a reference. The choice of considering this model was motivated by the possibility of implementing in the scaled test bench a real fuel cell, thus all the other elements were defined taking into account this possibility. Regarding the voltage level, in the HIL setup the rated DC bus voltage was set at 24 V.

Table 3.1 Main properties of the proposed fuel cell powertrain architectures for the comparative analysis (not scaled to the HIL bench); the three architectures were designed considering the same overall volume

Topology A	
Fuel cell stack rated power	65 kW
Battery pack capacity	6 kWh
Battery pack peak discharge power	90 kW
Topology B	
Fuel cell stack rated power	65 kW
Battery pack capacity	1.4 kWh
Battery pack peak discharge power	20 kW
Supercapacitors energy capacity	0.106 kWh
Supercapacitors peak discharge power	230 kW
Topology C	
Fuel cell stack rated power	65 kW
Supercapacitors energy capacity	0.184 kWh
Supercapacitors peak discharge power	400 kW

As for the secondary power sources, only the supercapacitor modules were actually scaled with the proper scale factor. Indeed, since the DC bus voltage level was directly linked to their state of charge, it was of primary importance to proper account for their discharge. As for the batteries, they were not scaled in terms of capacity, mainly due to the difficulty in finding a commercially available product with the required properties. However, this did not affect the reliability of the results as Li-ion batteries open circuit voltage is characterized by a low variation for SOC values in the range 10-90%. The actual properties of the components adopted in the experimental setup are shown in Table 3.2.

Table 3.2 Main properties of the actual components adopted in the HIL bench. *The real capacity of the adopted batteries was not scaled and was equal to 13 Ah; however, the scaled capacities, corresponding to 1.14 Ah and 0.13 Ah for Topology A and B respectively, were considered in the SOC evaluation algorithm and in terms of maximum power capabilities.

Emulated Fuel Cell	
Voltage range	58 – 30 V
Current range	0 – 9.3 A
Rated power	300 W (8.33 A @ 36 V)
Rated efficiency	40 %
Batteries	
Topology A rated voltage	24 V
Topology A scaled capacity*	13 (1.14) Ah
Topology B rated voltage	48 V
Topology B scaled capacity*	13 (0.13) Ah
Supercapacitor modules	
Topology B rated voltage	24 V
Topology B rated capacitance	6 F
Topology C rated voltage	24 V
Topology C rated capacitance	10 F

3.1.3 Comparative analysis: hydrogen consumption and durability estimations

To perform a comparative analysis among the different architectures, durability and energy consumption were considered. To evaluate the hydrogen consumption, the FCS-C300 hydrogen consumption curve, as a function of the stack power output, was adopted. The curve is showed in Figure 3.5. It should be noted that the curve reports the hydrogen mass flow as a function of the power output, however the consumption is directly linked to the stack current output. Consequently, the power output was converted into current output considering the nominal polarization curve. Thus, given the fuel cell current upstream the DC-DC converter, which was monitored by the control unit, it was possible to properly estimate the instantaneous hydrogen consumption.

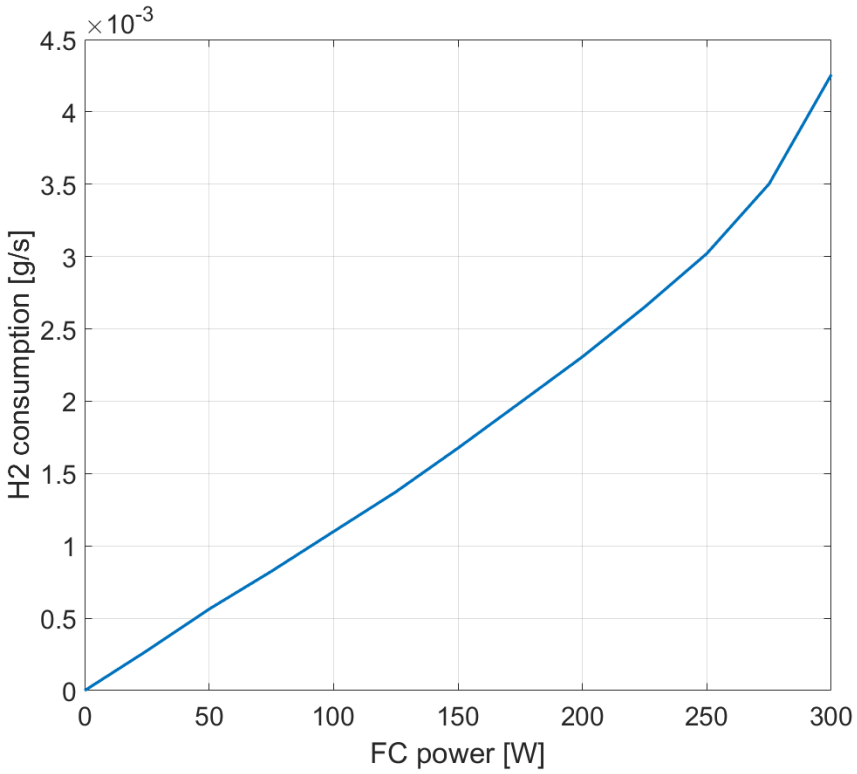

Figure 3.5 FCS-C300 hydrogen consumption curve.

To estimate the batteries SoC variation, a simple Coulomb counting strategy was adopted. This is a direct SoC estimation method that allows to evaluate the actual SoC by monitoring the battery current [132]. Despite the simplicity in terms of implementation, there are some drawbacks related to this method, including error accumulation and transducer accuracy, however, it was deemed that for the proposed analysis there was no need for more detailed methods. According to this approach, the following equations were used:

$$C_{\text{used}} = \int_{t_1}^{t_2} i_{\text{batt}}\, dt \tag{3.2}$$

$$SOC = \frac{C_{\text{nom}} - C_{\text{used}}}{C_{\text{nom}}} \tag{3.3}$$

Where C_{used} is the consumed capacity, C_{nom} is the nominal capacity, and i_{batt} is the battery current.

As for the durability of the systems, the analysis focused on the aging and life expectancy of the fuel cell system and auxiliary units. To address this issue, aging models available in literature were exploited. Starting with the aging of the fuel cell, the model proposed in [42] was considered. According to this approach, the expected lifetime of the fuel cell can be evaluated using the following equation:

$$T_{\text{lifetime}} = \frac{\Delta P}{k_p(\beta_1 n_1 + \beta_2 n_2 + \beta_3 t_1 + \beta_4 t_4)} \tag{3.4}$$

Where:

- $T_{lifetime}$ is the expected lifetime of the fuel cell system.
- ΔP is the maximum acceptable reduction in fuel cell output performance, imposed equal to 10%.
- k_p is an accelerating coefficient.
- $\beta_{i=1,\ldots,4}$ are aging coefficients representing the effects on durability related to load change cycling, start-stop cycles, idle and high-power conditions.
- n_1 and n_2 are, respectively, load changes and start-stop cycles.
- t_1 and t_2 are, respectively, the idle and high-power times.

The coefficients of the aging model are reported in Table 3.3.

Table 3.3 Fuel cell aging model coefficients.

Coefficient	Condition	Value	Unit
β_1	Load cycling	5.93e-5	%/cycle
β_2	Start and stop	1.96e-3	%/cycle
β_3	Low Power ($P_{FC} \leq 10\%$)	1.26e-3	%/h
β_4	High Power ($P_{FC} \geq 90\%$)	1.47e-3	%/h

As for the battery aging model, a semi-empirical model available in the literature was implemented [133]. According to this model, the battery capacity fade due to load cycling can be estimated using the following equation:

$$Q_{\text{loss}} = (A * T^2 + B * T + C) * e^{(D*T+E)*C_{\text{rate}}} * Ah \tag{3.5}$$

Where Q_{loss} is the capacity fade in %, T is the battery temperature in K, C_{rate} is the instantaneous charge/discharge rate, Ah is the ampere-hour throughput, and A, B, C, D and E are parameters depending on the battery chemistry. The maximum allowed battery capacity reduction was set equal to 20%.

Lastly, the supercapacitors life expectancy had to be determined. The model presented and described in [134] was adopted. This model evaluates the state of aging (SoA) of a supercapacitor using the following equation:

$$\frac{dSoA}{dt} = \frac{1}{T_{\text{life}}^{\text{ref}}} \cdot e^{\ln(2)\cdot\left(\frac{T_c - T_c^{\text{ref}}}{T_0}\right)} \cdot \left[e^{\ln(2)\cdot\left(\frac{V - V^{\text{ref}}}{V_0}\right)} + K\right] \cdot e^{k_c \cdot \frac{i_{\text{SC}}}{C_0}} \tag{3.6}$$

Where:

- SoA is the state of aging of the supercapacitor.
- T_{life}^{ref} is the supercapacitor lifetime at temperature T_c^{ref} and voltage V^{ref}.
- T_c and V are the case temperature and the supercapacitor voltage.
- T_0 and V_0 are the temperature and voltage reduction to double the lifetime.
- K is a correction factor for very high temperatures and very low voltages, set equal to 29×10^{-3}.
- k_c is the current coefficient, equal to 68 s/V.
- i_{SC} is the supercapacitor current.
- C_0 is the nominal supercapacitor capacity.

The end of life of the supercapacitor, corresponding to a SoA equal to 1, occurs when the capacity fade is equal to 20%.

3.1.4 Energy management strategies

Two EMSs were considered in the comparative analysis, one based on the power follower concept and the other based on fuzzy logic. Both are classified as rule-based strategies, thus are characterized by easy implementation and robustness,

which are key features in off-road vehicles, but may not lead to optimal solutions. For both strategies, the EMS algorithm evaluated the current setpoints and a PI controller tracked it determining the signals to be sent to the power converters. A schematic representation of the control strategies structures is shown in Figure 3.6. As it can be stated, the algorithm also included constraints related to batteries SoC, DC bus voltage, C rate and so on. Indeed, excessive bus voltage or batteries SoC reduction might lead to non-optimal operative conditions, while too high C rates can significantly reduce the batteries durability. Furthermore, the EMSs were different among the three topologies, even if the base principles were the same.

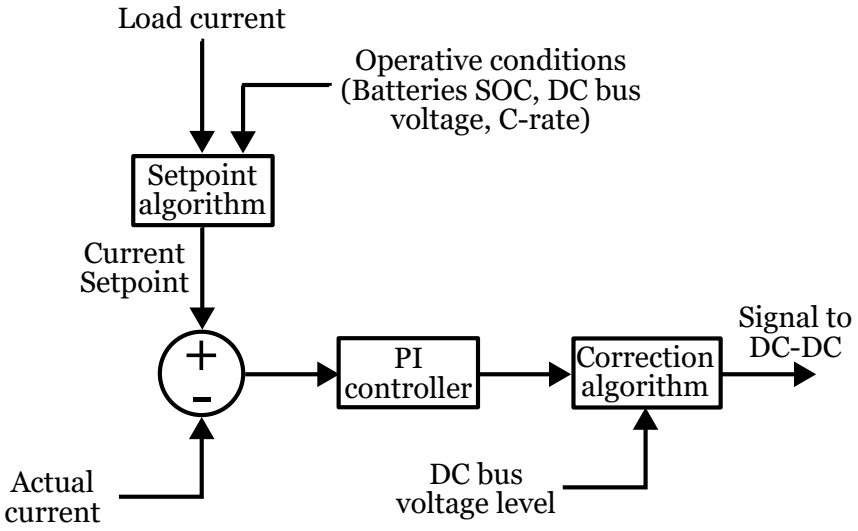

Figure 3.6 EMS structure schematic representation.

As for the power follower controllers, the current setpoints were evaluated using the following equations:

Topology A:

$$\text{Setpoint}_{i_{DC-DC,FC}} = i_{\text{load}} + K_1 \cdot \Delta SOC + K_2 \cdot C_{\text{rate}} \tag{3.7}$$

Topology B:

$$\begin{cases} \text{Setpoint}_{i_{DC-DC,FC}} = i_{\text{load}} + K_3 \cdot \Delta SOC + K_4 \cdot C_{\text{rate}} + K_5 \cdot \Delta V_{\text{bus}} \\ \text{Setpoint}_{i_{DC-DC,batt}} = i_{\text{load}} - i_{DC-DC,FC} + K_5 \cdot \Delta V_{\text{bus}} \end{cases} \tag{3.8}$$

Topology C:

$$\text{Setpoint}_{i_{DC-DC,FC}} = i_{\text{load}} + K_6 \cdot \Delta V_{\text{bus}} \tag{3.9}$$

For topology A, the current setpoint downstream the DC-DC on the FC side was determined considering the sum of three components considerign the load current, the batteries SoC and the C rate. Consequently, the fuel cell output was controlled so that it followed the load with corrections related to the auxiliary power source operating conditions. According to this, the fuel cell provided more power if the batteries SoC was low or their discharge current was high, whilst provided less power in case of high batteries SoC and high charging current. As for topology B, the current setpoint downstream the DC-DC on the FC side was evaluated considering, in addition to the previously mentioned parameters, the DC bus voltage level, which was directly linked to the supercapacitors SoC. Thus, the fuel cell provided more power to recharge the supercapacitors when the DC bus voltage was low, while provided less power in case of high voltage level. In this case, also the power converter on the batteries side had to be controlled. In this case, the current setpoint was determined considering the actual difference between the load and the current downstream the DC-DC on the FC side, and the DC bus voltage level. In this case, the SoC correction was not necessary as the surplus of power delivered by the FC to recharge the batteries had the effect to increase the DC bus voltage level and, consequently, to bring the batteries current setpoint to negative values. Lastly, in case of topology C the current setpoint was determined considering the actual load current and a correction factor that took into account for the supercapacitors SoC reduction.

As for the fuzzy logic controllers, they were defined considering the Mamdani rule-based system. Thus, input variables with membership functions, if-then rules, and output variables with membership functions had to be defined. Starting from topology A, the input variables were the load current and the batteries SoC, while the output variable was the FC current setpoint. The membership functions were defined classifying the load current into below zero (BZ), very low (VL), low (L), medium (M), high (H), very high (VH), and the batteries SoC into low, medium and high. As for the output variable, the membership function was defined classifying it into off (OFF), very low, low, medium, high, and very high. The adopted fuzzy rules adopted are shown in Table 3.4, while the graphical representation of the membership functions are shown in Figure 3.7. As it can be stated, trapezoidal

Table 3.4 Fuzzy rule table for the DC-DC current setpoint for topology A.

DC-DC FC current setpoint		**Load current**					
		BZ	**VL**	**L**	**M**	**H**	**VH**
SoC	*L*	VL	L	M	H	VH	VH
	M	OFF	VL	L	M	H	VH
	H	OFF	OFF	VL	L	M	H

Table 3.5 Fuzzy rule table for the DC-DC on the FC side current setpoint for topology B.

DC-DC FC current setpoint		**Load current**					
		BZ	**VL**	**L**	**M**	**H**	**VH**
DC bus voltage	*VL*	H	H	H	VH	VH	VH
	L	M	M	H	H	VH	VH
	M	OFF	VL	L	M	H	VH
	H	OFF	OFF	VL	L	M	H
	VH	OFF	OFF	OFF	VL	L	M

membership functions were adopted. The rules were defined to have a charge sustaining behaviour, so that when the batteries SoC was low, the fuel cell output was higher to recharge them, while in case of high SoC the output was lower to discharge them. However, the rules were defined to avoid excessive discharge and charge currents, thus the difference between the fuel cell output and the load demand could not be too high.

As for topology B, the membership functions of both the batteries SOC and the DC bus voltage level were defined classifying them into very low, low, medium, high and very high, and the load current into below zero, very low, low, medium, high and very high. The membership functions of the output variables were defined classifying the current setpoint of the FC into off, very low, low, medium, high and very high, and the current setpoint of the batteries into high charge (HC), charge (C), zero (Z), discharge (D) and high discharge (HD). The fuzzy rules adopted are shown in Table 3.5 and Table 3.6, while the membership functions are shown in Figures 3.8 and 3.9.

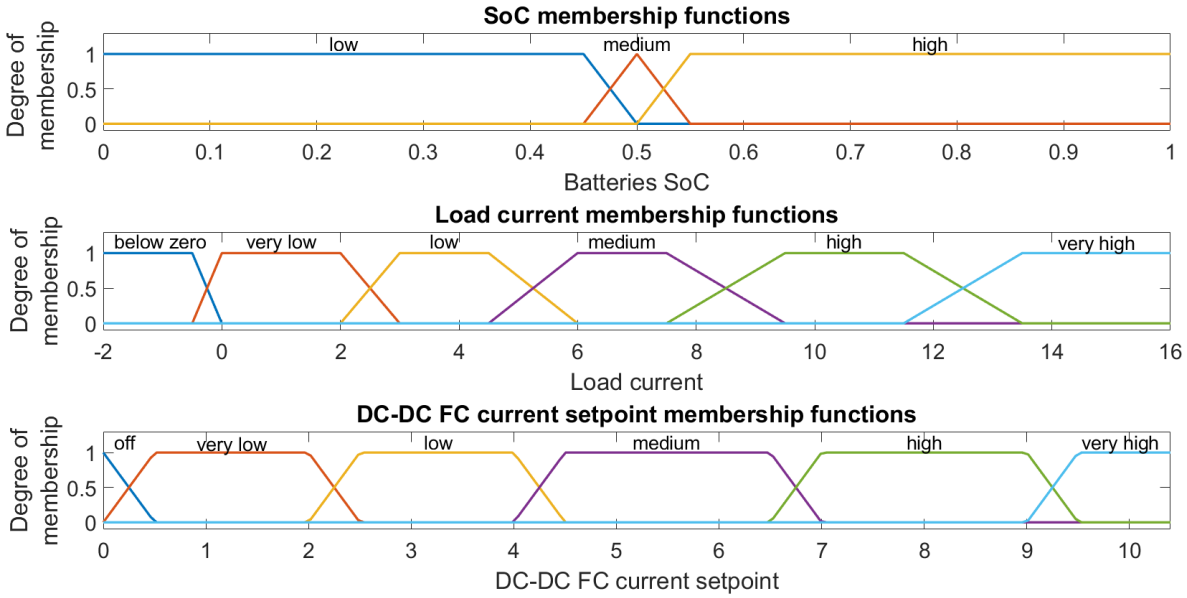

Figure 3.7 Membership functions for input and output variables for Topology A fuzzy controller.

Table 3.6 Fuzzy rule table for the DC-DC on the batteries side current setpoint for topology B.

DC-DC batt current setpoint		**DC bus voltage**				
		VL	**L**	**M**	**H**	**VH**
Batteries SoC	*VL*	D	Z	C	HC	HC
	L	HD	D	C	HC	HC
	M	HD	D	Z	C	HC
	H	HD	HD	D	Z	C
	VH	HD	HD	D	D	Z

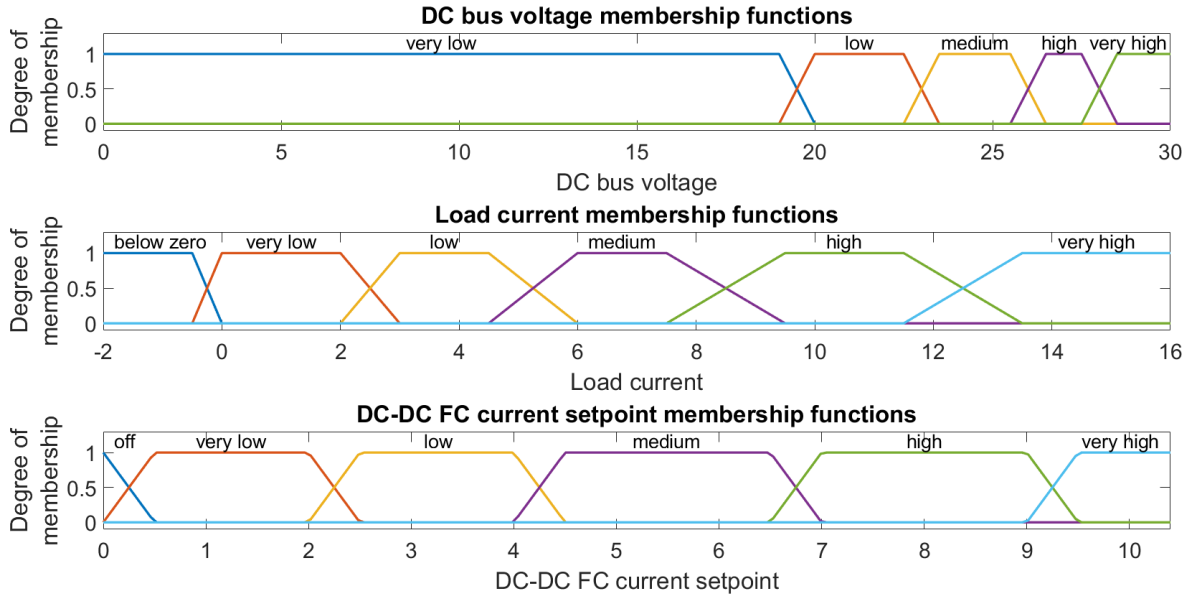

Figure 3.8 Membership functions for input and output variables for Topology B DC-DC on FC side current setpoint.

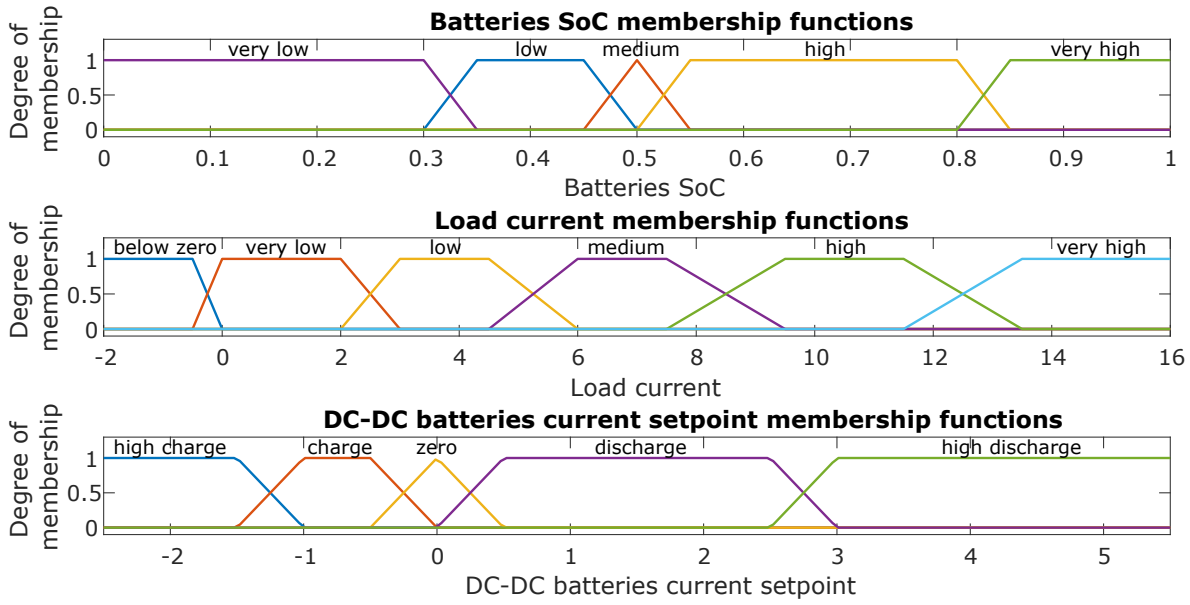

Figure 3.9 Membership functions for input and output variables for Topology B DC-DC on batteris side current setpoint.

Table 3.7 Fuzzy rule table for the DC-DC current setpoint for topology C.

DC-DC FC current setpoint		**Load current**					
		BZ	**VL**	**L**	**M**	**H**	**VH**
DC bus voltage	*VL*	H	H	H	VH	VH	VH
	L	M	M	H	H	VH	VH
	M	OFF	VL	L	M	H	VH
	H	OFF	OFF	VL	L	M	H
	VH	OFF	OFF	OFF	VL	L	M

The output of the fuel cell was controlled considering the DC bus voltage and the load current, in order to avoid excessive over or under voltage situations. As for the batteries, the current was controlled considering their SoC and the load, in addition constraints in terms of charge/discharge current were considered when defining the output membership functions. The batteries were recharged in case of very low SoC and/or high DC bus voltage level, while were discharged in case of low SoC and/or low DC bus voltage. Instead, in case of medium bus voltage and SoC levels, the batteries current was around zero. With respect to topology A, more membership functions were used for the SoC as the lower energy capacity of the battery pack required a stricter control.

Lastly, for Topology C, the membership functions of the input variables were defined classifying the load current into below zero, very low, low, medium, high, very high, and the DC bus voltage into very low, low, medium, high and very high. The membership functions of the output variable were defined classifying the current setpoint into off, very low, low, medium, high, and very high. The fuzzy rules adopted are shown in Table 3.7, while the membership functions are shown in Figure 3.10. In this case, the output of the fuel cell was defined considering the DC bus voltage and the load current. In case of low voltage levels, the output of the fuel cell was higher to charge the supercapacitors, while in case of high levels it was lower to avoid overvoltage.

The operating maps that were obtained from the fuzzy logic algorithms are shown in Figure 3.11.

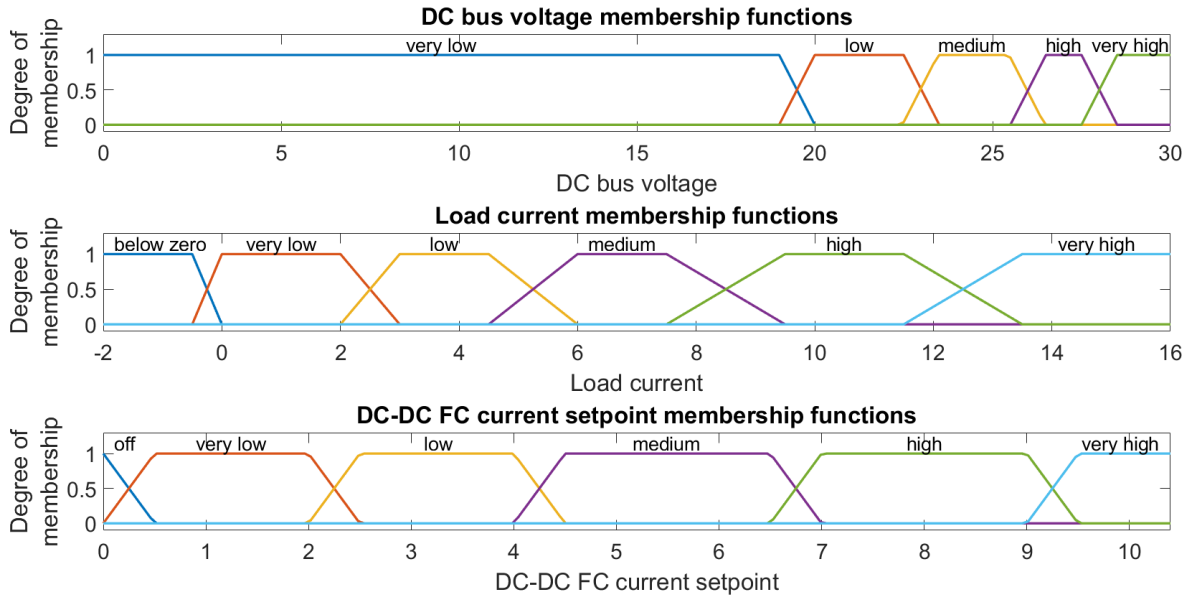

Figure 3.10 Membership functions for input and output variables for Topology C fuzzy controller.

As previously mentioned, the load follower and fuzzy logic algorithms evaluated the current setpoint as described in Figure 3.6. Consequently, the PI controller coefficients had to be carefully defined as they can have a huge impact on the effectiveness of the control. Into details, the PI coefficients should be determined with a view to minimize component degradation and, at the same time, ensure proper operation within the prescribed limits. This last aspect is particularly critical in case of topology B and C, which presented constraints on the DC bus voltage level. As a matter of fact, the fuel cell power output cannot be characterized by a too high response time as this may lead to an excessive reduction in the supercapacitors voltage. On the contrary, as described by equation3.4, to enhance durability the fuel cell power output should be as constant as possible. It is clear that mediation must be done to limit the fuel cell power output variation but ensuring that, in the case of intense and long-lasting peaks in the power demand, its response time is fast enough to avoid DC bus undervoltage. Combining all these considerations, for topologies B and C the PI coefficients were calibrated according to the worst-case scenario, where continuous acceleration and deceleration phases occurred. As for Topology A, since the battery pack could handle the load for a significantly longer amount of time, the

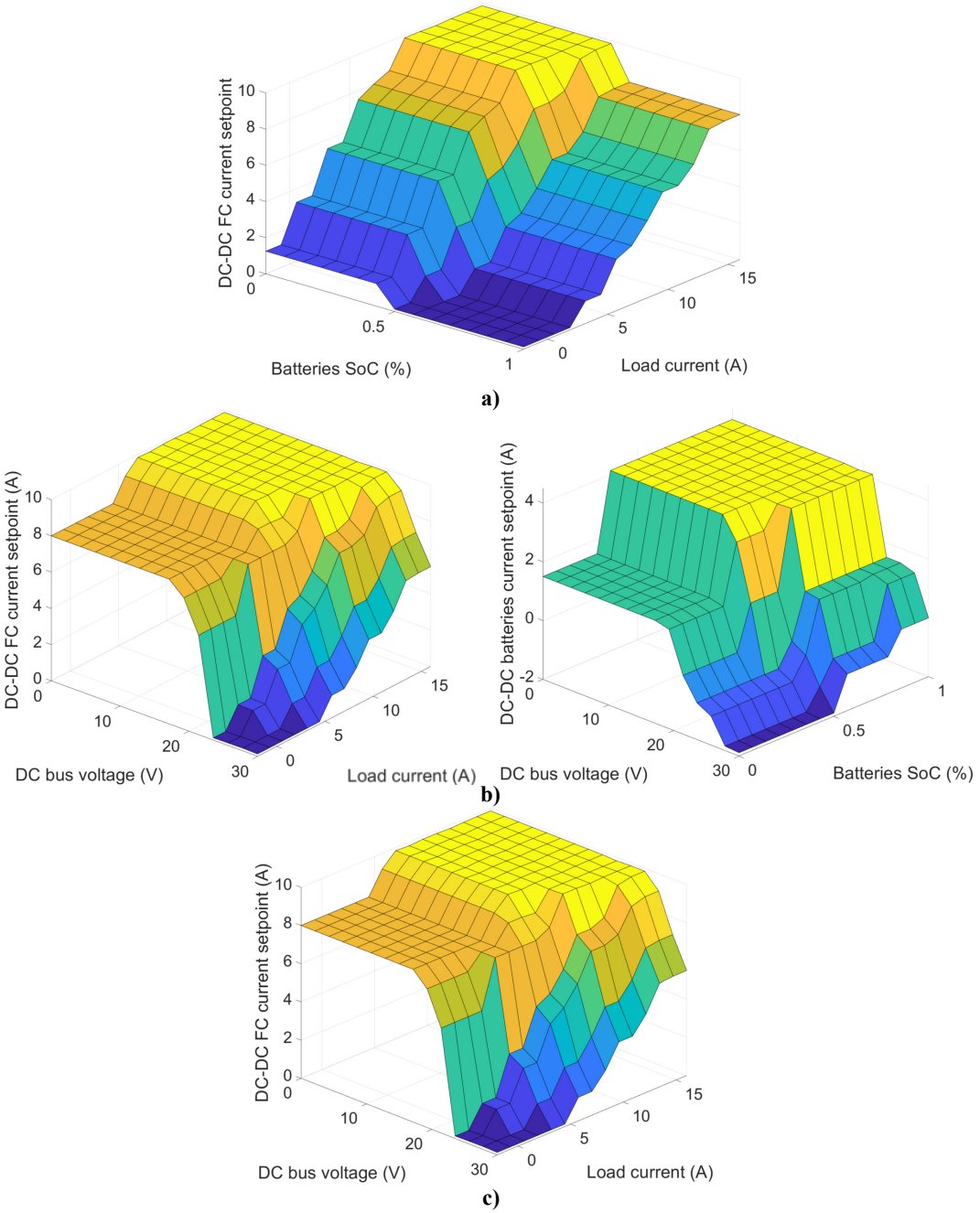

Figure 3.11 Operative maps determined according to the fuzzy logic. (a) Topology A, (b) Topology B, (c) Topology C.

Table 3.8 Coefficients adopted for the control strategies

Coefficient	Value
K_1	4.95
K_2	2.8 (discharge); 0.6 (charge)
K_3	10
K_4	2.8 (discharge); 0.6 (charge)
K_5	7.5
K_6	5.8
K_p Topology A	0.7
K_p Topology B	0.9 (DC-DC FC); 1.6 (DC-DC batteries)
K_p Topology C	2.5
K_i Topology A	1
K_i Topology B	3.3 (DC-DC FC); 3.5 (DC-DC batteries)
K_i Topology C	6.9

definition of the coefficients was less constrained. In this case, the main goal was to limit excessive long-lasting situations with high C-rates on the battery pack.

All the coefficients adopted in the control strategies are available in Table 3.8.

3.1.5 Experimental load profiles

The load profiles adopted for the comparative analysis consisted of the profiles already described in Section 2.4, to which other profiles were added to expand the analysis and include more tasks. The added profiles were obtained using the same approach, that is connecting a CAN analyzer to the tractor's CAN BUS network and monitoring the parameters of interest. The profiles obtained during the second monitoring campaign, unlike the two described in Section 2.4, focused on specific pre-defined tasks which were carried out for few minutes, thus were way shorter that the others. Into details, the tasks that were monitored during this additional monitoring campaign were:

- Road transportation handling an empty trailer.
- Road transportation handling a 6000 kg trailer.
- Use of a shredder (in the field).

- Use of a rotary harrow (in the field).

The additional work scenario profiles are shown in Figure 3.12. As it can be stated, while the shredder profile was characterized by low power oscillations, the other profiles were more critical. The handling of trailers scenarios were characterized by moderate/intense power variations, indeed they involve continuous acceleration and deceleration phases. The rotary harrow work scenario, instead, was particularly critical in terms of power absorption, with high-power demanding phases with more than 65 kW that lasted for a significant amount of time.

Combining those profiles with the atomizer and weeding work cycles described in Section 2.4 it was possible to have a good overview. Indeed, the atomizer and weeding scenarios were very useful since they better describe how the machine is generally used during normal daily activities, while the additional profiles can better describe how single operations can affect the durability of the system.

As for the load profiles emulation, the electronic load was controlled considering that the monitored data during the monitoring campaigns regarded mainly the ICE mechanical power output. However, since the electronic load must emulate the power required upstream the inverter, the efficiencies of the electric motor and inverter had to be considered. For simplicity, both were considered constant and equal to 95%. Thus, the total power absorbed by the electronic load was defined by the following equation:

$$P_{tot,EL} = \frac{P_{exp}}{\eta_{EM} \cdot \eta_{inverter}} + P_{FC,BoP} \tag{3.10}$$

Where $P_{tot,EL}$ is the total electronic load, P_{exp} is the power derived by the experimental load profiles, scaled with the proper scale factor, η_{EM} and $\eta_{inverter}$ are the electric motor and inverter efficiencies respectively, and $P_{FC,BoP}$ is the power absorbed by the fuel cell BoP (upstream the dedicated power converter).

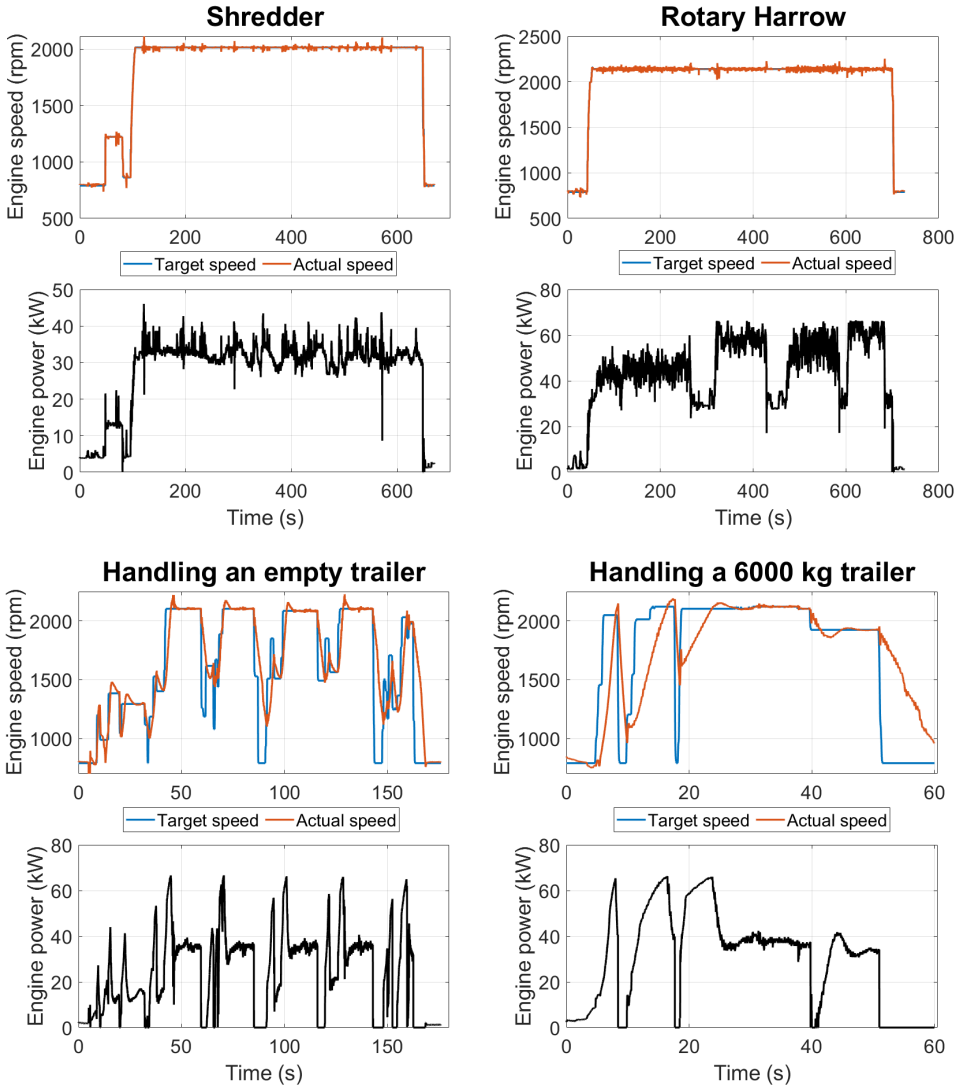

Figure 3.12 Additional load profiles for the HIL tests.

3.2 Results and Discussion

3.2.1 HIL tests results

The tests were performed considering all the described load profiles, configurations, and energy management strategies. All the tests started with the batteries SoC at 50% where present, and the supercapacitors voltage at the rated value. The results were analyzed to determine fuel economy and durability. Starting from the atomizer and weeding work cycles, the results of the HIL tests are shown in Figures 3.13-3.16. Analyzing the results, the first consideration that can be done is that topology A allowed for a reduction in the fuel cell power output variation. As previously mentioned, this can be attributed to the capacity of the secondary unit to handle the load for a relevant amount of time without exceeding operational limits. On the contrary, topologies B and C required a faster intervention of the fuel cell during long-lasting high-power situations to avoid excessive reduction in the DC bus voltage level. Into detail, for topology B the battery pack capacity was too small and its power capabilities were not enough to handle the load when the DC bus voltage started to decrease significantly, thus the fuel cell had to increase its power output. As for topology C, the supercapacitors limited energy capacity required the fuel cell to respond within a short time during long and intense power-demanding situations.

Regarding the additional load profiles, the results of the tests are shown in Figures 3.17 and 3.18. These figures show the results for the shredder and handling of trailers scenarios. As for the rotary harrow, due to the task intensity, only topology A managed to complete it. Indeed, in certain phases of the activity, the power required was higher than the net power of the fuel cell system, thus it was possible to accomplish the task only if the secondary unit had enough energy capacity to supply the difference for the required time.

Given the power profiles obtained during the HIL tests, it was possible to evaluate durability and fuel economy of the different topologies and energy management strategies. The results are summarized in Tables 3.9 and 3.10. The expected life values in the table were obtained dividing them by the expected life of the fuel cell for Topology A in the shredder cycle with the power follower control. Indeed, the purpose of the authors was not to provide the expected life in hours, but to compare the durability of the different topologies considering the same aging model.

Concerning the fuel cell system, for Topology A the results in terms of durability were generally better with the load follower controller, apart from the handling of trailers scenarios. Topology C instead showed better results using the fuzzy logic controller, with a fuel cell durability that was significantly higher in the weeding and atomizer work cycles, and in the handling of an empty trailer scenario. The result for Topology B instead were different depending on the considered scenario. Nevertheless, it emerged that the fuzzy logic controller enhanced the battery pack durability. Comparing the three architectures, Topology A showed the best results for the fuel cell life expectancy in all the considered scenarios, outperforming the other two proposed architectures.

Regarding the fuel economy, the differences were minimal among the different architectures and energy management strategies. Nevertheless, it was observed that topology C seemed to be the best in terms of energy consumption. This may be related to the low internal resistance of the supercapacitors and to the absence of a DC-DC on the secondary unit side, which reduced the conversion loss. However, the differences in terms of durability were much more of interest not only because they were significantly higher, but also for the specific case under investigation.

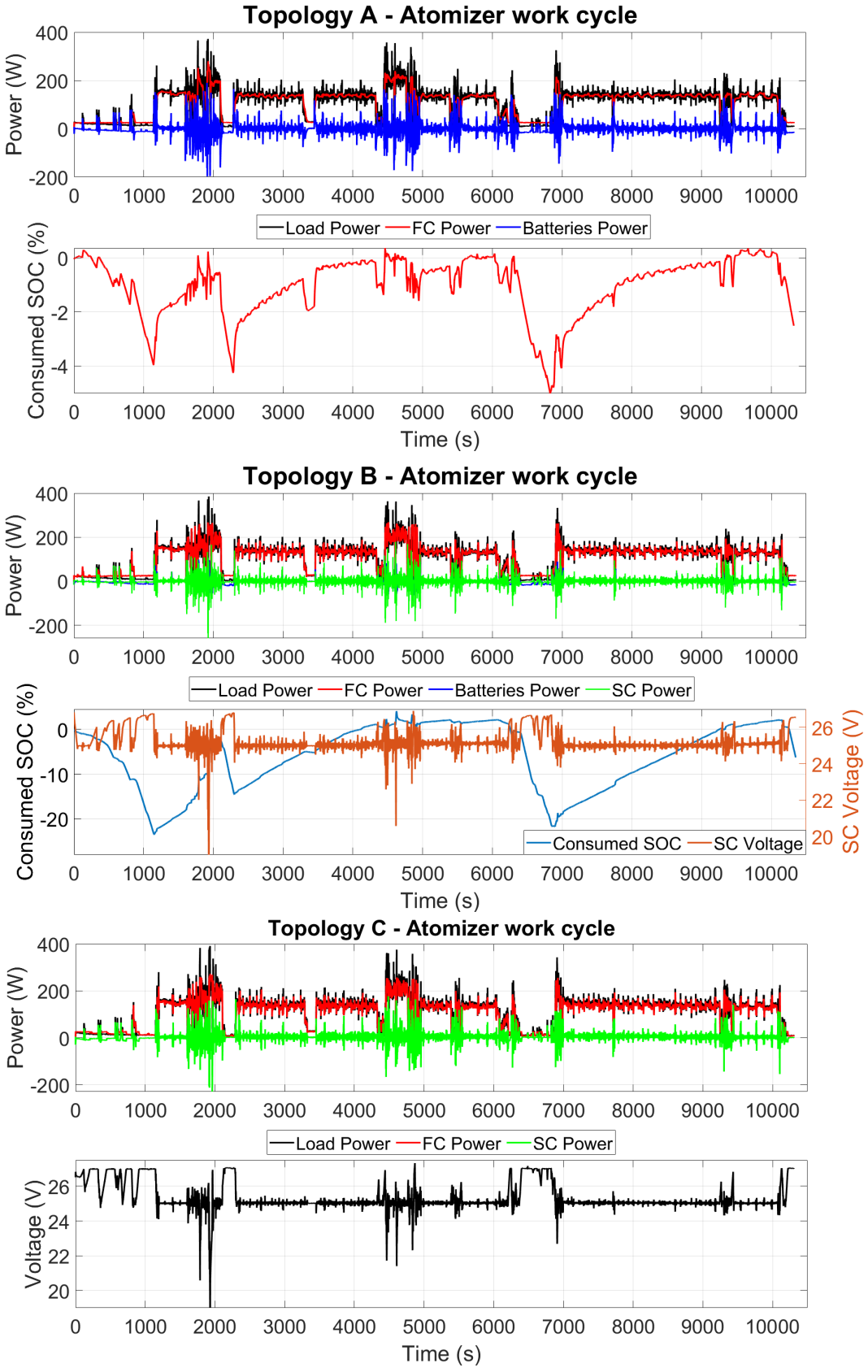

Figure 3.13 Atomizer work cycle results with power follower control strategy.

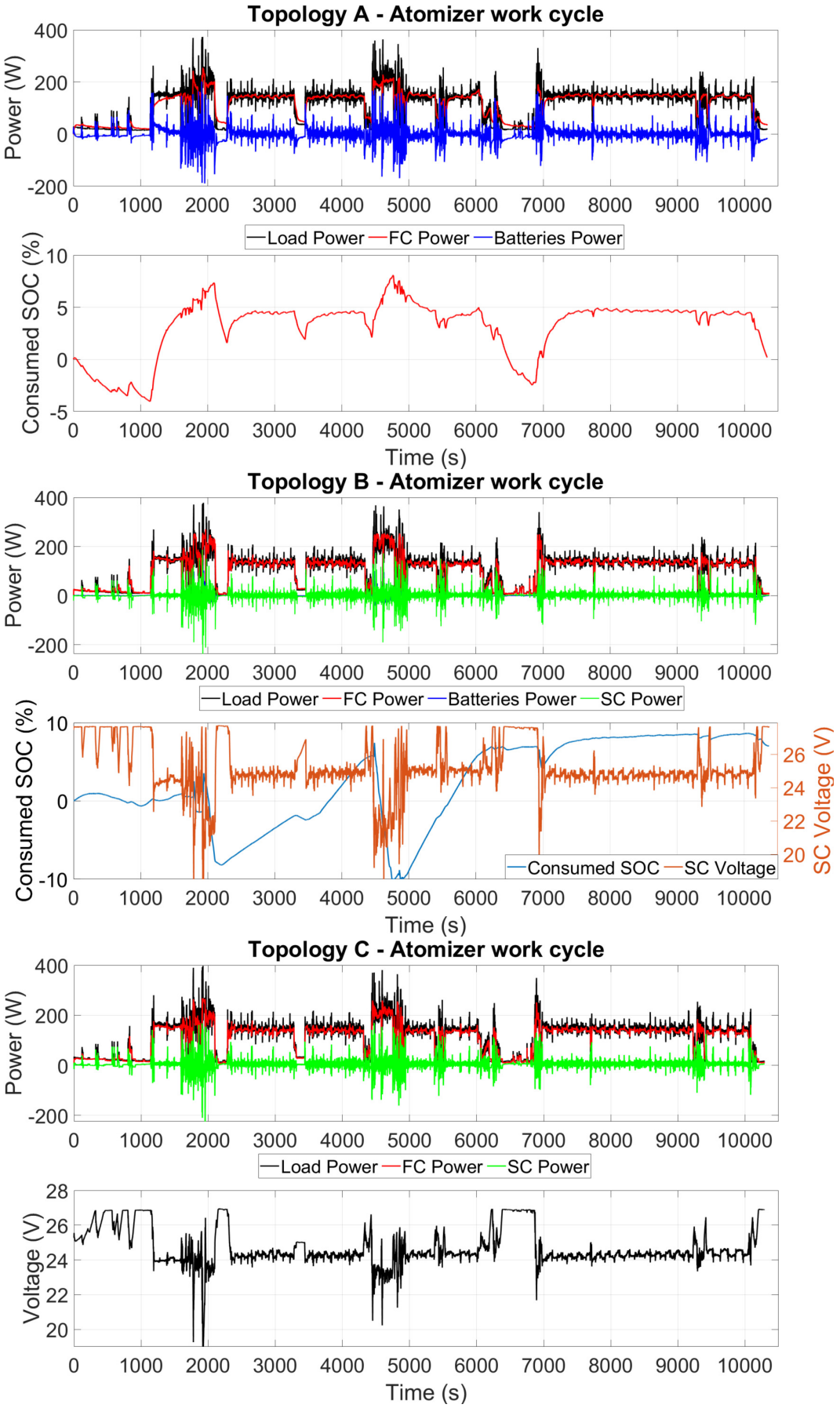

Figure 3.14 Atomizer work cycle results with fuzzy logic control strategy.

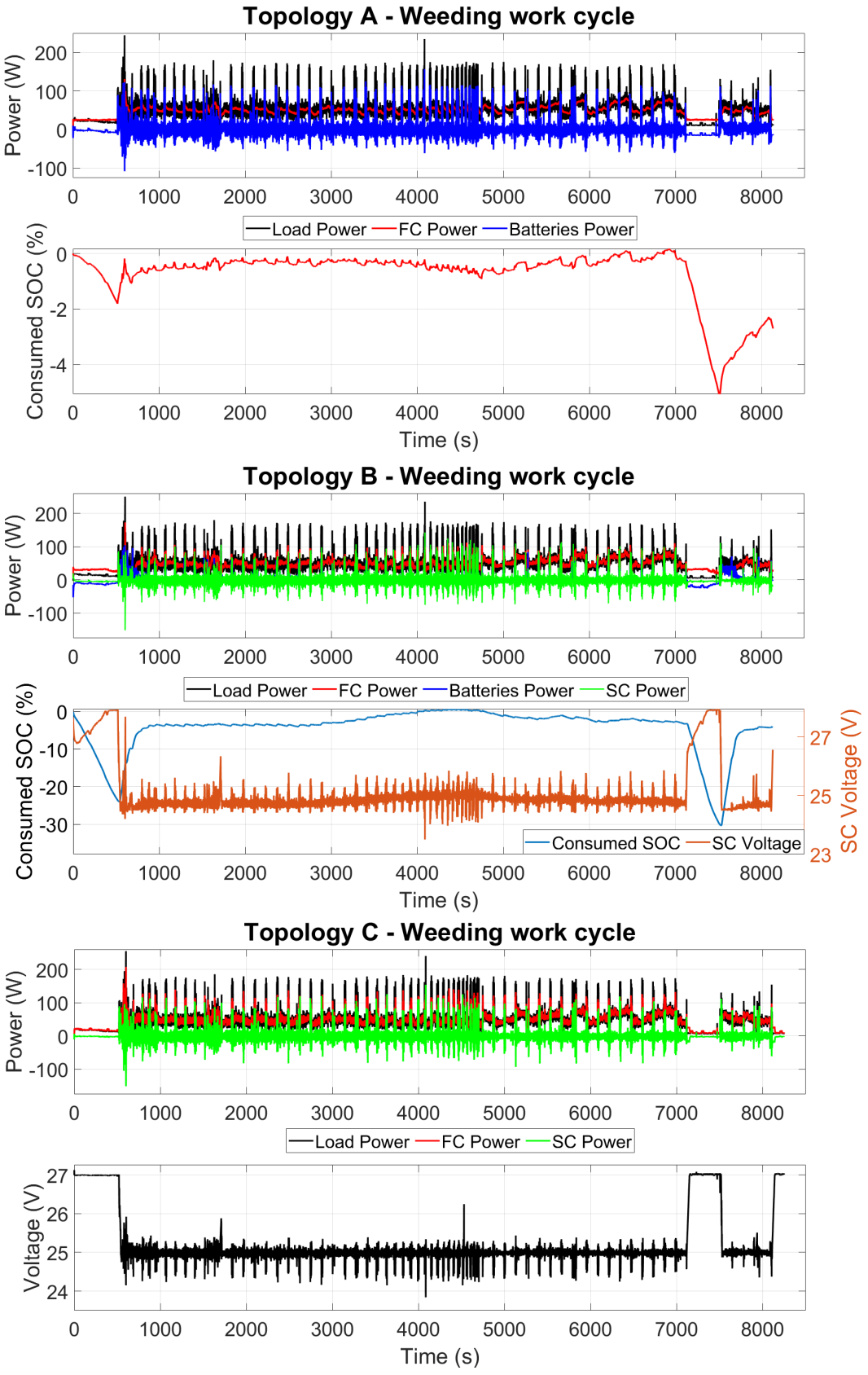

Figure 3.15 Weeding work cycle results with power follower control strategy.

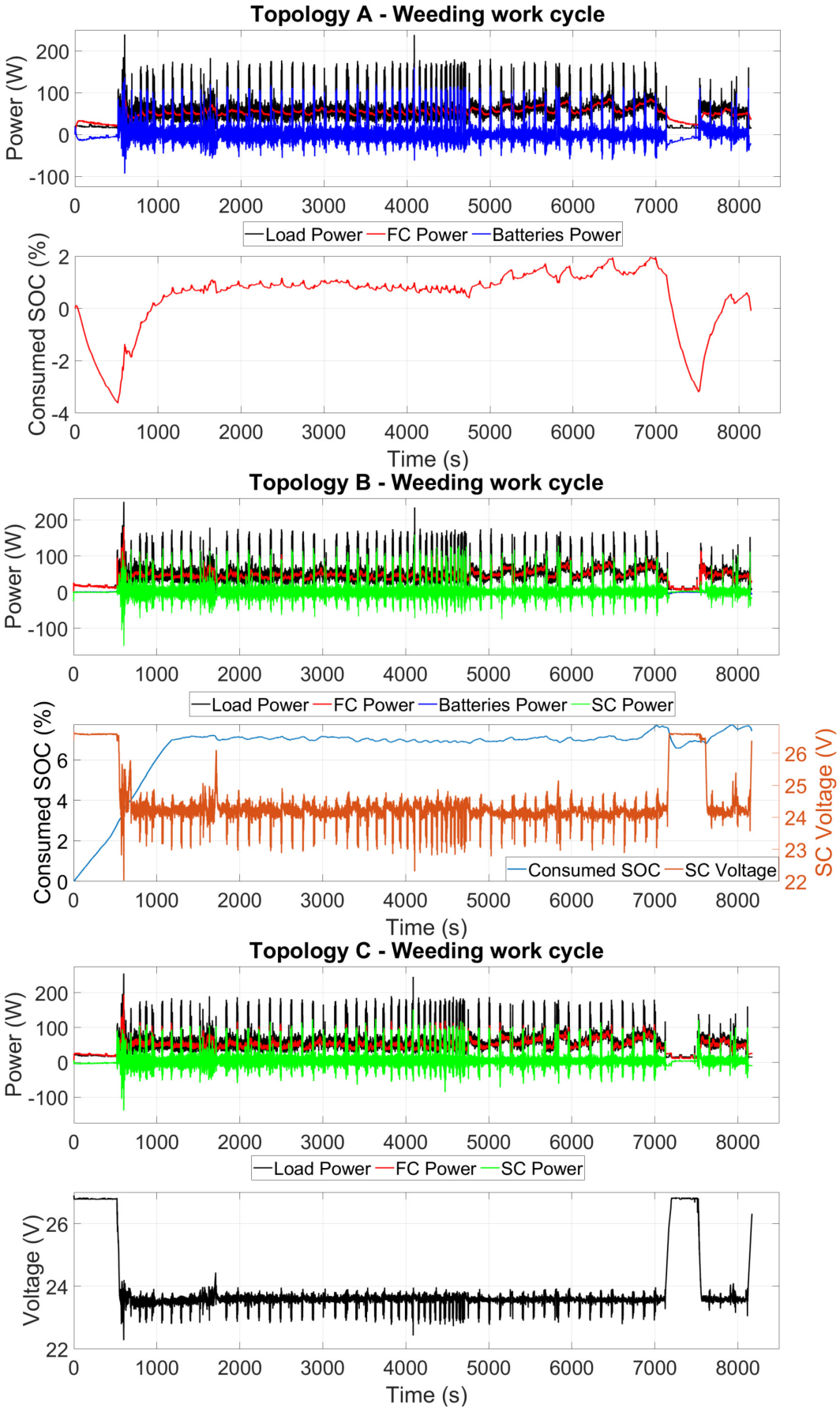

Figure 3.16 Weeding work cycle results with fuzzy logic control strategy.

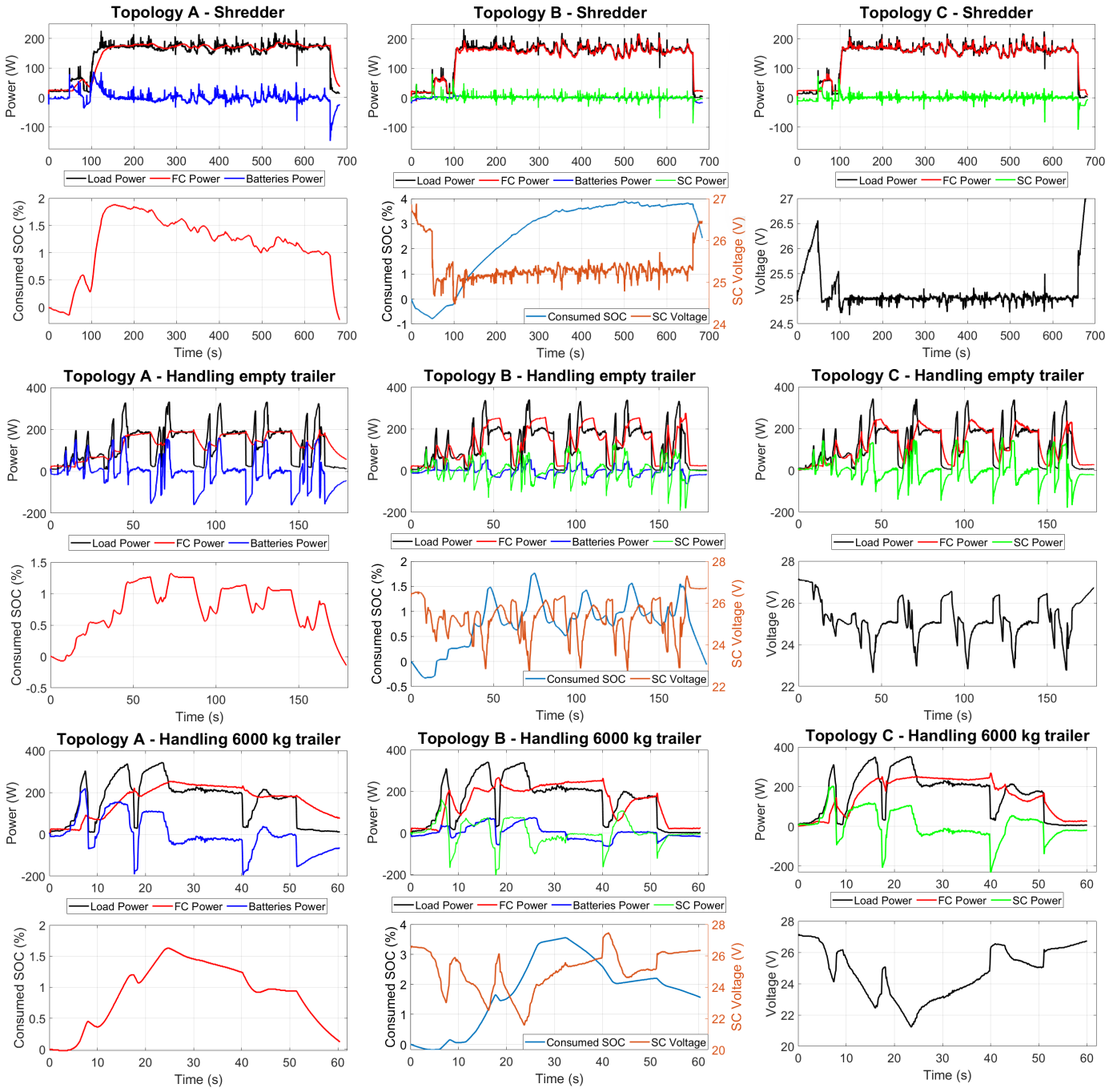

Figure 3.17 Shredder and handling of trailers work scenarios results with load follower control strategy.

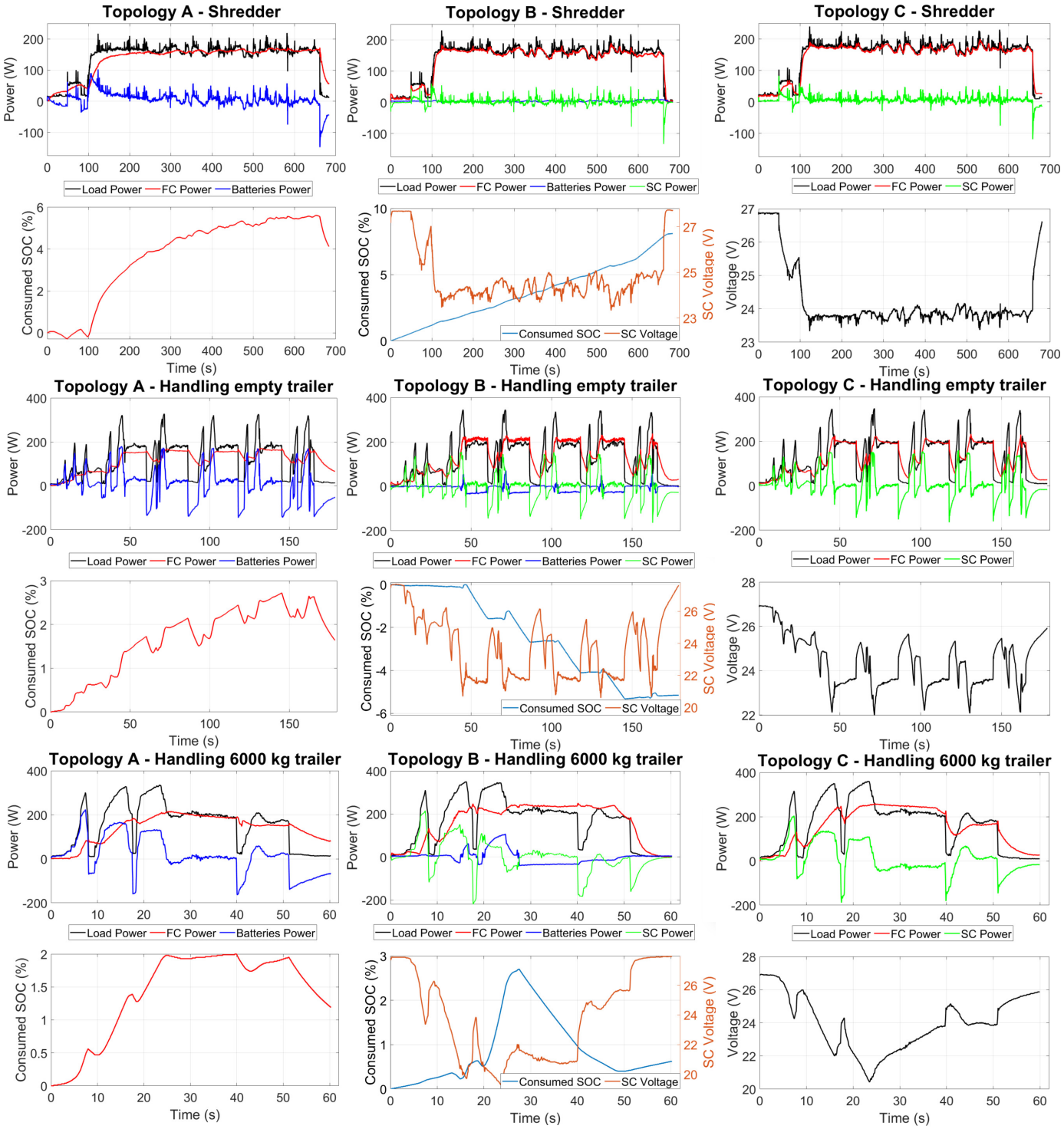

Figure 3.18 Shredder and handling of trailers work scenarios results with fuzzy logic control strategy.

Table 3.9 Comparison among the three different topologies according to the experimental results using the power follower control. Please note that the SOC variation is determined considering the difference between the final SoC and the initial SOC.

Work cycle	**Topology**	**Expected life Fuel cell**	**Expected life Batteries**	**Expected life Supercapacitors**	**Mean H_2 consumption (g/s)**	**SoC variation (%)**
Shredder	A	1.00	3.04	-	$1.91 \cdot 10^{-3}$	0.2
	B	0.83	2.95	31.9	$1.76 \cdot 10^{-3}$	-2.4
	C	0.80	-	44.6	$1.74 \cdot 10^{-3}$	-
Rotary Harrow	A	0.72	0.64	-	$3.03 \cdot 10^{-3}$	-14.3
	B			TEST FAILED		
	C			TEST FAILED		
Handling empty trailer	A	0.49	0.67	-	$1.61 \cdot 10^{-3}$	0.15
	B	0.48	0.42	6.4	$1.67 \cdot 10^{-3}$	0.06
	C	0.26	-	12.5	$1.50 \cdot 10^{-3}$	-
Handling 6000 kg trailer	A	0.66	0.50	-	$2.09 \cdot 10^{-3}$	-0.12
	B	0.37	0.24	3.1	$2.06 \cdot 10^{-3}$	-1.57
	C	0.55	-	7.6	$2.05 \cdot 10^{-3}$	-
Weeding	A	1.43	3.74	-	$0.62 \cdot 10^{-3}$	2.7
	B	0.56	1.71	19.9	$0.58 \cdot 10^{-3}$	4.1
	C	0.46	-	22.8	$0.58 \cdot 10^{-3}$	-
Atomizer	A	1.04	2.83	-	$1.37 \cdot 10^{-3}$	2.5
	B	0.70	1.83	25.5	$1.34 \cdot 10^{-3}$	6.2
	C	0.38	-	22.4	$1.33 \cdot 10^{-3}$	-

Table 3.10 Comparison among the three different topologies according to the experimental results using the fuzzy logic control. Please note that the SOC variation is determined considering the difference between the final SoC and the initial SOC.

Work cycle	Topology	Expected life Fuel cell	Expected life Batteries	Expected life Supercapacitors	Mean H_2 consumption (g/s)	SoC variation (%)
Shredder	A	0.81	2.31	-	$1.69 \cdot 10^{-3}$	-4.1
	B	0.87	2.15	29.2	$1.74 \cdot 10^{-3}$	-8.1
	C	0.77	-	49.9	$1.74 \cdot 10^{-3}$	-
Rotary Harrow	A	0.68	0.61	-	$3.02 \cdot 10^{-3}$	-15.2
	B			TEST FAILED		
	C			TEST FAILED		
Handling empty trailer	A	1.00	0.61	-	$1.45 \cdot 10^{-3}$	-1.6
	B	0.42	0.78	2.3	$1.79 \cdot 10^{-3}$	5.2
	C	0.53	-	15.1	$1.50 \cdot 10^{-3}$	-
Handling 6000 kg trailer	A	0.90	0.49	-	$1.85 \cdot 10^{-3}$	-1.2
	B	0.64	0.26	0.74	$2.15 \cdot 10^{-3}$	-0.6
	C	0.55	-	8.1	$2.05 \cdot 10^{-3}$	-
Weeding	A	1.28	3.27	-	$0.62 \cdot 10^{-3}$	-0.1
	B	0.78	6.00	16.6	$0.67 \cdot 10^{-3}$	-7.5
	C	0.83	-	6.6	$0.58 \cdot 10^{-3}$	-
Atomizer	A	0.82	2.40	-	$1.40 \cdot 10^{-3}$	-0.2
	B	0.48	2.52	11.9	$1.39 \cdot 10^{-3}$	-7.0
	C	0.83	-	34.9	$1.33 \cdot 10^{-3}$	-

3.2.2 Discussion

The analysis and subsequent interpretation of the results allowed for outlining several considerations.

Firstly, topology A outperformed the other two in terms of fuel cell durability with both power follower and fuzzy logic controllers. The main factor that led to this result was the limited on-board space availability. Indeed, considering topology B, the introduction of the supercapacitor module and of the bidirectional DC-DC converter yield to an excessive reduction of the battery pack capacity (from 6 kWh to 1.4 kWh considering the non-scaled powertrain). In addition, since the DC bus voltage was determined by the supercapacitors SoC, during intense and long-lasting high-power demanding situations the fuel cell power output had to vary fast enough to avoid potential bus undervoltage, as the battery pack could not handle a large part of the load due to its small size. Thus, the cross-effects of reduced battery pack power capability and DC bus voltage reduction due to the low energy capacity of the supercapacitors led to reduced durability for Topology B. The adoption of other battery technologies and chemistries might translate into different results, since the energy and power capacity may be very different. Regarding Topology C, the adoption of a secondary unit with only supercapacitors enhanced the problems related to their low-energy capacity. Thus, also in this case a higher fuel cell dynamics was required. Indeed, even if supercapacitors have a very high-power capability, their energy density was not enough to let them handle a large part of the load for enough time. On the contrary, topology A featured a battery pack capacity that was sufficient to satisfy intense and long-lasting high-power phases without issues related to excessive C-rates or DC bus under voltage.

Another relevant aspect that emerged analyzing the results was that the definition of the control strategy can have a huge impact on the durability of the fuel cell system. In some scenarios, the differences in the expected lifetime for the power follower and fuzzy logic control strategies were substantial. To better highlight this aspect, the comparison in terms of fuel cell durability for the three topologies with the two control strategies is shown in Figure 3.19. Analyzing the figure, it can be noted that in certain situations, given the same load profiles, the adoption of one strategy can double the expected lifetime with respect to the other control. This huge difference can be attributed to the variation of the FC current setpoint during the test. However, considering topology A, it was noted that the power follower controller

extended the lifetime during work scenarios involving field activities, while the fuzzy logic controller performed better in the handling of trailers scenarios. This can be attributed to the fact that the power follower controller caused higher FC output variations during the handling of trailers scenarios as they involve strong acceleration and deceleration phases that directly affected the current setpoint. It can be contested that also in the fuzzy logic controller the current setpoint was determined by the load current, however its influence on the setpoint was smoother. On the contrary, in case of field activities where the load was characterized by less intense variations, the power follower controller performed better as the setpoint was more stable than the fuzzy logic controller.

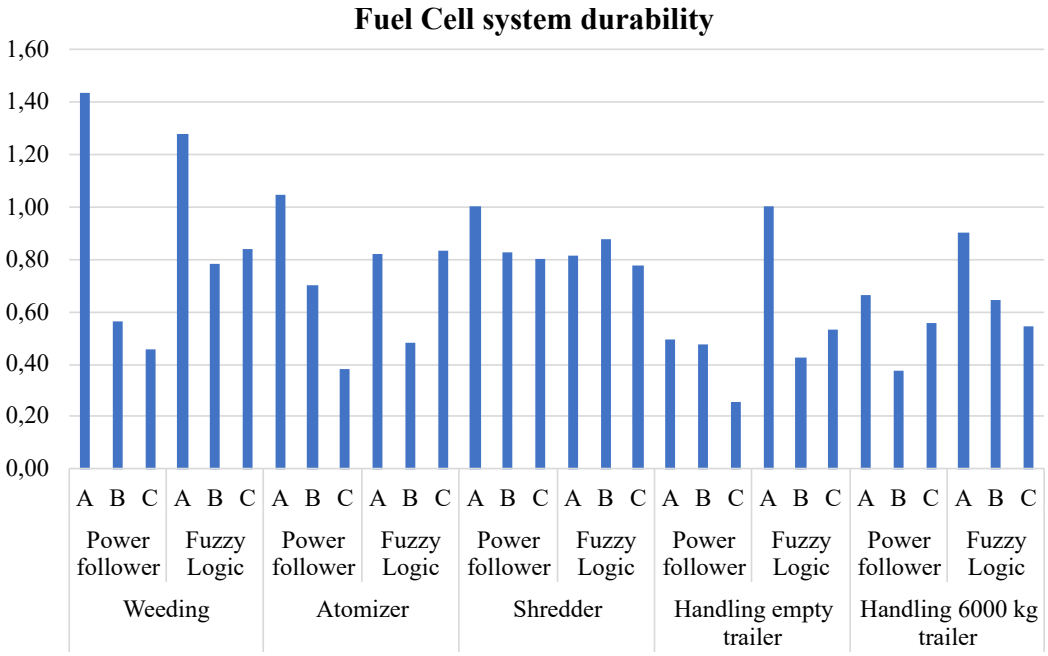

Figure 3.19 Comparison of the fuel cell system durability for the different topologies and control strategies. Please note that the results are normalized with respect to durability of the fuel cell for Topology A during the shredder work cycle and using the power follower control strategy.

Considering topology B, the comparison among the two controllers highlighted that the fuzzy logic controller performed generally better. The only case in which the power follower outperformed was the atomizer work cycle. However, with respect to topology A and C the determination of the better control was less clear. Lastly, in case of topology C the fuzzy logic controller obtained better results, in particular

considering the weeding and atomizer work scenarios. Again, this can be attributed to the fact that the fuzzy logic controller was able to reduce the stress on the fuel cell by smoothing the variations on its current setpoint.

In summary, the main outcomes of the analysis are the following:

- In case of scenarios with a predominance of strong acceleration and deceleration phases, or in case of a high-power and low-energy secondary unit, the fuzzy logic controller showed better results.
- In case of scenarios involving field activities and a high-energy secondary unit, the power follower controller outperformed the other.
- In case of a hybrid secondary unit with both high-power and high-energy components, the results strongly depended on the specific work scenario.

As for the fuel economy, the differences were not particularly relevant among the three architectures due to two main aspects. Firstly, the efficiency of the fuel cell system does not exhibit significant variations at medium-to-high power levels. On average, it ranges from a peak value of approximately 50%, which typically occurs at around 20–30% of the rated power, down to about 40%, or slightly lower, when operating at full load. Secondly, since the fuel cell system acted as primary energy source and supplied the low dynamics part of the load, for most of the time it operated at similar points for all the three topologies. Indeed, excluding situations with strong external load variations, in the other phases the power output of the fuel cell was on average the same. This aspect was further enhanced as a result of the high compactness required for the secondary units, which limited its capabilities in terms of contributions to satisfy the power demand. However, it was noted that topology C exhibited the best fuel economy. As previously stated, this can be attributed to the low internal resistance of the supercapacitors and the absence of a DC-DC on the secondary unit side, which reduced conversion losses.

Another element that emerged from the analysis was that the most stressful operative conditions were the on-road transportation phases. This was found to be coherent with the adopted fuel cell aging model, which clearly indicated that load cycling had a significant impact on the system durability. Furthermore, it was noted that, considering the on-field operations, the fuel cell was the element that showed the lower life expectancy with respect to batteries and supercapacitors. On

the contrary, in the handling of trailers scenarios the batteries showed the lowest durability. This can be related to the higher change rates and peaks in the power request, which led to high C-rates and, consequently, to a reduction in the expected lifetime. However, it should be pointed out that the results are affected by the adopted aging models. As for the supercapacitors, their expected life was significantly higher than the other two power sources in all the considered scenarios. As a consequence, the optimization of the control strategy and of the powertrain architecture should not be limited to a single work scenario, but should consider all the possible operative conditions under which the powertrain might operate, including field operations with different implements and on-road transportation with different payloads.

3.2.3 Limitations of the study

The adoption of a scaled HIL set up and of a power supply to emulate the fuel cell may introduce some limitation that must be acknowledged and discussed.

Firstly, a critical aspect concerns the behaviour of the fuel cell system's BoP. While the stack itself can be scaled in terms of voltage–current characteristics, the BoP warrants further investigation, particularly with regard to its power consumption and dynamic behavior. During the HIL tests, the authors added a term to the load profile that considered the power required by the BoP according to typical absorptions in high-power liquid-cooled fuel cell systems. Considering the power required by the auxiliaries of the reference FCS-C300 system would not be indicative as it is an air-cooled open-cathode stack and its BoP is much simpler. The absence of the air compressor, indeed, is one of the most relevant differences that could have a huge impact on the results. Given that the HIL test bench accounted for the BoP's power absorption by including an additional term added to the load profile, the dynamic behavior of the air compressor in another critical point of the analysis. The compressor is characterized by a certain dynamic response that cannot be taken into account in the proposed set-up, apart from limiting the change rate in the stack power output. As a consequence, the power output of the fuel cell system during the performed tests should be generally characterized by variations that must be coherent with the dynamic response of the non-scaled system. Considering this aspect, the control strategies were defined limiting the fuel cell power output variations to be compliant with the limits imposed by the non-scaled system. Analyzing the results,

the power profiles obtained by the fuel cell system were deemed to be reasonable and coherent with the dynamic behavior of the non-scaled counterpart.

Secondly, another limitation is related to the adoption of a programmable power supply to reproduce the fuel cell behavior. Indeed, the proposed set-up considered the stack polarization curve and adjusted the power supply voltage at each time step based on the actual current output. However, this approach may not fully capture the dynamic behavior of the stack considering both the voltage update time and the stack dynamics in terms of voltage variations with respect to the polarization curve. Nevertheless, the control unit updated the voltage level of the power supply approximately every 25 ms, and the control strategies limited the amplitude of the power output variations of the emulated stack, reducing the relevance of the stack dynamics. As a consequence, the concerns previously raised are not expected to have a significant impact on the results obtained.

Another limitation concerns the battery system. Specifically, the experimental set-up employs unscaled lead-acid batteries, which may neglect certain effects associated with C-rates and SoC depletion. Nevertheless, the battery power profiles observed during testing, taking into account their power capability and SoC levels, were considered consistent and reasonable when compared to those of appropriately scaled lithium-ion counterparts.

As for the fuel economy, the main issue is that the scaled components may not have the same efficiencies of the not scaled counterparts. Nevertheless, the authors deemed that this aspect did not affect the results as all the configurations are tested using the same experimental test bench.

Lastly, regarding the control strategies, only rule-based strategies were developed and implemented. The main reason for this was that these strategies are popular because of their ease of implementation and robustness. However, considering other more advanced control algorithms, such as machine learning or neural networks, the results might be different. In this context, the results should be interpreted that, considering only rule-based strategies, topology A seems to be the one with the best results, but with other strategies further tests should be performed.

3.3 Real Fuel Cell system implementation

Given the previously presented HIL bench with fuel cell emulation, the next step was to introduce a real fuel cell system. In this section, the set up of the FC system and hydrogen storage are presented. The components were characterized through dedicated experimental tests to extrapolate their nominal properties and operative parameters. Lastly, they were implemented in the HIL set up to replace the programmable power supply.

3.3.1 Fuel cell and hydrogen storage systems

The HIL test bench was developed considering the FCS-C300 fuel cell system, which was emulated by a power supply. This approach was adopted with a view to implement the real system in the set up. The FCS-C300 is an air-cooled open-cathode system developed by Horizon Fuel Cell Technologies (Singapore). Its main properties were described in Table 3.2. Additional information about the system, which are relevant when implementing it in a system, are reported in Table 3.11.

Table 3.11 FCS-C300 main properties.

FC type	PEM
Number of cells	60
Rated power	300 W
BoP supply voltage	12 V ($\pm$1 V)
H_2 pressure	0.45-0.55 bar
H_2 purity	$\geq$ 99.995% dry H_2
Max stack temperature	65°C
Humidification	self-humidified
Cooling	Air (integrated fans)
Start up time	$\leq$ 30 s

The manufacturer provides the system with an integrated controller that manages the fans and all the valves that are necessary for proper operation. As for the hydrogen storage system, a metal hydride tank was adopted. The adopted tank is the MyH2 900 manufactured by Hydro2Power Srl. The main properties of the tank are described in

Table 3.12. A picture of the fuel cell system and the metal hydride tank is shown in Figure 3.20.

Table 3.12 MyH2 900 main properties.

Alloy hydride	model AB2
Nominal capacity	81 g H_2
Max operating pressure	30 bar
Max operating temperature	65°C
Overall volume	1.7 litres
Overall weight	7 kg

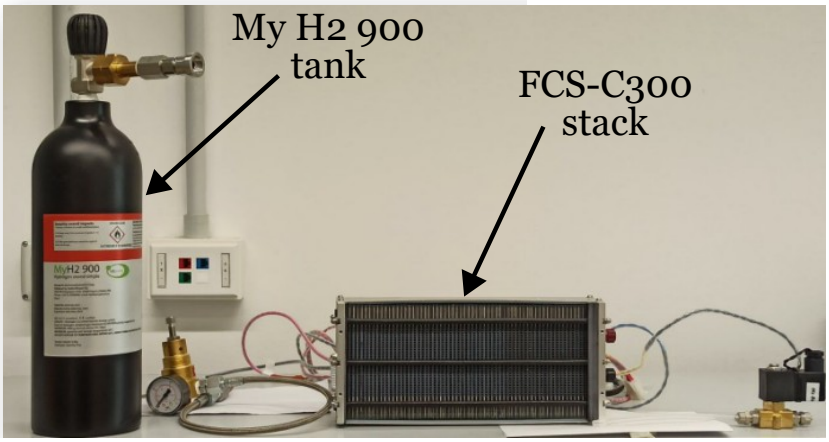

Figure 3.20 FCS-C300 and MyH2 900 tank.

Considering the MH tank, its internal pressure can reach up to 30 bar. The stack, instead, requires hydrogen at a pressure in the range of 0.45-0.55 bar. Thus, when connecting the tank with the fuel cell system, a pressure reducing valve must be implemented. Furthermore, to monitor the tank internal pressure, a pressure transducer should be added so that information about its state of charge can be extrapolated. Consequently, in the hydrogen connection between the tank and the fuel cell system a manual pressure reducing valve and a pressure transducer were implemented. The FCS-C300 system presented a solenoid valve, to regulate hydrogen flow, and a purge valve, both controlled by the system controller provided by the

manufacturer. The purge valve had the role to control humidity and remove excessive air gas

In addition, the fuel cell system presented a short-circuit unit (SCU), that approximately every 10 s short-circuits the stacks, with the effect of bringing to zero its output for about 100 ms. This function can be turned off in some specific case; however, this can significantly reduce the durability of the system. The main effects of this procedure are related to membrane regeneration, cells balancing, and so on.

The fuel cell system and the MH tank were characterized through dedicated experimental tests. The experimental set up for these tests is shown in Figure 3.21.

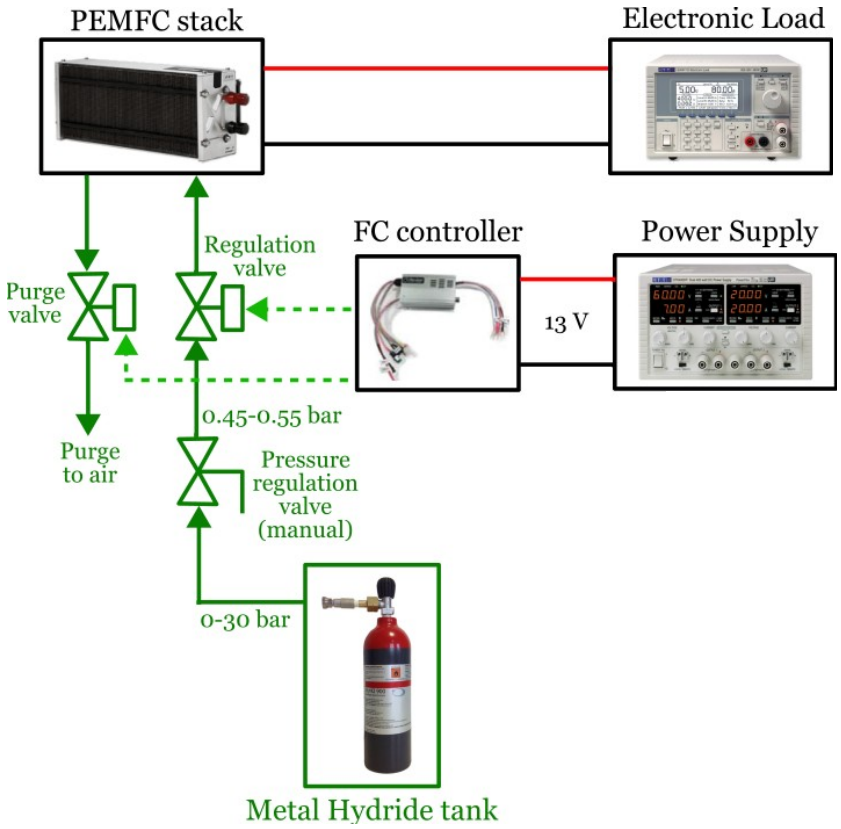

Figure 3.21 Experimental set up for the fuel cell system and the MH tank characterization tests.

3.3.2 Characterization tests

For the fuel cell system characterization, the polarization curve was determined at different levels of power output and confronted with the curve provided in the

datasheet by the manufacturer. The tests were carried out at an ambient temperature of 25°C. The results of the test are shown in Figure 3.22. As can be seen, the stack measured performances were better than those declared and provided in the datasheet, with a mean value of +4%. Furthermore, according to the manufacturer the stack has a rated power of 300 W @ 36 V; however during the test the stack reached an output of 330 W @ 43.3 V, indicating that the stack might reach even higher power levels. The authors decided to stop the test at 330 W to avoid any possible damage to the stack. The power absorbed by the auxiliaries (blowers, valves, controller) was observed to be almost independent of the load and with a value of around 15 W.

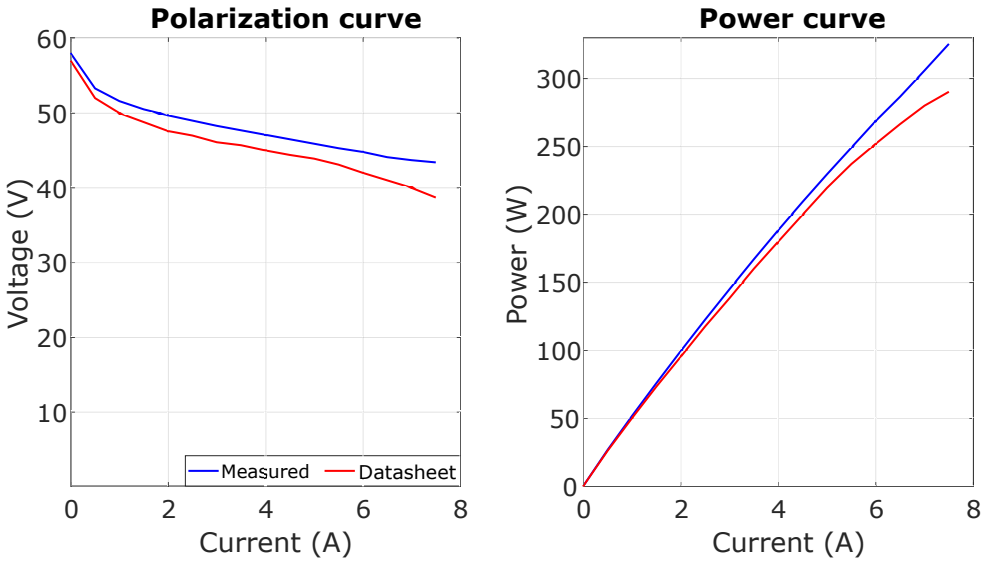

Figure 3.22 Results of the fuel cell stack characterization

Regarding the characterization of the metal hydride tank, the main goal was to determine the main parameters for the PCT diagrams and the heat absorbed during desorption. The attention focused on the desorption process as it is the relevant process when the fuel cell is providing power to a system, as in powertrain configurations. On the contrary, the absorption process that takes place when recharging the tank is carried out at refueling stations, thus was not of interest for the analysis proposed in this section.

As already discussed in Section 1.3, the equilibrium pressure of the MH tank can be described by the following equation:

$$p_{\text{eq}} = f\left(\frac{H}{M}\right) \cdot \exp\left(\frac{\Delta H}{R_g} \cdot \left(\frac{1}{T} - \frac{1}{T_{\text{ref}}}\right)\right) \tag{3.11}$$

The first parameter to be determined by the characterization procedure was the reaction enthalpy ΔH. This parameter can be evaluated considering the Van't Hoff equation, presented in 1.3, that describes how the equilibrium pressure in the plateau region varies with the temperature:

$$\frac{\Delta H}{R_g T} - \frac{\Delta S}{R_g} = \ln \frac{p_{eq}}{p_0} \tag{3.12}$$

Monitoring the internal pressure of the tank in the plateau region at different temperatures allowed to determine both the enthalpy and the entropy of the reaction. The results are shown in Table 3.13. The analysis was conducted monitoring the internal pressure at a maximum temperature of 30 °C and a minimum temperature of 19 °C. The maximum difference between the calculated pressure value using the Van't Hoff equation and the measured one was found to be equal to 2.8%. The Van't Hoff plot determined during the characterization procedure is shown in Figure 3.23.

Table 3.13 Enthalpy and entropy values for the desorption process of the MH tank.

ΔH	≈ 43500 J/mol
ΔS	≈ 160 J/(mol · K)

During the discharge of the tank, its internal pressure and external temperature were monitored. This set-up was adopted during all the performed tests in order to have enough data to complete the tank characterization. The data collected allowed to determine the PCT curves of the tank. Indeed, the parameters of Equation 3.11 were extrapolated. As a consequence, the relationship between pressure, temperature and hydrogen content was obtained. The results are exposed in Figure 3.24. This diagram shows the PCT curves at different temperatures calculated using Equation 3.11. The values of equilibrium pressure during desorption on the plateau of the PCT curves are described in Table 3.14.

The determination of the desorption reaction enthalpy also allowed to evaluate the heat absorbed by the tank during the discharge process. Indeed, it can be calculated

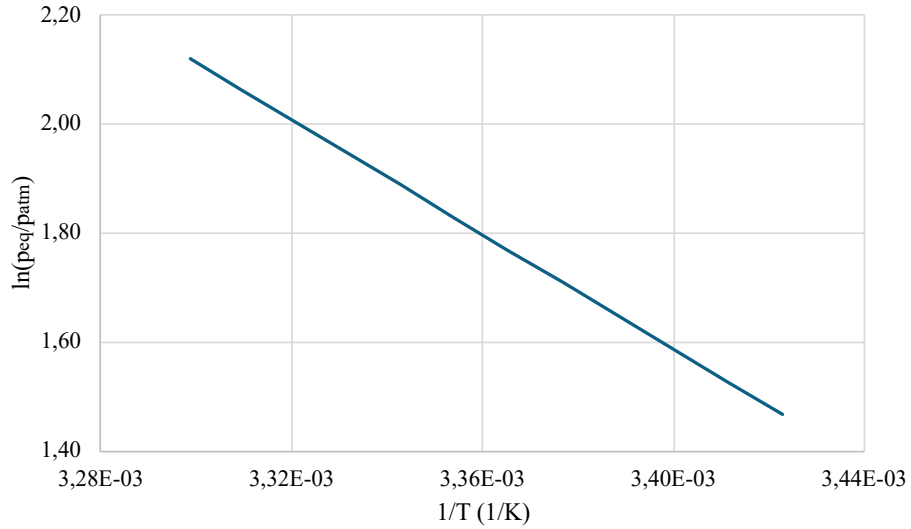

Figure 3.23 Van't Hoff plot for the hydrogen desorption process.

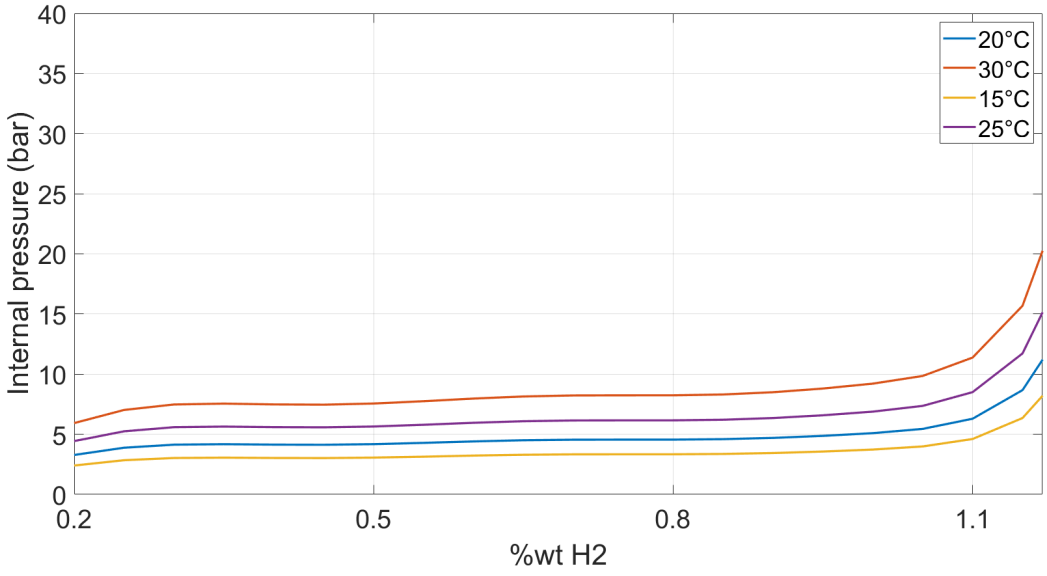

Figure 3.24 PCT curves for the MH tank.

Table 3.14 Tank internal pressure at the curve plateau during discharge at different tank temperatures.

Tank temperature (°C)	Pressure (bar)
30	8 ± 0.3 bar
25	6 ± 0.3 bar
20	4.5 ± 0.3 bar
15	3 ± 0.3 bar

as the product of the H_2 molar flux and the enthalpy. According to this, the heat absorbed by the tank as function of the hydrogen flow is shown in Figure 3.25.

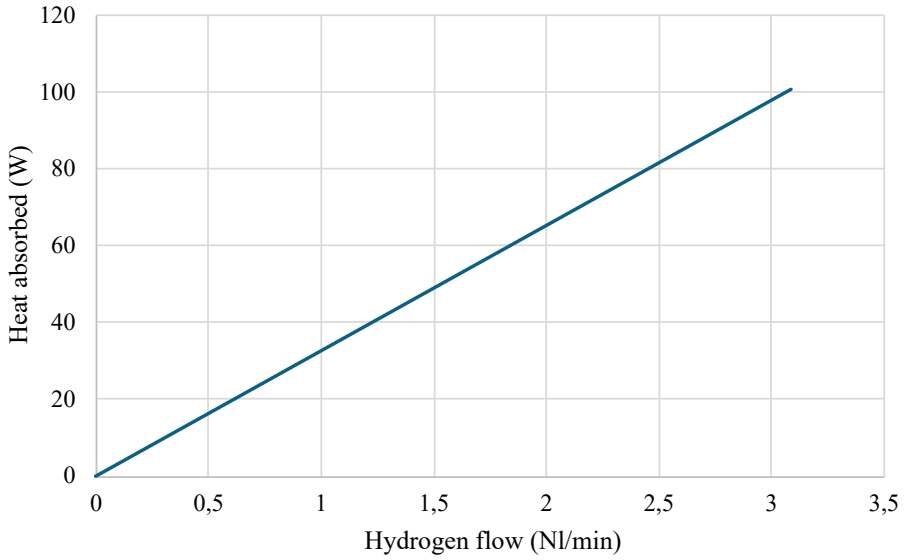

Figure 3.25 Heat absorbed by the tank during the desorption process as function of the hydrogen flow.

It should be noted that, according to the FCS-C300 manufacturer, the hydrogen consumed by the stack is equal to 3.1 Nl/min at 300 W of output power. Thus, considering the stack and the MH system, the heat absorbed by the tank at maximum power is approximately 1/3 of the electrical power delivered by the stack.

3.3.3 Test bench with real fuel cell system

Once completed the characterization procedure, the fuel cell system and the MH tank were implemented in the test bench replacing the power supply that, in the previous configuration, emulated the stack. The test bench configuration that was chosen corresponded to the FC + batt configuration, thus the experimental layout comprised two 12 V lead-acid batteries connected in series, the unidirectional DC-DC buck converter and the load unit, composed of an electronic load and a power supply. The schematic representation of the layout is shown in Figure 3.26.

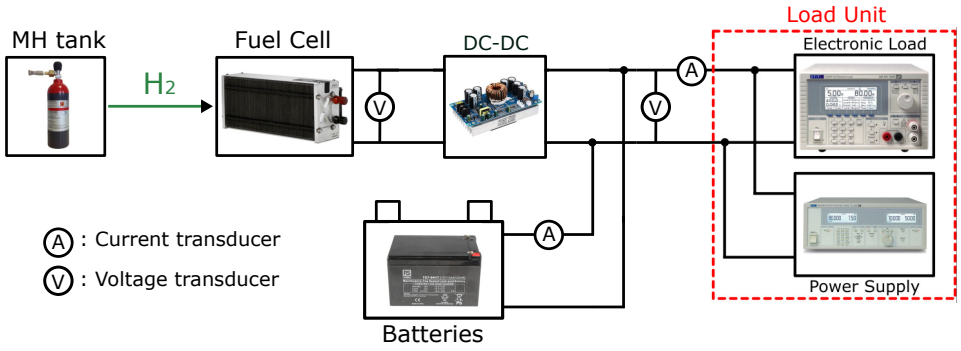

Figure 3.26 Schematic layout of the test bench configuration with fuel cell and MH tank implementation.

To test the behavior of the hybrid system, the Dynamic Stress Test (DST) profile, which is a power profile widely adopted for batteries testing [135], was selected. This profile is characterized by a 360 s sequence of power steps with seven discrete power levels. This profile was chosen as it considers both discharge and charge phases, with a peak of 100% of the nominal power in discharge and 40% in charge [136], so it can provide relevant information when testing power systems. The DST power profile is shown in Figure 3.27. Since the maximum power that the hybrid system must be able to deliver is equal to 330 W, the 100% in discharge corresponded to that value. In this case the additional power required by the FC BoP was not considered when controlling the load unit, indeed the auxiliaries of the FC system were powered using a DC-DC converter with a 12 V output connected to the bus DC, thus their power absorption was already considered without the need of adding it to the load power. Lastly, the maximum regenerative power during the charge phase was equal to approximately 130 W. As for the system control strategy, the power

follower algorithm with PI controller was adopted. The results of the DST test are shown in Figure 3.28.

Analyzing the results, it emerged that the hybrid system was able to complete the test. Furthermore, the effects of the SCU function of the FCS-C300 were noticeable. Indeed, approximately every 10 s the output of the stack became zero for 100 ms. Nevertheless, the test showed that this behavior did not affect negatively the system. In conclusion, the test with the real fuel cell system validated the HIL test bench configuration and, furthermore, allowed to develop a scaled fuel cell hybrid system.

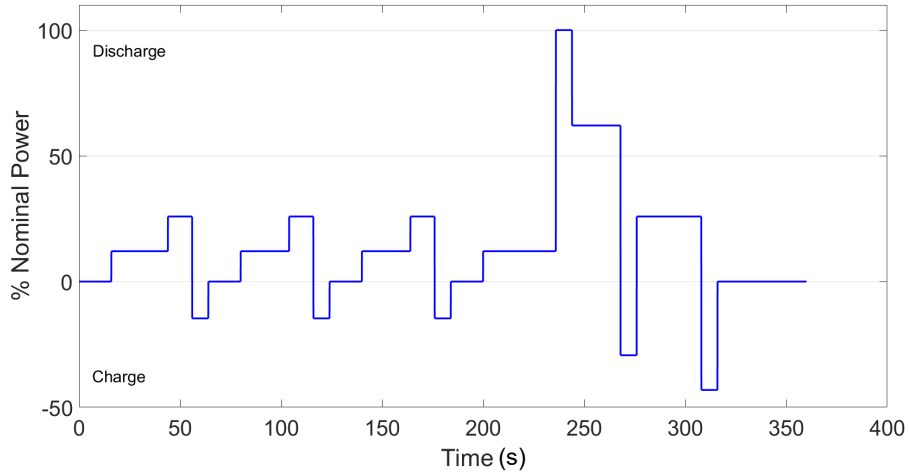

Figure 3.27 DST power profile.

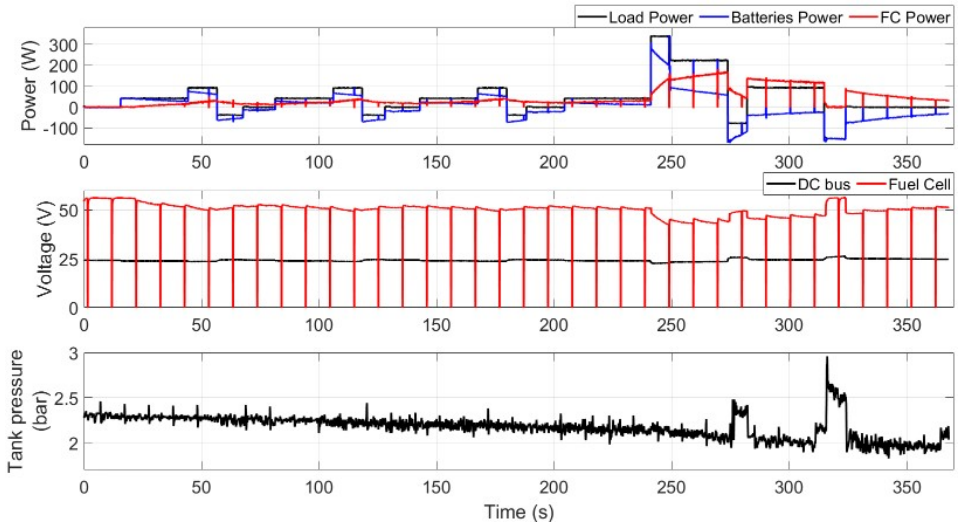

Figure 3.28 DST results.

3.3.4 Limitations

The implementation of a real fuel cell system in the scaled test bench can be a useful tool to perform analysis regarding high-power not-scaled configuration. Indeed, it can be used to develop optimized control strategies, analyze thermal coupling solution between the FC system and the MH tank, and evaluate the efficiency and hydrogen consumption of the hybrid system. Despite this, there are some limitations that need to be acknowledged.

Firstly, the power required by the BoP of a low-power open cathode stack differs significantly from that of a high-power stack. Indeed, the FCS-C300 is equipped with blowers to adduct oxygen and cool the stack at the same time, while a high-power system features the presence of a liquid cooling system and of an air compressor for the air adduction system. Consequently, the relation between power output and BoP power absorption is significantly different for the two systems.

Another difference is related to the dynamic response of the air compressor. An open cathode fuel cell system is able to manage abrupt changes in its power output since the blowers do not have problems in providing enough air at the cathode. On the contrary, for high-power systems with an air compressor the dynamic response of this component is critical in case of high variations of the stack output.

Thus, when scaling the fuel cell system to a low-power configuration, these aspects must be taken into account, otherwise the results of the analysis might be misleading. Possible solutions to compensate for these limitations could be: including the BoP power absorption in the load unit power demand using models to estimate it (for instance, a numerical model of the air compressor), and limiting the maximum change rate in the FC power output, so that it is compliant with the dynamic behavior of the BoP.

3.4 Conclusions

In this chapter, a scaled HIL test bench was developed to test different fuel cell powertrain configurations. The experimental set-up comprised the power units, the power electronics, a control unit and a load unit capable of emulating the power flow of the electric motor and the auxiliaries. According to literature, the HIL test bench was developed at power level.

In the first set-up, the fuel cell system was emulated using a programmable power supply that was controlled to reproduce the polarization curve of a real stack. Given the case study of a compact orchard tractor, the HIL test bench was used to test different powertrain configuration, featuring the presence of a battery pack, supercapacitors, or both, and different control strategies. In the proposed analysis, power follower and fuzzy logic strategies were developed. The different configurations and controllers were compared in terms of durability and fuel economy. Durability was evaluated using aging models available in literature, while fuel consumption was estimated. The load profiles were derived from data collected during monitoring campaigns and comprised a wide variety of tasks, including field operations with attached implements and road transportation.

The results showed that the configuration that exhibited the highest durability was the fuel cell + battery with the power follower controller. The most critical component was the fuel cell system in almost all the considered scenarios. It was also noted that the expected lifetime was significantly related to the control strategy and the configuration, with huge differences among the cases. In contrast, no relevant differences were noted in terms of fuel economy, even if the configuration fuel cell + supercapacitors seemed to be slightly better.

Lastly, a real fuel cell system with a metal hydride tank for hydrogen storage was implemented to replace the programmable power supply for FC emulation. Before implementation, experimental tests were carried out to characterize the FC system in terms of actual polarization curve and auxiliaries power absorptions, and the MH tank in terms of thermodynamic behavior and PCT curves. The characterization procedure allowed to determine the main properties and parameters of the components. Finally, a test with the real FC system in the configuration fuel cell + battery was performed. The results showed that the proposed HIL layout was capable of reproducing the behavior of a hybrid fuel cell powertrain system.

Chapter 4

Development of a hybrid fuel cell powertrain for an agricultural rover

Agricultural activities involve a wide variety of tasks that must be performed. These tasks can vary significantly in terms of power required, since different tools and implements may be used. In some cases, the traditional machinery is excessively oversized and operates far from the optimal efficiency point. To further reduce the environmental footprint and optimize field operations, low-power tasks can be delegated to smaller vehicles, rather than using the traditional oversized vehicle. In this context, autonomous driving rovers are interesting candidates to replace traditional machinery in those tasks were precision and/or autonomy are required. The direct consequences are improved efficiency and productivity, with reduced environmental impact. However, agricultural rovers are usually powered using a pure battery powertrain, thus endurance is critical and may affect the performance in the long term. The introduction of a hydrogen system that can extend the autonomy is, consequently, of particular interest.

Given these premises, in this chapter the design and development of a fuel cell hybrid powertrain for an autonomous driving agricultural rover, specifically designed for orchards and vineyards, is presented. The development of the system involved different steps, including:

- Co-simulation analysis to perform a preliminary numerical analysis.
- Development of a non-scaled test bench to validate the physical hardware.

- Implementation of the hybrid system on a prototype and experimental testing of the vehicle.

In the first step, a co-simulation model was develop to virtually test the behavior of the fuel cell powertrain and its control strategy according to typical work scenarios of the vehicle under investigation.

In the second step, a non-scaled test bench of the powertrain system was developed using a similar approach adopted in the previous chapter. Into details, the test bench comprised all the powertrain elements apart from the electric motors, which were emulated using a load unit. The test bench was used to validate the hardware before implementing it in the vehicle prototype.

Lastly, once the configuration, hardware, and control algorithm were validated, the fuel cell hybrid system was implemented in the rover prototype. The vehicle was then subjected to experimental tests to collect data and evaluate the behavior of the entire system.

4.1 Autonomous driving agricultural rovers

A promising solution to improve sustainability, food security, farm profitability, and reduce the use of fertilizers and pesticides is represented by the implementation of precision agriculture and smart farming practices [137]. The main goals of these practices are:

- **Resource optimization**: reducing the use of resources (such as water and energy), fertilizers, and pesticides.
- **Yield improvement**: increasing crop production by supporting the decision making process through collection of field data.
- **Sustainability**: reducing the environmental footprint of agricultural practices.
- **Cost reduction and profitability**: reducing the operational cost by increasing efficiency of farming activities.

In this context, the adoption of automation technologies in agriculture can be a strong ally to boost the diffusion of precision agriculture. Into detail, in the

last years agricultural robots have gained attention as their large-scale use can reduce the environmental footprint, improve profitability, limit soil compaction by lightweighting, reduce farm waste, and they do not require the presence of a human [138]. However, to achieve complete automation, an autonomous driving algorithm must be developed and implemented.

Modern agricultural robots are able to perform a wide variety of tasks including crop health monitoring, pest and disease detection, low-power field operations [139]. As a consequence, several rovers prototypes have been presented throughout the years by different manufacturers, and a certain number are, at present, commercially available, indicating that they can reach market competitiveness and be profitable products.

4.1.1 Agricultural rovers classification

Agricultural rovers can be classified based on different criteria. The classification proposed in [140] considers the following elements:

- Dimension.
- Type of traction and structure.
- Purpose.

Regarding dimension, they can be classified considering their overall volume: $< 1\ m^3$ small, $1 <= m^3$ and $< 10\ m^3$ medium, $>= 10\ m^3$ large. According to [140] there is a prevalence of medium and large rovers. This can be related to the fact that, according to the Food and Agriculture Organization of the United Nations (FAO), among the most widespread crops in the world there are sugar beets, corn, and wheat [141], which are crops that require open field cultivation and medium or high-power operations. The dimension of the rover, indeed, is directly linked to its capabilities. Small rovers generally perform only crop monitoring tasks or low-power operations, while larger ones can also perform more energy-consuming field tasks. An example of a small robot is the Burro rover [142], developed by the Burro company, which is a robot designed to operate in vineyards and orchards. This rover is powered with four right angle drive brushed motors, with a total peak power of 3.88 kW, has a 2.4 kWh battery with a rated voltage of 24 V, and has an overall volume of 138.2x92.1x72.64

cm. Instead, an example of a large rover is represented by AgBot 5.115T2, developed by Agxeed. This robot is powered by a 115 kW 4.1L 4-stroke diesel Engine, features the presence of a three-point linkage on both front and rear, weights up to 7800 kg and has a maximum overall volume that can reach 385.5x307.5x200 cm [143].

As for the type of traction and structure, two main categories can be defined, namely wheeled and tracked rovers. In case of tracked vehicles, the steering is generally performed by applying more or less drive torque to one side of the vehicle with respect to the other, thus achieving different speeds for right and left tracks. An example of a tracked rover is the aforementioned AgBot 5.115T2. In case of wheeled rovers, a further classification can be defined based on the configuration. In this case, the most common solutions are the following:

- Four fixed wheels.
- Four pivoting wheels.
- Two fixed and two pivoting wheels.
- Two fixed and two steering wheels.
- Four fixed wheels and steering frame.

A fixed wheel means that it only has the degree of freedom corresponding to rotational motion around its hub axis. In contrast, a pivoting wheel possesses an additional degree of freedom: a rotational motion about the vertical axis, which is perpendicular to the hub axis. A pivoting wheel can be motorized to actively control this additional degree of freedom. Lastly, a steering wheel has two degrees of freedom, similar to a pivoting wheel: a rotational motion around the wheel hub and a rotational motion around the vertical axis. While pivoting wheels may also be equipped with motors to manage their vertical-axis rotation, the steering wheel differs in that this motion is integrated into the steering system, enabling coordinated and precise trajectory control.

Examples of wheeled agricultural rovers are: the TED robot, developed by Naio Technologies Inc., which features four pivoting wheels [144]; the Prosp rover, manufactured by Robotics Plus, which is equipped with two fixed wheels and two motorized pivoting wheels [145]; the Indigo rover, manufactured by SwarmFarm Robotics, which features four fixed wheels and a steering frame [146]. An example

of an autonomous driving vehicle with two fixed and two steering wheels is the MK-V tractor, manufactured by Monarch [147]. Lastly, an example of a rover with four fixed wheels is represented by the previously mentioned Burro. According to [140], for small rovers, the most adopted solution is represented by four fixed wheels, while for medium and large vehicles solutions with pivoting wheels are preferred. Overall, wheels are more adopted than tracks, specially in case of small robots.

Lastly, agricultural robots can be classified based on their purpose. Different task can be accomplished by these vehicles, including monitoring, transport, field operations using attached implements or specific tools directly mounted on the robot. Into details, rovers can be single-purpose or multi-purpose. An example of a single purpose robot is the prototype presented in [148], where the authors developed a wheat precision seeding robot. On the contrary, an example of a multi-purpose rover is the IC20, manufactured by AutoAgri [149], which is an autonomous robot designed as a flexible multi-implement carrier. According to the analysis presented in [140], the majority of rovers is multi-purpose. Furthermore, it was noted that single-purpose rovers are, in most cases, small robots, while in case of large ones most of them are multi-purpose.

4.1.2 Case study: Ecothea Smilla agricultural rover

The agricultural rover considered for the implementation of the hybrid fuel cell propulsion system is the Smilla prototype, developed by the Italian company Ecothea Srl in collaboration with the Department of Mechanical and Aerospace Engineering (DIMEAS) of the Politecnico di Torino. This prototype was specifically designed to operate in orchards and vineyards using an autonomous driving algorithm.

According to the three aforementioned classification factors, the first prototype of Smilla was a multi-purpose medium-size rover with four fixed wheels. Since there was no physical steering, torque vectoring technique was used to perform turns and maneuvers. The powertrain consisted of four permanent magnet synchronous motors, each one mechanically linked using a right-angle planetary gear reducer with its corresponding wheel. The transmission ratio of the gear reduced was 12:1. Each motor had a rated power of 1.2 kW, could provide 5 Nm of continuous torque and up to 15 Nm of peak torque (service S3-20%). The main properties of the Smilla prototype are reported in Table 4.1.

Table 4.1 Rover main properties; the EM properties refer to the performance of a single unit.

Parameter	Value
Rover Track	1 m
Height	0.9 m
Length	1.9 m
Rover wheelbase	1.45 m
Wheel radius	0.2 m
Vehicle mass	396 kg
EM rated power	1.2 kW
EM rated torque	5 Nm
EM max torque	15 Nm (S3-20%)
Gearbox transmission ratio	12:1

The first prototype of this rover was powered using a Li-ion battery pack composed of 16 LiFePO4 cells connected in series. The rated capacity of each cell was 105 Ah. The battery pack featured the presence of a battery management system with active cell balancing. The main properties of the battery pack are summarized in Table 4.2. The rated energy capacity was equal to approximately 5.4 kWh. A scheme of the powertrain is represented in Figure 4.1. The on-board systems were powered using a DC-DC, with a rated output voltage of 12 V, connected to the battery pack.

Table 4.2 Battery pack main properties.

Parameter	Value
Cells chemistry	LiFePO4
Configuration	16s1p
Rated voltage	51.2 V (3.2 V per cell)
Rated capacity	105 Ah
Maximum current	150 A
Cell balancing	Active 0.6 A
Overall dimensions	461x402x241 mm

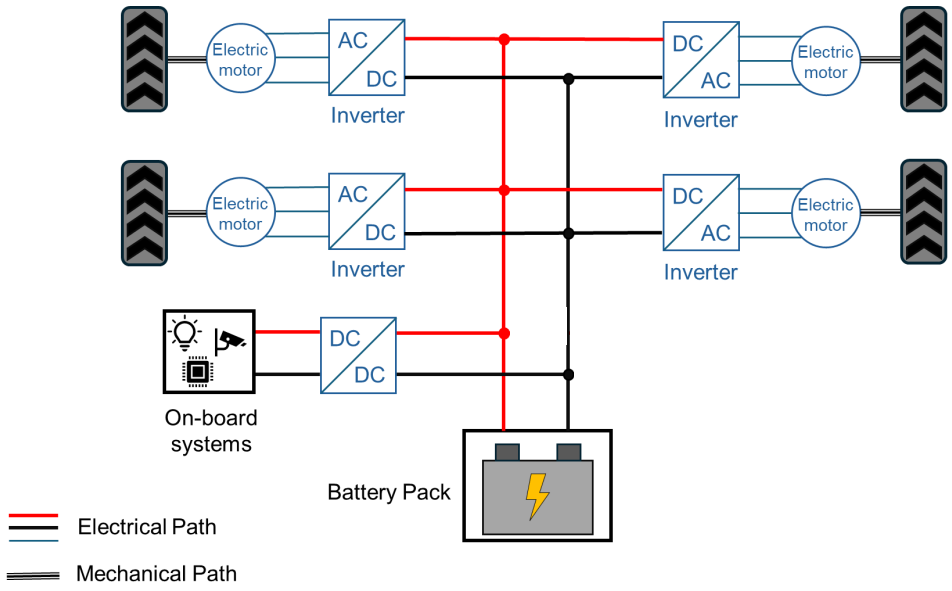

Figure 4.1 Smilla powertrain schematic representation.

The main frame of the rover was made using welded square tubular profiles, forming a rectangular structure. To this structure, a section that formed a cradle was bolted to the main frame. The battery pack was placed inside this cradle. The planetary gear reducers were housed in a special housing connected to the main frame through bolts. Lastly, the rover presented a front structure,specifically designed for the implementation of sensors and cameras, and an openable rear platform designed for transportation tasks. A picture of the Smilla prototype is shown in Figure 4.2.

Figure 4.2 Smilla prototype.

4.1.3 Fuel cell implementation: Smilla H2

Being the LiFePO4 battery pack the only on-board energy storage system, endurance could be a matter of concern. Given this, the idea behind the fuel cell hybrid powertrain configuration was to add a unit that was capable of extending the operating time. According to this, the proposed configuration consisted of adding to the existing powertrain a fuel cell range extender unit, comprising the FCS-C300 and MyH2 900 metal hydride tank. In fact, this solution is characterised by an easy implementation that does not require any particular modification to the main frame of the rover because of the compactness of the fuel cell and the MH tank. The unit is housed in the cradle near to the battery pack. The properties of the FC system and the MH tank were already described in Tables 3.11 and 3.12. Considering the hydrogen capacity of the tank and the fuel cell system efficiency, the range extender unit is expected to extend endurance of +25%. The innovative powertrain configuration with the implementation of the fuel cell range extender unit (FCREU) is shown in Figure 4.3. The FC controller is included in the "On-board system" block.

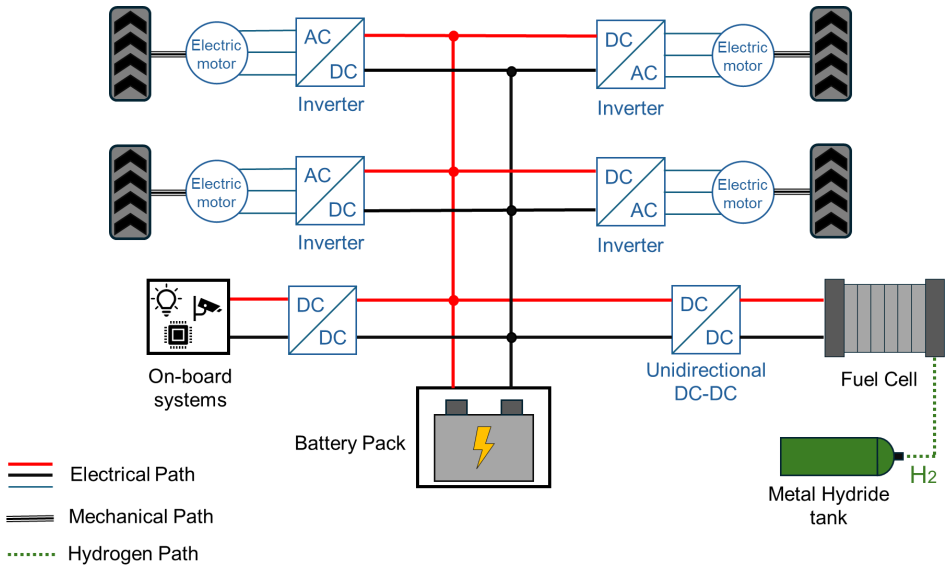

Figure 4.3 Smilla H2 powertrain configuration.

To allow the rover to operate almost continuously, a tank swap technique can be used. Indeed, once, turned off the FC, the empty tank can be easily disconnected thanks to its Swagelok connector and substituted with a full one. Furthermore, hydrogen can be produced from water using an electrolyser powered with electricity.

Therefore, implementing an electrolyser unit connected to a photovoltaic system, a farm will be able to produce autonomously hydrogen with almost zero associated emissions and, excluding the initial investment, also zero associated costs.

4.2 Smilla H2 co-simulation analysis

Co-simulation is a simulation technique that enables multiple models or tools, often representing different physical domains and using different solvers, to run together while exchanging information during the simulation. By synchronizing their execution, co-simulation makes it possible to combine specialized subsystems within a unified framework, improving the fidelity of complex multi-domain system analysis.

The co-simulation model developed for Smilla H2 consisted of a multibody model, developed in Hexagon Adams, used to simulate the dynamic behavior of the vehicle and of a Matlab/Simulink model, used to simulate the powertrain and the control unit. Once developed the models and their interface, virtual test scenarios considering typical maneuvers and working conditions are introduced. Finally, the simulation results are presented and discussed.

4.2.1 Multibody Model

The multibody model was developed to properly simulate the dynamic behavior of the vehicle. Considering the rover' structure, two main elements were considered: the body, including the main frame and housings for the battery pack, FCREU, motors and planetary reducers, and the wheels. The multibody model was developed as a series of rigid bodies with specific geometrical and inertial properties, connected to each other using different joints. Into detail, the body was modeled combining different geometric solids to obtain the rover geometry, while the wheels were modeled as simple cylindrical bodies. The wheels were linked to the body using revolute joints, permitting their rotational motion only around the hub axis. To account for the torque delivered by the motors, a torque element was applied to each wheel. It should be noted that the torque element considered the torque downstream the planetary gear reducer. The mass and inertial properties of the multibody

elements are reported in Table 4.3. Figure 4.4 shows a visualization of the multibody model.

Table 4.3 Multibody model inertial and barycentric properties

Parameter	Rover Body	Wheel
Mass	365 kg	7.75 kg
Moment of Inertia I_{xx}	94.6 kgm^2	0.17 kgm^2
Moment of Inertia I_{yy}	77.0 kgm^2	0.11 kgm^2
Moment of Inertia I_{zz}	31.4 kgm^2	0.11 kgm^2

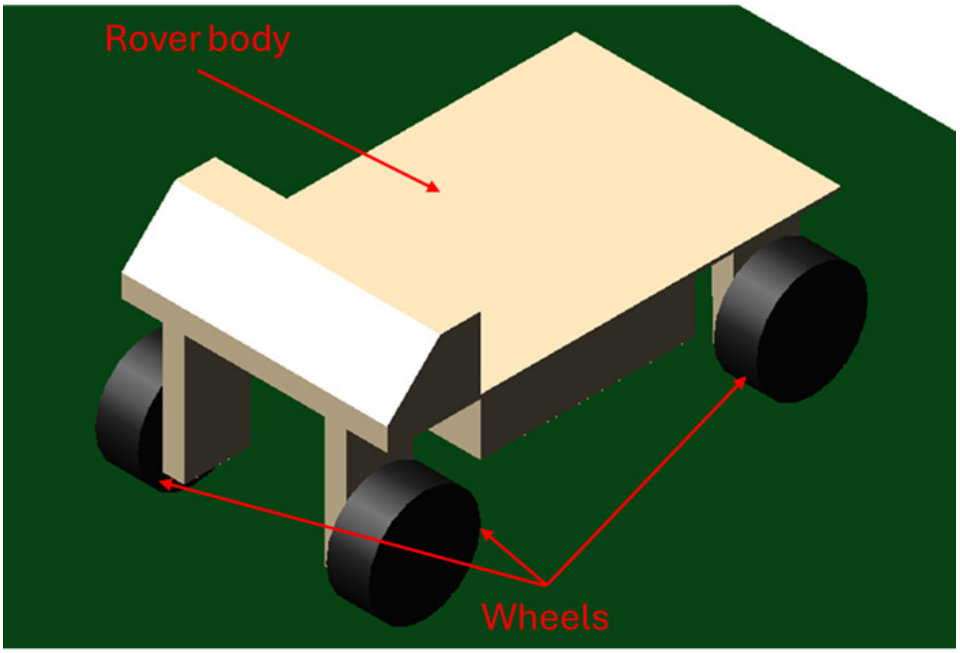

Figure 4.4 Smilla multibody model.

Lastly, the interaction between the wheels and the ground had to be modeled. To address this, contact forces were introduced. Starting from the normal contact force, it should consider the deformability of the ground [150]. Consequently, the following equation was adopted:

$$F_{contact,norm} = k \cdot p^e + c \cdot \frac{dp}{dt} \tag{4.1}$$

Where k and c represent the contact stiffness and damping, p is the ground-wheel interpenetration, and e is an empirical exponent that accounts for the system non-linearity. The parameters of this equation were defined considering data available in literature. Table 4.4 shows the values adopted for the numerical simulations.

Starting from the stiffness *k*, its value depends on several factors, including wheel pressure, vehicle speed, tire wear, and so on [151, 152]. In the model a value of 300000 N/m was adopted, which is consistent with the typical values obtained in compression tests on agricultural tires [153].

As for the damping coefficient *c*, according to [154] the damping coefficient of an agricultural tire with a radius of 0.406 m and a pressure of 2.2 bar was equal to 700 Ns/m. In addition to that, it can be stated that the damping coefficient generally decreases with the tire size, thus, since Smilla wheels have a pressure of 2.2 bar and a radius of 0.2 m, it is assumed that the damping coefficient was less than 700 Ns/m. Since no other data were available, it was chosen to perform simulations considering different values of c, namely 0, 100, 300, and 500 Ns/m.

Lastly, it was assumed that the maximum interpenetration between the ground and the wheel was equal to 0.01 m.

Table 4.4 Normal contact force parameters.

Parameter	**Value**
k	300000 N/m
c	0-500 Ns/m
e	2
p_{max}	0.01 m

The next step to model the tire-ground interaction regards the capability of the wheel to transmit traction force to the ground. To model this aspect, friction coefficients were implemented. Into detail, three coefficients were defined: the static friction, the kinetic friction and the rolling resistance coefficients.

The static friction coefficient was used to evaluate the maximum torque at which the tire began to slip, while the kinetic friction determined the maximum torque the tire was capable of transmitting once it began to slip. According to this, the

following relationship was used to evaluate the traction force developed by a single wheel [155]:

$$F_{\text{trac},i} = \begin{cases} \dfrac{T_{\text{wheel},i}}{R_{\text{wheel}}}, & \text{if } \dfrac{T_{\text{wheel},i}}{R_{\text{wheel}}} \leq \mu_{\text{static}} \cdot F_{\text{norm},i}, \\ \mu_{\text{kinetic}} \cdot F_{\text{norm},i}, & \text{if } \dfrac{T_{\text{wheel},i}}{R_{\text{wheel}}} > \mu_{\text{static}} \cdot F_{\text{norm},i}. \end{cases} \tag{4.2}$$

Where $F_{trac,i}$ and $F_{norm,i}$ are, respectively, the traction and normal forces on the i-wheel, $T_{wheel,i}$ is the torque at the i-wheel, R_{wheel} is the wheel radius, μ_{static} and $\mu_{kinetic}$ are, respectively, the static and kinetic friction coefficients. This modeling approach was already used in Section 2.3.

Lastly, the rolling resistance coefficient was used to evaluate the force resisting the motion when the wheel rolled on the ground. This force is mainly caused by the asymmetrical pressure distribution in the contact zone, which generates a vertical force that causes a resistance torque. To account for this resistance to the motion, the following equation was used:

$$F_{roll} = m_{rover} \cdot g \cdot \mu_{roll} \cdot cos\alpha \tag{4.3}$$

Where F_{roll} is the resistance force generated due to rolling resistance, m_{rover} is the rover total mass, g is the acceleration of gravity, and α is the road slope.

The static friction, kinetic friction, and rolling resistance coefficients strongly depend on the ground conditions. During the simulations, several different soils were considered, thus these coefficients were not constant.

Lastly, the resistive force due to the road slope was evaluated according to:

$$F_{slope} = m_{rover} \cdot g \cdot sen\alpha \tag{4.4}$$

In the co-simulation structure, the multibody model exchanged information with the Simulink model. Into details, at each time step the multibody received from Simulink the EMs torque values, then calculated the wheels and rover speeds, and the rover actual position and orientation.

4.2.2 Simulink model

The Simulink model had to simulate the control unit and the powertrain components. When considering the control unit, since the Smilla prototype was an autonomous driving rover, the autonomous driving algorithm had to be included.

Autonomous driving algorithm

The autonomous driving strategy consisted mainly of three elements: the path planning algorithm, the path following algorithm, and the kinematic model.

The path planning algorithm had to define the ideal trajectory the rover should follow to complete the pre-defined task [156]. The adopted methos was based on Dubins geometrical planner [157], according to which the ideal trajectory was defined combining segments and arcs given the start and finish points and their orientation. The ideal trajectory consisted of a sequence of points called waypoints. In case of Smilla H2 simulations, a 2D map of a typical orchard was built and the ideal trajectory was evaluated offline, thus upstream the co-simulation. Indeed, the waypoints of the ideal trajectory were an input of the simulation.

The path following algorithm instead had to determine the commands so that the rover could follow the ideal trajectory. As a consequence, given a point that had to be reached and the rover current position, this algorithm had to determine how to reach it. Into details, it consisted of two phases: the local goal point definition, and the determination of longitudinal and yaw speeds. The definition of a local goal point was performed using a pure-pursuit based strategy [158], according to which a local goal point was defined by the intersection of the optimal path and a circumference, centered on the rover center of mass, with a radius equal to a parameter defined as look-ahead distance. A waypoint was considered reached when the distance between it and the rover was below a parameter called distance threshold. AT each time step, once evaluated the local goal point, the path following algorithm evaluated the yaw angle ϑ necessary to reach it. This angle corresponded to the difference between the actual vehicle orientation and the direction given by the line linking the rover center of mass and the local goal point. Given the yaw angle, the algorithm evaluated the yaw and longitudinal speeds according to the following equations:

$$\dot{\vartheta} = \frac{\vartheta}{t} \tag{4.5}$$

$$v = v_t \cdot (1 - \frac{\vartheta}{\vartheta_{max}}) \tag{4.6}$$

Where $\dot{\vartheta}$ and v represent the yaw and longitudinal speeds respectively, t the cycle time, v_t the maximum reference rover speed, and ϑ_{max} the maximum steering angle (in this case equal to 360° as the rover could perform a pivot maneuver).

The last stage of the autonomous driving strategy was represented by the kinematic model. This model substantially linked the reference yaw and longitudinal speeds with the rover configuration. Since Smilla H2 was equipped with four fixed wheels, each one with a dedicated motor, this model, given the yaw and longitudinal reference speeds, evaluated the four wheels reference speeds to obtain them. For simplicity, the calculated reference speeds for wheels on the same side were equal. Thus, the reference speeds for the front and rear right wheels were the same, and so were those for the front and rear left wheels. Into details, the following equations were used:

$$\omega_l = \frac{v}{r} - \dot{\vartheta} \cdot \frac{l}{r} \tag{4.7}$$

$$\omega_r = \frac{v}{r} + \dot{\vartheta} \cdot \frac{l}{r} \tag{4.8}$$

Where ω_l and ω_r were, respectively, the reference rotational speeds of left and right wheels, r the wheel radius, l halftrack of the rover, v and $\dot{\vartheta}$ the longitudinal and yaw reference speeds obtained using equations 4.5 and 4.6.

Summarizing, the path planning stage determined the ideal trajectory given the orchard configuration and a mission to accomplish. This stage was performed offline and the output, consisting in a series of waypoints, was an initial input of the path following stage, which instead run in real-time during the co-simulation. This stage, indeed, received as inputs the waypoints and the rover actual position and calculated the reference yaw and longitudinal speeds that the rover had to reach in order to follow as close as possible the predefined trajectory. Lastly, the kinematic model received the yaw and longitudinal reference speeds and, given the rover geometry

and configuration, evaluated the reference wheels speeds. Thus, at each time step of the simulation the autonomous driving algorithm calculated the reference wheels speeds.

Once the reference wheels speeds were calculated, the control unit had to evaluate the torque commands for the electric motors. In this regard, a PI controller was implemented. The reference wheels speeds were provided by the autonomous driving algorithm, as previously described in detail, while the actual wheel speeds were evaluated by the multibody model. Based on the difference between the reference and actual values, the torque commands were determined. A dedicated PI controller was adopted for each wheel, however the proportional and integrative coefficients were the same. A calibration procedure was applied to determine these coefficients.

A scheme of the co-simulation structure representing the interaction between the autonomous driving algorithm and the multibody model is shown in Figure 4.5, while the model developed in Simulink is shown in Figure 4.6.

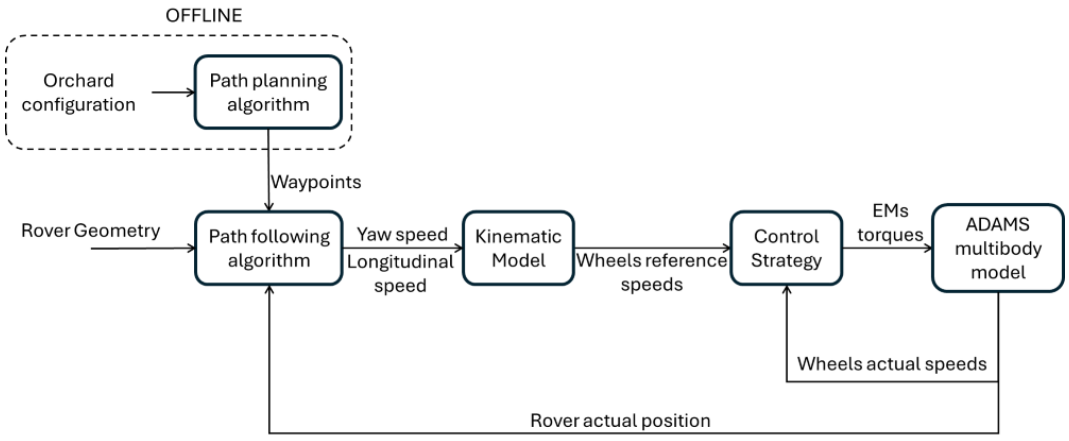

Figure 4.5 Co-simulation model structure for the interaction between the autonomous driving algorithm and the multibody model.

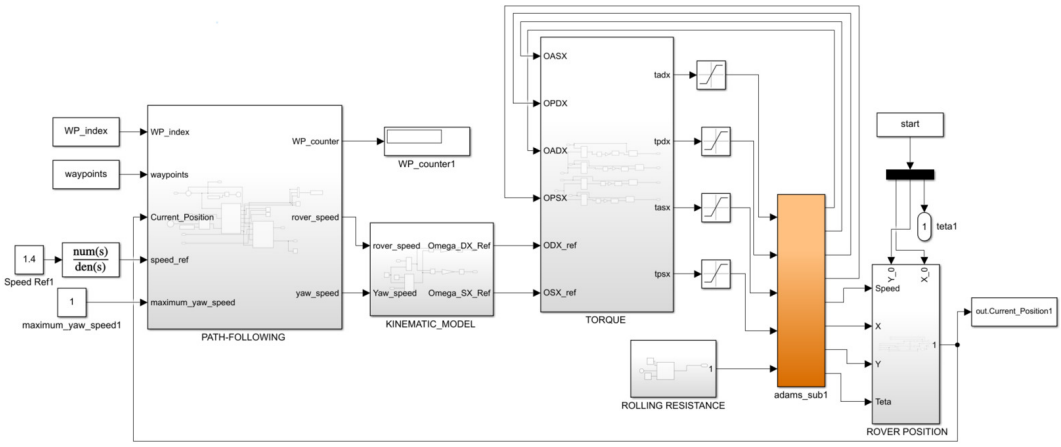

Figure 4.6 Simulink autonomous driving algorithm and interface with the multibody model.

Powertrain model

The numerical modeling of the powertrain was developed in Simulink using a physical network approach, the same used for the fuel cell powered tractor model developed in Section 2.2.

Into details, the model had to simulate the behavior of all the main components of the powertrain. Consequently, it included the following elements:

- Electric Motors and their mechanical coupling with the wheels.
- Battery pack.
- Fuel cell system.
- MH tank.
- Power converters.
- Energy management strategy.

The numerical model is shown in Figure 4.7. The powertrain model received from the autonomous driving algorithm and control unit model the motors torque commands, and from the multibody model the wheels speeds.

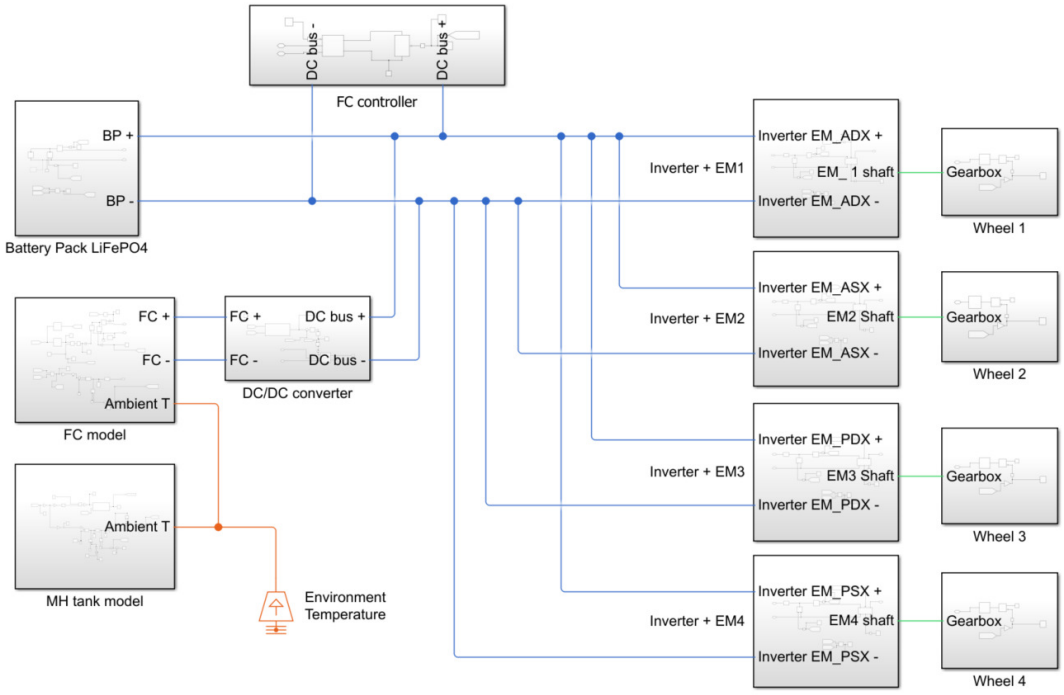

Figure 4.7 Co-simulation model structure for the interaction between the autonomous driving algorithm and the multibody model.

As for the electric motors, they were modelled considering their electric losses as a sum a torque-dependent term and a speed-dependent term. The first accounted for the ohmic losses in the copper windings, while the second considered the iron losses due to eddy currents [69]. Regarding the planetary gear reducers, they were modeled as a fixed-ratio gear with a load dependent efficiency. The efficiency at the nominal output torque was set equal to 90%, according to the datasheet provided by the gearbox manufacturer.

The battery pack was modeled using the equivalent circuit model already presented in Section 2.3 for the tractor battery pack. This model included the ohmic resistance and two polarization processes, activation and concentration. Some parameters of the numerical model, such as the ohmic resistance, were available from the datasheet of the LFP cells used in the real battery pack. Others, such as the open circuit voltage curve as function of the state-of-charge, were extrapolated through experimental tests. Combining parameters from the datasheet and from the experimental tests, a sufficiently detailed model was derived.

As for the fuel cell system, a dedicated numerical model was specifically designed. Into detail, the fuel cell stack was modeled as a voltage source using a lookup table that followed the experimental FCS-C300 polarization curve obtained during the characterization tests described in Section 3.3.2. In addition, the effects of the SCU were included in the model using a timer that, every 10 s, turned off the output for 100 ms. To account for the FC thermal behavior, a model consisting of a controlled heat flow rate source and a convective heat transfer element, was implemented. The heat flow rate source was controlled according to the fuel cell stack efficiency. It should be highlighted that the stack efficiency does not correspond to the fuel cell system efficiency, since the latter includes the effects of the BoP power absorption. Also the parameters of the convective heat transfer element were tuned using experimental data derived form the characterization tests. Lastly, the power absorption FC controller was included in the model, also in this case according to the data collected during the FCS-C300 characterization. Finally, the hydrogen consumption was modeled according to the consumption curve provided by the manufacturer.

Regarding the MH tank, it was modeled according to its PCT curves and its thermal behavior. The internal pressure was evaluated using equation 3.11, whose parameters were experimentally evaluated during the MH tank characterization test. Since this equation is temperature dependent and the desorption process is endothermic, the development of a thermal model was necessary. This model consisted mainly of a of a controlled heat flow rate source, which accounted for the heat absorbed during hydrogen release, a conductive heat transfer element, accounting for the tank wall thickness, and a convective heat transfer element, which considered the heat exchanged with the ambient air. The heat absorbed by tank was evaluated using equation 1.20. As it was done for the FC stack, the parameters of the MH tank thermal model were extrapolated using the experimental data obtained during the characterization test.

As for the power converters, they were modeled considering their efficiency. Into details, the efficiency was modeled as function of the output current. The peak efficiency for all power converters was assumed equal to 95%.

Lastly, the energy management strategy of the FCREU had to be defined. From a system integration point of view, the FCREU was considered as a separated unit that was added to the existing powertrain. Consequently, the control unit that determined

the range extender output was considered integrated within the FCREU and simply controlled the unidirectional DC-DC in terms of voltage and current output. Since the unit operates as a range extender, its output was not load-dependent. Into detail, a current output value, corresponding to the regime output, was defined. This value was then adjusted depending on the battery pack voltage. If the voltage exceeded a maximum threshold value, the FCREU current output was linearly brought to zero to avoid overvoltage. The regime current output value was imposed equal to 6 A, corresponding to a stack power output of 270 W. The battery pack voltage level beyond which the current de-rating was performed was imposed equal to 54 V, corresponding to a cell voltage of 3.38 V. In case of a voltage level higher than 55 V, the current setpoint was imposed 0. To track the current setpoint, a PI controller was adopted. The coefficients were chosen so that the system followed a low-dynamic behavior, in order to enhance the durability of the FC system. Indeed, due to the specific application, there was no need to adopt a reactive control since the fuel cell did not follow the load. It should be noted that, in this case, the PI controller loop was based on the stack current output upstream the DC-DC converter. A schematic representation of the control strategy is shown in Figure 4.8.

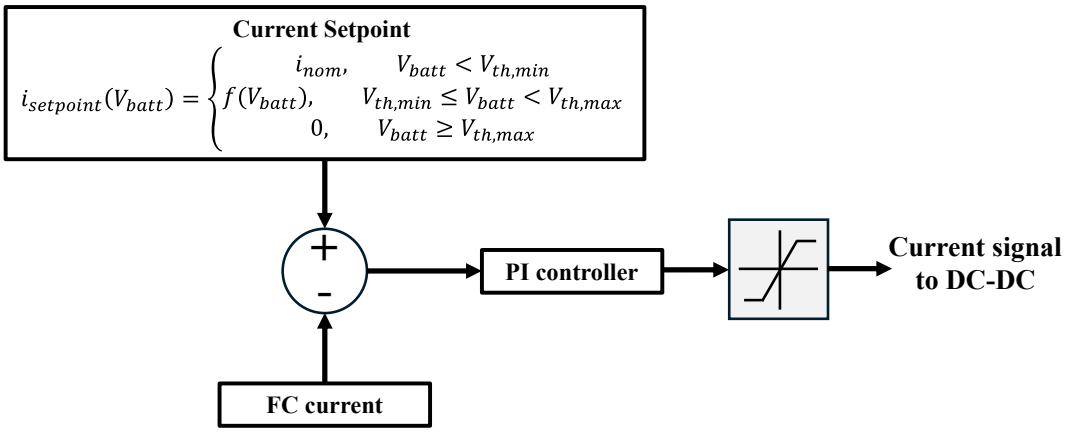

Figure 4.8 Smilla H2 range extender unit control strategy. For the numerical simulations, I_{nom} = 6 A; $V_{th,min}$ = 54 V; $V_{th,max}$ = 55 V.

4.2.3 Virtual Test Scenarios

To perform simulations, virtual test scenarios were defined. Into details, these scenarios consisted of a typical maneuver the rover must be able to perform in different conditions. A bi-dimensional map of an orchard, including equally spaced

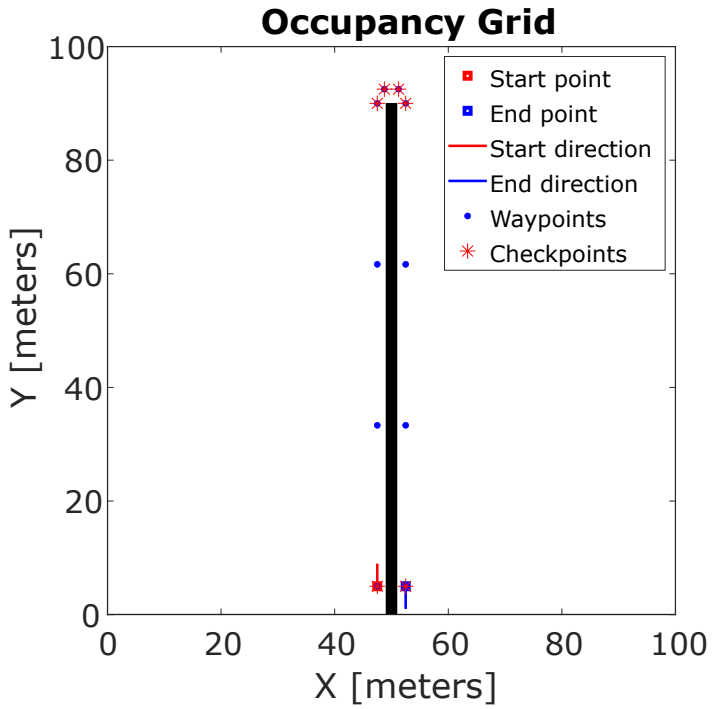

Figure 4.9 Co-simulation proposed maneuver.

fruit rows, was defined. The considered maneuver consisted of the rover moving within two fruit rows and approaching the end of the field, then performing a 180 degree turn to enter the next row. The proposed maneuver is shown in Figure 4.9. The map represents the maneuver performed in an orchard with a row spacing equal to 5 m. The black thick line represent the fruit row.

In order to consider different situations, simulations were performed varying the total rover payload and the soil conditions.

The payload of the rover ranged from 0 to 200 kg with 50 kg steps. Indeed, this rover was designed also for the transportation of materials, thus a numerical analysis of the effect of the payload on the rover performance was deemed of interest.

As for the soil conditions, the following terrains were considered: loam soil, hard soil, sandy soil, and muddy road. All these soils can be encountered by a vehicle for agricultural applications during its operational life.

Loam soil is generally composed with 40% sand, 40% silt, and 20% clay. For agricultural activities, loam is considered optimal for several reasons, including optimal water management, as it drains well enough to avoid excessive water but

is capable of retaining sufficient moisture for plant roots, fertility, it contains more nutrients than other soils, and workability, since it is relatively easy to cultivate being not too hard or too loose. Hard soil instead referred to a compacted and dense soil, difficult to dig or cultivate. However, in some situations an agricultural vehicle may encounter hard soil conditions, for example, when approaching the field the road may be compacted due to frequent vehicle passage. Sandy soil, instead, is mainly composed of large mineral particles, with low proportion of silt and clay. It is usually characterized by a loose structure, with excellent water drainage. However, compared to loam soil, it has a lower capacity in terms of water-holding properties. In agriculture, sandy soil is used for root vegetables, such as carrots and potatoes, and crops like peanuts and strawberries. Lastly, muddy soil conditions can occur in case of heavy rain weather conditions.

From a numerical point of view, different soils imply different tire-ground coefficients. These coefficients were derived from data available in the literature [159–161].

4.2.4 Results

As previously mentioned, the simulations were performed firstly considering loam soil and with different rover payloads: 0, 50, 100 and 200 kg. The coefficient adopted for the rover control were tuned considering the reference case of loam soil and 0 kg of payload. Starting from this case, the results of the simulation in terms of actual trajectory, wheel speeds and EM torques are shown in Figure 4.10.

Analyzing the figure, it can be noted that in the first part of the maneuver the wheel speeds were almost constant. This aspect was related to the fact that the start position was perfectly in line with the first checkpoint, thus, without any soil disturbance of other factors that may affect its trajectory, the rover simply had to move forward. In the second part instead, the rover performed the 180 degrees turn and then moved to the final checkpoint, but it can be noted that the actual trajectory was not perfectly straight. Instead, it slightly oscillated around the ideal one. However, this oscillation was not critical and was deemed acceptable and coherent with a real scenario. The maximum trajectory deviation was found to be equal to 0.44 m and occurred during the last part of the maneuver, thus when oscillating around the ideal trajectory.

As for the powertrain main parameters, the results are shown in Figure 4.11. Analyzing the figure, it can be noted that the range extender unit operated according the the proposed energy management strategy. In terms of temperatures, the regime was not reached due to the limited simulation time, however it was noted that the fuel cell temperature was reaching its plateau, which can be estimated around 45°C. On the contrary, the tank temperature was decreasing according to the thermal behavior of the desorption reaction. Also in this case, the regime condition was not reached. Regarding traction, the peak power delivered by the motors was equal to 2207 W, while the average power during the maneuver was equal to 649 W.

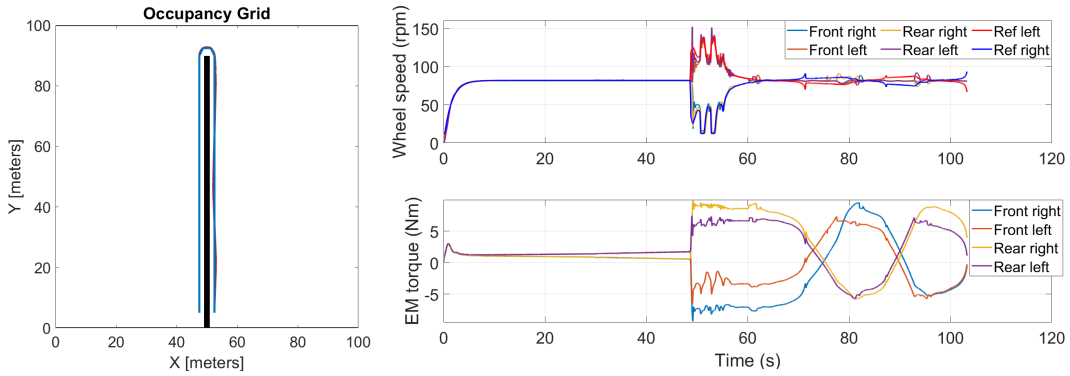

Figure 4.10 Co-simulation results for the reference case: 0 kg of payload and loam soil. Please note that in the left figure, the blue trajectory indicates the ideal one, while the red trajectory the one that the rover actually performed during the simulation.

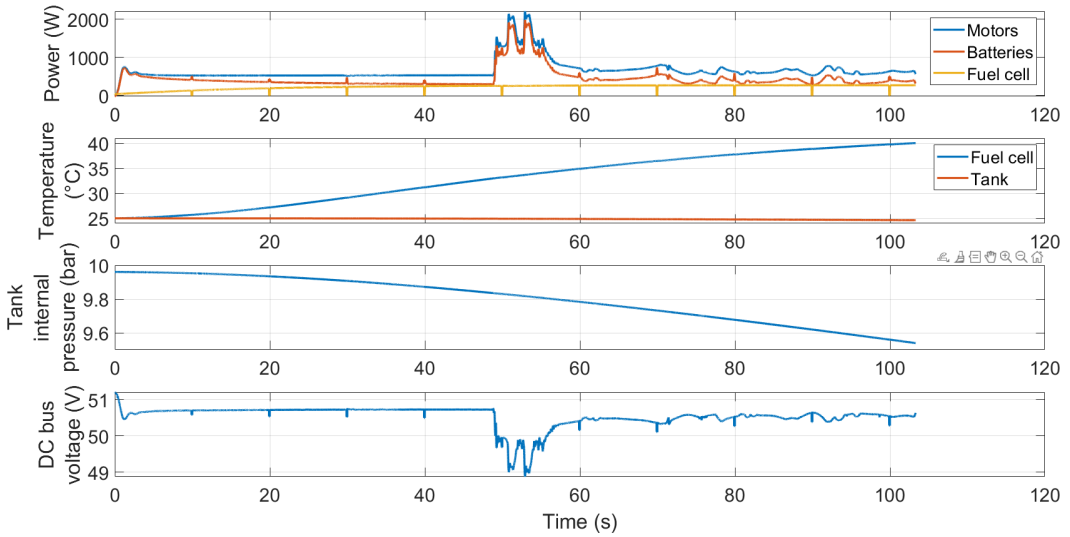

Figure 4.11 Co-simulation results for the powertrain model considering the reference case.

Regarding the influence of the payload on the rover performance, the results for the case with loam soil and 50 kg of payload are shown in Figures 4.12. The rover behavior is similar to the previous case but with more torque required to the motors. The maximum trajectory deviation was found to be equal to 0.48 m, while the average power for traction was equal to 688 W. Considering the cases with 100 and 200 kg, the results are shown in Figures 4.13 and 4.14. The maximum trajectory deviations were 0.66 m and 0.75 m respectively, while the average power for traction was of 713 W and 789 W respectively. In terms of actual performed trajectory, with higher payloads, the maximum trajectory deviation from the ideal one increased. Indeed, in case of 0 kg of payload it was equal to 0.44 m, but reached 0.75 m in case of 200 kg of payload. Regarding the fuel cell range extender unit, its behavior was the same in all the considered cases as it is independent of the payload.

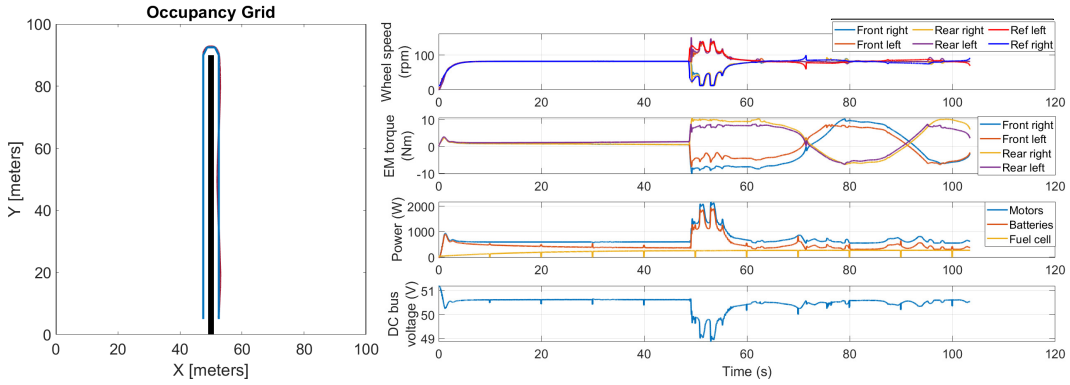

Figure 4.12 Co-simulation results considering loam soil and 50 kg of payload.

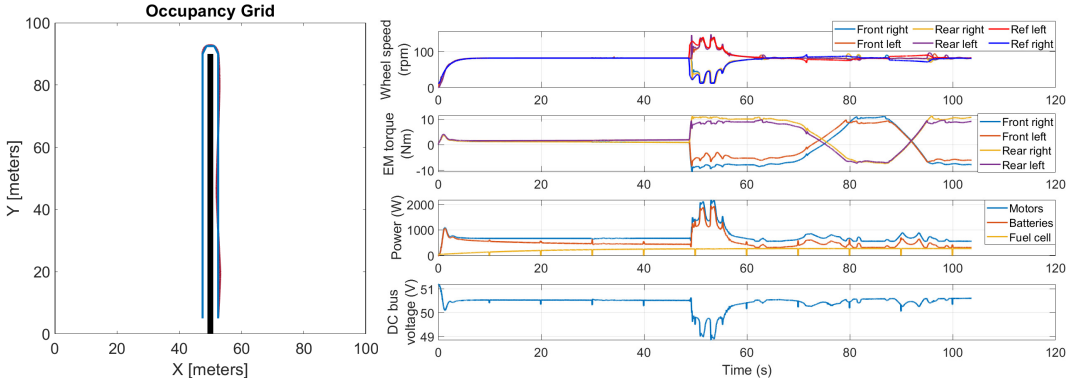

Figure 4.13 Co-simulation results considering loam soil and 100 kg of payload.

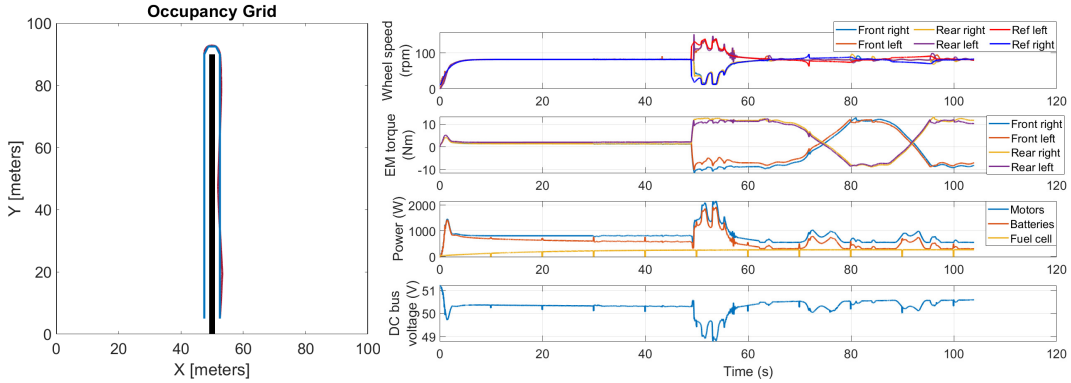

Figure 4.14 Co-simulation results considering loam soil and 200 kg of payload.

If the rover was capable of performing the predefined maneuver with all the considered payloads, the influence of the soil was more critical. Starting from the hard soil, the simulation results are shown in Figure 4.15. The maximum trajectory deviation was equal to 0.61 m, while the average power required for traction was equal to 565 W. Compared to the previous cases, it was noted that it occurred in the last part of the turning maneuver and thus was related to the difficulty in performing the 180° turn.

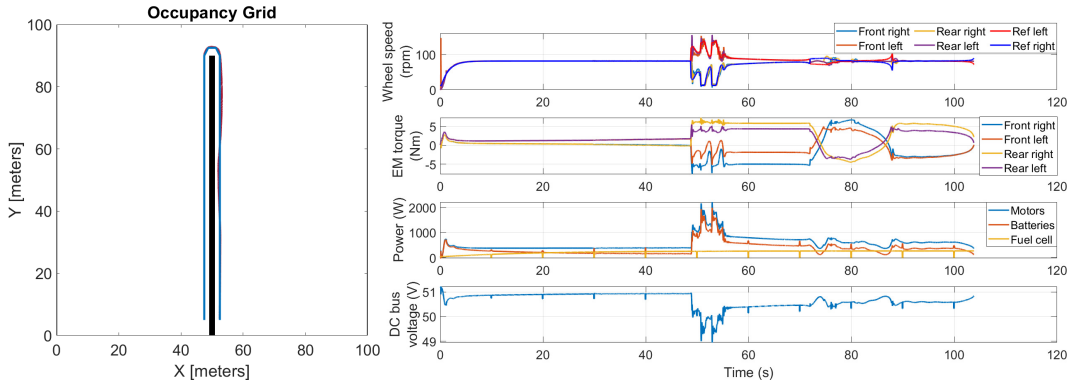

Figure 4.15 Co-simulation results considering hard soil and 0 kg of payload.

On the contrary, considering the cases of sandy and muddy soils, the rover was not capable of completing the task. The results for the sandy soil are shown in Figure 4.16. As it can be noted, the rover was not capable of performing the 180° turn due to under-steering. Similarly, also in case of muddy soil the rover did not manage to perform the turn. Comparing the different soils, the power required to move on a straight line with loam soil was equal to approximately 500 W, while it was a around 400 W for the hard soil, 1200 W for sandy soil and up to 2100 W for muddy soil.

A comparison in terms of trajectory deviation and power required for traction in all the different considered cases is shown in Table 4.5. As it can be noted, the influence of soil conditions on the required traction power is significantly higher than that of the payload. In terms of peak power, it was similar in all the considered scenarios, with the exception of the muddy soil case, in which it was significant higher due to the particularly critical work conditions.

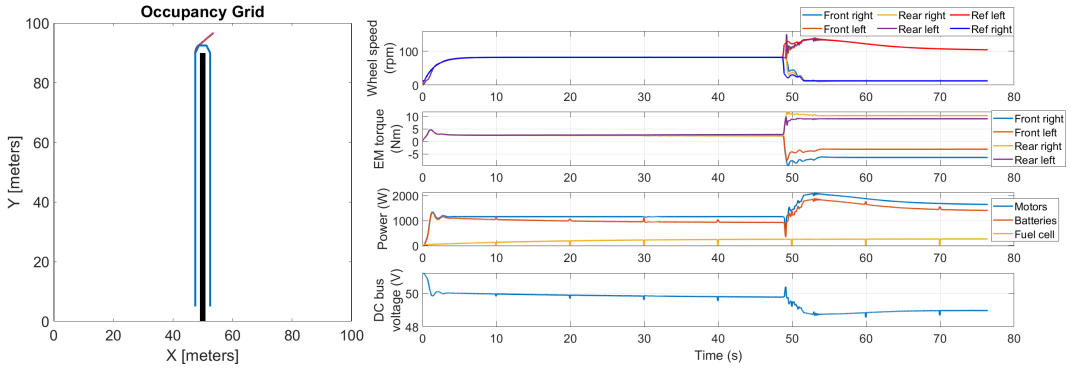

Figure 4.16 Co-simulation results considering sandy soil and 0 kg of payload.

Table 4.5 Comparison among the different cases.

Test scenario	**Trajectory deviation (m)**	**Mean Power (W)**	**Max Power (W)**
Loam, no payload	0.44	649	2251
Loam, 50 kg payload	0.48	688	2291
Loam, 100 kg payload	0.66	713	2216
Loam, 200 kg payload	0.75	789	2201
Hard, no payload	0.61	565	2255
Sandy, no payload	Failed	1327	2165
Muddy, no payload	Failed	2160	5470

4.2.5 Sensitivity analysis on the rover position error

The previously presented results did not consider the effects of possible errors in the rover position. These errors can include a not perfectly aligned initial position, and an error due to the GPS sensor accuracy. According to this, additional simulations

were performed introducing an error in the initial rover position of 20 cm, which was deemed a reasonable value, and the error due to the GPS sensor accuracy of 2 cm. Indeed, at each time step a random error within the accuracy range of the GPS sensor was added to the rover position.

Starting from the reference case of 0 kg of payload with loam soil, the results are shown in Figure 4.17. In this case, it can be noted that also in the first part the rover started oscillating around the ideal trajectory, furthermore it approached the 180° turn without being in the ideal position. Compared to the previous simulation, the maximum trajectory deviation increased up to 0.83 m, while the mean power was of 689 W (+6%).

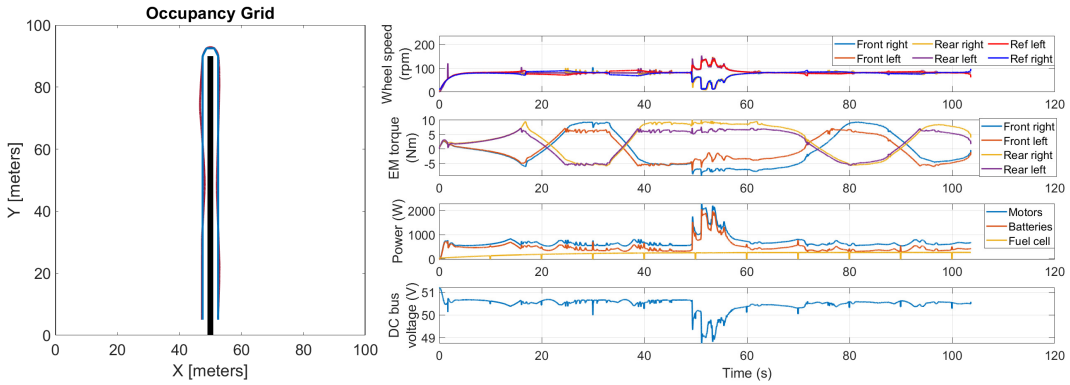

Figure 4.17 Co-simulation results considering loam soil, 0 kg of payload, and errors due to initial position misalignment and GPS sensor accuracy.

Figures 4.18-4.20 show the results for cases with 50 kg, 100 kg, and 200 kg, respectively. For the case with 50 kg, the average and maximum traction powers were 708 W and 2437 W, respectively, while the maximum trajectory deviation was 1 m. For the case with 100 kg of payload, average and maximum traction powers were 732 W and 2370 W, respectively. The maximum trajectory deviation was approximately 1 m. Lastly, for the case with 200 kg of payload, the average and maximum traction powers were 761 W and 2329 W, respectively, while the maximum trajectory deviation was 0.77 m.

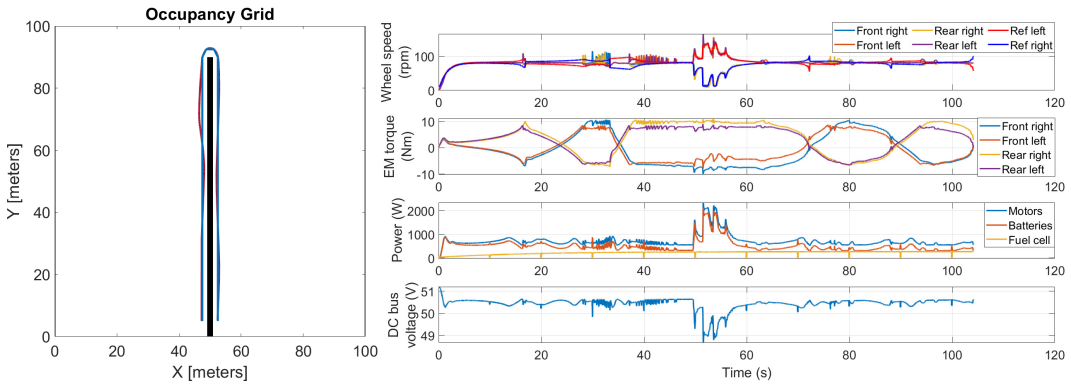

Figure 4.18 Co-simulation results considering loam soil, 50 kg of payload, and errors due to initial position misalignment and GPS sensor accuracy.

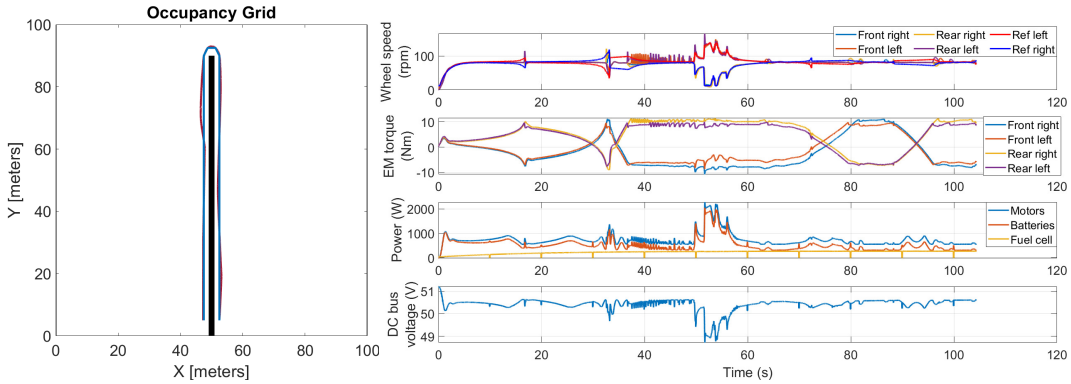

Figure 4.19 Co-simulation results considering loam soil, 100 kg of payload, and errors due to initial position misalignment and GPS sensor accuracy.

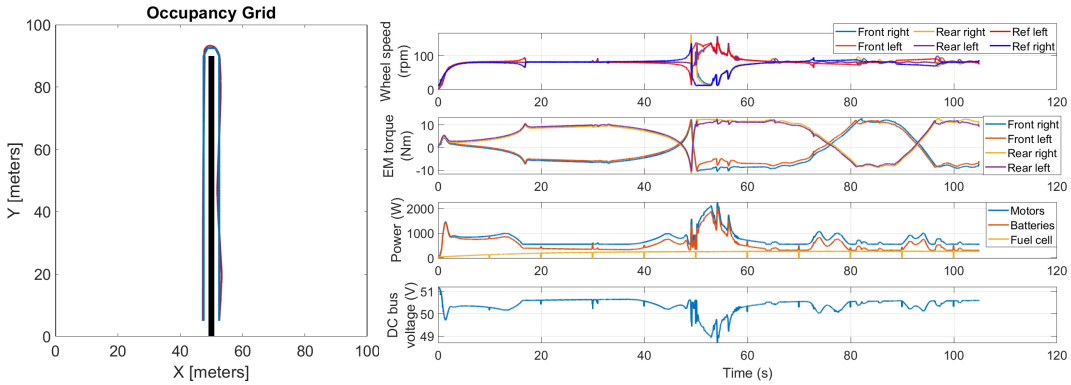

Figure 4.20 Co-simulation results considering loam soil, 200 kg of payload, and errors due to initial position misalignment and GPS sensor accuracy.

Overall, an initial increase in the rover payload caused a worsening in terms of trajectory deviation and wheels slip (cases with 50 kg and 100 kg), but the case with 200 kg instead showed better performance even compared to the 0 kg case, indicating that heavy payloads may improve the control stability. Indeed, with 50 kg and 100 kg of payloads, an increase in wheel slip was noted when starting the turn maneuver, while these oscillations disappeared with 200 kg.

Figure 4.21 shows the results for the case with 0 kg of payload and hard soil as terrain. In this case, the maximum trajectory deviation was 0.85 m, while the average and maximum traction powers were 686 W and 2335 W, respectively.

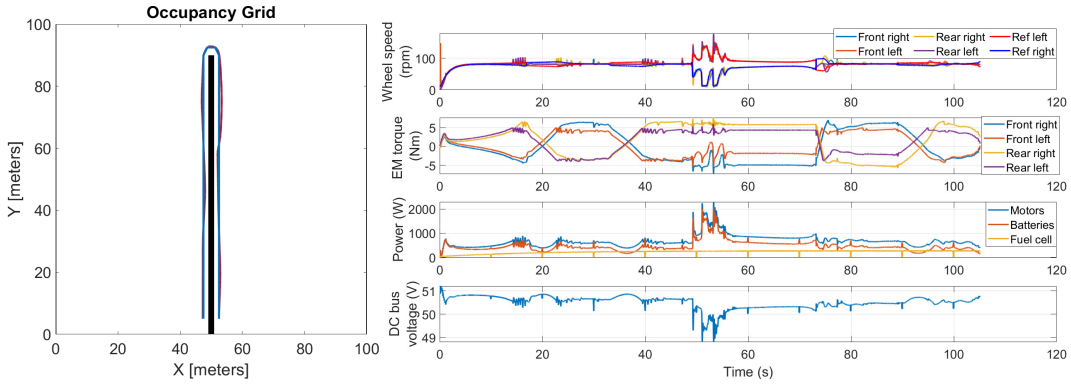

Figure 4.21 Co-simulation results considering hard soil, 0 kg of payload, and errors due to initial position misalignment and GPS sensor accuracy.

As for the sandy soil case, the results are shown in Figure 4.22. In this case, the rover was not able to complete the maneuver. Several oscillations on the wheel speed can be noted when trying to perform the turn, indicating that the friction coefficients of sandy soil are the limiting factor as they rover was not capable of transmitting enough force to the ground.

Lastly, the results for the case with muddy soil are shown in Figure 4.23. In this case, the wheel speed oscillations were very intense and occurred every time the reference wheel speed changed. This behavior can be observed even at the beginning of the simulation, when the rover had to accelerate to reach the reference speed.

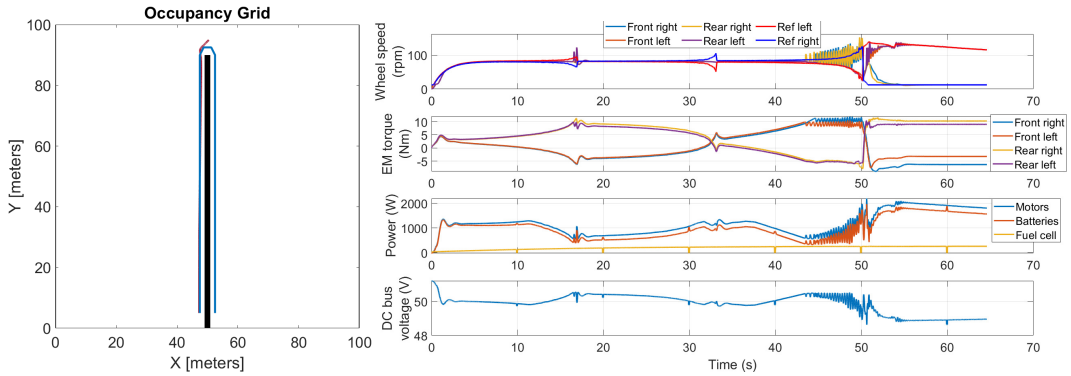

Figure 4.22 Co-simulation results considering sandy soil, 0 kg of payload, and errors due to initial position misalignment and GPS sensor accuracy.

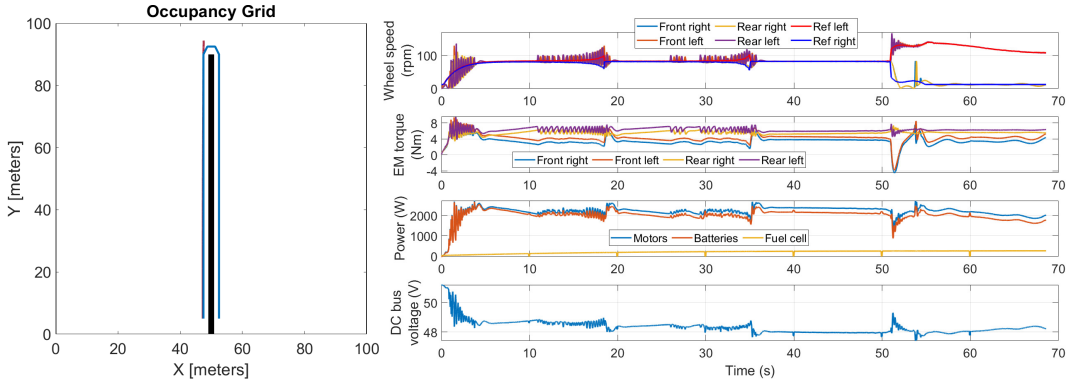

Figure 4.23 Co-simulation results considering muddy soil, 0 kg of payload, and errors due to initial position misalignment and GPS sensor accuracy.

4.2.6 Discussion

Given the rated capacity of the battery pack, equal to 5.4 kWh, the expected endurance without the range extender unit, considering the reference case of loam soil and 0 kg of payload, was estimated to be 7 hours and 50 minutes.

With the introduction of the fuel cell range extender unit, two different scenarios can be considered. In the first case, when the MH tank runs out of hydrogen, the fuel cell system is turned off and the vehicle continues performing the tasks without its contribution. Considering the current setpoint established by the control strategy and the MH tank capacity, this would occur after 6 hours of continuous operation. In this case, the expected endurance, considering loam soil and 0 kg of payload, is of 10 hours and 6 minutes (+29%).

In the second scenario, when the MH tank runs out of hydrogen it can be replaced with a fully charged one using a tank swap technique. Considering this solution, the expected endurance can be enhanced, reaching 12 hours and 30 minutes for the loam soil 0 kg payload case (+60%). In this scenario, the range extender unit can operate almost continuously, apart from the moment in which the tank is swapped which requires the fuel cell to be turned off. However, this operation is very easy, safe and quick.

Considering all the previously presented simulated scenarios, a comparison in terms of expected endurance for the different cases is presented in Table 4.6. In the comparison, also the scenarios with sandy and muddy soils were included. Even if the rover was not able to complete the task, they were deemed useful as they were representative of higher power demanding situations.

Table 4.6 Expected endurance for the different cases. Please note that the percentage values indicate the improvement compared to the no range extender case in the same scenario.

Test scenario	**Expected endurance**		
	No range extender	**Range extender w/o tank swap**	**Range extender w/ tank swap**
Loam, no payload	7 h 50 min	10 h 6 min (+29%)	12 h 30 min (+60%)
Loam, 50 kg payload	7 h 38 min	9 h 50 min (+29%)	12 h 2 min (+58%)
Loam, 100 kg payload	7 h 23 min	9 h 30 min (+29%)	11 h 25 min (+55%)
Loam, 200 kg payload	7 h 6 min	9 h 8 min (+29%)	10 h 46 min (+52%)
Hard, no payload	7 h 52 min	10 h 8 min (+29%)	12 h 39 min (+61%)
Sandy, no payload	4 h 49 min	6 h 13 min (+29%)	6 h 16 min (+30%)
Muddy, no payload	2 h 34 min	2 h 56 min (+14%)	2 h 56 min (+14%)

Analyzing the results, it can be stated that the benefits of introducing the range extender unit are maximized when the expected endurance exceeds 6 hours, thus with the possibility of using all the stored hydrogen. The improvement in endurance in those cases was estimated to be equal to +29% without the tank swap. On the contrary, if the expected endurance is lower than 6 hours, the benefits are reduced as not all the stored hydrogen can be exploited.

The adoption of the tank swap procedure can significantly extend the rover autonomy in those cases where the expected endurance is higher than 6 hours. In fact, if the expected endurance was slightly longer than that limit, the tank swap was not able to extend the autonomy because the remaining battery capacity was not enough to prolong the work time and the range extender unit solely could not provide enough power to propel the vehicle. If the expected endurance is lower than 6 hours, the tank swap cannot be performed as the batteries are completely discharged. On the other hand, in those cases where the expected endurance was significantly higher than 6 hours, the tank swap was capable of improving the endurance from +50 to +60%.

Overall, the co-simulation analysis showed that the implementation of the range extender unit can significantly improve the rover performance in terms of productivity and endurance.

The main outcomes of the co-simulation analysis can be summarized in the following list:

- The rover was capable of performing the proposed maneuver with loam and hard soils, and with a payload from 0 to the maximum considered value of 200 kg; on the contrary, with critical soils such as sandy and muddy terrains, the rover was not capable of performing the 180 degrees.
- Tire slipping was a critical factor with sandy and muddy soils, as the rover was not capable of performing the torque vectoring technique.
- The maximum trajectory deviation with loam and hard soils was estimated equal to 1 m.
- The average power for traction considering loam and hard soils was in the range 680-760 W, while the peak power was around 2400 W.

- The range extender unit operated as defined by the control strategy and was capable of extending the autonomy from +14 to +61% depending on the specific case.

4.3 Smilla H2 powertrain HIL test bench

In this section, the development of a HIL test bench for the testing of Smilla H2 powertrain is presented. The HIL simulation was developed at Power level, thus inverters and motors where not present, but their power absorption was emulated using a programmable electronic load. For simplicity, instead of using the Li-ion battery pack, which was mounted on the Smilla prototype, four series-connected 12 V lead-acid batteries were adopted. This represented a worse situation with respect to the actual powertrain, since lead-acid batteries present a higher internal resistance and their voltage is subject to more intense variations when under load.

The main goals of the HIL simulation were the following:

- Test and validate the hardware in terms of compatibility and operating conditions.
- Evaluate the behavior of the range extender control unit.
- Test the proposed EMS and its reliability under intense load variations.

4.3.1 HIL test bench experimental set-up

The experimental set-up consisted of the FCS-C300 system, the MH tank, their connection kit with valves and a pressure transducer for monitoring the tank internal pressure, the unidirectional DC-DC converter, the batteries, the programmable electronic load unit, and the control unit. Almost all these components were commercially available products that had to be integrated and interfaced. On the contrary, the control unit was developed specifically for this application instead of buying it. Consequently, it had to be designed and realized. Into details, this unit had to accomplish the following tasks:

- Communicate with a PC for programming and data logging.

- Collect data from transducers to monitor the operating conditions.
- Control the DC-DC output to perform the proposed EMS.
- Control the electronic load to reproduce the external load profile.

The control unit was developed around a micro-controller board. Data from the transducers were collected using a multi-channel analog-to-digital converter (ADC). The voltage and current signals for controlling the DC-DC converter were generated using two double-channel digital-to-analog converters (DACs). Two analog signals were used to control the DC-DC converter (current and voltage reference signals), while another analog signal was used to control the electronic load. The micro-controller communicated with DACs and ADC using SPI communication. To separate the ground of the power line from the ground of the micro-controller, analog optocouplers were implemented. Lastly, communication with the PC was enabled through a USB connection. Given the electrical scheme, a PCB was designed and realized.

As for the monitoring of the operating conditions, three current transducers and two voltage transducers were used. The three current transducers were placed at the fuel cell stack output (LEM CAS 6-NP), at the batteries output (LEM CAS 50-NP), and at the electronic load input (LEM CAS 50-NP). The voltage transducers (LEM LV-25 P) were placed one at the fuel cell stack output, and one at the DC bus. The electronic connection between the FCREU, the batteries, and the load was made using a specifically designed PCB. The circuit schematics of both the control and power boards are available in Appendix B.

Regarding the DC-DC converter, considering the FCS-C300 polarization curve, from which it could be noted that the stack voltage was in the range 60-30 V, and the DC bus rated voltage of 48 V, it was clear that it had to be a buck-boost unidirectional converter. In this regard, the Universal Buck-Boost Super Regulator DC-DC [162], manufactured by Elecdan Converter, was chosen. The main properties of this power converter are summarized in Table 4.7.

Lastly, the electronic load that was adopted in the experimental set-up was the EA-EL 9080-400. It had a rated power of 4.8 kW, with a voltage range of 0-80 V and a maximum current of 400 A.

Table 4.7 DC-DC main properties.

Parameter	Value
Type	Buck-Boost
Input voltage range	9-88 V
Input current max	27.5 A
Output voltage range	0-88 V
Output current range	0-27.5 A
Rated power	2.3 kW
Control signals voltage range	0-10 V

A schematic representation of the experimental set-up of the HIL test bench is shown in Figure 4.24. The FC controller was powered using a DC-DC converter connected to the 48 V DC bus, however this is not represented in the figure.

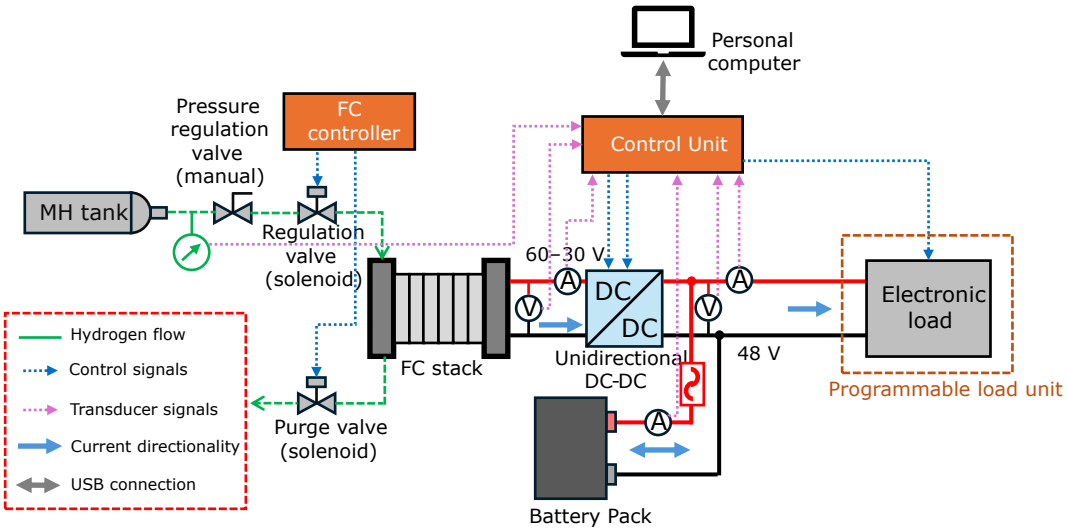

Figure 4.24 Smilla H2 HIL test bench set-up.

4.3.2 HIL tests results and discussion

To perform the HIL tests, it was chosen to adopt a profile similar to the DST, with no charging phases as the load unit was composed only of the electronic load. Moreover, even if the Smilla motors had a total power of 4.8 kW, it was decided to limit the maximum load power to 2.4 kW (half the maximum power).

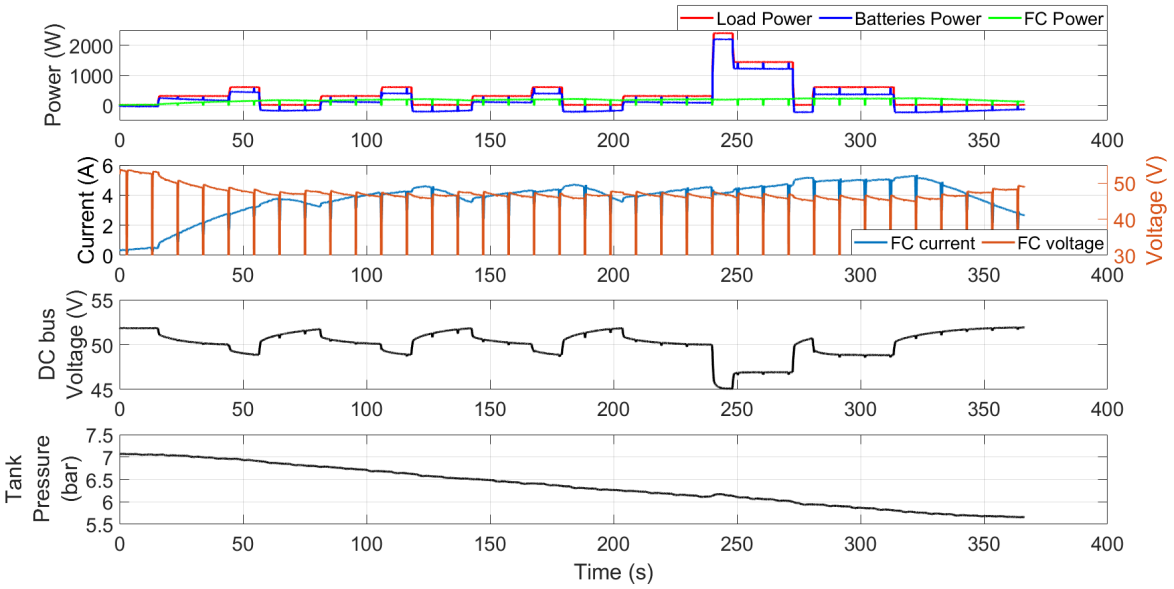

Figure 4.25 HIL test results.

The results of the test are shown in Figure 4.25. Observing the charts, several considerations can be outlined. First of all, the powertrain configuration managed to complete the test, with the range extender unit that was capable of recharging the batteries during low-power phases and of helping them satisfy the total power demand during high-power situations. Secondly, the DC bus voltage was characterized by significant variations. In fact, it oscillated between 52 and 45 V. This behavior was related to adoption of lead-acid batteries, which featured a high internal resistance that caused intense voltage drops in case of high currents. However, this behavior was expected to not happen when implementing the FCREU on Smilla, as Li-ion batteries have very low internal resistance.

As for the EMS, the system was able to control the FCREU output in accordance with the control strategy shown in Figure 4.8. The only differences were that the voltage limits were set to 51.5 and 53 V, while the current setpoint was limited to 5 A instead of 6 A. This last choice was motivated by the decision to apply a precautionary approach, thus a slightly lower maximum output was imposed. Observing the FC current plot, it can be noted that the stack output was not characterized by intense variation, apart from the effects of the SCU. Thus, the PI controller was properly calibrated and the fuel cell followed a low-dynamic behavior.

Regarding the MH tank behavior, it was noted that the internal pressure significantly decreased, as it was 7 bar at the beginning and reached 5.6 bar at the end. It should be noted that the tank was almost full when this test was performed. Despite at first glance this might have raised some doubts, it was motivated by some factors. First, when the tank's hydrogen content is above approximately 80% of the nominal capacity, the PCT curve is characterized by a high slope (as depicted in Figure 3.24, thus pressure varies significantly with small hydrogen content variations. In addition to that, the tank temperature at the beginning of the test was around 20°C. Despite a thermal coupling between the FCS-C300 and the MH tank was performed, substantially by simply positioning the tank near the stack blowers so that hot air was forced against the tank's walls, the tank temperature decreased and reached approximately 16°C at the end. This happened not only because of the endothermic behavior of the desorption reaction, but also because the environmental temperature during the test was around 12 °C. Indeed, the tank was preheated prior to the test to avoid excessive low temperature. Thus, the combined effect of temperature reduction and hydrogen consumption caused the relevant decrease in the tank internal pressure.

In conclusion, the analysis of the results of the HIL test led to the following consideration:

- The FCREU hardware was validated as the unit was capable of delivering power to the DC bus.
- The range extender control unit managed to perform the predefined EMS, thus the control algorithm was validated.
- The fuel cell system and the MH tank operated within their operational constraints without issues.

4.4 Smilla H2 fuel cell range extender implementation

Once validated the powertrain components through HIL testing, the next step was to implement the range extender unit in the Smilla prototype. The range extender unit comprised the same elements adopted in the HIL set-up, with the only difference in the control unit. Indeed, the power level of the control unit was removed. This choice was motivated by several elements: first of all, since the full electric powertrain

was already present, it was difficult to perform the electrical coupling inside the range extender unit. Furthermore, this was not necessary. For proper operation of the range extender unit, there was no need to monitor the batteries current or the load current. The only parameter that had to be known was the DC bus voltage for the EMS, however this was monitored placing a voltage transducer downstream the DC-DC. In addition, a part of circuit had to be added. Considering Smilla on-board PC, it had to know the operating condition of the range extender unit to perform safety procedures in case of warnings or issues. To address this, it was chosen to add CAN communication to the range extender unit. Indeed, Smilla featured a CAN bus network to control the inverters. Consequently, a part of circuit enabling CAN communication, realized using a MCP-2515 and a MCP-2551, both manufactured by Microchip Technology, was added. A simple CAN protocol, consisting of two messages indicating the operating conditions (fuel cell current, tank internal pressure, and so on), was defined.

For the physical mounting of the range extender unit, a steel housing was designed and manufactured. This housing was composed of a main body and a removable lid, both obtained through bent sheets. For the connection to the rover frame, elongated slots were added to the range extender housing. The rover frame was drilled to allow the housing to be fastened using bolts and nuts. The housing was also provided with a support for the pressure reducing valve of the tank connection kit. Furthermore, to guarantee enough air to be supplied to the fuel cell stack cathode, the main body of the housing was provided with openings on which ventilation grids were placed.

For the electrical connection, the range extender unit had to be connected to the rover powertrain with two main connections: the unit output connection, namely the connection between the range extender output and the DC bus, and the unit power supply connection, namely the connection that provided the power supply for the control unit logic and the FC controller. For both, Deutsch connectors were adopted.

Lastly, holes for the tubing (hydrogen supply, purge valve output) were provided.

The 3D CAD of the whole housing is shown in Figure 4.26.

As for the MH tank, its fastening to the rover frame was realized with two elements made using a 3D printer. These two elements had a shape that featured a hemispherical housing for the tank, and holes for the connection with bolts to the frame. The tank was fixed to them with metal clamps.

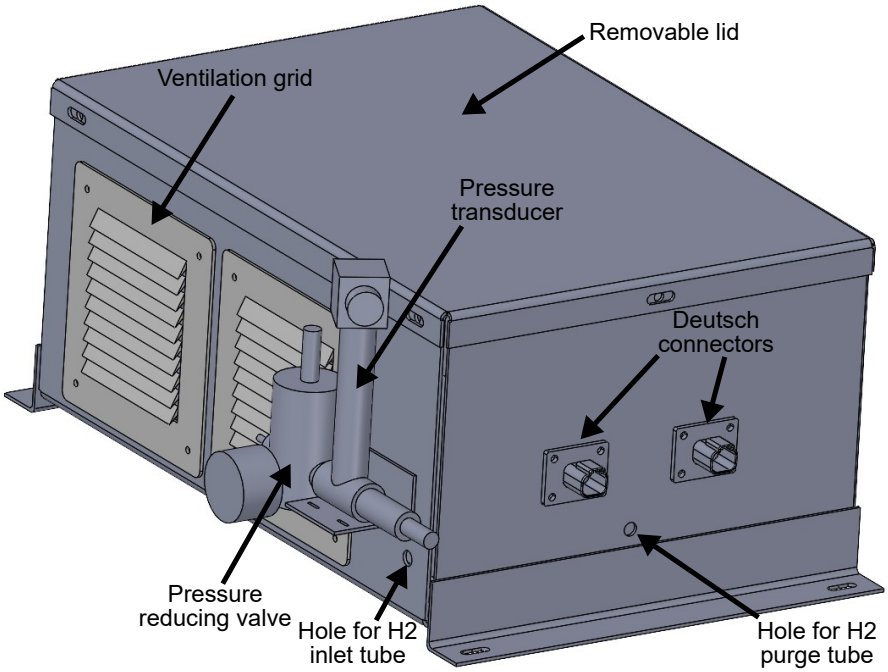

Figure 4.26 3D CAD of the range extender housing.

Pictures of the range extender unit mounted on Smilla are shown in Figure 4.27. Please note that these pictures were taken with the range extender system OFF; thus the hydrogen tubes were not connected. Indeed, it is suggested in the FC manual to disconnect the hydrogen input when turning the system off.

4.5 Smilla H2 experimental test

Once completed the on-board implementation and integration of the range extender unit, the next step was to perform experimental tests to evaluate the system behavior. The energy management strategy was the same presented in Figure 4.8. To perform these tests, two main elements were needed: a physical place to be used as the test location, and a test scenario to be performed.

4.5.1 Test conditions

Given that there was not enough time to consider field tests in a real orchard, the test location that was chosen was a warehouse made available by Ecothea. The main

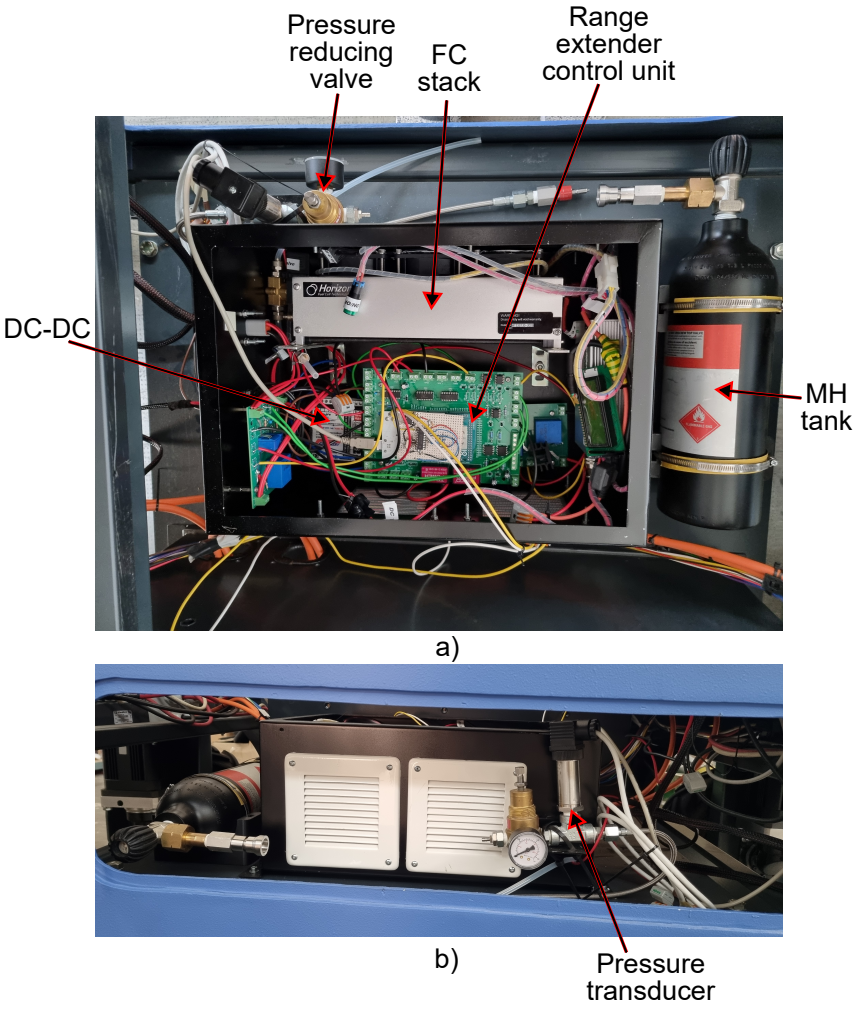

Figure 4.27 Photos of the range extender unit mounted on Smilla H2; a) top view, b) side view.

differences compared to performing tests in an orchard were: the ground, which in the warehouse was concrete, and the space availability, that was significant lower. Furthermore, it was complicated to adopt the autonomous driving algorithm, which was developed specifically for orchards and not for tight maneuvers in a narrow space. Consequently, the approach chosen at the beginning of the experimental campaign was based on the following assumptions and decisions:

- Instead of adopting the autonomous driving algorithm, the rover was manually controlled using a bluetooth joystick and a specifically designed control algorithm.
- The test scenario consisted of performing different maneuvers, including straight lines, turns, and inversions, within the warehouse.
- During the tests, no additional weights or attached implements were included.

The first task that the manual driving control algorithm had to address was the definition and translation of the joystick commands.

The bluetooth joystick that was adopted during the tests to control Smilla H2 was an XBOX controller. To control the rover, the driver had to indicate, through the joystick, two main parameters: longitudinal and yaw speed. This approach was chosen as it followed the same principles of the autonomous driving algorithm, in which the path following algorithm evaluated the reference longitudinal and yaw speeds. To address this, the control algorithm was developed so that the Right Trigger (RT) button indicated the rover longitudinal speed, while the Left Stick (LS) indicated the yaw speed. In addition, up and down arrows buttons were used to determine the forward/reverse direction. Lastly, the Left Trigger (RT) was used as safety button to indicate the presence of the driver. Indeed, if RT was not pressed, the other commands would not have any effect, and the rover would not have moved.

The next step was to determine, given the longitudinal and yaw speeds given by the driver through the controller, the reference wheels speeds. Keeping the same approach of the autonomous driving strategy, the kinematic model presented in Section 4.2.2 was adopted to determine the wheels reference speeds.

Next, the algorithm had to evaluate the torque commands to the motors. Also in this case, the same approach presented in Section 4.2.2 was used. Thus, a PI

controller was chosen. The actual wheels speeds were obtained by CAN messages sent by the inverters. Indeed, the inverters sent the motors actual speeds, and thus it was possible to evaluate the wheels speeds knowing the transmission ratio. The control algorithm featured a simple anti wind-up system to limit unstable behavior. Lastly, to avoid a sharp behavior of the rover, maximum variations at each time step of inputs and outputs of the algorithm were limited.

Lastly, once the torque commands were calculated, they had to be sent to the corresponding inverters. Since they were controlled through CAN communication, a PEAK PCAN-USB device, manufactured by PEAK-System Technik GmbH, connected to the vehicle CAN network was exploited to send the CAN messages. In addition, the connection to the CAN network was necessary as it was the only way to know the actual speeds of the wheels without increasing the complexity of the system. Figure 4.28 shows the joystick used for the tests and a schematic representation of the control algorithm.

A schematic map of the location test with the rover initial position is shown in Figure 4.29. This schematic representation was realized maintaining the proportion of the real test environment.

For collecting the experimental data during the test, a data logger unit consisting of a PCAN-GPS, manufactured by PEAK-System Technik GmbH, was programmed. This system was substantially the same as the one that was adopted during the monitoring of the agricultural tractor discussed in Section 2.4. This unit was powered using the rover 12 V line and was connected to the CAN network. Each 50 ms, CAN messages were collected and saved on a micro SD card, along with the time and the GPS position.

Once the control algorithm, the test location, and the data logger system were defined, the next step was to decide the mission profile. Into details, the following maneuvers were considered:

- Rover movement in forward and reverse directions on a straight line.
- Rover movement on a straight line, then slight turn on one side, and after another slight turn but on the other side (similar to an obstacle avoidance maneuver).
- Rover inversions.

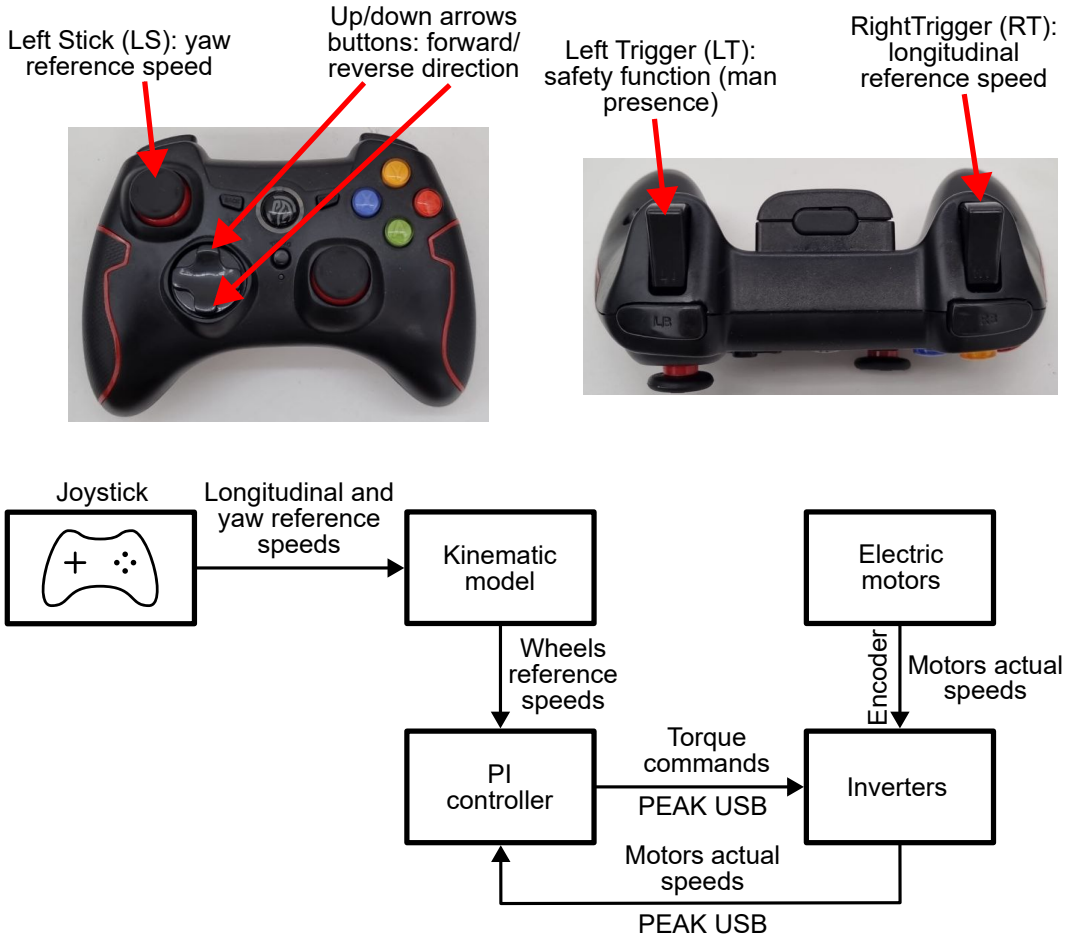

Figure 4.28 Top: Photos of th joystick used for the manual control with indication of the control buttons and their function; Bottom: Schematic representation of the control algorithm.

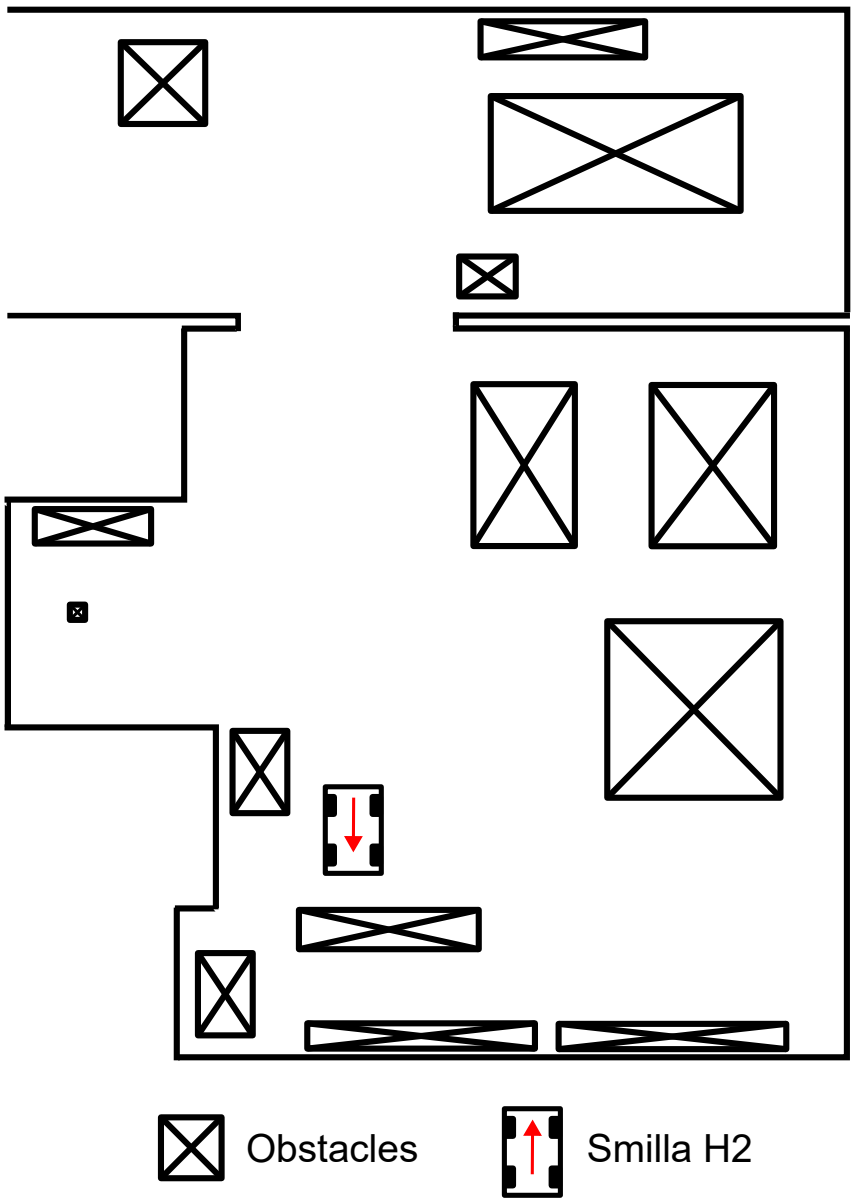

Figure 4.29 Schematic representation of the test location with the initial position of Smilla H2. Please note that the red arrow indicates the rover forward direction.

At the beginning of the test, the battery pack SoC was around 45%. As for the energy management strategy ,the current setpoint was set at 5 A.

4.5.2 Experimental test: Results and Discussion

In the following subsection, the results of the experimental test on Smilla H2 are presented and discussed. Before presenting the results, it is important to highlight that the aforementioned maneuvers were all performed in sequence during a single test session. Consequently, the results are presented considering the whole test but highlighting in the plots when the different maneuvers were performed. A schematic representation of the most relevant performed maneuvers is shown in Figure 4.30.

At the beginning of the test, the rover was oriented with its forward direction downward with respect to the floorplan. At the end of the test, after the third inversion, the rover was almost in the same initial position but oriented with the forward direction upward. The execution of all maneuvers took about 15 minutes. At the end of the last maneuver, the rover remained still with the range extender unit on for approximately three minutes to evaluate the behavior of the system when the motors do not require power for a certain amount of time.

The test results in terms of motors speeds are shown in Figure 4.31. Please note that Motor 1 refers to the front right motor, Motor 2 to the rear right motor, Motor 3 to the rear left and Motor 4 to the front left. Observing the plot, it was possible to determine that the rover was generally able to perform the maneuvers with a stable control. The only points in which a tire slipped significantly were when Motor 1 and Motor 3 exceeded 800 rpm, which occurred at time 210 s and 315 s respectively. However, this was not a problem as the rover managed to recover traction force in a very short time thanks to the control algorithm which was capable of understanding when a wheel was overspeeding.

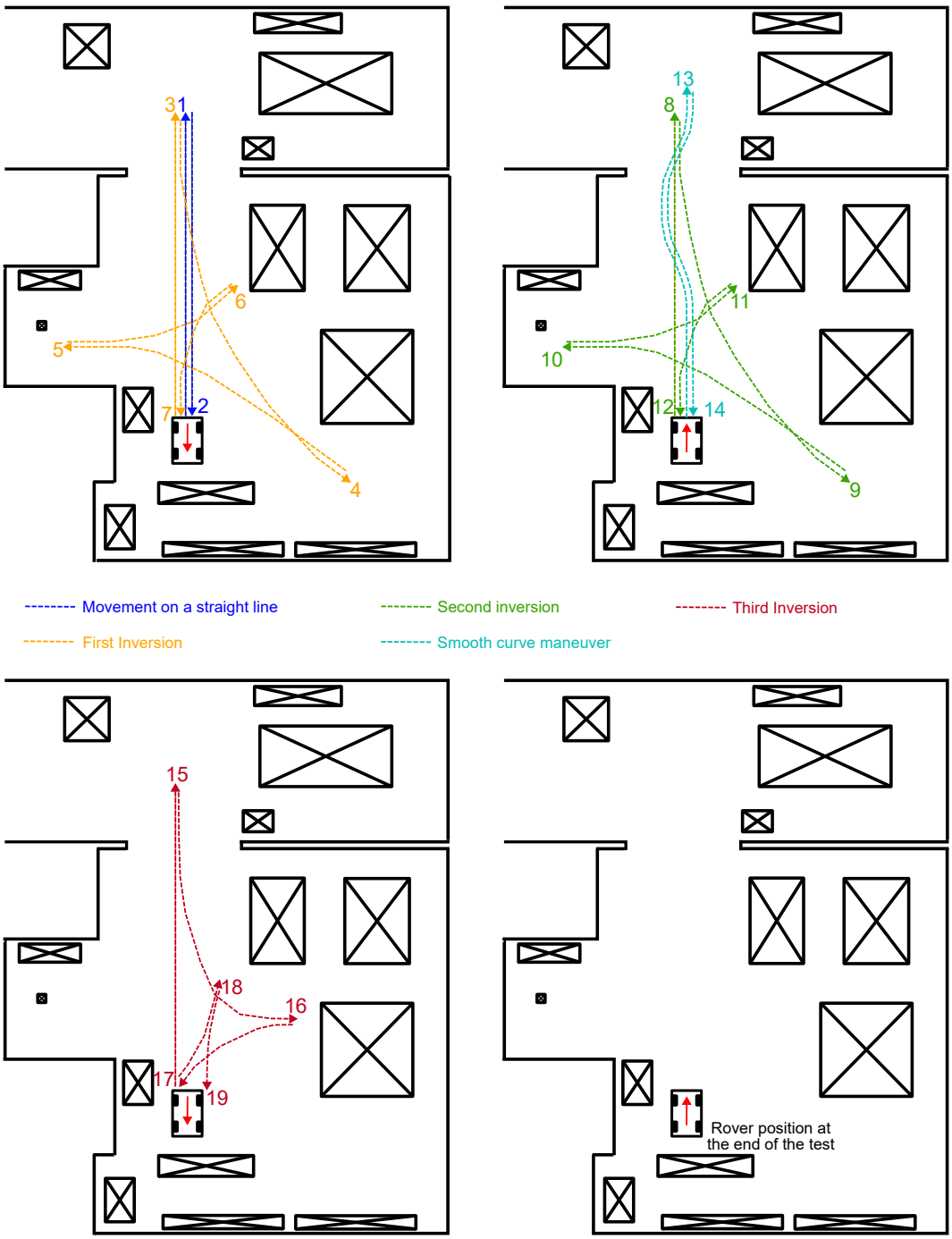

Figure 4.30 Schematic representation of the most relevant maneuvers performed during the test. Please note that the number indicates the chronological order. The scheme was divided into four parts, in which the rover is represented with the orientation at the beginning of the upcoming maneuvers; the last representation shows the rover position at the end of the test.

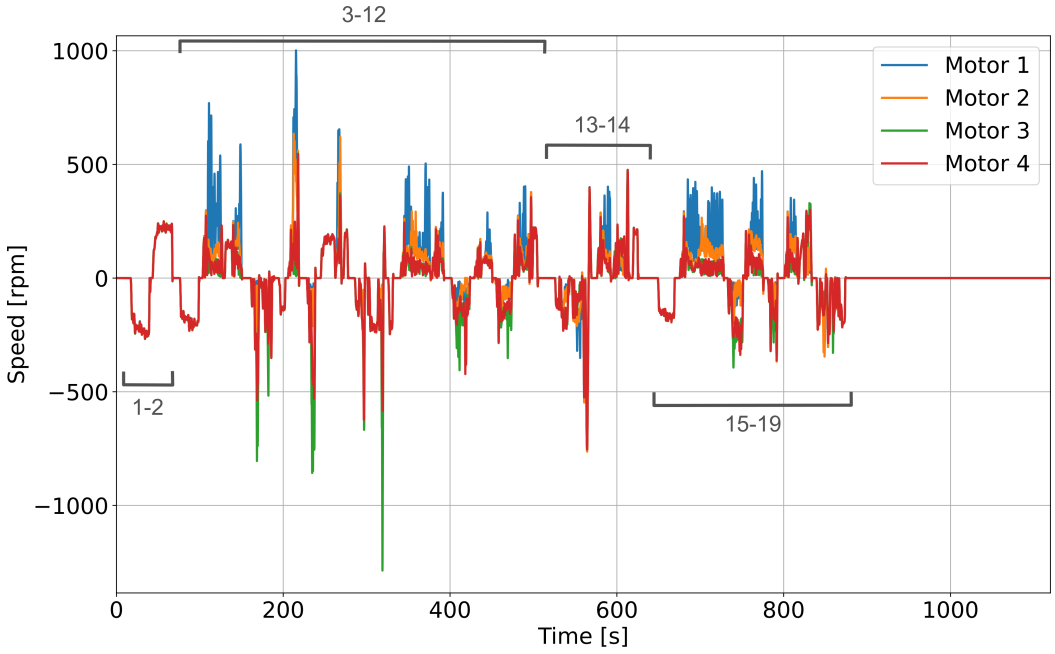

Figure 4.31 Electric Motors speeds during the experimental test. Please note that the number provided in gray indicate the corresponding maneuvers within the plot.

Figure 4.32 shows the total power required by the motors, the power output of the range extender, and the power output of the battery pack during the test. Observing the chart, it can be noted that the power output of the range extender, once reached the regime condition, was very stable (approximately at 200 W) during the whole test, even when peak power absorptions occurred. This consideration is valid considering that the SCU function, which was responsible for turning off the FC power output each 10 s, was necessary for the correct functioning of the fuel cell and generally prolongs its lifetime (as indicated by the FCS-C300 manufacturer).

Regarding the potential effects of the range extender unit in extending the endurance of the rover, it was observed that the the final battery pack SoC was almost the same as the initial one. Indeed, it was evaluated that the battery pack energy consumption equal to 0.45 Ah. Assuming that this cycle is repeated continuously, this would correspond to en energy consumption per hour of approximately 1.5 Ah, that would indicate an endurance of 70 hours straight. However, the last three minutes of the test, where the range extender recharged the batteries but no power was required by the motors, could have influenced the results. If that part is not considered, the expected endurance decreases to 40 hours. Instead, if the range extender unit is not be implemented, the expected endurance would be of approximately 17 hours. This

indicate that the range extender unit potentially extend the endurance of more than double.

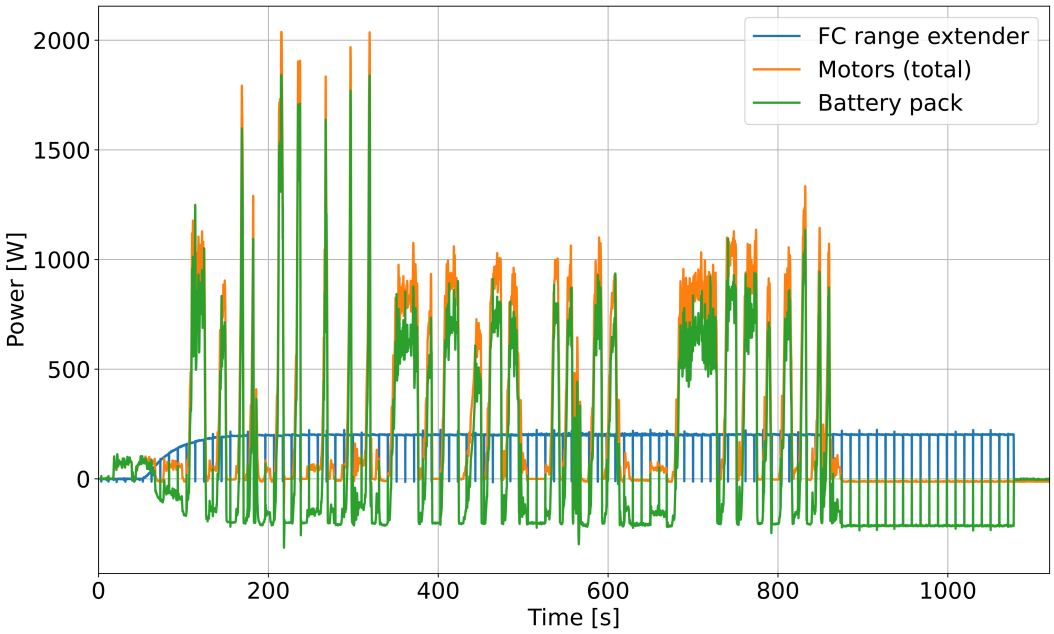

Figure 4.32 Total motors, range extender and battery pack power profiles during the test.

Despite the promising results in terms of improved endurance, it should be highlighted that the power absorptions during field operations in orchards are expected to be significantly higher. Thus, the beneficial effects might be not so relevant as observed in the considered test scenario.

The last consideration that can be made from the power profiles plot is that the power required for traction significantly increased during turns. Indeed, since the system adopted torque vectoring technique to turn, significant traction losses occurred due to slip and lateral friction.

Regarding the behavior of the fuel cell, Figures 4.33 and 4.34 show the stack voltage and current during the test.

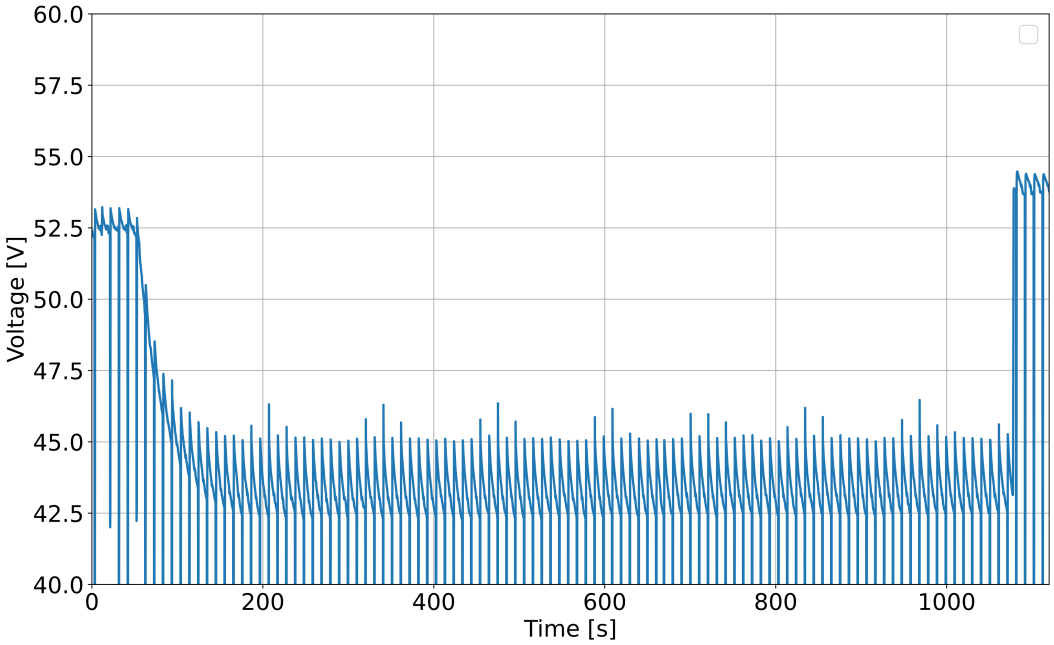

Figure 4.33 Fuel cell stack voltage.

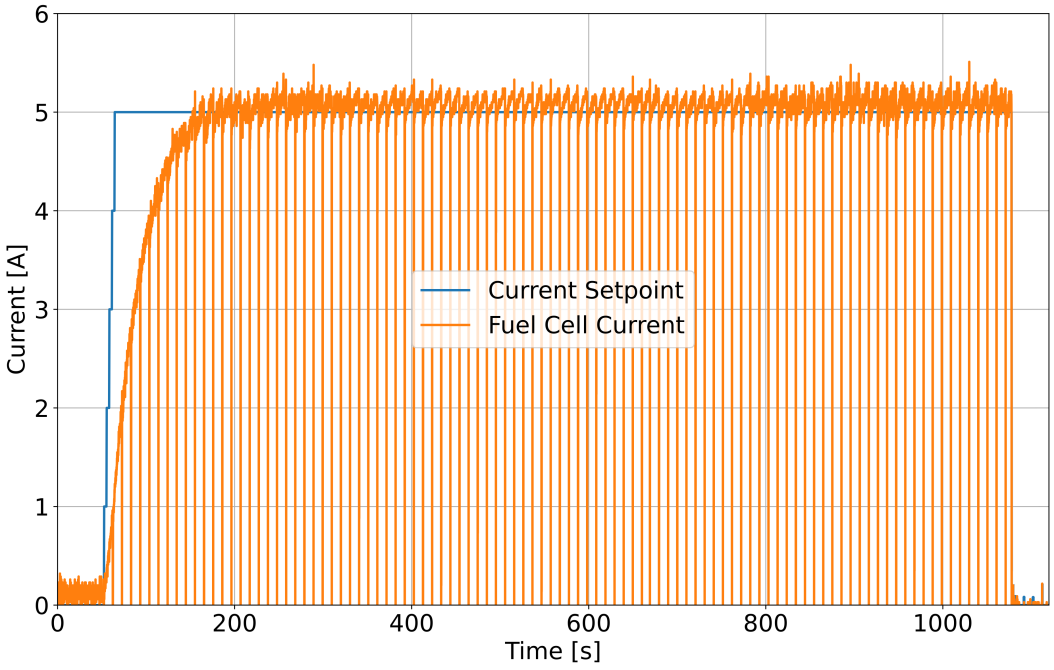

Figure 4.34 Fuel cell stack setpoint and actual current during the test.

As can be stated, the system was able to operate in accordance with the energy management strategy following the current setpoint. The average power output of the stack at regime condition was 220 W, thus the average electrical efficiency of the power circuit (protection diode and DC-DC converter) was around 92-93%, since the power output of the range extender was around 205 W.

Regarding the DC bus voltage, it was very stable throughout the whole test, with a recorded maximum of 52.6 V and a minimum of 51.4 V, as shown in Figure 4.35.

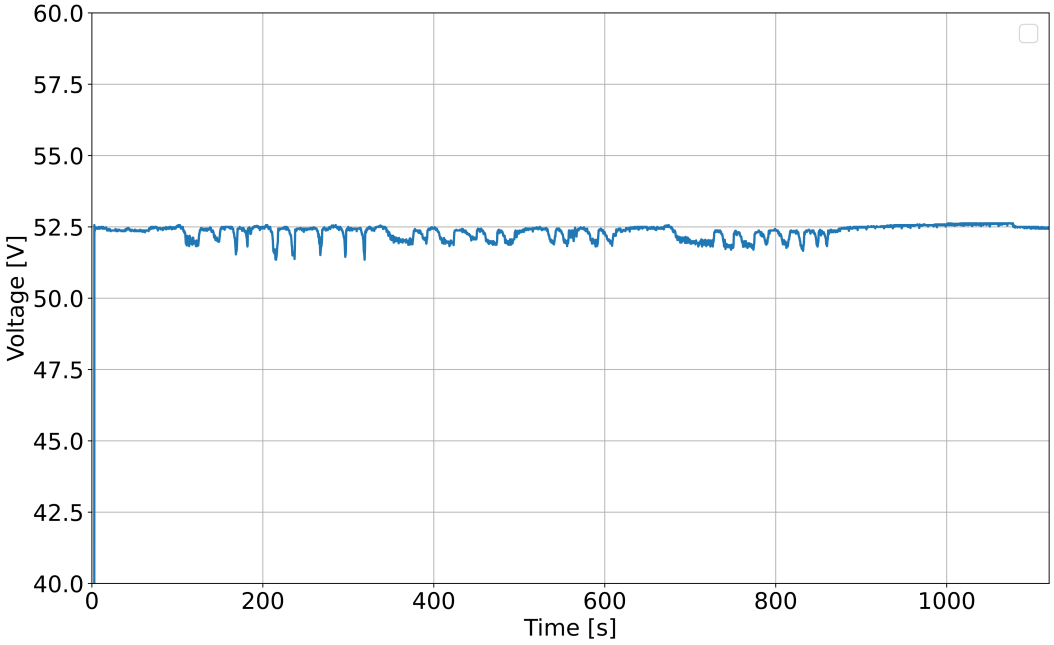

Figure 4.35 DC bus voltage during the test.

Lastly, the internal pressure of the MH tank is shown in Figure 4.36. The hydrogen content in the tank was estimated to be approximately 35-40% of the nominal capacity. At the beginning of the test, the internal pressure was 5.25 bar, while at the end it was around 3.4 bar. This variation was mainly due to the tank temperature, which decreased during the test as a result of the endothermic behavior of the desorption process. The test was carried out with an environmental temperature of 20°C, but the tank was preheated before and thus its temperature decreased significantly throughout the test. The hydrogen consumed during the test was estimated to be 3 grams, corresponding to 3.7% of the nominal capacity. Accordingly, in these conditions the time required to consume a fully charged tank

is expected to be 9 hours with the assumption that all 80 grams of hydrogen can be extracted from the tank.

It should be noted that in the proposed on-board integration, the thermal coupling between the FCS and the MH tank was only partially performed due to limited on-board space availability.

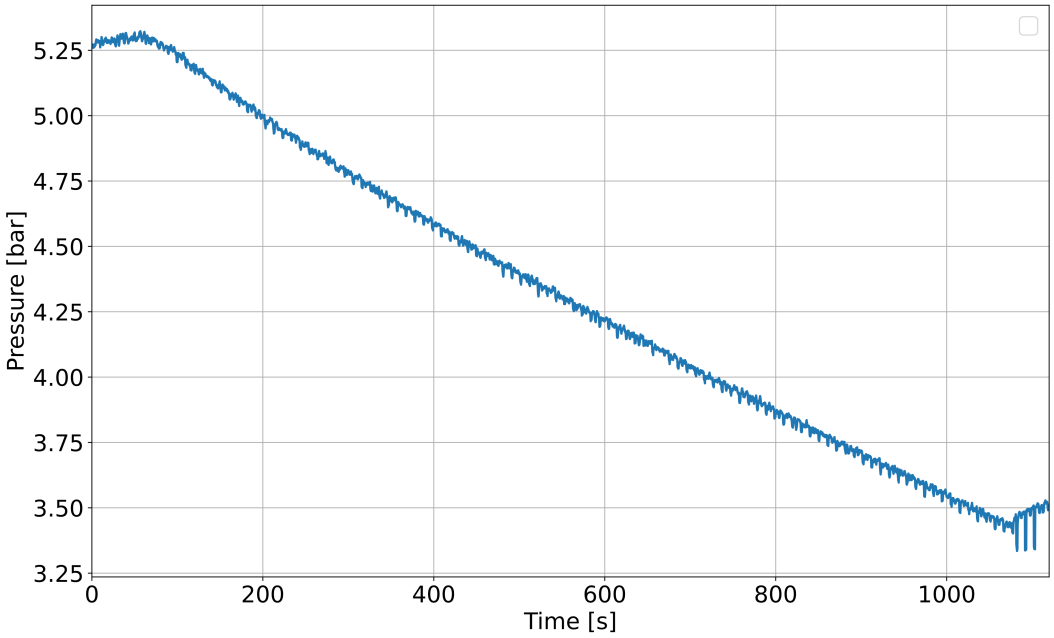

Figure 4.36 MH tank internal pressure during the test.

4.6 Conclusions

A promising solution to further improve the sustainability and productivity of the agricultural sector is represented by the adoption of autonomous driving agricultural rovers. Indeed, agricultural rovers allow for the introduction of precision farming techniques. However, these vehicle are generally powered using pure battery powertrain, which may lead to reduced endurance in case of long-term operations. In this context, fuel cell systems can address this issue and improve the rover performance.

The attention focused on the Smilla prototype, a medium-size rover specifically designed to operate in orchard and vineyards. A fuel cell range extender unit with metal hydride tank was designed, virtually tested, then implemented on the rover prototype, and finally experimentally tested.

The numerical analysis involved the development of a co-simulation model, comprising a multibody model of the rover, developed in Hexagon Adams, and a Matlab/Simulink model with both the autonomous driving algorithm and the powertrain models. For the powertrain model, numerical models of both the fuel cell system and the metal hydride tank were developed using the data obtained from the characterization tests described in Chapter 3. A virtual test scenario was designed to test the rover under certain work conditions it can encounter during its operative life. The results showed that the unit operated according to the designed EMS and was able to extending the endurance of the vehicle.

In the next step, a non-scaled HIL test bench was developed to validate the selected hardware for the range extender. The HIL set-up included the FC system, the MH tank, the power electronics, the range extender control unit, a battery pack with the same rated voltage of the one mounted on the rover, and a load unit. The control unit was designed and developed custom for this specific application, thus its validation was particularly critical. The results of the HIL tests validated the proposed hardware configuration and showed that the control unit successfully controlled the system.

Lastly, the range extender unit was implemented in the Smilla rover prototype. A case was designed and physically connected to the rover frame. Once the electrical connections were completed, experimental tests were performed with the rover that performed some pre-defined maneuvers. The results showed that the fuel cell range extender unit operated as prescribed by the EMS and was capable of extending the rover endurance significantly.

Chapter 5

Conclusion and future works

The growing awareness towards the environmental sustainability of anthropic activities is pushing the industrial and academic world to investigate innovative solutions to reduce the impact of several processes. Agriculture is no exception, as it contributes to the production of emissions and, at the same time, plays a crucial role in the global food supply chain. Accordingly, the main goal is to reduce the environmental impact of agricultural practices without affecting their productivity.

In this context, the research activity aimed to evaluate the potential benefits deriving from the implementation of fuel cell systems for off-road vehicles. Into details, the case study under investigation was an orchard tractor. This vehicle must be characterized by high compactness, durability, capability to work in harsh environments, and productivity. Consequently, the limited on-board space availability, peak power performance, and expected durability are the most relevant constraints that must be considered when designing the innovative system. The adoption of hybrid fuel cell powertrain, thanks to their properties that include high energy density, low refueling time, and zero local emissions, is a promising solution to achieve sustainability, productivity, and to effectively replace traditional systems.

To deeply investigate these aspects, firstly a numerical analysis was performed. In detail, given a case study of an orchard tractor with a 73 kW Diesel engine, a hybrid fuel cell powertrain was designed, featuring a fuel cell system as primary energy source and a battery pack as auxiliary power source, considering the aforementioned project constraints. All the powertrain elements, including the fuel cell system, the electric motor, the battery pack, the power electronics, the mechanical transmission,

and the vehicle dynamics, were numerically modeled in Matlab/Simulink using a physical network approach. A simple rule-based contorl strategy was developed to determine the power split between the fuel cell system and the batteyr pack. To determine typical work scenarios of the machine, the traditional counterpart was monitored using a CAN bus analyzer and a data logging system during typical activities. Once derived the typical work scenarios, numerical simulations were carried out to evaluate the performance of the fuel cell powered vehicle compared to the traditional counterpart. The simulations showed that the proposed fuel cell vehicle successfully completed the work cycles, showing satisfactory peak power performance. In terms of environmental impact, a potential reduction of -50% on average of the equivalent CO2 emissions was estimated considering the use of gray hydrogen to propel the vehicle. To expand the results, a Life Cycle Assessment analysis was performed, including the manufacturing and end-of-life stages, and covering different impact categories. The results of the analysis showed that the fuel cell vehicle can significantly reduce the overall impact in almost all the considered categories, with peaks up to more than -90% of reduction in some cases. As for the global warming potential, with gray hydrogen a reduction of -41% was estimated. This reduction can be further enhanced up to -74% using green hydrogen.

In the next step, a Hardware-in-the-loop test bench was developed to emulate the behavior of different hybrid fuel cell powertrain configurations. The test bench was developed with a scale factor and emulating the fuel cell system using a programmable power supply. The main goal of the experimental activity was to determine the best architecture for the orchard tractor, and to test different energy management strategies. Three different powertrain architectures were designed, which featured the same fuel cell system, the same overall volume but with different auxiliary power sources: a battery pack, a supercapacitor module, and a hybrid unit comprising both. Two different energy management strategies, once based on the power follower control and the other on fuzzy logic, were developed for each architecture. Experimental tests were carried out and the different systems were compared in terms of durability and fuel consumptions, showing that the fuel cell and battery solution outperformed the other two in terms of expected lifetime. On the contrary, the differences in terms of fuel economy were not so relevant. Lastly, the real fuel cell system, initially emulated using a power supply, was implemented to validate the adopted approach.

In the last part of the research activity, the possibility of replacing the orchard tractor with an autonomous agricultural rover, with a hybrid fuel cell powertrain, to perform low power tasks was investigated. Into details, the design and realization of the Smilla H2 prototype, developed in collaboration with Ecothea Srl, was presented and described. The rover presents a Li-ion battery pack as primary energy source, and a fuel cell range extender unit to improve the expected work time without significantly increase the overall volume and weight of the vehicle. The proposed solution was firstly investigated through a co-simulation model, then the powertrain hardware was validated though a full scale hardware-in-the-loop test bench specifically designed for the analysis. Lastly, a prototype of the rover was developed and experimentally tested to evaluate the effectiveness of the fuel cell range extender unit in improving the endurance. The results demonstrated that the unit can effectively extend the rover autonomy, making it a promising solution to replace the orchard tractor for low power field tasks.

The main findings of the research activity suggest several directions for future works. In the long term, the development of the full scale hybrid fuel cell powertrain for the orchard tractor could be subject of future activities. In the short term, the optimization of the control strategy, which can enhance the vehicle performance, might be performed. Furthermore, the analysis of the environmental benefits deriving from the implementation of the Smilla H2 prototype could be investigated. The optimization of the rover mechanical structure to reduce the overall weight and to enhance its performance might also be subject of research.

Bibliography

[1] Vipin Das, Sanjeevikumar Padmanaban, Karthikeyan Venkitusamy, Rajasekar Selvamuthukumaran, Frede Blaabjerg, and Pierluigi Siano. Recent advances and challenges of fuel cell based power system architectures and control – a review. *Renewable and Sustainable Energy Reviews*, 73:10–18, 2017.

[2] Omar Z. Sharaf and Mehmet F. Orhan. An overview of fuel cell technology: Fundamentals and applications. *Renewable and Sustainable Energy Reviews*, 32:810–853, 2014.

[3] S. R. Samms, S. Wasmus, and R. F. Savinell. Thermal stability of nafion® in simulated fuel cell environments. *Journal of The Electrochemical Society*, 143(5):1498, may 1996.

[4] Miriam M. Tellez-Cruz, Jorge Escorihuela, Omar Solorza-Feria, and Vicente Compañ. Proton exchange membrane fuel cells (pemfcs): Advances and challenges. *Polymers*, 13:3064, 2021.

[5] Antonio Nicolò Mancino, Carla Menale, Francesco Vellucci, Manlio Pasquali, and Roberto Bubbico. Pem fuel cell applications in road transport. *Energies*, 16:6129, 2023.

[6] Yun Wang, Daniela Fernanda Ruiz Diaz, Ken S. Chen, Zhe Wang, and Xavier Cordobes Adroher. Materials, technological status, and fundamentals of pem fuel cells – a review. *Materials Today*, 32:178–203, 2020.

[7] Di Wu, Chao Peng, Cong Yin, and Hao Tang. Review of system integration and control of proton exchange membrane fuel cells. *Electrochemical Energy Reviews*, 3:466–505, 2020.

[8] Li Sun, Jiong Shen, Qingsong Hua, and Kwang Y. Lee. Data-driven oxygen excess ratio control for proton exchange membrane fuel cell. *Applied Energy*, 231:866–875, 2018.

[9] Siliang Cheng, Chuan Fang, Liangfei Xu, Jianqiu Li, and Minggao Ouyang. Model-based temperature regulation of a pem fuel cell system on a city bus. *International Journal of Hydrogen Energy*, 40(39):13566–13575, 2015.

[10] Baitao Zhang, Xuhui Wang, Dapeng Gong, and Sichuan Xu. Experimental analysis of the performance of the air supply system in a 120kw polymer electrolyte membrane fuel cell system. *International Journal of Hydrogen Energy*, 47(50):21417–21434, 2022.

[11] Di Wu, Kai Li, Yan Gao, Cong Yin, and Hao Tang. Design and simulation of proton exchange membrane fuel cell system. *Energy Reports*, 7:522–530, 2021. 2021 The 4th International Conference on Electrical Engineering and Green Energy.

[12] Hiroyuki Yumiya, Mikio Kizaki, and Hisao Asai. Toyota fuel cell system (tfcs). *World Electric Vehicle Journal*, 7:85–92, 2015.

[13] International Energy Agency (IEA). Global hydrogen review. Technical report, IEA, 2024.

[14] Mengdi Ji and Jianlong Wang. Review and comparison of various hydrogen production methods based on costs and life cycle impact assessment indicators. *International Journal of Hydrogen Energy*, 46(78):38612–38635, 2021.

[15] Rami S. El-Emam and Hasan Özcan. Comprehensive review on the techno-economics of sustainable large-scale clean hydrogen production. *Journal of Cleaner Production*, 220:593–609, 2019.

[16] H. Ishaq and I. Dincer. A new energy system based on biomass gasification for hydrogen and power production. *Energy Reports*, 6:771–781, 2020.

[17] Jianlong Wang and yanan Yin. Progress in microbiology for fermentaqtive hydrogen production from organic wastes. *Critical Reviews in Environmental Science and Technology*, 49:825–865, 2019.

[18] Jianlong Wang and yanan Yin. Fermentative hydrogen production using pretreaqted microalgal biomass as feedstock. *Microbial Cell Factories*, 17:22, 2018.

[19] W. Wukovits and W. Schnitzhofer. Fuels – hydrogen production | biomass: Fermentation. In Jürgen Garche, editor, *Encyclopedia of Electrochemical Power Sources*, pages 268–275. Elsevier, Amsterdam, 2009.

[20] Zhi Ying, Yabin Wang, Xiaoyuan Zheng, Zhen Geng, Binlin Dou, and Guomin Cui. Experimental study and development of an improved sulfur–iodine cycle integrated with hi electrolysis for hydrogen production. *International Journal of Hydrogen Energy*, 45(24):13176–13188, 2020.

[21] Etienne Rivard, Michel Trudeau, and Karim Zaghib. Hydrogen storage for mobility: A review. *Materials*, 12:1973, 2019.

[22] Liejin Guo, Jinzhan Su, Zhiqiang Wang, Jinwen Shi, Xiangjiu Guan, Wen Cao, and Zhisong Ou. Hydrogen safety: An obstacle that must be overcome on the road towards future hydrogen economy. *International Journal of Hydrogen Energy*, 51:1055–1078, 2024.

[23] Qian Cheng, Ruiqiang Zhang, Zhusheng Shi, and Jianguo Lin. Review of common hydrogen storage tanks and current manufacturing methods for aluminium alloy tank liners. *International Journal of Lightweight Materials and Manufacture*, 7(2):269–284, 2024.

[24] Thanh Q. Hua, Hee-Seok Roh, and Rajesh K. Ahluwalia. Performance assessment of 700-bar compressed hydrogen storage for light duty fuel cell vehicles. *International Journal of Hydrogen Energy*, 42(40):25121–25129, 2017.

[25] R. Morales-Ospino, A. Celzard, and V. Fierro. Strategies to recover and minimize boil-off losses during liquid hydrogen storage. *Renewable and Sustainable Energy Reviews*, 182:113360, 2023.

[26] Mahvash Afzal, Rohit Mane, and Pratibha Sharma. Heat transfer techniques in metal hydride hydrogen storage: A review. *International Journal of Hydrogen Energy*, 42(52):30661–30682, 2017.

[27] Nejc Klopčič, Ilena Grimmer, Franz Winkler, Markus Sartory, and Alexander Trattner. A review on metal hydride materials for hydrogen storage. *Journal of Energy Storage*, 72:108456, 2023.

[28] S.H. Suárez, D. Chabane, A. N'Diaye, Y. Ait-Amirat, and A. Djerdir. Static and dynamic characterization of metal hydride tanks for energy management applications. *Renewable Energy*, 191:59–70, 2022.

[29] Z. Abdin, C.J. Webb, and E.MacA. Gray. One-dimensional metal-hydride tank model and simulation in matlab–simulink. *International Journal of Hydrogen Energy*, 43(10):5048–5067, 2018.

[30] B. Satya Sekhar, M. Lototskyy, A. Kolesnikov, M.L. Moropeng, B.P. Tarasov, and B.G. Pollet. Performance analysis of cylindrical metal hydride beds with various heat exchange options. *Journal of Alloys and Compounds*, 645:S89–S95, 2015. Supplement Issue: Proceedings from the 14th International Symposium on Metal-Hydrogen Systems: Fundamentals and Applications, 2014 (MH2014).

[31] Sera Ayten Cetinkaya, Tacettin Disli, Gamze Soyturk, <Onder Kizilkan, and C. Ozgur Colpan. A review on thermal coupling of metal hydride storage tanks with fuel cells and electrolyzers. *Energies*, 16:341, 2023.

[32] Gabriele Scarpati, Emmanuele Frasci, Giovanni Di Ilio, and Elio Jannelli. A comprehensive review on metal hydrides-based hydrogen storage systems for mobile applications. *Journal of Energy Storage*, 102:113934, 2024.

[33] Atul Rawat, Chandra Prakash Garg, and Priyank Sinha. Analysis of the key hydrogen fuel vehicles adoption barriers to reduce carbon emissions under net zero target in emerging market. *Energy Policy*, 184:113847, 2024.

[34] A.G. Olabi, Mohammad Ali Abdelkareem, Tabbi Wilberforce, Abdul Hai Alami, Ammar Alkhalidi, Mahmoud Mutasim Hassan, and Enas Taha Sayed. Strength, weakness, opportunities, and threats (swot) analysis of fuel cells in electric vehicles. *International Journal of Hydrogen Energy*, 48(60):23185–23211, 2023. The 6th International Hydrogen Technologies Congress (IHTEC-2022).

[35] Gregory Trencher and Joeri Wesseling. Roadblocks to fuel-cell electric vehicle diffusion: Evidence from germany, japan and california. *Transportation Research Part D: Transport and Environment*, 112:103458, 2022.

[36] Pouria Ahmadi and Erik Kjeang. Comparative life cycle assessment of hydrogen fuel cell passenger vehicles in different canadian provinces. *International Journal of Hydrogen Energy*, 40(38):12905–12917, 2015.

[37] Mohammad Waseem, Mohammad Amir, G. Sree Lakshmi, S. Harivardhagini, and Mumtaz Ahmad. Fuel cell-based hybrid electric vehicles: An integrated review of current status, key challenges, recommended policies, and future prospects. *Green Energy and Intelligent Transportation*, 2(6):100121, 2023.

[38] G. Di Ilio, P. Di Giorgio, L. Tribioli, G. Bella, and E. Jannelli. Preliminary design of a fuel cell/battery hybrid powertrain for a heavy-duty yard truck for port logistics. *Energy Conversion and Management*, 243:114423, 2021.

[39] Matti Liukkonen, Antti Lajunen, and Jussi Suomela. Feasibility study of fuel cell-hybrid powertrains in non-road mobile machineries. *Automation in Construction*, 35:296–305, 2013.

[40] Giuseppe De Lorenzo, Rosario Marzio Ruffo, and Petronilla Fragiacomo. Preliminary design of the fuel cells based energy systems for a cruise ship. *World Electric Vehicle Journal*, 14:263, 2023.

[41] R.K. Ahluwalia, X. Wang, A.G. Star, and D.D. Papadias. Performance and cost of fuel cells for off-road heavy-duty vehicles. *International Journal of Hydrogen Energy*, 47(20):10990–11006, 2022.

[42] Pucheng Pei, Qianfei Chang, and Tian Tang. A quick evaluating method for automotive fuel cell lifetime. *International Journal of Hydrogen Energy*, 33(14):3829–3836, 2008. TMS07: Symposium on Materials in Clean Power Systems.

[43] Xiuliang Zhao, Lei Wang, Yinglong Zhou, Bangxiong Pan, Ruochen Wang, Limei Wang, and Xueqing Yan. Energy management strategies for fuel cell hybrid electric vehicles: Classification, comparison, and outlook. *Energy Conversion and Management*, 270:116179, 2022.

[44] Mustafa Ergin Şahin, Frebe Blaabjerg, and Ariya Sangwongwanich. A comprehensive review on supercapacitor applications and developments. *Energies*, 15:674, 2022.

[45] Dai-Duong Tran, Majid Vafaeipour, Mohamed El Baghdadi, Ricardo Barrero, Joeri Van Mierlo, and Omar Hegazy. Thorough state-of-the-art analysis of electric and hybrid vehicle powertrains: Topologies and integrated energy management strategies. *Renewable and Sustainable Energy Reviews*, 119:109596, 2020.

[46] M.A. Hannan, F.A. Azidin, and A. Mohamed. Multi-sources model and control algorithm of an energy management system for light electric vehicles. *Energy Conversion and Management*, 62:123–130, 2012.

[47] Huizhong Gao, Zhijie Wang, Shaoping Yin, Jun Lu, Zhaoyuan Guo, and Weifeng Ma. Adaptive real-time optimal energy management strategy based on equivalent factors optimization for hybrid fuel cell system. *International Journal of Hydrogen Energy*, 46(5):4329–4338, 2021.

[48] Autoblog. World's first hydrogen fuel cell tractor debuts in italy, 2009. Accessed on 7th february 2025.

[49] EOX Tractors. Eox175 infra. Accessed on 10th february 2025.

[50] Fendt. Fendt shows first hydrogen tractor at german hydrogen summit, 2023. Accessed on 7th february 2025.

[51] Fendt. H2 fendt helios tractor on display as part of german hydrogen week 2024, 2024. Accessed on 7th february 2025.

[52] GOFAR. The world's first hydrogen-fueled vineyard tractor is here, 2023. Accessed on 10th february 2025.

[53] CNH. Steyr® and tu wien unveil fctrac biogenic hydrogen–powered tractor project, 2024. Accessed on 23rd february 2025.

[54] JCB. Jcb leads the way with first hydrogen fuelled excavator, 2020. Accessed on 10th february 2025.

[55] HD Hyundai. Hd hyundai xitesolution supplies korea's first 5-ton hydrogen forklift, 2024. Accessed on 10th february 2025.

[56] Komatsu. Komatsu develops medium-sized hydraulic excavator concept machine with a hydrogen fuel cell, 2023. Accessed on 10th february 2025.

[57] Komatsu. Hydrogen in our future development of a medium-sized hydraulic excavator powered by a hydrogen fuel-cell. Accessed on 10th february 2025.

[58] Kobelco Construction Machinery. Operational assessment of hydrogen-driven prototype fuel cell electric excavator: Development of construction machinery for carbon neutrality, 2023. Accessed on 10th february 2025.

[59] Volvo CE. Volvo ce starts testing of the world's first prototype hydrogen articulated hauler, 2022. Accessed on 10th february 2025.

[60] Manitou Group. Overview of the hydrogen strategy, 2022. Accessed on 10th february 2025.

[61] Hans Heinrich Vogt, Rodnei Regis de Melo, Sérgio Daher, Benedikt Schmuelling, Fernando Luiz Marcelo Antunes, Priscila Alves dos Santos, and Daniel Albiero. Electric tractor system for family farming: Increased autonomy and economic feasibility for an energy transition. *Journal of Energy Storage*, 40:102744, 2021.

[62] Gabriele Sara, Giuseppe Todde, Daniele Pinna, and Maria Caria. Evaluating an autonomous electric robot for real farming applications. *Smart Agricultural Technology*, 9:100595, 2024.

[63] Francesco Mocera, Aurelio Somà, Salvatore Martelli, and Valerio Martini. Trends and future perspective of electrification in agricultural tractor-implement applications. *Energies*, 16:6601, 2023.

[64] International Organization for Standardization. Iso 12934:2021 - tractors and machinery for agriculture and forestry — basic types — vocabulary, 2021. Available at: https://www.iso.org/standard/72617.html.

[65] Matteo Beligoj, Elia Scolaro, Luigi Alberti, Massimiliano Renzi, and Michele Mattetti. Feasibility evaluation of hybrid electric agricultural tractors based on life cycle cost analysis. *IEEE Access*, 10:28853 – 28867, 2022.

[66] Fendt. Fendt e100 v vario. Accessed on 23rd february 2025.

[67] Kubota. Kubota lxe series. Accessed on 23rd february 2025.

[68] Monarch. Monarch mk-v. Accessed on 23rd february 2025.

[69] Francesco Mocera, Valerio Martini, and Aurelio Somà. Comparative analysis of hybrid electric architectures for specialized agricultural tractors. *Energies*, 15:1944, 2022.

[70] Francesco Mocera and Valerio Martini. Numerical performance investigation of a hybrid ecvt specialized agricultural tractor. *Applied Sciences*, 12:2438, 2022.

[71] Landini. Landini rex4 full hybrid – technical innovation at eima 2022, 2022. Accessed on 23rd february 2025.

[72] Antonio Carraro. Top models at eima 2022, 2022. Accessed on 23rd february 2025.

[73] Valerio Martini, Francesco Mocera, and Aurelio Somà. Numerical investigation of a fuel cell-powered agricultural tractor. *Energies*, 15:8818, 2022.

[74] Alan Cruz Rojas, Guadalupe Lopez Lopez, J.F. Gomez-Aguilar, Victor M. Alvarado, and Cinda Luz Sandoval Torres. Control of the air supply subsystem in a pemfc with balance of plant simulation. *Sustainability*, 9:73, 2017.

[75] Yujie Wang, Zhendong Sun, and Zonghai Chen. Energy management strategy for battery/supercapacitor/fuel cell hybrid source vehicles based on finite state machine. *Applied Energy*, 254:113707, 2019.

[76] A. A. Golverk. The method for development of a diesel engine universal performance map. *SAE Transactions*, 103:1041–1048, 1994.

[77] Elena Vergori, Francesco Mocera, and Aurelio Somà. Battery modelling and simulation using a programmable testing equipment. *Computers*, 7:20, 2018.

[78] Francesco Mocera, Elena Vergori, and Aurelio Somà. Battery performance analysis for working vehicle applications. *IEEE Transactions on Industry Applications*, 56:644–653, 2020.

[79] Wilfried Voss. *A Comprehensible Guide to Controller Area Network*. Copperhill Technologies Corporation, 2005.

[80] Wilfried Voss. *A Comprehensible Guide to J1939*. Copperhill Technologies Corporation, 2008.

[81] Anders Nordelöf, Maarten Messagie, Anne-Marie Tillman, Maria Ljunggren Söderman, and Joeri Van Mierlo. Environmental impacts of hybrid, plug-in hybrid, and battery electric vehicles-what can we learn from life cycle assessment? *The International Journal of Life Cycle Assessment*, 19:1866–1890, 2014.

[82] Johannes Buberger, Anton Kersten, Manuel Kuder, Richard Eckerle, Thomas Weyh, and Torbjörn Thiringer. Total co2-equivalent life-cycle emissions from commercially available passenger cars. *Renewable and Sustainable Energy Reviews*, 159:112158, 2022.

[83] International Organization for Standardization. Iso 14040:2006 - environmental management — life cycle assessment — principles and framework, 2006. available at: https://www.iso.org/standard/37456.html.

[84] International Organization for Standardization. Iso 14044:2006 - environmental management — life cycle assessment — requirements and guidelines, 2006. available at: https://www.iso.org/standard/38498.html.

[85] Salvatore Martelli, Valerio Martini, Francesco Mocera, and Aurelio Somà. Life cycle assessment comparison of orchard tractors powered by diesel and hydrogen fuel cell. *Energies*, 17:4599, 2024.

[86] Zhichao Liu, Tao Li, Qiuhong Jiang, and Hongchao Zhang. Life cycle assessment–based comparative evaluation of originally manufactured and remanufactured diesel engines. *Journal of Industrial Ecology*, 18:567–576, 2014.

[87] G. Larsson and P.-A. Hansson. Environmental impact of catalytic converters and particle filters for agricultural tractors determined by life cycle assessment. *Biosystems Engineering*, 109(1):15–21, 2011.

[88] Yahong Dong, Yating Zhao, Md. Uzzal Hossain, Yan He, and Peng Liu. Life cycle assessment of vehicle tires: A systematic review. *Cleaner Environmental Systems*, 2:100033, 2021.

[89] Lorenzo Usai, Christine Roxanne Hung, Felipe Vásquez, Max Windsheimer, Odne Stokke Burheim, and Anders Hammer Strømman. Life cycle assessment of fuel cell systems for light duty vehicles, current state-of-the-art and future impacts. *Journal of Cleaner Production*, 280:125086, 2021.

[90] U.S. Department of Energy. DOE Technical Targets for Polymer Electrolyte Membrane Fuel Cell Components, 2021. Accesso: 25 marzo 2025.

[91] Andrew Simons and Christian Bauer. A life-cycle perspective on automotive fuel cells. *Applied Energy*, 157:884–896, 2015.

[92] Marco Miotti, Johannes Hofer, and Christian Bauer. Integrated environmental and economic assessment of current and future fuel cell vehicles. *The International Journal of Life Cycle Assessment*, 22:94–110, 2017.

[93] X. Tuaev and P. Strasser. 4 - small angle x-ray scattering (saxs) techniques for polymer electrolyte membrane fuel cell characterization. In Christoph Hartnig and Christina Roth, editors, *Polymer Electrolyte Membrane and Direct Methanol Fuel Cell Technology*, volume 2 of *Woodhead Publishing Series in Energy*, pages 87–119. Woodhead Publishing, 2012.

[94] Toshihiko Yoshida and Koichi Kojima. Toyota mirai fuel cell vehicle and progress toward a future hydrogen society. *The Electrochemical Society Interface*, 24(2):45, jan 2015.

[95] Mitja Mori, Diego Iribarren, Julie Cren, Emmanuelle Cor, Andrej Lotrič, Jure Gramc, Boštjan Drobnič, Laurent Rey, Felipe Campos-Carriedo, Gonzalo Puig-Samper, Eleonora Bargiacchi, Javier Dufour, and Rok Stropnik. Life cycle sustainability assessment of a proton exchange membrane fuel cell technology for ecodesign purposes. *International Journal of Hydrogen Energy*, 48(99):39673–39689, 2023. Integrated Hydrogen Energy Systems.

[96] Yong Yang Jayanti Sinha, Stephen Lasher and Peter Kopf. Direct hydrogen pemfc manufacturing cost estimation for automotive applications. fuel cell tech team review 2008, 2008. Accesso: 14 aprile 2025.

[97] J. Sinha S. Sriramulu E.J. Carlson, P. Kopf and Y. Yang. Cost analysis of pem fuel cell systems for transportation, 2005. Accesso: 14 aprile 2025.

[98] Alicia Benitez, Christina Wulf, Andreas de Palmenaer, Michael Lengersdorf, Tim Röding, Thomas Grube, Martin Robinius, Detlef Stolten, and Wilhelm Kuckshinrichs. Ecological assessment of fuel cell electric vehicles with special focus on type iv carbon fiber hydrogen tank. *Journal of Cleaner Production*, 278:123277, 2021.

[99] Qiang Dai, Jarod C. Kelly, Linda Gaines, and Michael Wang. Life cycle analysis of lithium-ion batteries for automotive applications. *Batteries*, 5:48, 2019.

[100] Jens F. Peters and Marcel Weil. Providing a common base for life cycle assessments of li-ion batteries. *Journal of Cleaner Production*, 171:704–713, 2018.

[101] Nowsheen Sharmili, Rakesh Nagi, and Pingfeng Wang. A review of research in the li-ion battery production and reverse supply chains. *Journal of Energy Storage*, 68:107622, 2023.

[102] Oscar Lagnelöv, Gunnar Larsson, Anders Larsolle, and Per-Anders Hansson. Life cycle assessment of autonomous electric field tractors in swedish agriculture. *Sustainability*, 13:11285, 2021.

[103] Anders Nordelöf, Emma Grunditz, Anne-Marie Tillman, Torbjörn Thiringer, and Mikael Alatalo. A scalable life cycle inventory of an electrical automotive traction machine—part i: design and composition. *The International Journal of Life Cycle Assessment*, 23:55–69, 2018.

[104] Anders Nordelöf, Emma Grunditz, Sonja Lundmark, Anne-Marie Tillman, Mikael Alatalo, and Torbjörn Thiringer. Life cycle assessment of permanent magnet electric traction motors. *Transportation Research Part D: Transport and Environment*, 67:263–274, 2019.

[105] Anders Nordelöf and Anne-Marie Tillman. A scalable life cycle inventory of an electrical automotive traction machine—part ii: manufacturing processes. *The International Journal of Life Cycle Assessment*, 23:295–313, 2018.

[106] B. Sudha, Anusha Vadde, and S. Sachin. A review: high power density motors for electric vehicles. *Journal of Physics: Conference Series*, 1706:012057, 2020.

[107] Briac Baudais, Hamid Ben Ahmed, Gurvan Jodin, Nicolas Degrenne, and Stéphane Lefebvre. Life cycle assessment of a 150 kw electronic power inverter. *Energies*, 16:2192, 2023.

[108] Fernando Enzo Kenta Sato and Toshihiko Nakata. Energy consumption analysis for vehicle production through a material flow approach. *Energies*, 13:2396, 2020.

[109] Edemilson J. Mantoam, Thiago L. Romanelli, and Leandro M. Gimenez. Energy demand and greenhouse gases emissions in the life cycle of tractors. *Biosystems Engineering*, 151:158–170, 2016.

[110] Jacopo Bacenetti. How does annual utilisation can affect the environmental impact of tractors? a life-cycle assessment comparing hypothetical scenarios for farmers and agricultural contractors in northern italy. *Biosystems Engineering*, 213:63–75, 2022.

[111] Miyuru Kannangara, Farid Bensebaa, and Madhav Vasudev. An adaptable life cycle greenhouse gas emissions assessment framework for electric, hybrid, fuel cell and conventional vehicles: Effect of electricity mix, mileage, battery capacity and battery chemistry in the context of canada. *Journal of Cleaner Production*, 317:128394, 2021.

[112] Pouria Ahmadi and Alireza Khoshnevisan. Dynamic simulation and life-cycle assessment of hydrogen fuel cell electric vehicles considering various hydrogen production methods. *International Journal of Hydrogen Energy*, 47(62):26758–26769, 2022. SI: Progress in Hydrogen Production, Storage and Distribution (Ahmadi).

[113] Daniela Lovarelli, Jacopo Bacenetti, and Marco Fiala. A new tool for life cycle inventories of agricultural machinery operations. *Journal of Agricultural Engineering*, 47(1):40–53, Mar. 2016.

[114] Andrej Lotrič, Mihael Sekavčnik, Igor Kuštrin, and Mitja Mori. Life-cycle assessment of hydrogen technologies with the focus on eu critical raw materials and end-of-life strategies. *International Journal of Hydrogen Energy*, 46(16):10143–10160, 2021. Hydrogen and Fuel Cells.

[115] David da Silva Vasconcelos, Jorge Alberto Soares Tenório, Amilton Barbosa Botelho Junior, and Denise Crocce Romano Espinosa. Circular recycling strategies for lfp batteries: A review focusing on hydrometallurgy sustainable processing. *Metals*, 13(3):543, 2023.

[116] María-Pilar Martínez-Hernando, Enrique García-Franco, David Bolonio, Marcelo F. Ortega, and María-Jesús García-Martínez. Life cycle sustainability assessment of the platinum supply chain in the european union. *Sustainable Production and Consumption*, 46:679–689, 2024.

[117] Lucien Duclos, Maria Lupsea, Guillaume Mandil, Lenka Svecova, Pierre-Xavier Thivel, and Valérie Laforest. Environmental assessment of proton exchange membrane fuel cell platinum catalyst recycling. *Journal of Cleaner Production*, 142:2618–2628, 2017.

[118] Mark A. J. Huijbregts, Zoran J. N. Steinmann, Pieter M. F. Elshout, Gea Stam, Francesca Verones, Marisa Vieira, Michiel Zijp, Anne Hollander, and Rosalie van Zelm. Recipe2016: a harmonised life cycle impact assessment method at midpoint and endpoint level. *The International Journal of Life Cycle Assessment*, 22:138–147, 2017.

[119] Xianxian Xu, Quan Zhou, and Dehai Yu. The future of hydrogen energy: Bio-hydrogen production technology. *International Journal of Hydrogen Energy*, 47(79):33677–33698, 2022.

[120] Zhikai Chen, Haiyang Huang, Ting Shi, Xueyuan Peng, and Jianmei Feng. Efficiency improvement and thermo-economic analysis of proton exchange membrane fuel cell system with energy recovery for both air and hydrogen. *Applied Thermal Engineering*, 233:121114, 2023.

[121] Jimiao Zhang and Jie Li. Revolution in renewables: Integration of green hydrogen for a sustainable future. *Energies*, 17:4148, 2024.

[122] Miles Krebs-Moberg, Mandy Pitz, Tiara L. Dorsette, and Shabbir H. Gheewala. Third generation of photovoltaic panels: A life cycle assessment. *Renewable Energy*, 164:556–565, 2021.

[123] Muhammad Haider Ali Khan, Tarun Sitaraman, Nawshad Haque, Greg Leslie, Serkan Saydam, Rahman Daiyan, Rose Amal, and Sami Kara. Strategies for life cycle impact reduction of green hydrogen production – influence of electrolyser value chain design. *International Journal of Hydrogen Energy*, 62:769–782, 2024.

[124] Franc Mihalič, Mitja Truntič, and Alenka Hren. Hardware-in-the-loop simulations: A historical overview of engineering challenges. *Electronics*, 11:2462, 2022.

[125] A. Bouscayrol. Different types of hardware-in-the-loop simulation for electric drives. In *Proceeding of the IEEE International Symposium on Industrial Electronics*, Cambridge, UK, 2008.

[126] Mehroze Iqbal, Julien Laurent, Amel Benmouna, Mohamed Becherif, Haitham S. Ramadan, and Frederic Claude. Ageing-aware load following control for composite-cost optimal energy management of fuel cell hybrid electric vehicle. *Energy*, 254:124233, 2022.

[127] Henning Lohse-Busch, Kevin Stutenberg, Michael Duoba, Xinyu Liu, Amgad Elgowainy, Michael Wang, Thomas Wallner, Brad Richard, and Martha Christenson. Automotive fuel cell stack and system efficiency and fuel consumption based on vehicle testing on a chassis dynamometer at minus 18°c to positive 35°c temperatures. *International Journal of Hydrogen Energy*, 45(1):861–872, 2020.

[128] Xiao-Guang Yang, Teng Liu, and Chao-Yang Wang. Thermally modulated lithium iron phosphate batteries for mass-market electric vehicles. *Nature Energy*, 6:176–185, 2021.

[129] Zekalabs. Tinoprime 20kw. https://zekalabs.com/products/isolated-power-converters/dc-dc-isolated-converter-20kw-500a/, 2025. Accessed: 2025-05-25.

[130] Eaton. Supercapacitor modules. https://www.eaton.com/us/en-us/catalog/capacitors/supercapacitor-modules.html, 2025. Accessed: 2025-05-25.

[131] Noshin Omar, Mohamed Abdel Monem, Yousef Firouz, Justin Salminen, Jelle Smekens, Omar Hegazy, Hamid Gaulous, Grietus Mulder, Peter Van den Bossche, Thierry Coosemans, and Joeri Van Mierlo. Lithium iron phosphate based battery – assessment of the aging parameters and development of cycle life model. *Applied Energy*, 113:1575–1585, 2014.

[132] Juan Pablo Rivera-Barrera, Nicolás Muñoz-Galeano, and Henry Omar Sarmiento-Maldonado. Soc estimation for lithium-ion batteries: Review and future challenges. *Electronic*, 6:102, 2017.

[133] J. Nájera, J.R. Arribas, R.M. de Castro, and C.S. Núñez. Semi-empirical ageing model for lfp and nmc li-ion battery chemistries. *Journal of Energy Storage*, 72:108016, 2023.

[134] Thibaut Kovaltchouk, Bernard Multon, Hamid Ben Ahmed, Judicaël Aubry, and Pascal Venet. Enhanced aging model for supercapacitors taking into account power cycling: Application to the sizing of an energy storage system in a direct wave energy converter. *IEEE Transactions on Industry Applications*, 51(3):2405–2414, 2015.

[135] David C. Robertson, Jon P. Christophersen, Taylor Bennett, Lee K. Walker, Fang Wang, Shiqiang Liu, Bin Fan, and Ira Bloom. A comparison of battery testing protocols: Those used by the u.s. advanced battery consortium and those used in china. *Journal of Power Sources*, 306:268–273, 2016.

[136] Jon P. Christopherson. Battery test manual for electric vehicles. Technical Report INL/EXT-15-35503, Idaho National Laboratory, Idaho Falls, ID, USA, May 2015.

[137] Konstantina Ragazou, Alexandros Garefalakis, Eleni Zefeiriou, and Ioannis Passas. Agriculture 5.0: A new strategic management mode for a cut cost and an energy efficient agriculture sector. *Energies*, 15:3113, 2022.

[138] Maria Spagnuolo, Giuseppe Todde, maria Caria, Nicola furnitto, Giampaolo Schillaci, and Sabina Failla. Agricultural robotics: A technical review addressing challenges in sustainable crop production. *Robotics*, 14:9, 2025.

[139] Lei Liu, Fan Yang, Xiangyi Liu, Yuefeng Du, Xiaoyu Li, Guorun Li, Du Chen, Zhongxiang Zhu, and Zhenghe Song. A review of the current status and common key technologies for agricultural field robots. *Computers and Electronics in Agriculture*, 227:109630, 2024.

[140] Mattia Scanavino. Progettazione e simulazione di rover elettrici a guida autonoma per applicazioni agricole, 2023.

[141] FAO. Faostat database: Crops and livestock products (qcl). https://www.fao.org/faostat/en/data/QCL, 2025. Accessed on 16th August 2025.

[142] Burro. Burro. https://burro.ai/burro/, 2025. Accessed on 16th August 2025.

[143] Agxeed. Agbot 5.115t2. https://www.agxeed.com/our-solutions/agbot-5-115t2/, 2025. Accessed on 16th August 2025.

[144] Naio. Ted robot. https://www.naio-technologies.com/en/ted-robot/, 2025. Accessed on 16th August 2025.

[145] Robotics Plus. Robotics plus prospr. https://www.roboticsplus.co.nz/products/ground-vehicles/unmanned-ground-vehicle, 2025. Accessed on 16th August 2025.

[146] SwarmFarm Robotics. https://www.swarmfarm.com/applications/, 2025. Accessed on 16th August 2025.

[147] Monarch. Mk-v tractor. https://www.monarchtractor.com/mk-v-electric-tractor, 2025. Accessed on 16th August 2025.

[148] Lin Haibo, Dong Shuliang, Liu Zunmnin, and Yi Chuijie. Study and experiment on a wheat precision seeding robot. *Journal of Robotics*, 1:1–9, 2024.

[149] AutoAgri. Ic-20. https://autoagri.no/ic-20/, 2025. Accessed on 17th August 2025.

[150] Francesco Mocera, Aurelio Somà, and Andrea Nicolini. Grousers effect in tracked vehicle multibody dynamics with deformable terrain contact model. *Applied Sciences*, 10:6581, 2020.

[151] Carl Becker and Schalk Els. Agricultural tyre stiffness change as a function of tyre wear. *Journal of Terramechanics*, 102:1–15, 2022.

[152] J.A. Lines and K. Murphy. The stiffness of agricultural tractor tyres. *Journal of Terramechanics*, 28(1):49–64, 1991.

[153] Woo-Jin Chung Hyun-Woo Han Ji-Tae Kim Young-Jun Park Yoonna Park Hogil Yoo, Jooseon Oh. Measurement of stiffness and damping coefficient of rubber tractor tires using dynamic cleat test based on point contact model. *International Journal of Agricultural and Biological Engineering*, 14(1):157–164, 2021.

[154] Đỗ Minh Cường, Zhu Shi Hong, Đinh Vương Hùng, and Nguyễn Thị Ngọc. Study on the vertical stiffness and damping coefficient of tractor tire using semi-empirical model. *Hue University Journal of Science: Agri-716 culture and Rural Development*, 83, 2013.

[155] Valerio Martini, Francesco Mocera, and Aurelio Somà. Carbon footprint enhancement of an agricultural telehandler through the application of a fuel cell powertrain. *World Electric vehicle Journal*, 15(3):91, 2024.

[156] Lixing Liu, Xu Wang, Xin Yang, Hongjie Liu, Jianping Li, and Pengfei Wang. Path planning techniques for mobile robots: Review and prospect. *Expert Systems with Applications*, 227:120254, 2023.

[157] Andrei M. Shkel and Vladimir Lumelsky. Classification of the dubins set. *Robotics and Autonomous Systems*, 34(4):179–202, 2001.

[158] Steve Macenski, Shrijit Singh, Francisco Martín, and Jonatan Ginés. Regulated pure pursuit for robot path tracking. *Autonomous Robots*, 47:685–694, 2023.

[159] Cheng Hu, Jingwei Gao, Jincheng Diao, and Xiaobo Song. Numerical simulation of tire steering on sandy soil based on discrete element method. *AIP Advances*, 11(1):015015, 01 2021.

[160] Peter D. Cenek, Neil J Jamieson, and Maurice W. McLarin. Frictional characteristics of roadside grass types. In *Proceedings of the International Surface Friction Conference: Road and Runways: Improving Safety through Assessment and Design*, Christchurch, New Zealand, May 2005.

[161] D. Samuelraj, S. Jaichandar, G. Rajan, and S. Govindan. Coefficient of friction in different road conditions by various control methods - an overall review. *International Journal of Mechanical and Production Engineering Research and Development*, 8:9–20, 2018.

[162] Elecdan Converter. Universal buck-boost converter. https://elecdan-converter.com/universal-buck-boost-mini-regulator-dc-dc-3kw/, 2025. Accessed on 21th August 2025.

Appendix A

LCA analysis

The LCA analysis impact assessment was performed using the Ecoinvent v3.0 database, which is a widely used life cycle inventory database providing transparent and peer-reviewed data on material, energy, and emission flows, enabling consistent and reproducible life cycle assessment studies. The software used for the analysis was the OpenLCA software. In the following subsections, some examples about the adopted approach are provided.

A.1 Production phase impact assessment

The production phase impact assessment considered all the impact associated to the manufacturing of a part, starting from the raw material extraction to the final product. To provide an example, according to this approach the impact for the manufacturing of 1 kg of steel sheet was evaluated considering the following elementary flows:

- Mining of 1.6 kg iron ores, assuming an average iron content of 60%.
- Production of approximately 1 kg of pig iron from iron ores.
- Production of 1 kg of steel from pig iron through basic oxygen furnace process.
- Hot and sheet rolling manufacturing processes to obtain the final product, namely a steel sheet.

When considering a whole component, for example the electric motor, its impact was evaluated considering the impact associated to the production of all its materials and sub-components. To provide an example, the impact assessment for the production of the 75-kW electric motor was obtained considering:

- The production of approximately 22.6 kg of electrical steel and 3 kg of stainless steel; according to the previous approach, the impact was evaluated starting from the raw material extraction to the manufactured sub-component, and the same approach was used for the other sub-components.
- The production of 11 kg of Aluminum.
- The production of 4.8 kg of Copper.
- The production of 1.3 kg of permanent magnets.
- The production of 0.5 kg of epoxy resin.
- The production of 4.8 kg of wires.
- The production of 3.5 kWh of electric energy for motor assembly.

Thus, once defined the impact of the process to manufacture a sub-component (such as steel sheet, wires, and so on), the impact of a component (such as the electric motor) was obtained by the sum of all the impacts related to the production of its sub-components. The impact of the whole vehicle was then evaluated considering the production of all its components, their transport, and the energy required for assembly.

A.2 Use phase fuel production impact assessment

In the Ecoinvent database, it is possible to find the impact associated to the production of both diesel and hydrogen. The impact associated to the fuel transport generally is not included and must be added. To provide an example, the impact for the production of 1 kg hydrogen was modeled considering the actual production mix:

- Production of 0.62 kg of hydrogen through steam methane reforming.

- Production of 0.20 kg of hydrogen through coal gasification.
- Production of 0.15 kg of hydrogen as by product in refineries.
- Production of 0.03 kg of hydrogen through water electrolysis powered with PV panels.

To the impact associated to the fuel production, the contribution related to fuel transport was added.

A.3 End-of-life impact assessment

Regarding the End-of-life impact assessment, the approach was the following: given a component whose materials had to be recycled, first the energy required to its transport to the recycling facility had to be considered; next, the energy required to disassembly and to sort the obtained sub-components and materials was considered; Lastly, the obtained materials and sub-components underwent recycling processes depending on the specific case. As a consequence, during the end-of-life impact assessment, there were flows that always had a positive contribution in terms of emissions (namely, the transport to the recycling facility and the energy required for disassembly). When considering the recycling process, the negative contributions to the emissions were evaluated considering that, if a part was recycled, the impact related to its production in terms of raw material extraction and treatments to obtain the final material was recovered. Obviously, the recovery rate had to be considered.

To provide an example, the recycling process for 1 kg steel was modeled as follows:

- Production of iron scrap, sorted and pressed, from the original component (positive contribution).
- Recycling process of 1 kg of iron scrap in an electric arc furnace (positive contribution).
- Outputs: 0.88*1.6 kg mining of iron ores, 0.88*1.0 kg of pig iron, 0.88*1.0 kg of steel (produced through basic oxygen furnace process) (negative contribution).

Accordingly, the negative contribution, and consequently the reduction in the total cradle-to-grave emissions, was evaluated considering that if 1 kg of material was recycled with a certain recovery rate, the impact associated to the production of 1*RR kg of that material was "recovered". On the contrary, if a material had to be landfilled, no negative contribution, and thus no reduction in the total emissions, could be achieved.

Appendix B

HIL test bench control units schematics

B.1 HIL test bench for the comparative analysis

In this section, the circuit schematics of the control unit developed for the scaled HIL test bench, used for the comparative analysis of different fuel cell hybrid architectures presented in Section 3.1, is shown.

The control unit was developed as a three-level structure. The lower level was the power stage level, in which the power sources and the electronic load were connected electronically. This layer also contained the voltage and current transducers. The second layer was the signal level, whose role was to generate the control signals. This level contained the operational amplifiers, the optocouplers, and all the elements that were used for signal generations. Lastly, the upper level consisted of the micro-controller board. Wires were used to connect the micro-controller board ports to the other levels of the control unit. The control unit also had to deliver 12 V and 5 V for the transducers power supplies. The circuit schematics of the power and signal levels are shown in Figures B.1 and B.2. A 3D figure of the control unit PCB is shown in Figure B.3. The Gerber files of the PCBs are available at the following url: https://doi.org/10.5281/zenodo.17482092.

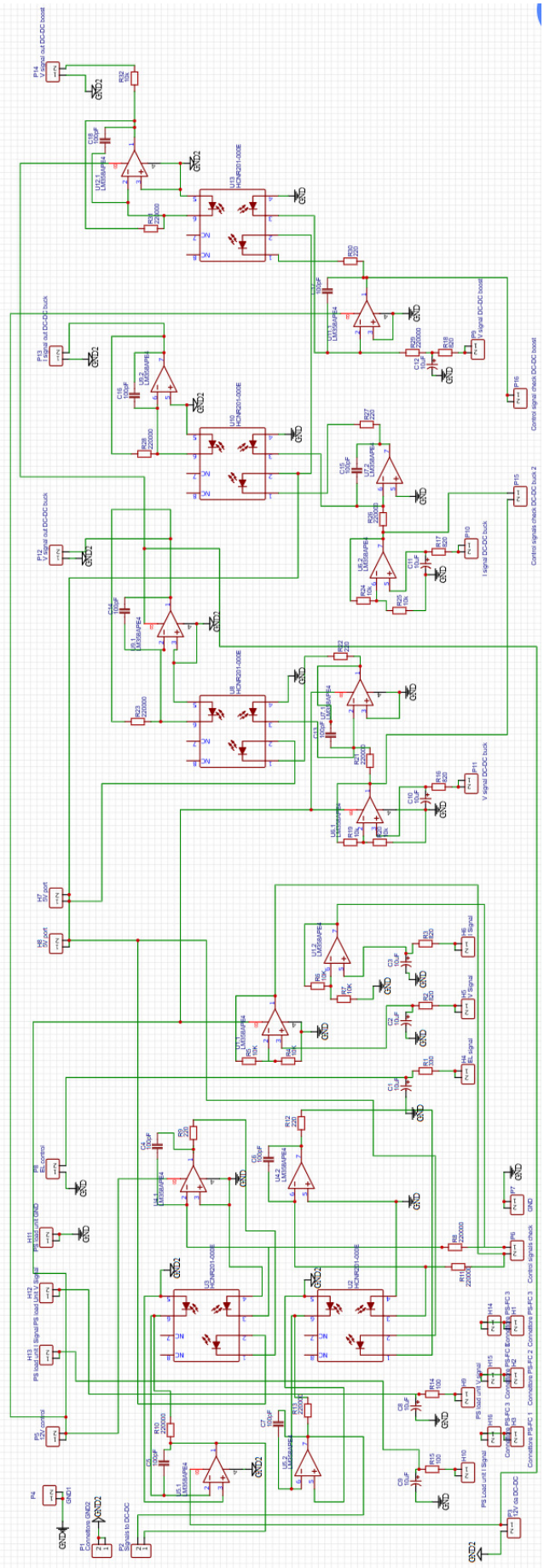

Figure B.1 Signal level circuit schematics.

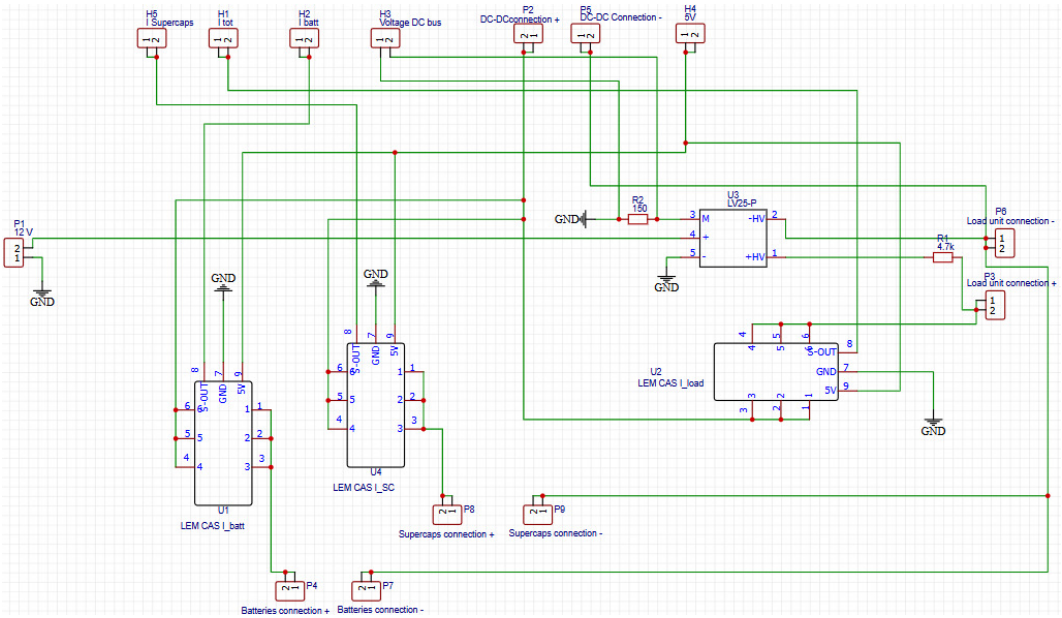

Figure B.2 Power level circuit schematics.

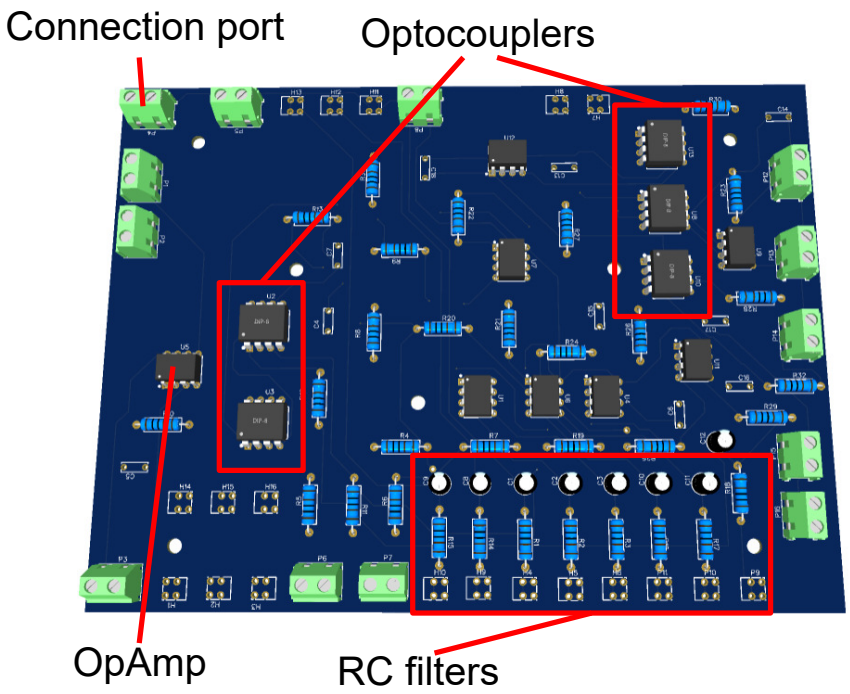

Figure B.3 3D image of the control layer PCB.

B.2 HIL test bench for Smilla H2 powertrain

In this section, the circuit schematics of the control unit developed for the HIL test bench of the Smilla H2 powertrain are shown and described.

The approach adopted during the design stage was similar to that used for the design of the control unit developed for the previous HIL analysis. The main difference is that the upper layer, namely the micro-controller layer, was integrated in the control layer, and thus the structure was reduced to a double layer one.

The control layer was improved by substituting the generation of the control signals, previously generated directly by the micro-controller as PWM signals and then filtered with RC filters to be converted into analog, with the adoption of DACs. This allowed to improve resolution (from 8 bits to 12 bits) and precision. In addition, an 8-channel ADC was added to collect data from the transducers. In the previous configuration, the analog signals from the transducers were directly read by the micro-controller. Also in this case, the consequences of adding an ADC were improved resolution (from 10 bits to 12 bits) and stability. In addition, the power supply of the control section was generated with an isolated DC-DC converter and a voltage regulator to guarantee a stable voltage level. The power supply for the optocouplers was generated with another identical dedicated system.

As for the power layer, the structure was composed of current transducers on the battery and load sides, and of a voltage transducer to monitor the DC bus voltage level. The adopted components are the LEM CAS 50-NP as current transducers and the LEM LV 25-P as voltage transducer. A fuse was placed on the batteries side to protect the circuit.

The circuit schematics for the control layer is shown in Figure B.4, and a 3D image of the PCB is shown in Figure B.5. The circuit schematics of the power layer is shown in Figure B.6. The PCBs Gerber files are available at the following url https://doi.org/10.5281/zenodo.17482157.

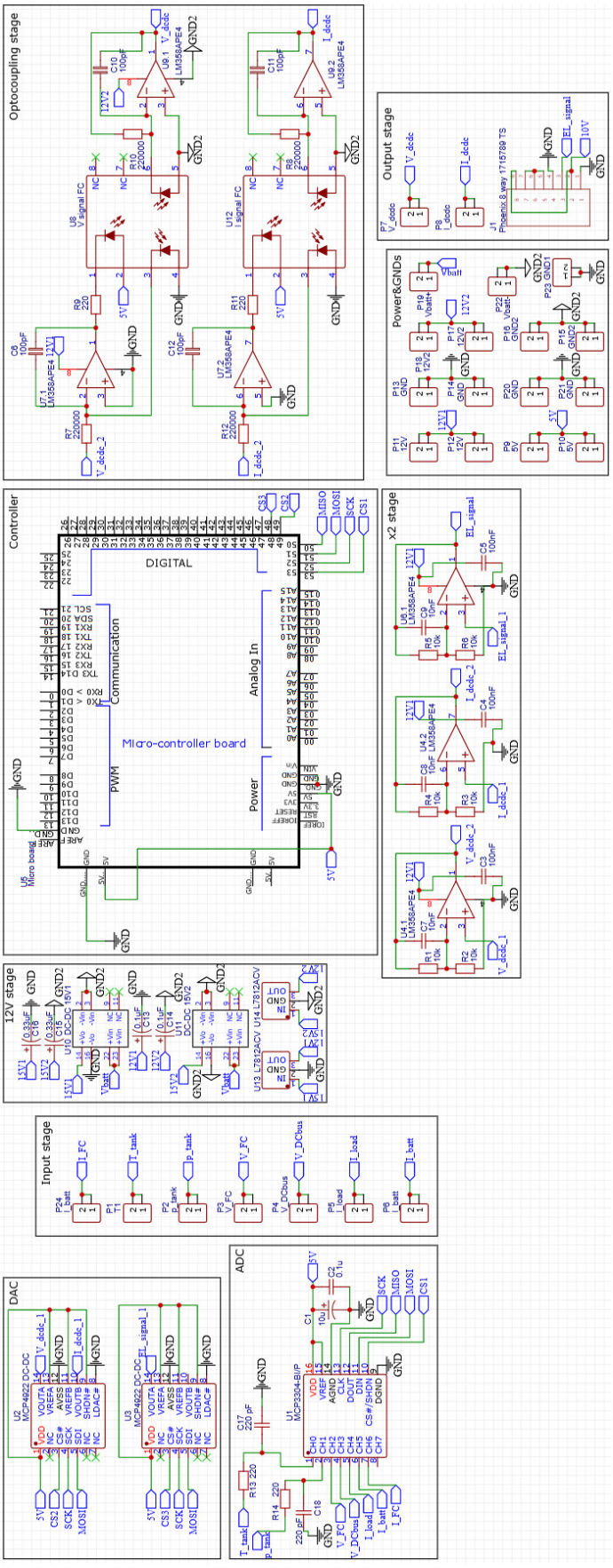

Figure B.4 Smilla HIL control unit top layer.

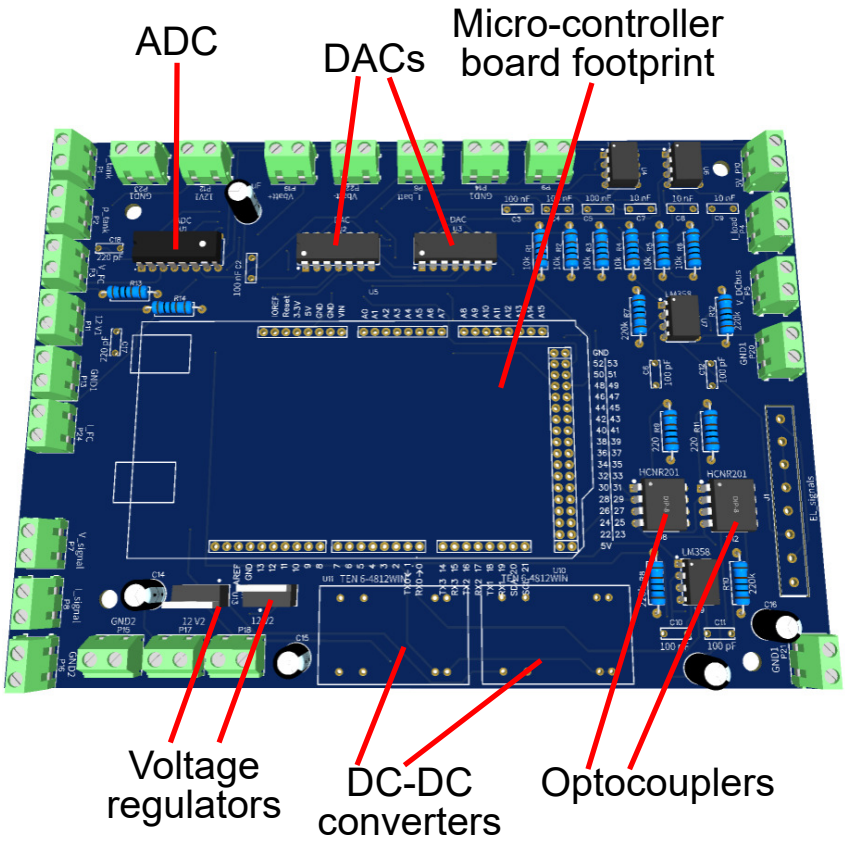

Figure B.5 3D image of the control layer PCB for Smilla HIL test bench.

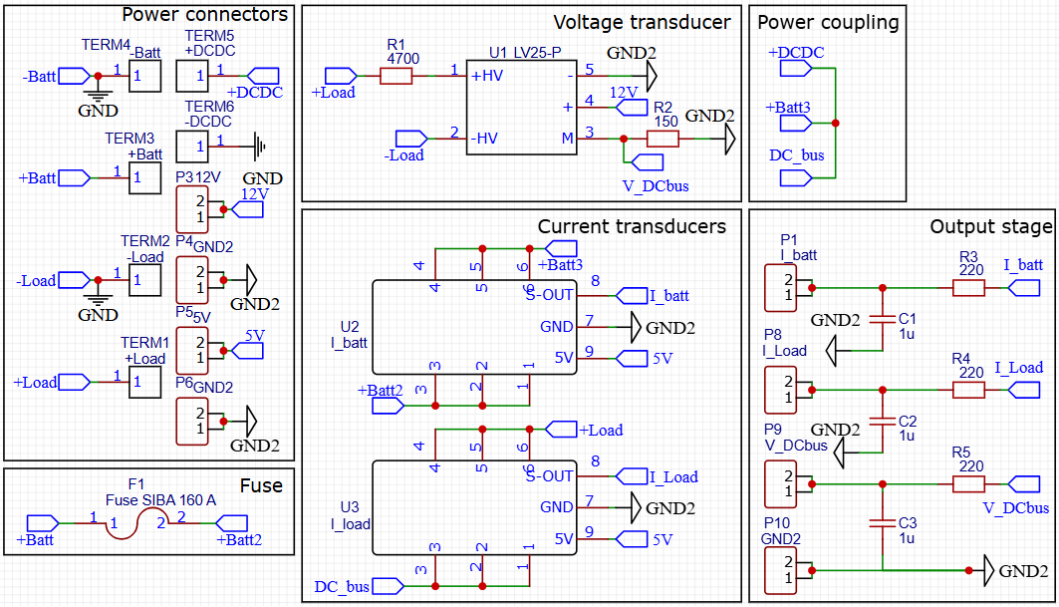

Figure B.6 Smilla HIL control unit power layer.